Learning and Analytics in Intelligent Systems 11

Nenad Filipovic *Editor*

Computational Bioengineering and Bioinformatics

Computer Modelling in Bioengineering

Springer

Learning and Analytics in Intelligent Systems

Volume 11

The main aim of the series is to make available a publication of books in hard copy form and soft copy form on all aspects of learning, analytics and advanced intelligent systems and related technologies. The mentioned disciplines are strongly related and complement one another significantly. Thus, the series encourages cross-fertilization highlighting research and knowledge of common interest. The series allows a unified/integrated approach to themes and topics in these scientific disciplines which will result in significant cross-fertilization and research dissemination. To maximize dissemination of research results and knowledge in these disciplines, the series publishes edited books, monographs, handbooks, textbooks and conference proceedings.

More information about this series at http://www.springer.com/series/16172

Nenad Filipovic
Editor

Computational Bioengineering and Bioinformatics

Computer Modelling in Bioengineering

Springer

Editor
Nenad Filipovic
Faculty of Engineering
University of Kragujevac
Kragujevac, Serbia

ISSN 2662-3447 ISSN 2662-3455 (electronic)
Learning and Analytics in Intelligent Systems
ISBN 978-3-030-43657-5 ISBN 978-3-030-43658-2 (eBook)
https://doi.org/10.1007/978-3-030-43658-2

This Springer imprint is published by the registered company Springer Nature Switzerland AG
The registered company address is: Gewerbestrasse 11, 6330 Cham, Switzerland

Contents

Role of Atomic and Molecular Non-observable Properties in the Understanding and Description of Real Observables of the Chemical Systems. A Review

Ivan Juranić(✉)

University of Belgrade, IChTM, Centre for Chemistry, Studentski trg 16, 11000 Belgrade, Serbia
ijuranic@chem.bg.ac.rs

Abstract. Chemical species can be characterized by various observable features: mass, enthalpy of formation, charge (ions), dipole moment, magnetic susceptibility, electrical susceptibility, electromagnetic spectra, refraction index, polarizability, electron density distribution etc. But, on the other hand, the understanding of chemical an physical behavior is usually based on specific non-observable features - for example: electronegativity, partial atomic charges, nucleophilicity, atomic and molecular orbitals, aromaticity, hyperconjugation, … All non-observable features generally have no physical unit, and are not amenable to experimental measurements. For that reason the values ascribed to them are strongly dependent on the definition(s). For example, we know (and use) various electronegativity scales: Pauling's, Mulliken's, Alfred-Rochov's [1, 2], Sanderson's, Allen's, and other. They are based on different theoretical assumptions, and produce (on many instances, significantly) different numerical values. On the other hand, all scales follow similar general trend, indicating that the values reflect some intrinsic chemical property.

1 Introduction

Electronegativity, as a concept, is highly powerful for rationalization of atomic and molecular properties and reactivity, and many attempts were made to obtain the scale which will precisely mimic them. The first electronegativity scale was proposed by Pauling [3]. It was based on the fact that the energy, D, of a heteronuclear bond, A&B, is generally higher than the average bond energies of the homonuclear bonds, A&A and B&B. (This is actually the root of idea of *resonance*.)

$$D(AB) = \frac{1}{2}[D(AA) + D(BB)] + \Delta_{AB}$$

The square root of the stabilization term, Δ_{AB}, was found to be proportional to atomic constants that were defined by Pauling as atomic electronegativities,

$$\sqrt{\Delta_{AB}} \propto \chi_A - \chi_B.$$

N. Filipovic (Ed.): ICCB 2019, LAIS 11, pp. 1–11, 2020.
https://doi.org/10.1007/978-3-030-43658-2_1

It was quickly recognized that electronegativity of an atom depends on the other bonds in the molecule (*e.g.* on hybridization).

Another method for definition of electronegativity is well designed for account of mode of bonding. Mulliken electronegativities are defined as a balance between electron attracting and electron releasing ability [4]:

Hence, Mulliken defined the electronegativity of an orbital ν (another unobservable) of an atom A as the mean of the correspondent ionization potential ($I_{A\nu}$) and electron affinity ($E_{A\nu}$),

$$\chi_{A\nu} = \frac{1}{2}(I_{A\nu} + E_{A\nu})$$

Based on Mulliken's definition, a number of 'improved' models emerge [5–9]. Many of them have rather sophisticated computational methodology, but in essence a little improvement was achieved.

Generally, use of Mulliken electronegativities is most popular due the simplicity of the calculation method.

Situation with partial atomic charges (PAC) is even more complicated, because more than 30 different scales are known, and can be divided in four classes, based on the method for defining them.

Concept of partial atomic charges, which is also important term in chemistry, is closely connected to the electronegativity. First definition is known as Coulson's net atomic charges [10].

$$q_A = Z_A - \sum_{\mu \in A} P_{\mu\mu}$$

where q_A is the net atomic charge on A^{th} nucleus, Z_A the charge of A^{th} nucleus (atomic number), and $P_{\mu\mu}$ the density matrix given by the summation of multiplications of M.O. coefficients (c) over occupied orbitals;

$$P_{\mu\mu} = \sum_{i=1}^{occ} c_{\mu i} c_{\nu i}$$

Originally it was introduced for the analysis of Hückel molecular orbitals, but quickly is upgraded with Mulliken definition [11] which is better suited for the analysis of all valence orbitals population.

$$q_A = Z_A - \sum_{\mu \in A} \sum_{\nu \in A} P_{\mu\eta} S_{\mu\nu}$$

where $S_{\mu\nu}$ is the overlap matrix. Therefore, the Mulliken's net atomic charges give similar values to the Coulson net atomic charges.

Further variant based on the same (Mulliken's) idea is proposed by Mayer [12, 13] involving much more sophisticated model for interatomic electron density partition. Amount of such variants for the calculation of PAC is very large, but it is hard to pick one which is more reliable than the other.

Density functional theory is a quantum-chemical method for accurate calculation of electron density distribution. It stems from the basic idea of quantum chemistry, that all molecular properties are derived from the distribution of electron density in molecule(s). Corollary, it justifies the use of partial atomic charges in molecule which reflect the distribution of electron density. Specificity of DFT method(s) is in the inclusion of electron correlation in the calculation of electron distribution in molecule. Besides DFT, many semiempirical methods implicitly include electron correlation in the distribution of electron density calculations. Therefore, they offer a quick computation methodology for the calculation of the distribution of electron density in the molecule.

2 Observables Correlated with Partial Atomic Charges

Partial atomic charges were tested as a reliable method for the calculation of the observable properties of molecules [14].

The observable which is naturally most directly related to PAC, is the **dipole moment** of molecules. In the special case of diatomic molecules, dipole moments can be used for experimental determination of partial atomic charges.

There are number of results on **ESCA and ^{1}H-NMR chemical shifts**, [15–20] dependence on partial atomic charges. PAC values were proven to be important, but chemical shifts in ESCA and NMR are markedly influenced by general electron density distribution.

Many studies were devoted to **Electrostatic effects between molecules**. The models for the prediction of conformations and properties of polymers [21, 22] and proteins [23, 24] are mostly based on electrostatic interactions between partially charged atoms in the neighboring polymer chains. Optimization of these interaction may lead to definition of electrostatic potential surfaces, and from them can be inferred a special scale of partial atomic charges. These charges are very reasonable for the atoms on the surface of molecules, but are quite unreasonable for atoms buried inside the complex molecule.

It was proven that **Electronic polarizability** is strongly coupled with atomic charges, [25, 26] and was mostly applied for the structures in the solid state [27].

Chromatographic retention indices were well correlated with molecular descriptors based on atomic partial charges [28, 29]. Using similar methodology, the odor thresholds were successfully predicted, too.

Surface tension, boiling point, [29, 30] simulation of bulk densities, surface tension, and molecular orientation at liquid/vapor interface of molecular system, [31] hydration free energy estimates, [32] and many other simulations of observables are based on PAC [33–35].

A common chemist's intuition hints that **acid dissociation constants** should be directly related to the partial charge on acidic hydrogen [36]. The acid dissociation constant, K_a, which describes the extent to which the compound dissociates in the gas phase or in the solution, is a fundamental property of many chemical compounds. It is a key feature which governs the chemical reactivity of the substances in any solvent, and the interaction with the solvent itself. In aqueous solution, the pK_a is a proxy for several pharmacokinetic properties. Jointly with integrity, lipophilicity, solubility, and

permeability, pK_a has been considered as one of the five key physico-chemical profiling screens to predict the key properties that affect ADME(T) characteristics [37].

Because no strongly founded method exists for the calculation of partial atomic charges in molecules, we intentionally used a fast semi empirical molecular orbital method, MNDO-PM3 (which by default calculates Mulliken partial atomic charges). This was chosen as one well balanced for hydrogen-bonding interactions. Basic MNDO underestimates hydrogen bonding, and MNDO-AM1 overestimates it [38–40].

The idea was tested on demanding example: the set of unsaturated and epoxy polycarboxylic acids presented in Scheme 1.

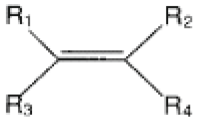

a

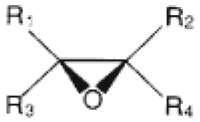

b

1. $R_1 = H$; $R_2 = H$; $R_3 = COOH$; $R_4 = COOH$

2. $R_1 = H$; $R_2 = COOH$; $R_3 = COOH$; $R_4 = H$

3. $R_1 = CH_3$; $R_2 = H$; $R_3 = COOH$; $R_4 = COOH$

4. $R_1 = CH_3$; $R_2 = COOH$; $R_3 = COOH$; $R_4 = H$

5. $R_1 = H$; $R_2 = H$; $R_3 = COOH$; $R_4 = CH_2COOH$

6. $R_1 = H$; $R_2 = CH_2COOH$; $R_3 = COOH$; $R_4 = COOH$

7. $R_1 = COOH$; $R_2 = CH_2COOH$; $R_3 = H$; $R_4 = COOH$

SCHEME 1

For these 14 acids the 32 dissociation constants were measured [41]. The simple correlation with calculated charge on acidic hydrogen failed (as can be seen on Fig. 1).

A logical explanation is that solvation plays important role in the course of the dissociation to ions. When partial charges on all atoms in carboxylic group (-C(=O)OH) are included, the "composite" charge, Q, as a weighted sum of atomic charges, according to the formula (Eq. 1) can be derived:

$$Q = q_H + A \cdot q_{O-} + B \cdot q_C + C \cdot q_{O=} + D \tag{1}$$

The values of the parameters (after the renormalization) are:

$$-1 \pm 0.0940 \,(\text{for } qH) \quad A = -0.4931 \pm 0.0235;$$
$$B = -0.0820 \pm 0.0321; \; C = -0.0368 \pm 0.0249;$$
$$D = 0.1728 \pm 0.0344; \quad (r = 0.9456, \; n = 32).$$

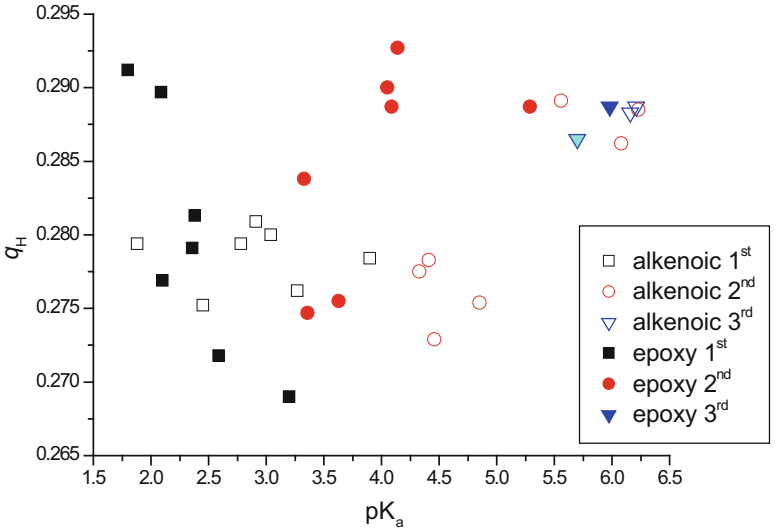

Fig. 1. Relation between measured pK_a values of β-alkenoic acids (hollow markers) and corresponding epoxy acids (filled markers), and of calculated charges on carboxylic hydrogen for 1st, 2nd, and 3rd dissociation.

This correlation is plotted on Fig. 2.

The magnitude of parameters A-D could give insight into the mechanistic details of reactions involving carboxylic group. The major weight of charges on hydrogen and on hydroxylic oxygen, supports the well-established concept of polarity of O-H bond as a dominant factor determining the efficiency of carboxylic acids dissociation. This is directly confirmed by polylinear correlation including only charges on hydrogen and hydroxylic oxygen. The correlation with charges calculated by the equation:

$$\mathrm{Q'} = qH + \mathrm{A} \cdot qO- + \mathrm{B} \tag{2}$$

is only slightly inferior to that from Eq. (1) [-1 ± 0.1070 (for qH); A $= -0.5480 \pm 0.0267$; B $= 0.1372 \pm 0.0314$; $r = 0.9384$, $n = 32$].

The obvious achievement of this approach is a single basis for the evaluation of all dissociation steps of polycarboxylic acids.

An extensive study is made to find what influences the accuracy of prediction by this approach [42]. In some cases the quality of correlation is slightly improved by addition of the simulation of solvent (medium). When charges are calculated by some *ab initio* method, the use of charges derived from Natural Bonds Analysis (NBO) gives better correlation.

The method is successfully applied for the prediction of pK_a of protonated amines, too. Because here is no carboxylic group, the method is slightly modified [43]. We decided to include in correlation the charge on vicinal nitrogen atom (q_N) along with the partial atomic charge on hydrogen (q_H):

$$\mathrm{pK_{a(calc)}} = \mathrm{A} \times q_H + \mathrm{B} \times q_N + \mathrm{C} \times I + \mathrm{D} \tag{3}$$

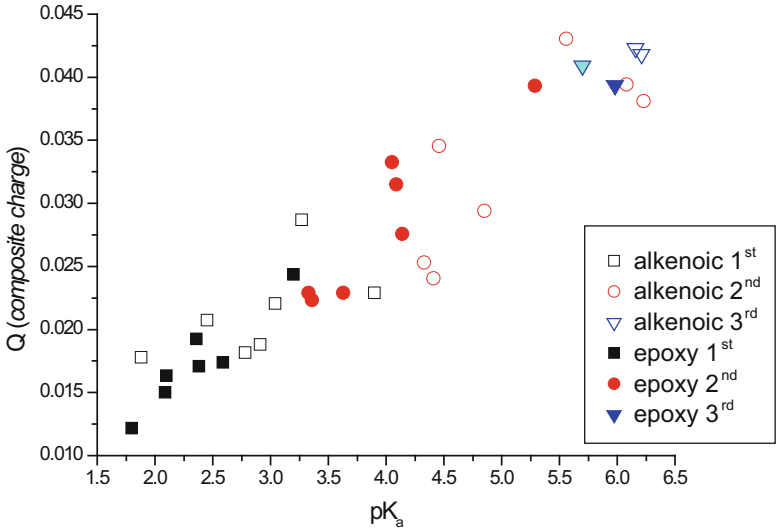

Fig. 2. Relation between measured pK_a values of β-alkenoic (hollow symbols) and corresponding epoxy acids, and of calculated "composite" charges derived from charges of all atoms in carboxyl group.

Here, *I* is the index variable to distinguish between primary, secondary and tertiary amines. We didn't deeply analyze this variable, but it is clear that it must account for differences in steric hindrance, solvation, and other effectors for acidity of ammonium ions. For this purpose it is set to have integer values. Polylinear regression of data of 57 amines gives the following statistics:

$$A = -140.878;\ B = -11.775;\ C = -1.250;\ D = 52.773$$

$$n = 57;\ r = 0.937;\ sd = 0.604;\ F = 126.306$$

The correlation between pK_a and $pK_{a(calc)}$ of ammonium ions is presented on Fig. 3.

This simple model works equally accurate as various other very sophisticated approaches, and can be valuable aid in estimation of pK_a values of aliphatic amines. In Fig. 3 is obvious that the scattering of data is minimal for primary amines. A likely reason for it is that among secondary and tertiary amines the cyclic amines (with N atom in the ring) are included, which can have markedly reduced steric hindrance. We didn't check quinuclidine, because its peculiar structure (bridgehead tricyclic amine) will set it as outlier.

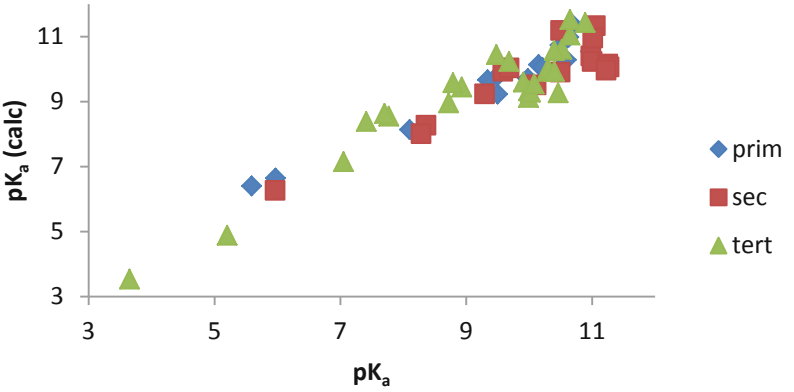

Fig. 3. Correlation of experimental and calculated (Eq. 3) pK_a values for 57 aliphatic amines. Standard deviation of estimate is 0.593.

The analogous approach was successfully applied for the correlation of the rate constants for the esterification of substituted pyrimidine acids with diazo diphenyl methane (DDM) [44] (Table 1).

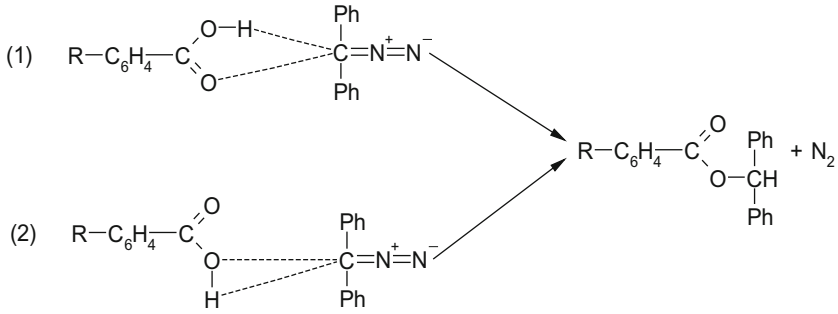

Transition states
SCHEME 2.

The reaction kinetics is compatible with either transition state shown on Scheme 2: Concerted five (1) and three (2) membered transition states for the esterification of carboxylic acids with DDM.

A straightforward correlation of log k_2 rate constants with charges on the carboxylic hydrogen (q_H) was satisfactory having regression coefficient r = 0.9708 (Fig. 4, Left). n = 11, s = 0.001.

An analysis is done on the contribution of the partial charges on every atom of the carboxylic group of each acid to the composite charge Q, obtained according to Eq. (1), as shown in Fig. 4, Right (r = 0.9911).

The calculated parameters are as follows: $q_H = 1.00 \pm 0.23$, $A = 0.06 \pm 0.19$, $B = 0.32 \pm 0.14$ $C = 1.44 \pm 0.10$, denoting the relative contribution of the atomic charges to the overall charge expression of the carboxylic group.

Table 1. Various 2,6-disubstituted-4-pyrimidine carboxylic acids subjected to calculation by AM1 semiempirical MO method, including solvation effects of DMF.

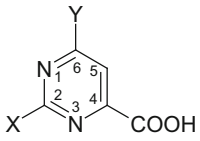

	N (1)	N (3)	X	Y
1			$-SCH_3$	-OH
2			-H	-OH
3			-H	-H
4			-Cl	$-CH_3$
5			-OH	$-CH_3$
6	$-CH_3$	-H	=O	=O
7			-OH	-OH
8	$-CH_3$	$-CH_3$	=O	=O
9			-SH	-OH
10			-Cl	-Cl
11			$-CH_3$	-OH

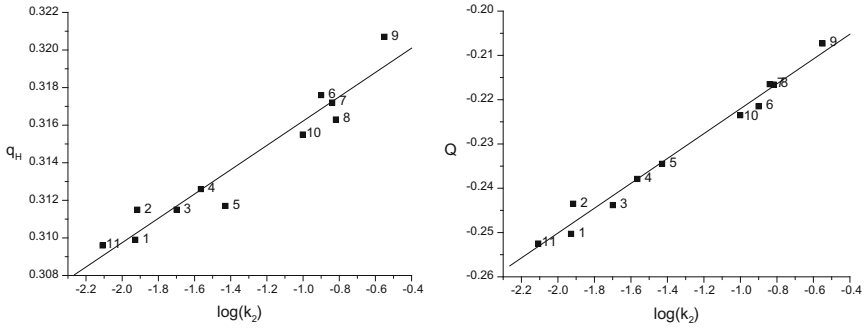

Fig. 4. Left: Correlation of the log (k_2) values with calculated charges on carboxylic hydrogen (q_H): Right: the same correlation of log k_2 with derived charges (Q) according to the Eq. (1).

Among most probable transition states for this reaction, the first one on the Scheme 2, above, is compatible with the values of parameters obtained by polylinear regression of Eq. 1. In other words, high value of parameter C shows the dominant role of carbonyl oxygen interaction with DDM in the transition state of the reaction.

In these calculations, only the most stable conformations of molecules were considered. Preliminary results show that for conformationally mobile molecules, the distribution among various conformations markedly influence the reactivity. A weighted contribution of most stable conformations of the same acid could give more accurate description of reactivity.

3 Conclusion

In this short review is shown that calculated partial atomic charges (the easily obtainable non-observable property) can be used for relatively accurate estimation of (observable) pK_a values of carboxylic acids and of protonated amines. Similar approach can enable to decide on most probable mechanism for the reaction with carbene precursors, too.

Acknowledgments. Ministry of Education, Science, and Technological Development of the Republic of Serbia supported this work, Grant No. 172035. Author gratefully acknowledge the computational time provided on the PARADOX cluster at the Scientific Computing Laboratory of the Institute of Physics, Belgrade.

References

1. Allred, A.L., Rochow, E.G.: A scale of electronegativity based on electrostatic force. J. Inorg. Nucl. Chem. **5**(4), 264–268 (1958). https://doi.org/10.1016/0022-1902(58)80003-2
2. Ghosh, D.C., Chakraborty, T.: Gordy's electrostatic scale of electronegativity revisited. J. Mol. Struct. (THOECHEM) **906**, 87–93 (2009). https://doi.org/10.1016/j.theochem.2009.04.007
3. Pauling, L.: The nature of the chemical bond. IV. The energy of single bonds and the relative electronegativity of atoms. J. Am. Chem. Soc. **54**, 3570–3582 (1932). https://doi.org/10.1021/ja01348a011
4. Mulliken, R.S.: New electroaffinity scale; together with data on valence states and on valence ionization potentials and electron affinities. J. Chem. Phys. **2**, 782–793 (1934). https://doi.org/10.1063/1.1749394
5. Hinze, J., Jaffé, H.H.: Electronegativity. I. Orbital electronegativity of neutral atoms. J. Am. Chem. Soc. **84**, 540–546 (1962)
6. Hinze, J., Whitehead, M.A., Jaffé, H.H.: Electronegativity. II. Bond and orbital electronegativities. J. Am. Chem. Soc. **85**, 148–154 (1963)
7. Hinze, J., Jaffé, H.H.: Electronegativity. III. Orbital electronegativities and electron affinities of transition metals. Can. J. Chem. **41**, 1315–1328 (1963). https://doi.org/10.1139/v63-183
8. Hinze, J., Jaffé, H.H.: Electronegativity. IV. Orbital electronegativities of the neutral atoms of the periods three A and four A and of positive ions of periods one and two. J. Phys. Chem. **67**, 1501–1506 (1963). https://doi.org/10.1021/j100801a024
9. Iczkowski, R.P., Margrave, J.L.: Electronegativity. J. Am. Chem. Soc. **83**, 3547–3551 (1961). https://doi.org/10.1021/ja01478a001
10. Coulson, C.A., Longuet-Higgins, H.C.: The electronic structure of conjugated systems. II. Unsaturated hydrocarbons and their hetero-derivatives. Proc. Roy. Soc. (London) A **192**, 16–32 (1947). https://doi.org/10.1098/rspa1947.0136
11. Mulliken, R.S.: Electronic population analysis on LCAO-MO molecular wave functions. I. J. Chem. Phys. **23**(10), 1833–1840 (1955). https://doi.org/10.1063/1.1740588
12. Mayer, I.: Charge, bond order and valence in the AB initio SCF theory. Chem. Phys. Lett. **97**(3), 270–274 (1983). https://doi.org/10.1016/0009-2614(83)80005-0
13. Mayer, I.: Charge, bond order and valence in the AB initio SCF theory. Chem. Phys. Lett. **117**(4), 396 (1985). https://doi.org/10.1016/0009-2614(85)85253-2
14. Juranić, I.: Molecular descriptors as proxies for the modeling of the materials and their environmental impact. Mater. Prot. **57**(3), 359–369 (2016). https://doi.org/10.5937/ZasMat1603359J
15. Oliferenko, A.A., Palyulin, V.A., Pisarev, S.A., Neiman, A.V., Zefirov, N.S.: Novel point charge models: reliable instruments for molecular electrostatic. J. Phys. Org. Chem. **14**, 355–369 (2001). https://doi.org/10.1002/poc.378

16. Abraham, R.J., Griffiths, L., Perez, M.: ^{1}H NMR spectra. Part 30: ^{1}H chemical shifts in amides and the magnetic anisotropy, electric field and steric effects of the amide group. Magn. Reson. Chem. **51**(3), 143–155 (2013). https://doi.org/10.1002/mrc.3920
17. Abraham, R.J., Bardsley, B., Mobli, M., Smith, R.J.: ^{1}H chemical shifts in NMR. Part 21–prediction of the ^{1}H chemical shifts of molecules containing the ester group: a modelling and ab initio investigation. Magn. Reson. Chem. **43**(1), 3–15 (2004). https://doi.org/10.1002/mrc.1491
18. Binev, Y., Aires-de-Sousa, J.: Structure-based predictions of ^{1}H NMR chemical shifts using feed-forward neural networks. J. Chem. Inf. Comput. Sci. **44**, 940–945 (2004). https://doi.org/10.1021/ci034228s
19. Chis, V., Pîrnău, A., Vasilescu, M., Varga, R.A., Oniga, O.: X-ray, ^{1}H NMR and DFT study on 5-para-X-benzylidene-thiazolidine derivatives with X = Br, F. J. Mol. Struct. (THOECHEM) **851**(1–3), 63–74 (2008). https://doi.org/10.1016/j.theochem.2007.10.041
20. Pazderski, L., Toušek, J., Sitkowski, J., Kozerski, L., Szłyk, E.: Experimental and quantum-chemical studies of ^{1}H, ^{13}C and ^{15}N NMR coordination shifts in Pd(II) and Pt(II) chloride complexes with quinoline, isoquinoline, and 2,2 -biquinoline. Magn. Reson. Chem. **45**(12), 1059–1071 (2007). https://doi.org/10.1002/mrc.2105
21. Shirts, R.B., Stolworthy, L.D.X.: Conformational sensitivity of polyether macrocycles to electrostatic potential: partial atomic charges, molecular mechanics, and conformational prediction. J. Inclusion Phenom. Mol. Recognit. Chem. **20**(4), 297–321 (1994). https://doi.org/10.1007/bf00708876
22. Wang, B., Truhlar, D.G.: Partial atomic charges and screened charge models of the electrostatic potential. J. Chem. Theory Comput. **8**(6), 1989–1998 (2012). https://doi.org/10.1021/ct2009285
23. Mehler, E.L., Solmajer, T.: Electrostatic effects in proteins: comparison of dielectric and charge models. Protein Eng. Des. Sel. **4**(8), 903–910 (1991). https://doi.org/10.1093/protein/4.8.903
24. Bertonati, C., Honig, B., Alexov, E.: Poisson-Boltzmann calculations of nonspecific salt effects on protein-protein binding free energies. Biophys. J. **92**(6), 1891–1899 (2007). https://doi.org/10.1529/biophysj.106.092122
25. Schröder, C.: Comparing reduced partial charge models with polarizable simulations of ionic liquids. Phys. Chem. Chem. Phys. **14**(9), 3089 (2012). https://doi.org/10.1039/c2cp23329k
26. Tsiper, E.V., Soos, Z.G.: Electronic polarization in pentacene crystals and thin films. Phys. Rev. B **68**(8), 085201-10 (2003). https://doi.org/10.1103/physrevb.68.085301
27. Tsiper, E.V., Soos, Z.G., Gao, W., Kahn, A.: Electronic polarization at surfaces and thin films of organic molecular crystals: PTCDA. Chem. Phys. Lett. **360**(1–2), 47–52 (2002). https://doi.org/10.1016/s0009-2614(02)00774-1
28. Anker, L.S., Jurs, P.C., Edwards, P.A.: Quantitative structure-retention relationship studies of odor-active aliphatic compounds with oxygen-containing functional groups. Anal. Chem. **62**(24), 2676–2684 (1990). https://doi.org/10.1021/ac00223a006
29. Stanton, D.T., Jurs, P.C.: Development and use of charged partial surface area structural descriptors in computer-assisted quantitative structure-property relationship studies. Anal. Chem. **62**(21), 2323–2329 (1990). https://doi.org/10.1021/ac00220a013
30. Katritzky, A.R., Mu, L., Lobanov, V.S.: Correlation of boiling points with molecular structure. 1. A training set of 298 diverse organics and a test set of 9 simple inorganics. J. Phys. Chem. **100**, 10400–10407 (1996). https://doi.org/10.1021/jp953224q
31. Ghatee, M.H., Zolghadr, A.R., Moosavi, F., Ansari, Y.: Studies of structural, dynamical, and interfacial properties of 1-alkyl-3-methylimidazolium iodide ionic liquids by molecular dynamics simulation. J. Chem. Phys. **136**, 124706-14 (2012). https://doi.org/10.1063/1.3696004

32. Knight, J.L., Yesselman, J.D., Brooks III, C.L.: Assessing the quality of absolute hydration free energies among CHARMM-compatible ligand parameterization schemes. J. Comput. Chem. **34**, 893–903 (2013). https://doi.org/10.1002/jcc.23199
33. Lísal, M., Chval, Z., Storch, J., Izák, P.: Towards molecular dynamics simulations of chiral room-temperature ionic liquids. J. Mol. Liq. **189**, 85–94 (2014). https://doi.org/10.1016/j.molliq.2013.04.017
34. Bhatta, R.S., Yimer, Y.Y., Perry, D.S., Tsige, M.: Improved force field for molecular modeling of poly(3hexylthiophene). J. Phys. Chem. B **117**, 10035–10045 (2013). https://doi.org/10.1021/jp404629a
35. Núnez-Rojas, E., García-Melgarejo, V., de la Luz, A.P., Alejandre, J.: Systematic parameterization procedure to develop force fields for molecular fluids using explicit water. Fluid Phase Equilib. **490**, 1–12 (2019). https://doi.org/10.1016/j.fluid.2019.02.018
36. Vitnik, Ž.J., Vitnik, V.D., Pokorni, S.V., Juranić, I.O.: Correlation of pK_a values for series of benzoic acids with the theoretically calculated atomic charges. In: Physical Chemistry 2012, 11th International Conference on Fundamental and Applied Aspects of Physical Chemistry, Belgrade, September 2012, Proceedings, A-9-P, pp. 61–63 (2012)
37. Wang, H., Ulander, J.: High-throughput pK_a screening and prediction amenable for ADME profiling. Expert Opin. Drug Metabol. Toxicol. **2**, 139–155 (2006)
38. Grierson, L., Perkins, M.J., Rzepa, H.S.: A comparison of the MNDO and AM1 SCF-MO methods for dipolar cycloaddition and the claisen reaction. J. Chem. Soc. Chem. Commun. 1779 (1987)
39. Rzepa, H.: Cheletropic elimination reactions. A comparison of the MNDO, AM1 and ab initio SCF-MO methods. J. Chem. Res. 224 (1988)
40. Juranic, I., Rzepa, H.S., Yi, M-Y.: Molecular orbital studies of molecular exciplexes. Part 1: AM1 and PM3 calculations of the ammonia-oxygen complex and its solvation by water. J. Chem. Soc. Perkin Trans. 877 (1990)
41. Pfendt, L., Dražić, B., Popović, G., Drakulić, B., Vitnik, Ž., Juranić, I.: Determination of all pK_a values of some di- and tri-carboxylic unsaturated and epoxy acids and their polylinear correlation with the carboxylic group atomic charges. J. Chem. Res. (S) **2003**, 247 (2003)
42. Vitnik, Ž.: Correlations between physical and chemical properties of carboxylic acids with a calculated atomic charges. Ph.D. thesis, University of Belgrade, 12 December 2011
43. Juranić, I.: Simple method for the estimation of pK_a of amines. Croat. Chem. Acta **87**(4), 343–347 (2014). https://doi.org/10.5562/cca2462
44. Jovanović, B., Juranić, I., Mišić-Vuković, M., Brkić, D., Vitnik, Ž.: Kinetics and mechanism of the reaction of substituted 4-pyrimidine carboxylic acids with diazodiphenylmethane in dimethylformamide. J. Chem. Res. (S) **2000**, 506–507 (2000)

Heart Mechanical Model Based on Holzapfel Experiments

Milos Kojic[1,2,3(✉)], Miljan Milosevic[2,4], Bogdan Milicevic[2,5], and Vladimir Simic[2,5]

[1] The Department of Nanomedicine, Houston Methodist Research Institute, 6670 Bertner Avenue, R7 117, Houston, TX 77030, USA
mkojic42@gmail.com
[2] Bioengineering Research and Development Center BioIRC Kragujevac, Prvoslava Stojanovica 6, 34000 Kragujevac, Serbia
[3] Serbian Academy of Sciences and Arts, Knez Mihailova 35, 11000 Belgrade, Serbia
[4] Belgrade Metropolitan University, Tadeusa Koscuska 63, 11000 Belgrade, Serbia
[5] Faculty for Engineering Sciences, University of Kragujevac, Sestre Janic 6, 34000 Kragujevac, Serbia

Abstract. We have formulated orthotropic material model for human heart tissue based on experimental investigation of passive material properties of myocardium [1]. The Cauchy stress/stretch and shear stress/amount of shear relation curves are used, which are established experimentally under different loading conditions: biaxial extension and triaxial shear. The averaged curves obtained from all considered specimens in [1] are reconstructed and used in our FE computational model. A computational procedure for determination of stresses for current stretches and amounts of shear at integration points of the FE model is implemented in the code PAK. Compressibility condition is imposed to couple the normal stresses using a penalty formulation. Applicability and reliability of this material model is tested on simple 3D models and on a heart wall segment under passive conditions. This numerical model offers an accurate description of the ventricular mechanics and can be used in studying heart problems in order to improve medical treatment of heart diseases.

Keywords: Heart mechanics · Heart material model · Biaxial loading · Sommer and Holzapfel experiment

1 Introduction

Cardiovascular diseases (CVDs) remain the leading cause of death in the developed world, accounting for an estimate of 17.3 million every year. The treatment of heart diseases by established therapies could only in part improve the outcome, but novel therapies need to be developed to affect the disease process more fundamentally. The application of ICT (Information and Communication Technologies), especially biomechanical simulations, in solving the problems of heart diseases and improving therapies, has been recognized as important activity in the health care sector. Nowadays, there are models and supercomputers capable of simulating complex physiological events.

N. Filipovic (Ed.): ICCB 2019, LAIS 11, pp. 12–21, 2020.
https://doi.org/10.1007/978-3-030-43658-2_2

In the field of cardiac modeling, computational simulations provide a powerful tool to understand heart function and its behavior under different conditions and pathologies. The common method used for cardiac multi-scale modeling is the finite element method (FEM) for nonlinear mechanics and drug delivery. Despite all effort made in past in the field of ICT, the developed computational models are still far away from the everyday clinical use.

The heartbeat can be decomposed in three different physical problems: electrophysiology, solid mechanics and fluid dynamics. The myocardium is generally regarded as an anisotropic material with respect to its fiber orientations, although there is evidence of its orthotropic behavior. When modeling the solid mechanics of the heart, two sources of stresses should be accounted - the passive and active. The final stresses produced in the tissue are obtained by summation of these two stresses.

Passive stresses are depends on the structural properties of the cells and the connective tissues. From early stages [2] soft tissue behavior was described as non-linear over finite strains. Various computational models have been formulated in modeling the heart wall, mainly in the form of strain potential [3–5]. The model presented in this work is based on the recently published experimental investigation of professor Holzapfel and his research group [1]. The model presented here is based on these experimental findings and is implemented in our finite element program PAK [6]. Here, we briefly summarize the model formulation using the experimental constitutive curves without hysteresis. We show model accuracy and applicability to simple heart geometry.

2 Materials and Methods

2.1 Material Model Based on Holzapfel Experiments [1]

In Fig. 1 are shown the basic definitions of the local axes lying in the myocardial sheets (3–4 cell wide): f_0 - fiber direction, s_0 - sheet direction, and n_0 - normal to the myocardium sheet.

Experimental curves for stress vs. stretch without hysteresis are shown in Fig. 1b. Figure 1b represents the average biaxial Cauchy stress-stretch relationship obtained from all considered myocardial specimens for a stretch level of 10%. For simplicity, the authors refer to the average between the two paths as the 'elastic' tissue behavior. Figure 1b shows the average 'elastic' behavior of all tested specimens at different ratios between MFD and CFD (1:1; 1:0:75; 0:75:1; 1:0:5, and 0:5:1). We will further use the stretch ratio of the sheet stretch λ_2 vs. fiber stretch λ_1, which are shown in the Fig. 1b as. 1.1:1.05 (1.047), 1.1: 1.075 (1.023), 1.1:1.1 (1.0), 1.075:1.1 (0.977) and 1.05:1.1 (0.954).

Shear stresses acting on a material element are shown in Fig. 2a. Size of specimens used in experiments was $4 \times 4 \times 4$ mm. The average constitutive stress-strain curves are shown in Fig. 2b. They are given for the three modes according to notation in Fig. 2a. The curves are obtained by cycling loading and correspond to different level of ultimate shear strain. Maximum shear strains are at level 0.5.

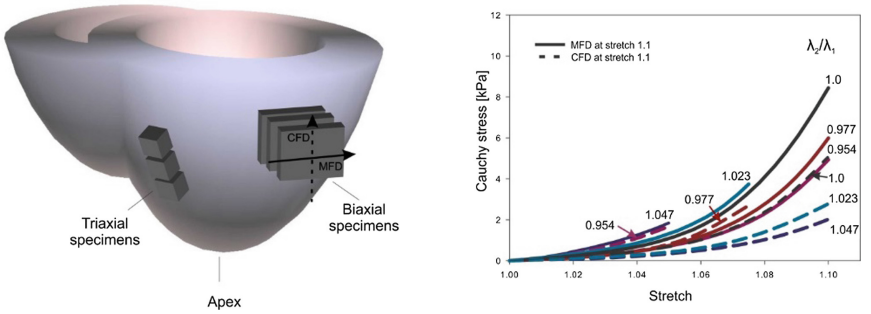

Fig. 1. Left panel: 3D schematic of heart biventricular model and specimen obtained from heart tissue according to [1], together with material local coordinate system. Right panel: Experimental curves without hysteresis for biaxial loading of myocardium tissue reconstructed from [1], where MFD is the fiber direction f_0, and CFD is sheet direction s_0. Average 'elastic' biaxial Cauchy stress vs. stretch relationship of all considered human LV myocardial specimens subjected to a max. stretch of 10% with different stretch ratios between MFD and CFD: different stretch ratios, where black curves correspond to 1:1, red to 1:0:75, green to 0:75:1, blue to 1:0:5 and cyan to 0:5:1).

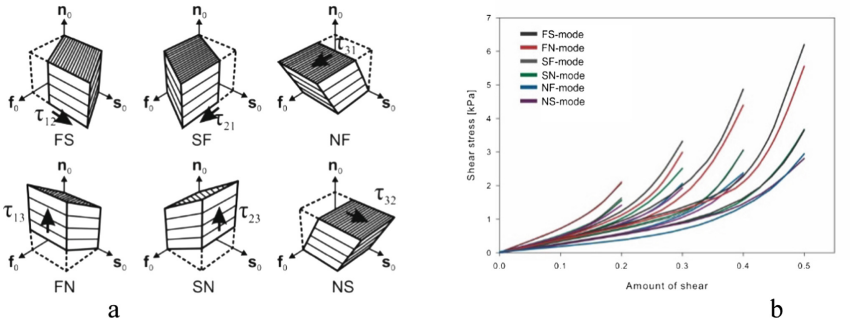

Fig. 2. (a) Shear stresses acting on material element, according to [1]; (b) Shear stress constitutive curves, without hysteresis, reconstructed from Fig. 13 of Reference [1], which contains average 'elastic' triaxial shear stress vs. 'amount of shear' relation of all considered human myocardial specimens.

2.2 Determination of Stretches in the Material Local Coordinate System

The constitutive curves are experimentally determined in the material local system f_0, s_0, n_0, Fig. 1a. Cauchy (true) stresses are expressed in terms of stretches. We here present a computational procedure for determination of stretches in the local system in terms of displacements. Following [7], we have that change of the elementary material element is:

$$d^t\mathbf{s} = {}^t_0\mathbf{F}d^0\mathbf{s} \tag{1}$$

and

$${}^t_0\lambda\,{}^t\mathbf{n} = {}^t_0\mathbf{F}^0\mathbf{n} \tag{2}$$

where $d^t\mathbf{s}$ and $d^t\mathbf{s}$ are elementary material elements in the current and initial configurations; ${}^t\mathbf{n}$ and ${}^0\mathbf{n}$ are unit normals; ${}^t_0\lambda$ is the stretch and ${}^t_0\mathbf{F}$ is deformation gradient with respect to the undeformed configuration. Hence we have

$$ {}^t_0\lambda = \left| {}^t_0\mathbf{F}\,{}^0\mathbf{n} \right| \tag{3} $$

and

$$ {}^t\mathbf{n} = \frac{1}{{}^t_0\lambda}\,{}^t_0\mathbf{F}\,{}^0\mathbf{n} \tag{4} $$

Deformation gradient is calculated as

$$ {}^t_0\mathbf{F} = \frac{\partial {}^t\mathbf{x}}{\partial {}^0\mathbf{x}} = \mathbf{I} + \frac{\partial {}^t\mathbf{u}}{\partial {}^0\mathbf{x}} \tag{5} $$

where ${}^0\mathbf{x}$ and ${}^t\mathbf{x}$ are position vectors of a material point at initial and current configurations, respectively; ${}^t\mathbf{x}$ is vector of the same material point in the current configuration; and ${}^t\mathbf{u}$ is the displacement vector.

2.3 Determination of Normal Stresses from Current Stretches

We use experimental curves given in Fig. 1c. The concept of determination of normal stresses is displayed in Fig. 3. For simplicity of presentation, we omit the indexes 't' and '0' for the time and initial configuration; and also the iteration counter – therefore variables as stretch, strains, etc. correspond to the current known configuration within the incremental-iterative scheme of the FE computational procedure. For the current iteration we calculate the stretches λ_1 and λ_2 from (3) for the fiber direction $\mathbf{f}_0$ and sheet direction $\mathbf{s}_0$, respectively.

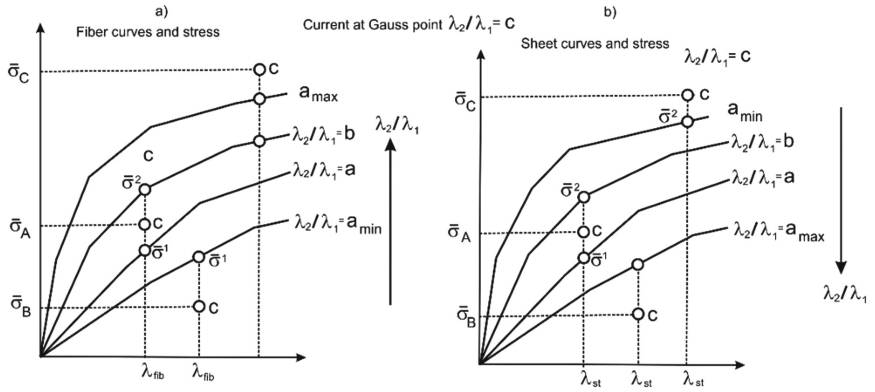

Fig. 3. Interpolation of normal stresses in the local (material) coordinate system

Therefore, we know the ratio $\lambda_2/\lambda_1 = c$. Now, we need to calculate the stresses $\bar{\sigma}_i$ in the local system. If the stretch in the local (material) coordinate direction is λ_i, we find the two closest curves - for that direction and the loading/unloading state – among which falls the current ratio c, i.e.

$$c \geq a, \ \mathrm{c} \leq \mathrm{b} \tag{9}$$

$$\bar{\sigma}_i = \frac{c-a}{b-a}\left(\sigma_i^2 - \sigma_i^1\right) \tag{10}$$

where σ_i^1 and σ_i^2 are stresses at the lower and upper curves, respectively. For the 3D model we use characteristics for the normal direction to be the same as for the sheet direction. Special cases when $\lambda_2/\lambda_1 < a_{\min}$ and $\lambda_2/\lambda_1 > a_{\max}$ for the fiber and sheet directions are implemented in the code, assuming linear interpolations in these domains.

Tangent modulus relates stress increment with respect to the increment of strain in the local material direction, hence we have

$$\bar{E}_{Ti} = \lambda_i \frac{\partial \bar{\sigma}_i}{\partial \lambda_i}, \ no \ sum \ on \ i \tag{11}$$

We use the diagonal tangent constitutive matrix (with these tangent moduli) in the local coordinate system for calculating the element stiffness matrix.

2.4 Determination of Shear Stresses from Current Shear Strains

Following Fig. 2a we can express the mechanical work due to shear stresses as:

$$W_{shear} = \tau_{12}\frac{\partial \bar{u}_2}{\partial \bar{x}_1} + \tau_{21}\frac{\partial \bar{u}_1}{\partial \bar{x}_2} + \tau_{23}\frac{\partial \bar{u}_3}{\partial \bar{x}_2} + \tau_{32}\frac{\partial \bar{u}_2}{\partial \bar{x}_3} + \tau_{31}\frac{\partial \bar{u}_1}{\partial \bar{x}_3} + \tau_{13}\frac{\partial \bar{u}_3}{\partial \bar{x}_1} \tag{12}$$

For easer presentation, we introduce one-dimensional shear stress and 'shear strains':

$$\boldsymbol{\tau}^{shT} = [\tau_{12}\tau_{21}\tau_{23}\tau_{32}\tau_{13}\tau_{31}] \tag{13}$$

$$\bar{\mathbf{e}}^{shT} = \left[\frac{\partial \bar{u}_1}{\partial \bar{x}_2}\frac{\partial \bar{u}_2}{\partial \bar{x}_1}\frac{\partial \bar{u}_2}{\partial \bar{x}_3}\frac{\partial \bar{u}_3}{\partial \bar{x}_2}\frac{\partial \bar{u}_1}{\partial \bar{x}_3}\frac{\partial \bar{u}_3}{\partial \bar{x}_1}\right] \tag{14}$$

The following steps are used for the shear deformation:

1. Determine the local strain-displacement matrix $\bar{\mathbf{B}}$,

$$\bar{\mathbf{B}} = \mathbf{T}^{\varepsilon T}\mathbf{B} \tag{15a}$$

where $\mathbf{T}^{\boldsymbol{\varepsilon}}$ is the strain-displacement transformation matrix [8, 9]. This matrix is also used for the normal stress components.

2. Use the shear stresses in the local (material) coordinate system for calculation of the nodal force vector, as

$$\tau_4 = \tau_{12} + \tau_{21},\ \tau_5 = \tau_{23} + \tau_{32},\ \tau_6 = \tau_{13} + \tau_{31} \tag{15b}$$

3. Calculate nodal forces,

$$\mathbf{F} = \int_V \bar{\mathbf{B}}^T \bar{\boldsymbol{\sigma}} dV \tag{15c}$$

where $\bar{\boldsymbol{\sigma}}$ is the six-component stress matrix in the local system, which includes the normal and shear components.

4. Use average shear moduli in local system as

$$\bar{G}_4 = \frac{1}{2}\left(\bar{G}_{42} + \bar{G}_{21}\right), \quad \bar{G}_5 = \frac{1}{2}\left(\bar{G}_{23} + \bar{G}_{32}\right), \quad \bar{G}_6 = \frac{1}{2}\left(\bar{G}_{13} + \bar{G}_{31}\right) \tag{15d}$$

Calculate the stiffness matrix with the diagonal constitutive matrix $\bar{\mathbf{C}}$, which includes terms given in (11) and (15d), as

$$\mathbf{K} = \int_V \bar{\mathbf{B}}^T \bar{\mathbf{C}} \bar{\mathbf{B}} dV \tag{15e}$$

2.5 Compressibility Condition – Penalty Formulation

We use the penalty formulation for imposing the compressibility condition. According to the variational principle, we have the equation [9]:

$$\delta \dot{W}_{ext} + \delta \dot{W}_{\text{int}} + \delta \dot{W}_{constr} = 0 \tag{16}$$

where $\dot{W}_{ext}$, $\dot{W}_{\text{int}}$ and $\dot{W}_{constr}$ are powers due to external loading, internal stresses and constraints, respectively. In case of compressibility, the constraint can be written as:

$$\dot{W}_{constr} = \frac{1}{2}\lambda_p \int_V \left(\frac{\partial v_i}{\partial x_i} - c_V \dot{\sigma}_m\right)^2 dV \tag{17}$$

where λ_p is penalty factor, v_i are velocities, $\dot{\sigma}_m$ is the mean stress rate, and c_V is compressibility coefficient.

3 Numerical Examples

We have selected two basic 3D examples to show reliability of this sophisticated material model. First examples is simple 3D element with prescribed displacements in x and y directions (Fig. 4a), to show applicability of the model in biaxial stretch conditions. Displacements are linearly changing in time, and are prescribed with different ratios, as in the experiment, $u_x/u_y = 0.5/1.0$, 0.75/1.0, 1.0/1.0, 1.0/0.75 and 1.0/0.5. Field of displacements in x and y directions for the case $u_x/u_y = 1.0/0.5$ is shown in Fig. 4b–c, while change of u_x and u_y over time is shown in Fig. 4d.

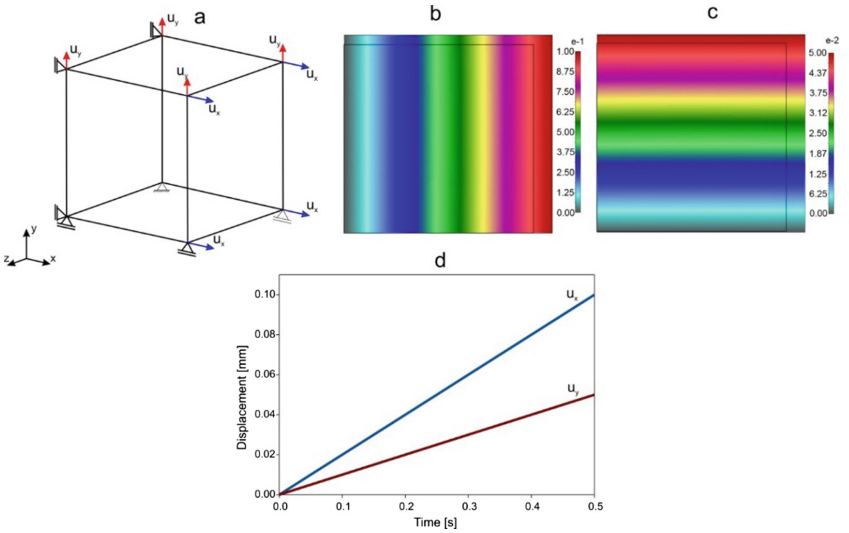

Fig. 4. (a) 3D model with prescribed displacements u_x and u_y. (b) Field of displacement u_x for 1.0 (MFD) : 0.5 (CFD) (c) Field of displacement u_x for 1.0/0.5 ratio (d) Change of displacements u_x and u_y over time for 1.0 (MFD) : 0.5 (CFD) ratio.

Results of the FE simulations regarding biaxial Cauchy stress vs. stretch relationship are plotted in Fig. 5. It is assumed that material is incompressible.

Second example is the same 3D model subjected to displacement in y direction to mimic pure shearing conditions (Fig. 6). Displacement field u_y is shown in Fig. 6b, while comparison of the experimental and numerical results for the stress-amount of shear (here it is the shear strain) relationship is displayed in Fig. 6c.

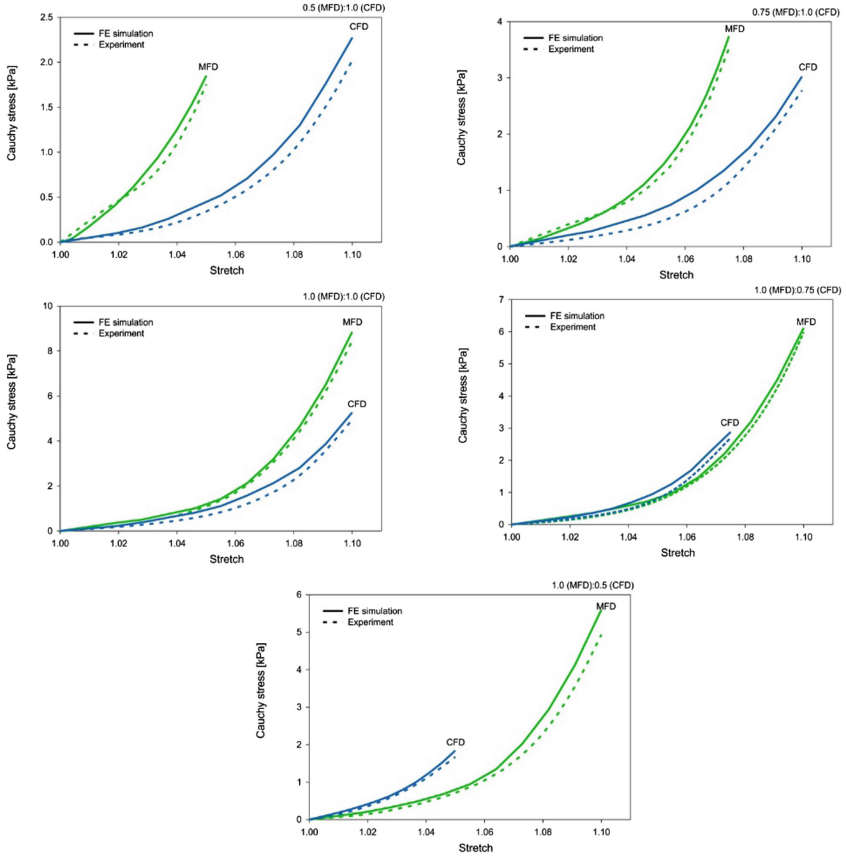

Fig. 5. Comparison of experimental and FE numerical biaxial Cauchy stress vs. stretch relationship. One 3D finite element is subjected to maximum stretch of 0.1, with different ratios between MFD and CFD (0.5 : 1.0, 0.75 : 1.0, 1.0 : 1.0, 1.0 : 0.75 and 1.0 : 0.5).

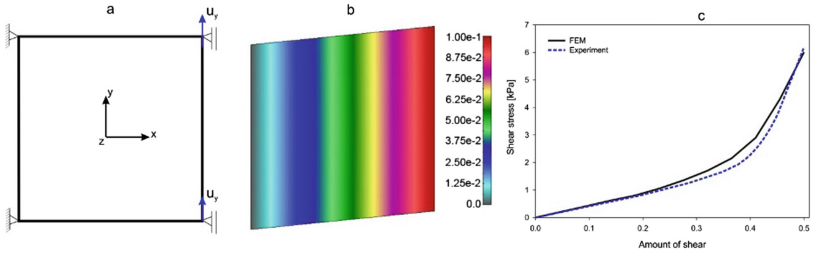

Fig. 6. (a) Model geometry and boundary conditions in plane XY; (b) Displacement fields u_y for maximum value of 0.1; (c) Amount of shear vs shear stress diagram.

3.1 2D Model of Real Heart Wall Segment

Here we used the same example as presented in [10], with passive stresses in heart model calculated using the above described orthotropic material model. The geometry of the model is shown in Fig. 7a, and the first layer is shown in Fig. 7b.

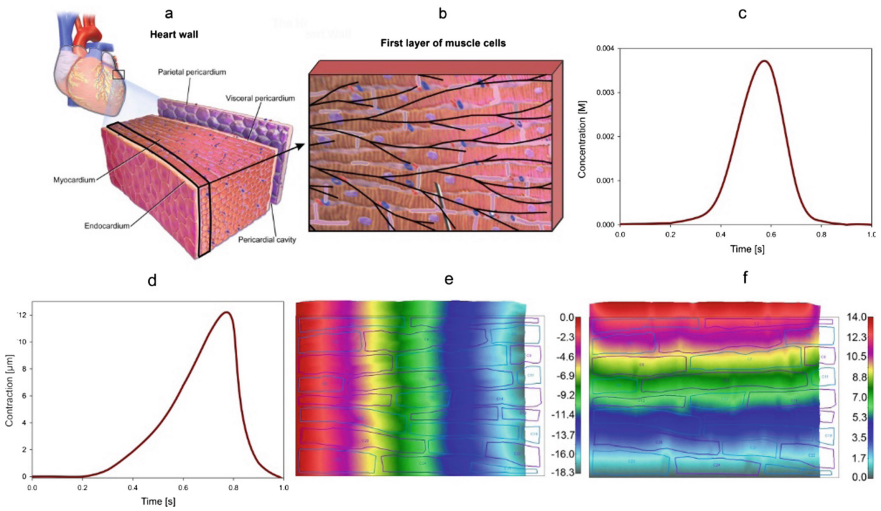

Fig. 7. (a) Small domain of heart wall tissue [11]; (b) First layer of muscle cells close to sub-endocardium; (c) Prescribed change of calcium concentration in heart tissue; (d) Contraction of the right side of heart tissue over time; (e) Displacement field u_x at t = 0.8 s; (f) Displacement field u_y at t = 0.8 s.

Electromechanical coupling used in our models is according to the expression for generation of the active stress σ_{act} within muscle sarcomere and along the fiber of the heart muscle, according to [12],

$$\sigma_{act} = \frac{\left[Ca^{2+}\right]^n}{\left[Ca^{2+}\right]^n + C_{50}^n} \sigma_{\max}[1 + \eta(\lambda - 1)] \tag{18}$$

where Ca^{2+} is calcium concentration; $\sigma_{\max}$ is maximum isometric stress, C_{50} is concentration for 50% availability of actin sites for the cross bridge binding, n is related to the rate of this availability to concentration, η is parameter which is governing the rate of muscle fiber deformation; and λ the fiber stretch. Input function of calcium is shown in Fig. 7c, which was used to compute the active stress. This stress acts as a distributed external loading on the muscle tissue causing muscle deformation and motion [12]. Contractions in x direction are shown in Fig. 7d, while field of displacements at t = 0.8 for both x and y directions are shown in Fig. 7e and f, respectively.

4 Summary and Conclusions

We here presented new orthotropic material model for passive stress response of myocardium. Model is based on experimental investigation of prof. Holzapfel and his research team. The presented 3D examples showed accuracy and applicability of numerical model. Simple 2D model with real muscle cells demonstrates applicability of the model in investigation of realistic coupled electro-mechanical behavior of the whole heart.

Acknowledgments. The authors acknowledge support from the City of Kragujevac, Serbia.

Funding. This work is supported by the SILICOFCM project that has received funding from the European Union's Horizon 2020 research and innovation programme under grant agreement No 777204. This research was also funded by Ministry of Education and Science of Serbia, grants OI 174028 and III 41007.

References

1. Sommer, G., Schriefl, A.J., Andrä, M., Sacherer, M., Viertler, C., Wolinski, H., Holzapfel, G.A.: Biomechanical properties and microstructure of human ventricular myocardium. Acta Biomater. **24**, 172–192 (2015)
2. Roy, C.: The elastic properties of the arterial wall. J. Physiol. **3**, 125–159 (1881)
3. Holzapfel, G.A., Ogden, R.W.: Constitutive modelling of passive myocardium: a structurally based framework for material characterization. Philos. Trans. R. Soc. A **367**, 3445–3475 (2009)
4. Gültekin, O., Sommer, G., Holzapfel, G.A.: An orthotropic viscoelastic model for the passive myocardium: continuum basis and numerical treatment. Comput. Methods Biomech. Biomed. Eng. **19**(15), 1647–1664 (2016)
5. McEvoy, E., Holzapfel, G.A., McGarry, P.: Compressibility and anisotropy of the ventricular myocardium: experimental analysis and microstructural modeling. J. Biomech. Eng. **140**, 081004–1,10 (2018)
6. Kojic, M., Slavkovic, R., Zivkovic, M., Grujovic, N., Filipovic, N., Milosevic, M.: PAK - finite element program for linear and nonlinear analysis. Univ Kragujevac and R&D Center for Bioengineering, Kragujevac, Serbia (2010)
7. Kojic, M., Bathe, K.J.: Inelastic Analysis of Solids and Structures. Springer, Heidelberg (2005)
8. Kojic, M., Slavkovic, R., Zivkovic, M., Grujovic, N.: Metod konacnih elemenata I – linearna analiza, Masinski Fakultet. Univerzitet u Kragujevcu, Kragujevac (2010). ISBN 86-80581-27-5
9. Bathe, K.J.: Finite Element Procedures. Prentice Hall, Hew Jersey (2006). ISBN-13: 978-0979004957
10. Kojic, M., Milosevic, M., Simic, V., Milicevic, B., Geroski, V., Nizzero, S., Ziemys, A., Filipovic, N., Ferrari, M.: Smeared multiscale finite element models for mass transport and electrophysiology coupled to muscle mechanics. Front. Bioeng. Biotechnol. **7** (2019). https://doi.org/10.3389/fbioe.2019.00381, ISSN: 2296-4185
11. Santiago, A.: Fluid-electro-mechanical model of the human heart for supercomputers. Universitat Politècnica de Catalunya, Bacelona (2018)
12. Hunter, P.J., McCulloch, A.D., Ter Keurs, H.E.D.J.: Modelling the mechanical properties of cardiac muscle. Prog. Biophys. Mol. Biol. **69**, 289–331 (1998)

Finite Element Models with Smeared Fields Within Tissue – A Review of the Current Developments

Milos Kojic[1,2,3(✉)], Miljan Milosevic[2,4], Vladimir Simic[2], Vladimir Geroski[2], Bogdan Milicevic[2], Arturas Ziemys[1], and Nenad Filipovic[5]

[1] The Department of Nanomedicine, Houston Methodist Research Institute, 6670 Bertner Avenue R7 117, Houston, TX 77030, USA
mkojic42@gmail.com
[2] Bioengineering Research and Development Center BioIRC Kragujevac, Prvoslava Stojanovica 6, 34000 Kragujevac, Serbia
[3] Serbian Academy of Sciences and Arts, Knez Mihailova 35, 11000 Belgrade, Serbia
[4] Belgrade Metropolitan University, Tadeusa Koscuska 63, 11000 Belgrade, Serbia
[5] Faculty for Engineering Sciences, University of Kragujevac, Sestre Janic 6, 34000 Kragujevac, Serbia

Abstract. In this review we present the current stage and developments in the finite element modeling of mass transport by the smeared concept, introduced and conducted by the first author over several years. The basis of this methodology represents the formulation of a composite smeared finite element (CSFE). The CSFE consists of domains which can be at different length scale, where we have separate physical fields for each of the domains and with the corresponding governing laws. The continuum domains within the CSFE also include 1D transport represented in a continuum form by the appropriate transport tensors. The fields are coupled by the connectivity elements at each node, representing transport properties of the walls separating the domains. Formulation of this methodology and applications on various biomedical problems have been published in a number of recent publications. Here, we give an overview of these achievements and show some results of the current research.

Keywords: Smeared finite element methodology · Composite smeared finite element · Biological systems · Multiscale models

1 Introduction

The fundamental process in living organisms is material transport. It includes transport of oxygen, various molecules as drugs, metabolic transport within tissue and organ liquids, transport of waste generated by cell functions, ionic transport within cells and through biological membranes, electrical signals, etc. The efforts over centuries were directed to find the laws for extremely complex phenomena related to mass transport in the organs, from the macro-world to molecular and atomic scales. Research has been

N. Filipovic (Ed.): ICCB 2019, LAIS 11, pp. 22–34, 2020.
https://doi.org/10.1007/978-3-030-43658-2_3

experimental, rather than theoretical due to complexity of problems. Various laws of physics and chemistry were implemented for the description of the transport phenomena. In last decades the analytical interpretation of the transport laws were enhanced by computational modeling due to enormous advances in computer technology and computational methodology. But, still, there is today a need for improvement of computational methods in order to generate software as a tool for achieving better therapy and cure successfully various deceases. We further give some basic data about the complexity of the environment where the mass transport takes place, and computational approaches in modeling the transport.

Considering tissue, we first can state that tissue is a composite medium with two distinct domains: extracellular and intracellular space. Next, extracellular space can be considered as a porous medium where the extracellular matrix represents the solid phase while the pores are filled with biological fluid. There exists a fluid flow within tissue because fluid due to transport through capillary walls from capillary system to pores, and in the reverse direction; and due to action of the lymphatic system which serves as a fluid drainage. Furthermore, molecules and other particulates are transported between the capillaries and extracellular space, but also to cells (and in reverse direction) through cell membranes. Additionally, interior of cells is complex, with the cytosol, cytoskeleton and organelles. In a simplified description, it is adopted that the governing laws for transport within the continuum domains and through biological barriers (vessel walls, and cell and organelle membranes) can be described according to the Darcy velocity-pressure relationship for convection and Fick's law for diffusion [1].

There are additional complexities in transport within tumors, due to irregular blood vessel branching and variability of vessel diameters and lengths, and geometric and viscous resistance [2–6]. A summary of the characteristics of blood flow within tumor vasculature is given in [7]. Mass exchange within the cell interior represents a separate field of the overall biomedical and clinical investigations. There are various factors which affect mass exchange within cells. These factors range from biochemical to mechanical, to signaling pathways [8]. Special methodologies and software have been developed for modeling mass exchange within cells, as a 'virtual cell' [9, 10].

Traditional computational methods include modeling of transport within blood vessels, tissue and cell interior. A simplified approach for transport in blood vessel, which is suitable for certain applications, goes back to the "network" method [11], with application of the Hagen-Poiseuille law [12] for fluid, and Fick's law for diffusion within moving fluid according to pipe flow conditions. Transport of rigid elliptical particles in flow within small vessels was studied in [13], while in [14] trajectories of different particle shapes within a net of small channels are investigated experimentally and numerically. By modeling deformable cell motion in fluid through a capillary narrowing, a critical pressure-diameter of cell relationship for cancerous cells in metastatic processes was calculated in [15].

Further, we list our references for mass transport with application to the medical problems. First, we introduced in [16] a correction function for diffusivity in the Fick's law in case of particulate transport within extracellular space. This correction is due to the molecular interaction between the transported molecules and the surrounding.

Molecular dynamics (MD) was used for calculation of the equivalent diffusion coefficient for the finite element modeling [17–21]. This multiscale hierarchical model was implemented into various biomedical problems [22–24]. The subsequent methodology for mass transport is based on the smeared concept representation. Formulation of the composite smeared finite element (CSFE) is introduced in [25] and further generalized and applied in biomedical engineering in [26–31].

In the next section we summarize the basic equations which describe the smeared FE methodology, while in Sect. 3 we briefly present the relations for coupling of ionic transport with electrical field and electromechanical coupling. In Sect. 4 are given several numerical examples solved by using the smeared field methodology. In the last section we present conclusions regarding the generality and advantages of the smeared FE models with respect to the traditional ones.

2 Smeared Finite Element Model Formulation

Here we summarize the fundamental relations in the formulation of the smeared finite element model. There were few basic steps in this formulation.

First, we introduced composite smeared finite element (CSFE) in [25] and generalized in [29], as a FE which contains as many domains as there are physical domains to be modeled: capillary domain, lymph domain, extracellular domain, domains of different types of cells, and organelles within cells. In case of electrophysiology, we additionally have the domain of the nerve network. This general CSFE is schematically shown in Fig. 1. Number of domains is N_d.

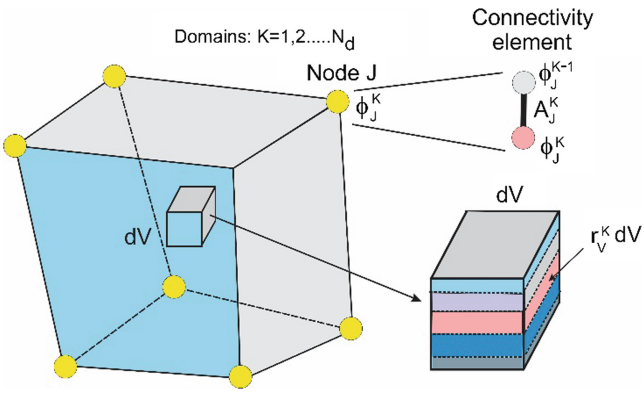

Fig. 1. Composite smeared finite element (CSFE), according to [29].

Each of the domains K occupies the volume V^K of the element volume V, as

$$V^K = r_V^K V \tag{1}$$

where r_V^K is the volumetric fraction. Each domain has its own physical filed ϕ^K, with the nodal values ϕ_J^K as shown in the Fig. 1, with interpolation

$$\phi^K = \sum_J N_J \phi_J^K \tag{2}$$

where N_J are interpolation functions and summation goes over all nodes. We consider gradient driven physical fields: concentration for diffusion, pressure for flow through porous media, temperature for heat conduction, electric potential for electrical conduction, with the corresponding constitutive law: Fick's law for diffusion, Darcy's law for fluid flow, Furrier's law for heat conduction, Ohm's law for electrical conduction. The balance equation for a domain K has a standard FE form [1, 29],

$$\left(\frac{1}{\Delta t}\mathbf{M} + \mathbf{K}\right)^{K(i-1)} \Delta\mathbf{\Phi}^{K(i)} = \mathbf{Q}^{Kext} + \mathbf{Q}_V^K - \frac{1}{\Delta t}\mathbf{M}^{K(i-1)}\left(\mathbf{\Phi}^{(i-1)} - \mathbf{\Phi}^t\right)^K - \mathbf{K}^{K(i-1)}\mathbf{\Phi}^{K(i-1)} \tag{3}$$

where

$$M_{IJ}^K = \int_V c_m^K N_I N_J r_V^K dV$$

$$K_{IJ}^K = \int_V D^K N_{I,k} N_{J,k} r_V^K dV, \; sum\, on\, k, \; k = 1, 2, 3$$

$$Q_{VI}^K = \int_V N_I q_V^K r_V^K dV \tag{4}$$

where $\mathbf{\Phi}^K$ is the nodal vector; c_m^K and D^K are the "mass coefficient" and transport coefficient, respectively. We have that $c_m^K = 1$ and D^K is diffusivity for diffusion; $c_m^K = 0$ and D^K is the Darcy permeability coefficient for fluid flow; for heat conduction $c_m^K = \rho c_T$ and D^K is heat conduction coefficient. For electrical potential we have that the "mass" matrix is

$$M_{IJ} = \varepsilon \int_V N_{I,k} N_{J,k} dV, \; sum\, on\, k, \; k = 1, \; 2, \; 3 \tag{5}$$

and D^K is the electrical conductivity.

In case of smeared domain representing the transport through a network of practically 1D transport conditions, as in capillary, lymph or neural fibers, we first need to transform the 1D to the continuum (2D or 3D) mathematical representation. This can be achieved by introducing a transport tensor D_{ij} (details are given in [25, 29]) as

$$D_{ij} = \frac{1}{A_{tot}} \sum_K D^K A^K \ell_i^K \ell_j^K \tag{6}$$

where summation goes over all 1D line elements in the vicinity of a considered point of the space in the FE model; A^K are the cross-sectional areas, ℓ_i^K are directional cosines,

and A_{tot} is the total cross-sectional area of the line elements. Note that the mass matrices do not need the transformation of the form (6).

Continuum fields within the CSFE are coupled by 2-node connectivity elements at each FE node, as schematically shown in Fig. 1. These elements take into account transport characteristics of walls for 1D domains, or membrane transport in case of cells or organelles. The balance equations have the form (3). The "mass" matrices can be expressed as

$$M_{11} = M_{22} = \frac{1}{3} c_{mJ} A_J h, \; M_{12} = M_{21} = \frac{1}{6} c_{mJ} A_J h \tag{7}$$

where c_{mJ} is the "mass coefficient" for the wall of the 1D line models (according to the above definition for continuum); while in case of electrical field, the coefficient is capacitance of the wall [30]. The terms A_J and h are the interface area belonging to the node J and wall/membrane thickness, respectively. The wall transport matrix is

$$K_{11} = K_{22} = -K_{12} = -K_{21} = D_{wall} A_J \tag{8}$$

where D_{wall} is the wall/membrane transport coefficient. In case of diffusion or heat transfer, there is additionally a convective matrix which can be expressed as

$$K^v_{11} = -K^v_{22} = -K^v_{21} = K^v_{12} = -\frac{1}{2} k_h A_J (\Phi_1 - \Phi_2) \tag{9}$$

where Φ_1 and Φ_2 stand for pressures or temperatures, respectively; and k_h is the hydraulic coefficient.

3 Coupling Ionic Transport with Electrical Field and Electromechanical Coupling

In case of transport of ions through tissue there is coupling between electrical field and ion concentration. The balance equation for ions in a continuum relies on the Nenrst-Plank equation and can be written in the form [9]

$$\frac{\partial c}{\partial t} = \frac{\partial}{\partial x_i} \left[D \frac{\partial c}{\partial x_i} + \frac{DzF}{RT} c \frac{\partial V_e}{\partial x_i} \right], \; sum\, on\, i: \; i = 1, \, 2, \, 3 \tag{10}$$

where c is concentration, D is diffusivity, z is molecule valence, F is the Faraday constant, R is the gas constant, T is absolute temperature, and V_e is electrical potential. The source term - second within the parenthesis of the expression (10), gives the nodal mass flux within the domain K as

$$Q^{KE}_J = \frac{DFz}{RT} \int_V N_J \frac{\partial}{\partial x_i} \left(c \frac{\partial V_e}{\partial x_i} \right) r^K_V dV \tag{11}$$

On the other hand, the ion concentration affects the field of electrical potential. The nodal current due to change of ion concentration in the domain can be evaluated through the expression

$$I^{Kc}_J = \int_V N_J \sum_m z_m F \frac{\partial c_m}{\partial t} r^K_V dV \tag{12}$$

where summation includes all transported ions. The transport matrix can be expressed as [30]

$$K_{11} = -K_{21} = A_J\left(P_n f_n + P_d \frac{N}{e^N - 1} f_n k_{pH}^o\right)$$
$$K_{22} = -K_{12} = A_J\left(P_n f_n + P_d \frac{N e^N}{e^N - 1} f_n k_{pH}^i\right) \tag{13}$$

where P_n and P_d are permeability coefficients for neutral and ionized forms of molecules, f_n and k_{pH} are material constants which take into account chemical and electrochemical characteristics of the transported molecules (details are given in [9, 30, 32]); the upper indices "i" and "o" denote sides of the membrane; and $N = \frac{zFE}{RT}$, where E is the membrane electric potential.

Besides the current through membrane according to capacitance and conduction, with the matrices given by Eqs. (7) and (8), there exists additional current I_{ion} due to flow of various charged molecules through the membrane; this flow depends on the membrane potential [33, 34]. Detailed derivation of expression for I_{ion} for sodium and potassium molecules is given in Appendix 2 of reference [30].

Electromechanical coupling is the vital process in muscles and has been investigated over centuries. We used in our models the expression for generation of the active stress $\boldsymbol{\sigma}_{act}$ within muscle sarcomere and along the fiber of the heart muscle, according to [35]

$$\sigma_{act} = \frac{\left[Ca^{2+}\right]^n}{\left[Ca^{2+}\right]^n + C_{50}^n} \sigma_{\max}[1 + \eta(\lambda - 1)] \tag{14}$$

where Ca^{2+} is calcium concentration; $\boldsymbol{\sigma}_{\max}$ is maximum isometric stress, C_{50} is concentration for 50% availability of actin sites for the cross bridge binding, n is related to the rate of this availability to concentration, $\boldsymbol{\eta}$ is parameter which is governing the rate of muscle fiber deformation; and λ the fiber stretch. Calcium concentration depends on the membrane potential and we use smeared model for calculating the field of electric potential, then determine calcium concentration and compute the active stress. This stress acts as a distributed external loading on the muscle tissue causing muscle deformation and motion [36].

4 Numerical Examples

We have selected three examples which are typical for application in biomedical engineering problems. They illustrate the main features of our smeared finite element models.

4.1 Application of CSFE in Estimation Transport Parameters

In reference [37] drug transport properties in a mouse model of murine breast cancer (4T1) liver metastases were investigated. The study provided insight into origins of drug transport-based therapeutic resistance in metastases and proposed strategies to overcome

those resistances. Here we use our CSFE element to simulate 10 and 70 kDa dextran diffusion in order to estimate of the apparent diffusion coefficients inside tumor. This is achieved by fitting tumor intensity profiles with the molecule concentration.

The tumor is represented by 1/8 sphere within surrounding cubic domain as the surrounding breast tissue (Fig. 2a). The size of tumor in the model was set to values based on IVM data: 160, 167, and 163 μm, respectively. IVM imaging revealed that there are no capillaries within tumor (volumetric fraction $r_v = 0$) so that dextran permeation relies on diffusion characterized by diffusivity D. Surrounding cubic liver domain was modeled with 20% capillary volume and tissue diffusion coefficient 10 $\mu m^2/s$ [37]. The quantified dextran intensity in liver (Fig. 2b) was used as a systemic input concentration profile which induces a diffusion gradient transport of dextran into tumors. Numerical simulations of dextran diffusion into the tumor from liver were run for the time period of 280–300 s maximum; an example of concentration field is shown in Fig. 2c and an example of fitted profile is shown in Fig. 2d. It was found that diffusion coefficient within tumor for dextran 10 kDa was D = 5–9 $\mu m^2/s$ (mean value 7.3 $\mu m^2/s$) while for 70 kDa dextran it was D= 0.1–0.3 $\mu m^2/s$ (mean value 0.2 $\mu m^2/s$) which was quite similar to other studies experimental values.

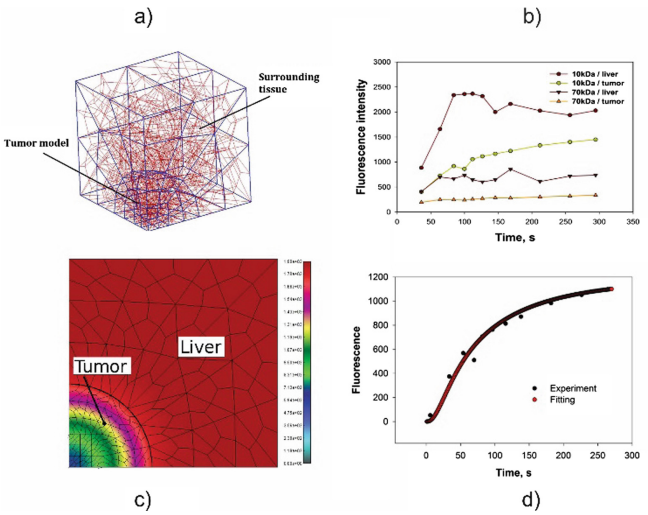

Fig. 2. (a) Finite element model of spherical tumor with surrounding tissue (3D representation); (b) Dextran 10 and 70 kDa fluorescence kinetics in a 4T1 tumor and surrounding liver (used as input concentration curves); (c) Concentration field of 10 kDa red dextran tracer calculated using CSFE 3D model of 160 μm 4T1 metastatic tumor; (d) Example of fitted fluorescence curves of 10 kDa dextran in a tumor to determine diffusion coefficient (according to [37]). (Color figure online)

4.2 3D Model of Heart Ventricles with Purkinje Fibers, Tissue and Muscle Cells

Here, we first present calculation of the electrical field using detailed and smeared model, and then show results for deformation of the heart wall due to electro-mechanical coupling.

Electrical signal within the heart wall is transmitted by the neural fibers forming the so called Purkinje network. Purkinje fibers are located in thin layer between hart wall layer and internal myocardium. In order to appropriately take into account this network in our CSFE element of a 3D real model of heart walls (which can include LV, RV and other compartments of the heart), we generated additional layer of uniform 3D FE elements which represents the domain of Purkinje network. Parameters needed for this domain are: thickness of Purkinje network layer, volume fraction of fibers within this layer, and conductivity tensor.

Procedure for generation of additional layer is outlined in Fig. 3, together with resulting mesh for two examples: ¼ sphere model, and heart with ventricles. This procedure is implemented in our in-house software CAD. As a result, we have the fractal based Purkinje 1D network which is projected to 3D real model of human heart.

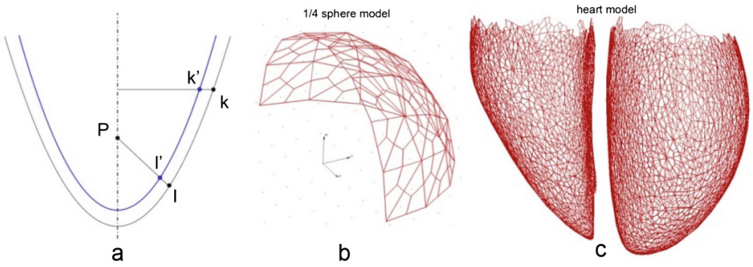

Fig. 3. Additional layer with uniform mesh for Purkinje network (a) 3D additional domain; (b) Domain of ¼ sphere; (c) Heart model with RV and LV.

A 3D mesh of Purkinje fibers, Fig. 4a, is manually created for the heart ventricle model. Algorithm for generation of uniform layer is applied to a 3D tissue with the thickness 0.1 mm; the mesh is shown in Fig. 4b. Corresponding conductivity tensor, based on 1D Purkinje mesh from Fig. 4a, is calculated according to Eq. (6) for uniform mesh from Fig. 3b, and used in smeared model.

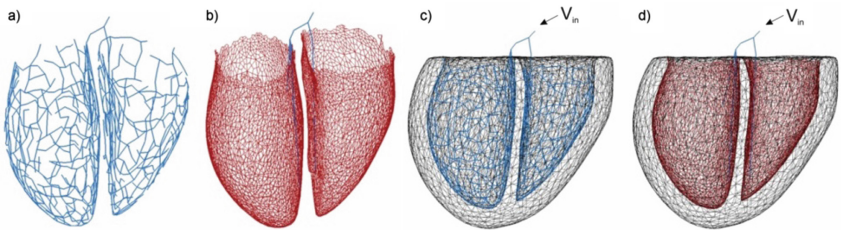

Fig. 4. (a) Purkinje fibers in detail model; (b) Uniform layer in smeared model, (c) Detail model with Purkinje fibers; (d) Smeared model with uniform layer.

Detailed model of biventricular heart and corresponding smeared model are shown in Figs. 4c, d. Inlet function of potential $V_{in}(t)$ is prescribed at inlet of fibers, and has the shape shown in Fig. 5.

Data used in the detailed and corresponding smeared model are (G_a in [$AV^{-1}m^{-1}$], G_m in [Siemens/cm^2], C_m in [F/cm^2]):

Large nerve fibers: $G_a - 10^{11}$; $G_m - 10^5$; $C_m - 0.1$

Small nerve fibers: $G_a - 10^{11}$; $G_m - 10^5$; $C_m - 0.1$

Extracellular Space: G_a x – 10^7; y – 10^7; z – 10^7

Diameter of small nerves is: 0.1 μm

In Fig. 5 is displaying electrical potential in extracellular space (tissue) domain of detailed (black line) and smeared model (blue dots fibers). It can be seen that solutions for the detailed and smeared model are practically the same.

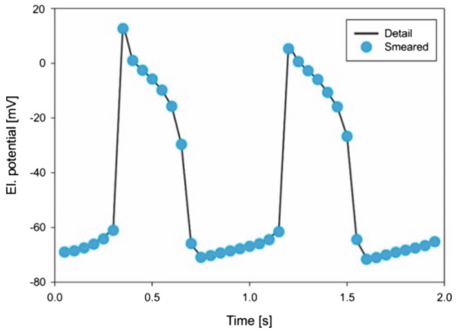

Fig. 5. Electrical potential vs. time for extracellular space - detailed vs. smeared.

Fields of electrical potential in extracellular space, for detailed model (upper panels) and smeared model (lower panels) for few time moments (0.05 s, 0.3, 0.35, 0.5 and 0.75) of the first cycle of the action potential function, are given in Figs. 6, 7 and 8: for XY, view inside of left and right ventricles, and rotated view (results are presented as dots), respectively. It can be noticed good agreement between the two models.

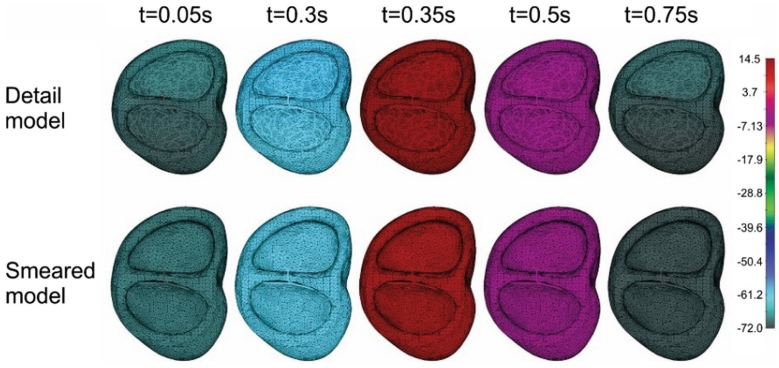

Fig. 6. Electrical potential in tissue for detail model (upper panel), and smeared model (lower panel) - view XY.

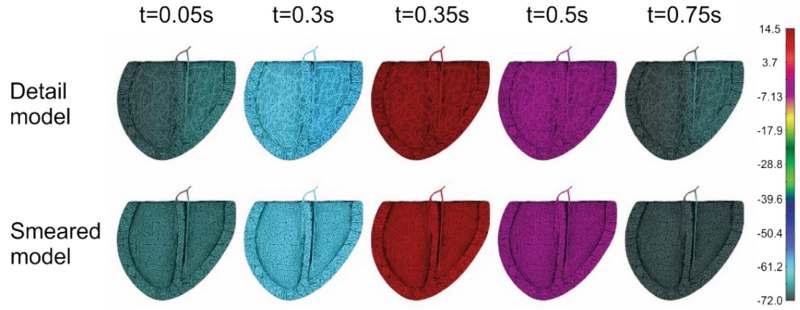

Fig. 7. Electrical potential in tissue for detail model (upper panel), and smeared model (lower panel) - view YZ inside ventricles.

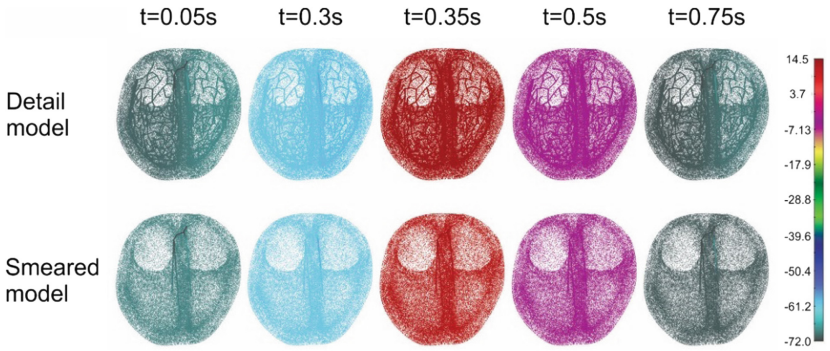

Fig. 8. Electrical potential in tissue for detail model (upper panel), and smeared model (lower panel).

The same 3D biventricular heart model is used for the coupled electro-mechanical simulation, with constrains in septum zone (Fig. 9a), and with the real fibers mesh orientation shown in Fig. 9b and c.

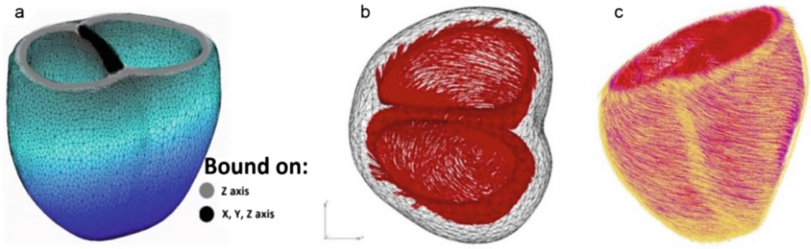

Fig. 9. Heart electromechanical model. (a) boundary conditions in the model; orientation of the fibers: top (b) and side (c) view.

The above described electrical field is used, and the active stress is calculated according to Hunter's relation for excitation-contraction coupling (14). Passive stresses are determined using constitutive relations for linear elastic material model with Young's modulus of $E = 1000$ Pa and Poisson ratio of $\mu = 0.49$. Displacements of the heart wall for the first cycle of the electrical signal (Fig. 5) are show in Fig. 10.

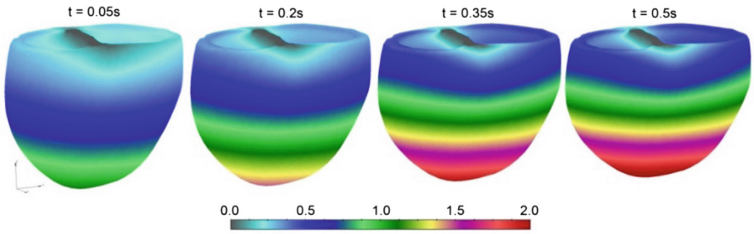

Fig. 10. Displacements in coupled electro-mechanical model of biventricular heart for one cycle of the electrical wave.

5 Conclusions

The presented finite element methodology of coupled smeared physical fields in the composite media opens new possibility of solving complex problems in various domains of science and technology. This is particularly important in computational modeling of large scale bioengineering problems, such as drug delivery within tumors and entire organs. The smeared physical fields can further be coupled to mechanics as in case of muscles or heart.

Acknowledgments. The authors acknowledge support from the City of Kragujevac, Serbia.

Funding. This work is supported by the grant NCI U54 CA210181. Also, it is supported by the SILICOFCM project that has received funding from the European Union's Horizon 2020 research and innovation programme under grant agreement No 777204. This research was also funded by Ministry of Education and Science of Serbia, grants OI 174028 and III 41007.

References

1. Kojic, M., Filipovic, N., Stojanovic, B., Kojic, N.: Computer Modeling in Bioengineering - Theoretical Background, Examples and Software. Wiley, Chichester (2008)
2. Less, J.R., Skalak, T.C., Sevick, E.M., Jain, R.K.: Microvascular architecture in a mammary carcinoma: branching patterns and vessel dimensions. Cancer Res. **51**, 265–273 (1991)
3. Roberts, W.G., Palade, G.E.: Neovasculature induced by vascular endothelial growth factor is fenestrated. Cancer Res. **57**, 765–772 (1997)
4. Sevick, E.M., Jain, R.K.: Geometric resistance to blood flow in solid tumors perfused ex vivo: effects of tumor size and perfusion pressure. Cancer Res. **49**, 3506–3512 (1989)

5. Sevick, E.M., Jain, R.K.: Viscous resistance to blood flow in solid tumors: effect of hematocrit on intratumor blood viscosity. Cancer Res. **49**, 3513–3519 (1989)
6. Sevick, E.M., Jain, R.K.: Effect of red blood cell rigidity on tumor blood flow: increase in viscous resistance during hyperglycemia. Cancer Res. **51**(51), 2727–2730 (1991)
7. Jain, R.: Determinants of tumor blood flow: a review. Cancer Res. **48**, 2641–2658 (1988)
8. Rangamani, P., Iyengar, R.: Modelling spatio-temporal interactions within the cell. J. Biosci. **32**, 157–167 (2007)
9. Schaff, J., Fink, C.C., Slepohenko, B., Carson, J.H., Loew, L.M.: A general computational framework for modeling cellular structure and function. Biophys. J. **73**, 1135–1146 (1997)
10. Moraru, I.I., Schaff, J.C., Slepchenko, B.M., Blinov, M.L., Morgan, F., Lakshminarayana, A., Gao, F., Li, Y., Loew, L.M.: Virtual cell modelling and simulation software environment. IET Syst. Biol. **2**, 352–362 (2008)
11. Lipowsky, H.H., Zweifach, B.W.: Network analysis of microcirculation of cat mesentery. Microvasc. Res. **7**, 73–83 (1974)
12. Kojic, M., Milosevic, M., Simic, V., Ferrari, M.: A 1D pipe finite element with rigid and deformable walls. J. Serbian Soc. Comput. Mech. **8**, 38–53 (2014)
13. Isailovic, V., Kojic, M., Milosevic, M., Filipovic, N., Kojic, N., Ziemys, A., Ferrari, M.: A computational study of trajectories of micro- and nano-particles with different shapes in flow through small channels. J. Serbian Soc. Comput. Mech. **8**, 14–28 (2014)
14. Kiseliovas, V., Milosevic, M., Kojic, M., Mazutis, L., Kai, M., Liu, Y.T., Yokoi, K., Ferrari, M., Ziemys, A.: Tumor progression effects on drug vector access to tumor-associated capillary bed. J. Controlled Release **261**, 216–222 (2017)
15. Kojić, N., Milošević, M., Petrović, D., Isailović, V., Sarioglu, A.F., Haber, D.A., Kojić, M., Toner, M.: A computational study of circulating large tumor cells traversing microvessels. Comput. Biol. Med. **63**, 187–195 (2015)
16. Ziemys, A., Kojic, M., Milosevic, M., Kojic, N., Hussain, F., Ferrari, M., Grattoni, A.: Hierarchical modeling of diffusive transport through nanochannels by coupling molecular dynamics with finite element method. J. Comput. Phys. **230**, 5722–5731 (2011)
17. Ziemys, A., Kojic, M., Milosevic, M., Ferrari, M.: Interfacial effects on nanoconfined diffusive mass transport regimes. Phys. Rev. Lett. **108**, 236102 (2012)
18. Kojic, M., Milosevic, M., Kojic, N., Ferrari, M., Ziemys, A.: On diffusion in nanospace. J. Serbian Soc. Comput. Mech. **5**, 84–109 (2011)
19. Kojic, M., Milosevic, M., Kojic, N., lsailovic, V., Petrovic, D., Filipovic, N., Ferrari, M., Ziemys, A.: Transport phenomena: computational models for convective and diffusive transport in capillaries and tissue. In: De, S., Hwang, W., Kuhl, E. (eds.) Multiscale Modeling in Biomechanics and Mechanobiology, pp. 131–156. Springer, London (2015)
20. Kojic, M., Ziemys, A., Milosevic, M., Isailovic, V., Kojic, N., Rosic, M., Filipovic, N., Ferrari, M.: Transport in biological systems. J. Serbian Soc. Comput. Mech. **5**, 101–128 (2011)
21. Kojic, M., Milosevic, M., Kojic, N., Kim, K., Ferrari, M., Ziemys, A.: A multiscale MD–FE model of diffusion in composite media with internal surface interaction based on numerical homogenization procedure. Comput. Methods Appl. Mech. Eng. **269**, 123–138 (2014)
22. Yokoi, K., Kojic, M., Milosevic, M., Tanei, T., Ferrari, M., Ziemys, A.: Capillary-wall collagen as a biophysical marker of nanotherapeutic permeability into the tumor microenvironment. Cancer Res. **74**, 4239–4246 (2014)
23. Ruiz-Esparza, G.U., Wu, S., Segura-Ibarra, V., Cara, F.E., Evans, K.W., Milosevic, M., Ziemys, A., Kojic, M., Meric-Bernstam, F., Ferrari, M., Blanco, E.: Polymer nanoparticles encased in a cyclodextrin complex shell for potential site- and sequence-specific drug release. Adv. Funct. Mater. (2014). https://doi.org/10.1002/adfm.201400011

24. Kojic, M., Milosevic, M., Kojic, N., Starosolski, Z., Ghaghada, K., Serda, R., Annapragada, A., Ferrari, M., Ziemys, A.: A multi-scale FE model for convective-diffusive drug transport within tumor and large vascular networks. Comput. Methods Appl. Mech. Eng. **294**, 100–122 (2015)
25. Kojic, M., Milosevic, M., Simic, V., Koay, E.J., Fleming, J.B., Nizzero, S., Kojic, N., Ziemys, A., Ferrari, M.: A composite smeared finite element for mass transport in capillary systems and biological tissue. Comput. Meth. Appl. Mech. Eng. **324**, 413–437 (2017). https://doi.org/10.1016/j.cma.2017.06.019
26. Kojic, M., Milosevic, M., Simic, V., Koay, E.J., Kojic, N., Ziemys, A., Ferrari, M.: Extension of the composite smeared finite element (CSFE) to include lymphatic system in modeling mass transport in capillary systems and biological tissue. J. Serbian Soc. Comput. Mech. **11**(2), 108–120 (2017)
27. Milosevic, M., Simic, V., Milicevic, B., Koay, E.J., Ferrari, M., Ziemys, A., Kojic, M.: Correction function for accuracy improvement of the composite smeared finite element for diffusive transport in biological tissue systems. Comput. Methods Appl. Mech. Eng. **338**, 97–116 (2018). https://doi.org/10.1016/j.cma.2018.04. ISSN 0045-7825
28. Kojic, M., Milosevic, M., Simic, V., Koay, E.J., Kojic, N., Ziemys, A., Ferrari, M.: Multiscale smeared finite element model for mass transport in biological tissue: from blood vessels to cells and cellular organelles. Comput. Biol. Med. **99**, 7–23 (2018). https://doi.org/10.1016/j.compbiomed.2018.05.022
29. Kojic, M.: Smeared concept as a general methodology in finite element modeling of physical fields and mechanical problems in composite media. J. Serbian Soc. Comput. Mech. **12**(2), 1–16 (2018)
30. Kojic, M., Milosevic, M., Simic, V., Ziemys, A., Filipovic, N., Ferrari, M.: Smeared multiscale finite element model for electrophysiology and ionic transport in biological tissue. Comput. Biol. Med. **108**, 288–304 (2019)
31. Santagiuliana, R., Milosevic, M., Milicevic, B., Sciumè, G., Simic, V., Ziemys, A., Kojic, M., Schrefler, B.A.: Coupling tumor growth and bio distribution models. Biomed. Microdevice (2019). https://doi.org/10.1007/s10544-019-0368-y
32. Zhang, X., Shedden, K., Rosania, G.R.: A cell-based molecular transport simulator for pharmacokinetic prediction and cheminformatic exploration. Molec. Pharm. **3**, 704–716 (2006)
33. Noble, D.: A modification of the Hodgkin-Huxley equations applicable to Purkinje fibre action and pace-maker potentials. J. Physiol. **160**, 317–352 (1962)
34. O'Hara, T., Virág, L., Varró, A., Rudy, Y.: Simulation of the undiseased human cardiac ventricular action potential: model formulation and experimental validation. PLoS Comput. Biol. **7**, e1002061–e1002090 (2011)
35. Hunter, P.J., McCulloch, A.D., ter Keurs, H.E.D.J.: Modelling the mechanical properties of cardiac muscle. Prog. Biophys. Mol. Biol. **69**, 289–331 (1998)
36. Kojic, M., Milosevic, M., Simic, V., Milicevic, B., Geroski, V., Nizzero, S., Ziemys, A., Filipovic, N., Ferrari, M.: Smeared multiscale finite element models for mass transport and electrophysiology coupled to muscle mechanics. Front. Bioeng. Biotechnol. **7**, 381 (2019)
37. Ziemys, A., Yokoi, K., Kai, M., Liu, Y.T., Kojic, M., Simic, V., Milosevic, M., Holder, A., Ferrari, M.: Progression-dependent transport heterogeneity of breast cancer liver metastases as a factor in therapeutic resistance. J. Controlled Release **291**, 99–105 (2018). ISSN 0168–3659

Composite Smeared Finite Element – Application to Electrical Field

Vladimir Geroski[1], Miljan Milosevic[2,3(✉)], Vladimir Simic[1,2], Bogdan Milicevic[1,2], Nenad Filipovic[1], and Milos Kojic[2,4,5]

[1] Faculty for Engineering Sciences, University of Kragujevac, Sestre Janic 6, 34000 Kragujevac, Serbia
[2] Bioengineering Research and Development Center BioIRC Kragujevac, Prvoslava Stojanovica 6, 34000 Kragujevac, Serbia
[3] Belgrade Metropolitan University, Tadeusa Koscuska 63, 11000 Belgrade, Serbia
miljan.m@kg.ac.rs
[4] The Department of Nanomedicine, Houston Methodist Research Institute, 6670 Bertner Ave., R7 117, Houston, TX 77030, USA
[5] Serbian Academy of Sciences and Arts, Knez Mihailova 35, 11000 Belgrade, Serbia

Abstract. In this paper we present application of recently developed composite smeared finite element (CSFE) to electrophysiology problems and ionic transport, mainly in heart tissue. The main advantage of the CSFE is that discrete transport, approximated by 1D finite elements within nervous system, can be transformed into a continuum framework. The governing balance equation for electrical flow within neuron fibers is defined according to the cable theory. This governing equation is then transformed into continuum format represented by formulating a conductivity tensor. We include transport of ions which affects the electrical potential, therefore there exists a coupling between ion concentration and the electrical field. Besides general presentation of the smeared FE methodology, we give some additional details regarding the derivation of the coupling relations within the CSFE, and also accuracy analysis of the element. Accuracy is tested on several simple 2D and 3D examples of Purkinje fibers network with different electrical potential. Using the smeared field approach, we can analyze various complex problems in a simple form, with all important physical properties included in the model.

Keywords: Composite smeared finite element · Electrophysiology · Nerve network · Ionic transport · Conductivity tensor

1 Introduction

Material transport, as a fundamental process in living organisms, includes ionic transport within cells and through biological membranes, electrical signals, etc. Tremendous efforts have been made over centuries to find the laws for the extremely complex transport phenomena, while in last decades the analytical interpretation of the transport laws

N. Filipovic (Ed.): ICCB 2019, LAIS 11, pp. 35–43, 2020.
https://doi.org/10.1007/978-3-030-43658-2_4

were enhanced by computational modeling. But, still, there is today a need for improvement of computational methods in order to develop computational methods and software for achieving better therapy and cure successfully various deceases.

Due to the enormous complexity of the biological system, it would be almost impossible to generate a detailed computational model for the physical fields related to mass transport, electrophysiology and coupled fields. It is desirable to have a methodology feasible for practical applications. We have introduced a smeared concept for mass transport in capillary system and tissue in [1] and further generalized and applied in biomedical engineering in references [2–7].

In the next section we summarize the basic equations which describe the smeared FE methodology, while in Sect. 4 we give several numerical examples solved by using this methodology. In the last section we present conclusions regarding the generality and advantages of the smeared FE models with respect to the traditional ones.

2 Smeared Finite Element Model Formulation

In this section we summarize the fundamental relations in the formulation of the smeared finite element model. There were few basic steps in this formulation. First, the composite smeared finite element as introduced (CSFE) in [1] and generalized in [5], represents a FE which contains separate domains which correspond to physical domains to be modeled. In case of electrophysiology, there is also the domain of the nerve network. This general CSFE is schematically shown in Fig. 1a. Number of domains is N_d.

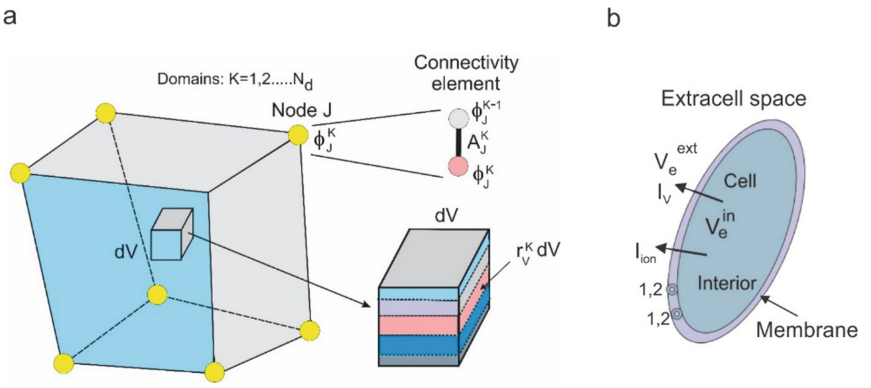

Fig. 1. (a) Composite smeared finite element (CSFE), according to [5]. (b) Cell with current I_V through membrane due to membrane potential difference, and ionic current I_{ion} due to molecule flow included in connectivity elements 1, 2.

Each of the domains K occupies the volume V^K of the element volume V and has its own physical field ϕ^K, with the nodal values ϕ_J^K as shown in the figure. We consider gradient driven physical field of the electric potential for electrical conduction, with the corresponding constitutive law - Ohm's law for electrical conduction. The balance

equation for a domain K has a standard FE form [5, 8],

$$\left(\frac{1}{\Delta t}\mathbf{M}+\mathbf{K}\right)^{K(i-1)}\Delta\mathbf{\Phi}^{K(i)}=\mathbf{Q}^{Kext}+\mathbf{Q}_V^K-\frac{1}{\Delta t}\mathbf{M}^{K(i-1)}\left(\mathbf{\Phi}^{(i-1)}-\mathbf{\Phi}^t\right)^K - \mathbf{K}^{K(i-1)}\mathbf{\Phi}^{K(i-1)} \tag{1}$$

where

$$\begin{gathered} M_{IJ}^K=\int\limits_V c_m^K N_I N_J r_V^K dV \\ K_{IJ}^K=\int\limits_V D^K N_{I,k} N_{J,k} r_V^K dV,\ sum\ on\ k,\ \ k=1,\ 2,\ 3 \\ Q_{VI}^K=\int\limits_V N_I q_V^K r_V^K dV \end{gathered} \tag{2}$$

where $\mathbf{\Phi}^K$ is the nodal vector; c_m^K and D^K are the "mass coefficient" and transport coefficient, respectively. For example, we have for heat conduction that $c_m^K=\rho c_T$ and D^K is heat conduction coefficient, while for diffusion $c_m^K=1$ and D^K is diffusion coefficient. For electrical potential we have that the "mass" matrix is

$$M_{IJ}=\varepsilon\int\limits_V N_{I,k}N_{J,k}dV,\ sum\ on\ k,\ k=1,\ 2,\ 3 \tag{3}$$

and D^K is the electrical conductivity.

Continuum fields within the CSFE are coupled by 2-node connectivity elements at each FE node, as schematically shown in Fig. 1a. These elements take into account transport characteristics of walls or membrane transport in case of cells, as 1D domains. The balance equations have the form (1). The "mass" matrices can be expressed as

$$M_{11}=M_{22}=\frac{1}{3}c_{mJ}A_J h,\ M_{12}=M_{21}=\frac{1}{6}c_{mJ}A_J h \tag{4}$$

where c_{mJ} is capacitance coefficient of the wall in case of electrical field [6]. The terms A_J and h are the interface area belonging to the node J and wall/membrane thickness, respectively. The wall transport matrix is

$$K_{11}=K_{22}=-K_{12}=-K_{21}=D_{wall}A_J \tag{5}$$

where D_{wall} is the wall/membrane transport coefficient.

The governing balance equation of electrical flow within neural fibers relies on the so-called cable theory. For the axial current flow along a nerve without lateral flow, the basic relation is

$$I_x=-G_a\frac{\partial V_e}{\partial x} \tag{6}$$

where $\mathrm{I_x}$ is the current density along the fiber axis x, G_a is axial conductivity and V_e is electric potential. In case of large neural fibers, there is practically only the axial

flow, and the FE model consists of the 1D elements with a standard form (1) of balance equations.

In case when there is the lateral flow through the wall, that flow can be expressed in the form (taking that current going out of the fiber is positive),

$$I_{mem} = G_m\left(V_e^{in} - V_e^{ext}\right) + C_m\left(\frac{\partial V_e^{in}}{\partial t} - \frac{\partial V_e^{ext}}{\partial t}\right) + I_{ion} \tag{7}$$

where G_m and C_m are the wall conductivity and capacitance, respectively; V_e^{in} and V_e^{ext} are potentials within fiber and in the surrounding; and I_{ion} is ionic current due to flow of various charged molecules through the wall, which depends on the membrane potential [9, 10]. The lateral flow is modeled by connectivity elements 1, 2 at double nodes along fibers and on the cell membranes (Fig. 1b). Detailed derivation of expression for I_{ion} for sodium and potassium molecules is given in Appendix 2 of reference [6].

3 Conductivity Tensor for Purkinje Network

Due to enormous number of nerves in the heart, generating a true detailed model, with all those nerves included, is complex, not practical, and is very time consuming. In order to develop model which is suitable for general applications some simplifications are needed. This is achieved by our smeared concept, applicable to 1D transport as in capillaries, lymph vessels or neural fibers. We need to transform the 1D flow to the continuum (2D or 3D) mathematical representation. This can be achieved by introducing a transport tensor $\mathbf{G}_{ij}$ (details of the derivation are given in [11]) as (Fig. 2):

$$G_{ij} = \frac{1}{A_{tot}} \sum_K G_K A_K \ell_{Ki} \ell_{Kj} \tag{8}$$

where $A_{tot} = \sum_K A_K = \frac{\pi}{4} \sum_K d_K^2$ is the total cross-sectional area of nerve, ℓ_{Kj} is the directional cosine of the nerve axis with respect to the coordinate axis j, G_K is conductivity for nerve K. In case of general nerve mesh we take points within the space and consider all nerves in the selection domain (vicinity) as schematically shown in Fig. 4a. Then, in a point B of a continuum, we calculate the coefficients of the conductivity tensor according Eq. (8) where summation goes over all points A_K in the vicinity of the point B, Fig. 4b.

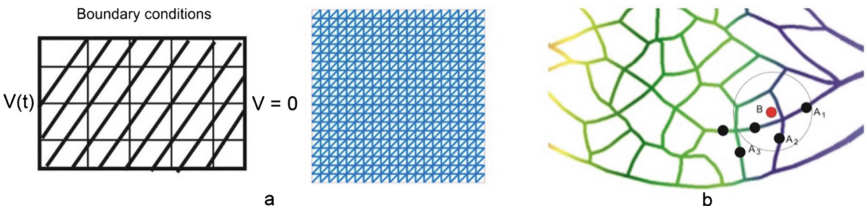

Fig. 2. (a) Detailed model with prescribed potentials V(t) at boundaries. (b) Interpolations of coefficients of conductivity tensor: summation over all points A_K in the vicinity of the point B

Interpolation for direction factors for case from Fig. 4b can be done following procedure presented in [11], which includes distances between point B and points A_1, A_2, A_3,…, A_n, denoted as L_1, L_2, L_3,…, L_n. Using this procedure interpolation coefficients c_1, c_2, c_3, …, c_n can be calculated and used for calculation of resulting conductivity tensor at node B as:

$$G_{ij} = \frac{1}{A_{tot}} \sum_{K} c_K G_K A_K \ell_{Ki} \ell_{Kj} \tag{9}$$

where c_K stands for c_k. Note that if point B (FE node) is on the fiber, then summation goes over $K = 1$ only.

4 Numerical Examples

Accuracy for smeared model is tested on several simple 2D examples by comparison with detailed models.

4.1 Simple 2D Model

Mesh for detailed model, 2D tissue, and 1D domain of small neural fibers are presented as blue lines in Figs. 3a, b, c, and inlet activation Purkinje function is shown in Fig. 1d.

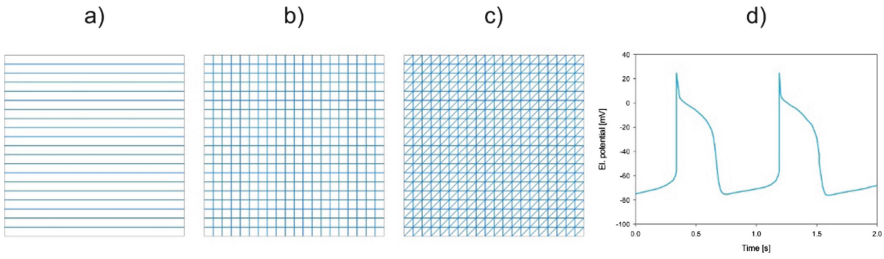

Fig. 3. Detailed model for: (a) parallel-aligned small neural fibers, (b) orthogonal cross-aligned fibers, (c) with diagonal fibers, (d) inlet Purkinje activation function

Parameters of the model are as follows: dimension of the domain is L = 10, Area = 100 [mm^2], FE mesh division in 20 × 20, and time steps used in simulations are 400 × 0.005 s. Electric potential of V_{in} is Purkinje activation function in [mV] prescribed at the left border of 1D nodes of the model, while $V_{out} = 0$ is prescribed at the right boundary. The fibers are with diameter of $D_{pipe} = 0.1$ [mm], conductivity is Ga = 1000 [$AV^{-1}m^{-1}$], membrane conductivity is Gm = 1000 [$AV^{-1}m^{-1}$], while capacitance of cell membrane is Cm = 1 [$S/\mu m^2$]. Conductivity in extracellular space is assumed to be isotropic with G = 0.001 [$AV^{-1}m^{-1}$]. Volumetric fractions of nerve domain for models at Fig. 1. are: r_V = 0.1459 for parallel-aligned, $r_V = 0.298$ for orthogonal cross-aligned, and $r_V = 0.502$ for diagonal-aligned fibers. Results for 2D detailed and smeared models for parallel, orthogonal and diagonal aligned fibers are shown in Figs. 4 and 5, respectively.

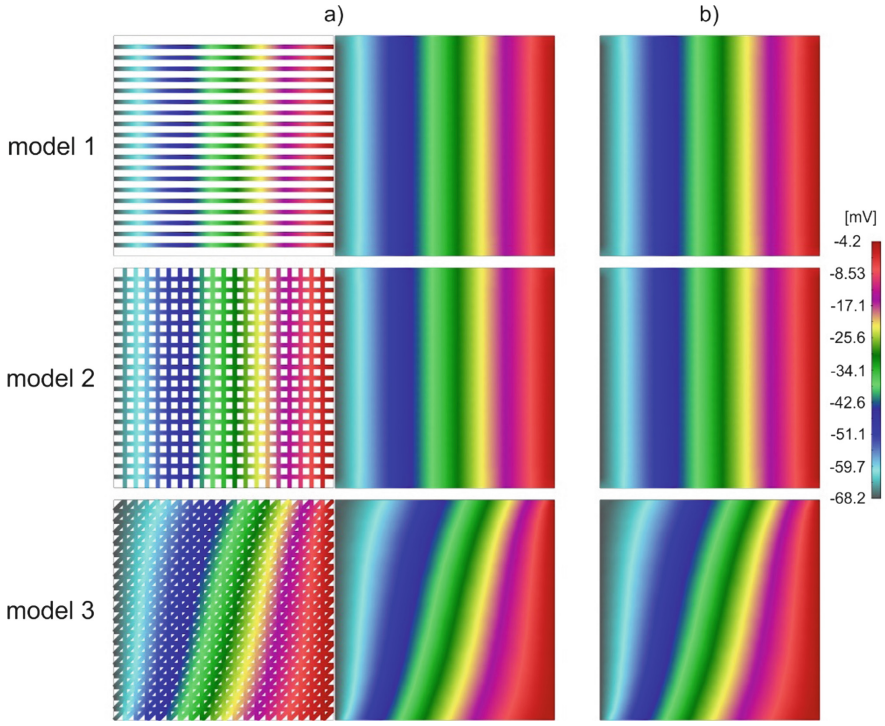

Fig. 4. Electrical potential for (a) detailed model – neural fibers and tissue, (b) smeared model – tissue. Model 1 represents parallel-aligned, model 2 is for orthogonal, model 3 is for diagonal-aligned fibers included.

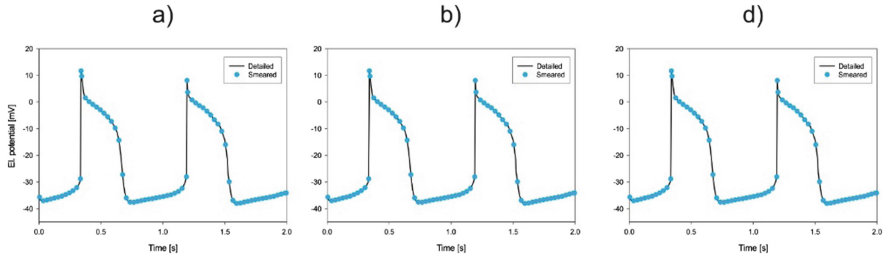

Fig. 5. Graph for electrical potential vs time for detailed and smeared model for (a) parallel-aligned fibers, (b) orthogonal cross-aligned and (c) for diagonal-aligned fibers included.

4.2 A Real 2D Model of Heart Wall with Purkinje Fibers

Example for accuracy analysis of CSFE model and conductivity tensor is based on a two dimensional fractal network of Purkinje fibers in the human heart [12], as shown in Fig. 6.

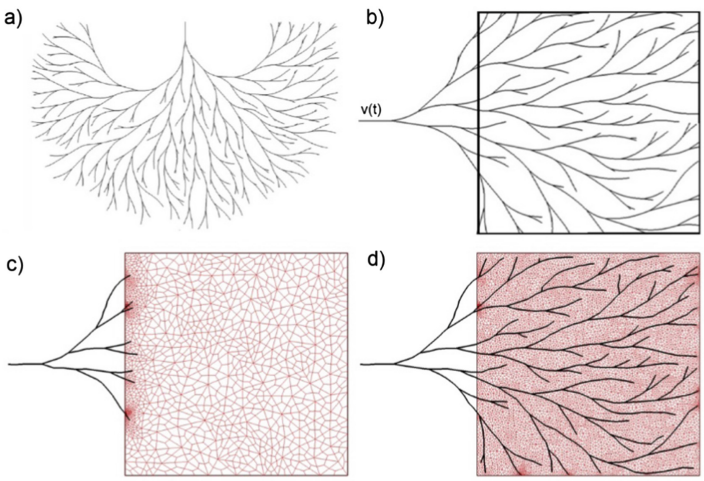

Fig. 6. Generation of the Purkinje network in the human heart. (a) Two-dimensional fractal network [12]. (b) Referent model for testing accuracy of smeared model, (c) FE mesh of referent smeared model (d) FE mesh of detailed model

Referent domains used in our simulations are shown in Fig. 6b and d. We consider two different models: detailed and smeared. Detailed model contains 1D elements, embedded in surrounding 2D tissue.

Reconstruction of 1D fibers from 2D network is done using our in-house Imaging CAD which allows manual segmentation of 1D elements. Inlet potential is prescribed at left side of the model (constant V(t) or Purkinje V(t) function), Fig. 6b and c. On right side we used isolated system or prescribed $V = 0$ potential. Results for detailed and smeared model are shown in Fig. 7, in case of prescribed $V = 0$ potential.

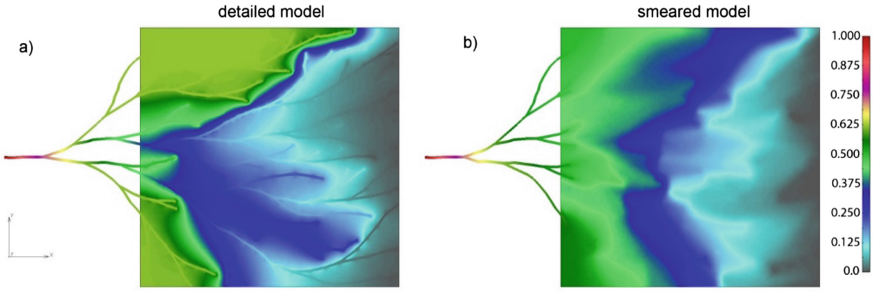

Fig. 7. Field of electric potential in case of detailed (a) and smeared (b) model.

Figure 8 shows mean potential within tissue vs. time, assuming that the initial potential is equal to zero. Results from Figs. 7 and 8 show that smeared model with appropriately calculated conductivity tensor is accurate enough as detailed model and can be further used in coupled electromechanical simulations.

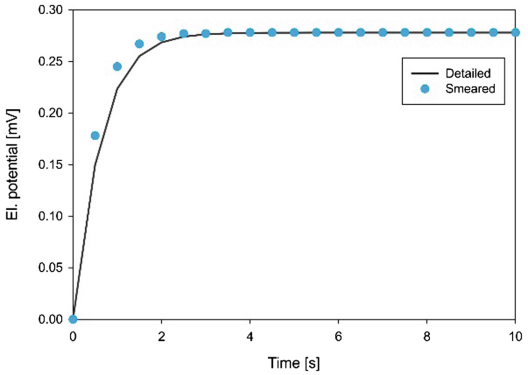

Fig. 8. Graph for electrical potential for detailed and smeared model.

5 Conclusion

Presented FE models based on the smeared concept offer a novel computational tool for practical applications in biomedical investigations of electrical transport. Selected examples demonstrate accuracy and efficiency of the smeared method. Besides the good accuracy, the smeared models are easy to generate when modeling the processes within complex geometries. The calculated field of electrical potential can further be used for electro-mechanical coupling and modeling the mechanics of the heart.

Acknowledgments. The authors acknowledge support from the City of Kragujevac, Serbia.

Funding. This work is supported by the grant NCI U54 CA210181. Also, it is supported by the SILICOFCM project that has received funding from the European Union's Horizon 2020 research and innovation programme under grant agreement No 777204. This research was also funded by Ministry of Education and Science of Serbia, grants OI 174028 and III 41007.

References

1. Kojic, M., Milosevic, M., Simic, V., Koay, E.J., Fleming, J.B., Nizzero, S., Kojic, N., Ziemys, A., Ferrari, M.: A composite smeared finite element for mass transport in capillary systems and biological tissue. Comp. Meth. Appl. Mech. Engrg. **324**, 413–437 (2017). https://doi.org/10.1016/j.cma.2017.06.019
2. Kojic, M., Milosevic, M., Simic, V., Koay, E.J., Kojic, N., Ziemys, A., Ferrari, M.: Extension of the composite smeared finite element (CSFE) to include lymphatic system in modeling mass transport in capillary systems and biological tissue. J. Serb. Soc. Comp. Mech. **11**(2), 108–120 (2017)
3. Milosevic, M., Simic, V., Milicevic, B., Koay, E.J., Ferrari, M., Ziemys, A., Kojic, M.: Correction function for accuracy improvement of the composite smeared finite element for diffusive transport in biological tissue systems. Comput. Methods Appl. Mech. Eng. **338**, 97–116 (2018). https://doi.org/10.1016/j.cma.2018.04.012. ISSN 0045-7825
4. Kojic, M., Milosevic, M., Simic, V., Koay, E.J., Kojic, N., Ziemys, A., Ferrari, M.: Multiscale smeared finite element model for mass transport in biological tissue: from blood vessels to cells and cellular organelles. Comput. Biol. Med. **99**, 7–23 (2018). https://doi.org/10.1016/j.compbiomed.2018.05.022

5. Kojic, M.: Smeared concept as a general methodology in finite element modeling of physical fields and mechanical problems in composite media. J. Serbian. Soc. Comp. Mech. **12**(2), 1–16 (2018)
6. Kojic, M., Milosevic, M., Simic, V., Ziemys, A., Filipovic, N., Ferrari, M.: Smeared multiscale finite element model for electrophysiology and ionic transport in biological tissue. Comput. Biol. Med. **108**, 288–304 (2019)
7. Santagiuliana, R., Milosevic, M., Milicevic, B., Sciumè, G., Simic, V., Ziemys, A., Kojic, M., Schrefler, B.A.: Coupling tumor growth and bio distribution models. Biomed. Microdevice (2019). https://doi.org/10.1007/s10544-019-0368-y
8. Kojic, M., Filipovic, N., Stojanovic, B., Kojic, N.: Computer Modeling in Bioengineering - Theoretical Background, Examples and Software. Wiley, Chichester (2008)
9. Noble, D.: A modification of the Hodgkin-Huxley equations applicable to Purkinje fibre action and pace-maker potentials. J. Physiol. **160**, 317–352 (1962)
10. O'Hara, T., Virág, L., Varró, A., Rudy, Y.: Simulation of the undiseased human cardiac ventricular action potential: model formulation and experimental validation. PLoS Comput. Biol. **7**, e1002061–e1002090 (2011)
11. Kojic, M., Simic, V., Milosevic, M.: Composite smeared finite element - some aspects of the formulation and accuracy. IPSI Trans. Internet Res. (2017)
12. Costabal, F.S., Hurtado, D.E., Kuhl, E.: Generating Purkinje networks in the human heart. J. Biomech. **49**, 2455–2465 (2016)

Application of Composite Smeared Finite Element Model in Drug Delivery Inside Organs

Vladimir Simic[2], Miljan Milosevic[2,4], Arturas Ziemys[1], and Milos Kojic[1,2,3](✉)

[1] The Department of Nanomedicine, Houston Methodist Research Institute, 6670 Bertner Ave., R7 117, Houston, TX 77030, USA
mkojic42@gmail.com
[2] Bioengineering Research and Development Center BioIRC Kragujevac, Prvoslava Stojanovica 6, 34000 Kragujevac, Serbia
[3] Serbian Academy of Sciences and Arts, Knez Mihailova 35, 11000 Belgrade, Serbia
[4] Belgrade Metropolitan University, Tadeusa Koscuska 63, 11000 Belgrade, Serbia

Abstract. We here implement the smeared field finite element methodology, formulated by the last listed author, which is presented in numerous of recent publications. This methodology enables modeling physical fields in biological systems in a simple way, which otherwise, by detailed representation of each biological constituents (capillaries, cell membranes, cell interior, etc.), would not be practical to use. Here we summarize the basic concept of the smeared modeling by describing briefly formulation of a composite smeared finite element (CSFE). Besides the standard FE representation of continuum fields of molecular transport, 1D transport is included in a continuum form using the appropriate transport tensors. Physical fields are coupled by the connectivity elements at each node, representing transport properties of the walls separating the domains. In this paper, methodology is applied to determine concentration field within liver of a mouse, generated from images, containing a tumor. Also, evolution of drug concentration within tumor is presented, which is important for improvement of cancer therapy.

1 Introduction

Material transport within living organisms includes transport of oxygen, various molecules as drugs, metabolic transport within tissue and transport of waste products generated by cell functions, ionic transport within cells and through biological membranes, etc. Most of the research in mass transport and drug delivery is experimental, rather than theoretical, due to complexity of problems. In last decades the analytical solutions of the transport laws were replaced by computational modeling due to enormous advances in computer technology and computational methodology. Still, there is a need for improvement of computational methods in order to develop suitable methods and software as a tool for improving therapy and cure successfully various deceases.

Regarding the computational models, we need simplifications for representing the biological medium in which drug molecules are traversing. First, we assume that tissue is a composite medium with two distinct domains: extracellular and intracellular space. Extracellular space is considered as a porous medium where the extracellular matrix

N. Filipovic (Ed.): ICCB 2019, LAIS 11, pp. 44–52, 2020.
https://doi.org/10.1007/978-3-030-43658-2_5

represents the solid filled with biological fluid. Fluid flow within tissue exists due to transport which occurs through capillary walls from capillary system, and in the reverse direction - from lymphatic system which represents fluid drainage. Furthermore, molecules and other particles are migrating from the capillaries to extracellular space, but also to cells and cell membranes, and in reverse direction. Cell interior with the cytosol, cytoskeleton and organelles also represent complex structure. Governing laws for transport within the continuum domains and through biological barriers (vessel walls, and cell and organelle membranes) can be described according to the Darcy velocity-pressure relationship for convection and Fick's law for diffusion [1].

There are additional complexities in transport within tumors, due to irregular blood vessel branching and variability of vessel diameters and lengths, and geometric and viscous resistance [2–6]. Blood flow characteristics within tumor vasculature are given in [7]. Mass exchange within the cell interior represents a separate field of the overall biomedical and clinical investigations with various factors which take part in mass exchange within cells. These factors range from biochemical to mechanical, to signaling pathways [8].

Traditional computational methods include modeling of transport within blood vessels, tissue and cell interior. A simplified approach for transport in blood vessel, which is suitable for certain applications, goes back to the "network" method [9], with application of the Hagen-Poiseuille law [10] for fluid, and Fick's law for diffusion within moving fluid according to pipe flow conditions. Molecular dynamics (MD) was used for calculation of the equivalent diffusion coefficient for the finite element modeling [11–15]. Formulation of the composite smeared finite element (CSFE) is introduced in [16] and further generalization of this concept and its application in biomedical engineering in [17–22].

In Sect. 2 basic diffusion equations for smeared FE methodology formulation are summarized, while in Sect. 3 we present liver model containing a tumor. In last section we give few concluding remarks.

2 Formulation of the Composite Smeared Finite Element Model

In this section we summarize the fundamental relations for the smeared finite element model and a step-by-step procedure which is required using this formulation.

We introduced our composite smeared finite element (CSFE) in [16] and generalized in [20], as a type of finite element which contains as many domains as there are physical domains: capillary, lymph, extracellular, domains of different types of cells, and organelles within cells. A schematic representation of the CSFE (according to our references) is shown in Fig. 1, where N_d stands for number of different domains.

Each of the listed domains K occupies the volume V^K of the element volume V, as

$$V^K = r_V^K V \tag{1}$$

where r_V^K is the volumetric fraction. Each domain has its own concentration filed C^K, with the nodal values C_J^K as shown in the Fig. 1, with interpolation

$$C^K = \sum_J N_J C_J^K \tag{2}$$

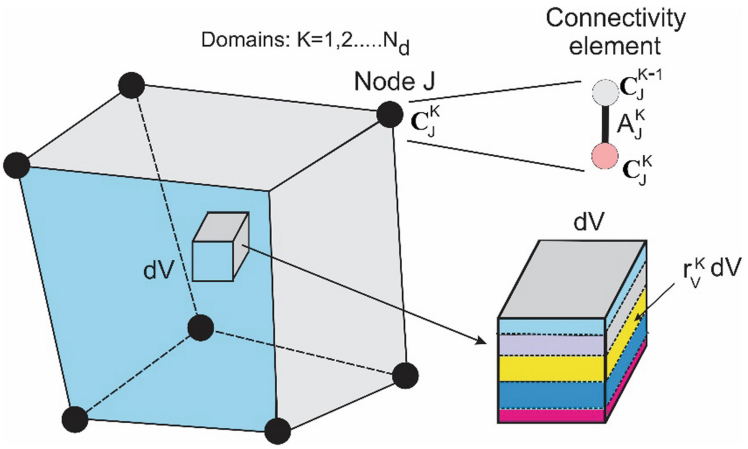

Fig. 1. Composite smeared finite element (CSFE), according to [20].

where N_J stands for interpolation functions and summation goes over all nodes. Transport inside physical fields is considered as gradient driven - by Fick's law for diffusion. The balance equation for a domain K has a standard FE form [20]

$$\left(\frac{1}{\Delta t}\mathbf{M}+\mathbf{K}\right)^{K(i-1)}\Delta\mathbf{C}^{K(i)}=\mathbf{Q}^{Kext}+\mathbf{Q}_V^K-\frac{1}{\Delta t}\mathbf{M}^{K(i-1)}\left(\mathbf{C}^{(i-1)}-\mathbf{C}^t\right)^K-\mathbf{K}^{K(i-1)}\mathbf{C}^{K(i-1)} \quad (3)$$

where

$$\begin{aligned} M_{IJ}^K &= \int_V N_I N_J r_V^K dV \\ K_{IJ}^K &= \int_V D_{ij}^K N_{I,i} N_{J,j} r_V^K dV, \quad sum\ on\ i,j:\ i,j=1,2,3 \\ Q_{VI}^K &= \int_V N_I q_V^K r_V^K dV \end{aligned} \quad (4)$$

where $\mathbf{C}^K$ is the nodal vector, D_{ij}^K is diffusion tensor, N_I are interpolation functions, and q_V^K is the source term.

In case of smeared domain representing the transport through a network of practically 1D transport conditions as in capillaries or lymph channels, it is necessary to transform the 1D to the continuum representation. This can be achieved by introducing a transport tensor D_{ij} (details are given in [16] and [20]) as

$$D_{ij}=\frac{1}{A_{tot}}\sum_K D^K A^K \ell_i^K \ell_j^K \quad (5)$$

where summation goes over all 1D line elements in the vicinity of a considered point of the space in the FE model; D^K are diffusivities, A^K are the cross-sectional areas, ℓ_i^K are directional cosines of 1D elements; and A_{tot} is the total cross-sectional area of the line elements.

Continuum fields within the CSFE are coupled by connectivity elements at each FE node, as it is shown in Fig. 1. These elements take into account transport characteristics of walls for 1D domain, or membrane transport in case of cells or organelles. The balance equations have the form (3). The "mass" matrices can be expressed as

$$M_{11} = M_{22} = \frac{1}{3} A_J h, \quad M_{12} = M_{21} = \frac{1}{6} A_J h \tag{6}$$

where A_J and h are the interface area belonging to the node J and wall/membrane thickness, respectively. The wall transport matrix is

$$K_{11} = K_{22} = -K_{12} = -K_{21} = D_{wall} A_J \tag{7}$$

where D_{wall} is the wall/membrane transport coefficient. In case of diffusion with fluid flow through the wall, there is additionally a convective matrix which can be expressed as

$$K^v_{11} = -K^v_{22} = -K^v_{21} = K^v_{12} = -\frac{1}{2} k_h A_J (P_1 - P_2) \tag{8}$$

where P_1 and P_2 are pressures on the two sides of the wall; and k_h is the hydraulic coefficient.

3 Smeared FE Model for Mouse Liver with Tumor

This section provides insight into smeared concept applicability by modeling diffusion process of drug molecule inside a mouse liver with tumor. Altogether, the computational model represents a complex biological system with different physical fields.

Geometry and composition of 3D mouse liver smeared model with large blood vessel network is shown on Fig. 2 (generated at R&D Center BIOIRC from micro-CT scan of a mouse liver). Micro computed tomography (micro-CT) was used by the Preclinical Imaging Core at the Houston Methodist Research Institute to scan the vascular structure of a mouse liver. Model consists of 1D FEs for large blood vessels (7736 elements), 3D composite smeared elements (38932 elements) for tissue and capillary representation, and connectivity elements (373 elements) for connecting large blood vessels with continuum nodes (capillary domain DOF) of smeared FEs. As an addition, there is one separate tumor within liver (160 elements). Total number of nodes is 53454. Data for this example are the same as in [16].

Prescribed conditions for diffusion in larger vessels (at input/output nodes of 1D elements mesh) are: inlet concentration is bolus type c(t) (C_{in}), presented in Fig. 3, and outlet concentration is set to be 0 (C_{out}). Characteristics of fluid/diffusion flow through blood vessels (large vessels and capillaries) are: viscosity is 10^{-3} Pa s, and diffusion coefficient is 1000 mm^2/s.

Characteristics of blood vessel walls are: hydraulic permeability coefficient is 10^{-12} mm/ (Pa s), diffusion coefficient is set to 0.1 mm^2/s and wall thickness is about 10% of the vessel diameter. Tissue characteristics are: diffusion coefficient is 0.1 mm^2/s, and Darcy coefficient is 10^{-12} mm^2/ (Pa s).

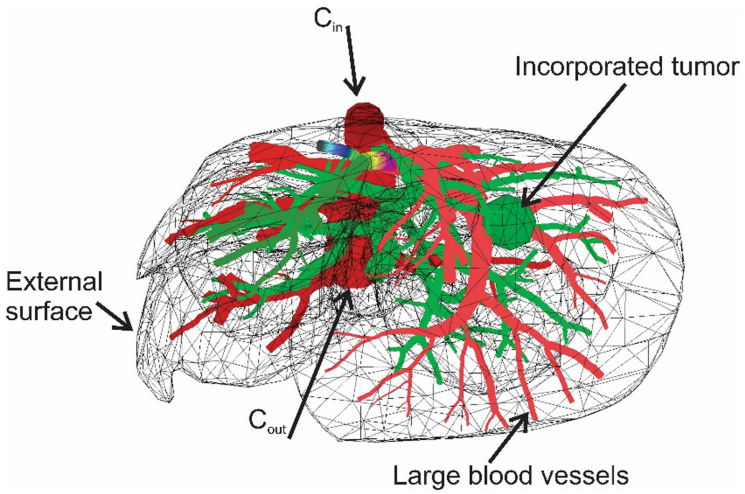

Fig. 2. FE 3D model of mouse liver: geometry, tumor domain and pressure field within large vessels with surrounding external surface.

Parameters of smeared model are: average capillary diameter is 0.025 mm, capillary wall thickness is 0.0025 mm, capillary volume fraction is 10%, diffusion coefficient of capillary wall is 10^{-6} mm^2/s, and hydraulic permeability of capillary wall is 10^{-12} mm/ (Pa s). Time steps used in FE simulation are divided on two periods: First period has 30 $\times$ 2s steps, while second contains 3 $\times$ 5 s.

Additionally, we have one tumor domain with following initial characteristics: diffusion coefficient in extracellular space is set to be 100 mm^2/ s, Darcy coefficient is 1 mm^2/ Pa s, hydraulic coefficient is 1 mm/ Pa s, while diffusion coefficient in small capillaries inside of tumor is 100 mm^2/ s. Diffusion coefficient of capillary wall is also 100 mm^2/ s and partitioning coefficient between tumor- tissue boundary is 0.8. There is one type of cells inside of tumor domain with diffusion coefficient set to 100 mm^2/s as well as diffusion coefficient in cell membrane, also set to be 100 mm^2/s. Volumetric fraction of capillaries inside tumor is set to be 2.78% (0.0278).

Using these material data and boundary conditions, we have solved for concentrations within the liver and tumor using our smeared methodology, with following concentration vs. time diagrams. Some of the results are summarized below.

Concentration field within tissue, large vessels and tumor (marked with black dashed line) is shown in Fig. 3 for three different time steps. The largest values of the concentrations are noticeable in blood vessels, following a decrease going to capillaries and tissue. There is a slight difference between concentrations inside tissue and tumor domain, following diffusion process that occurs from blood vessels to capillaries and to tissue. Figure 4 displays evolution of mean concentration, with inlet bolus type of concentration at large blood vessels c(t), inside tissue domain of liver, with accompanied tumor concentration curve.

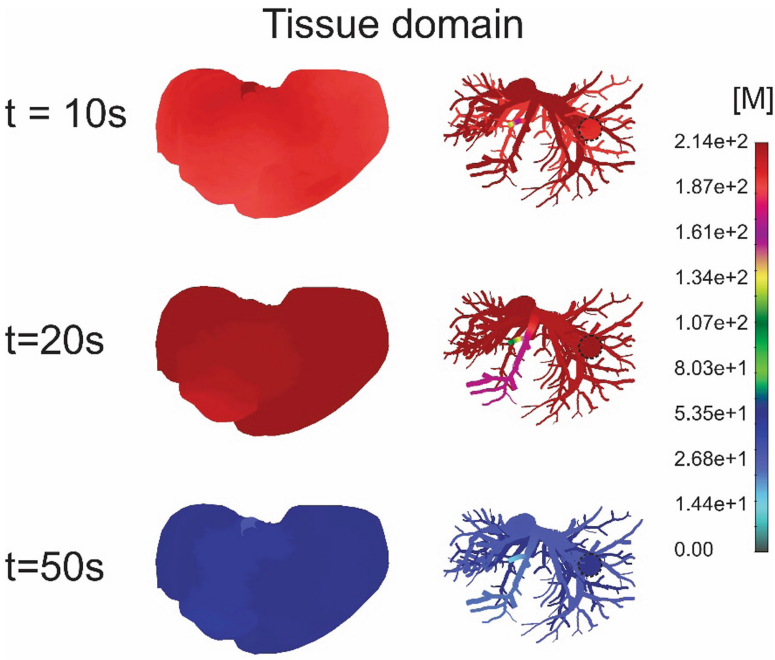

Fig. 3. Concentration field in liver with tumor inside tissue domain for three different time steps. Left panel- concentration in surrounding tissue domain, right panel- concentration inside large vesicles and tumor (marked with dashed black line).

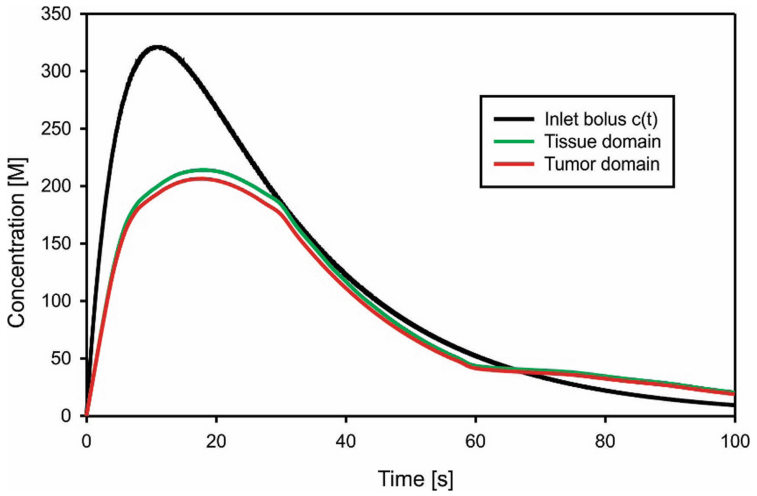

Fig. 4. Mean concentration evolution in liver. The inlet concentration c(t) at large vessels has a bolus character and generates bolus-type profiles of mean concentration in tissue of the liver and within tumor—reduced with respect to c(t). Volumetric fraction of capillaries inside of tumor is $r_V = 0.0287$.

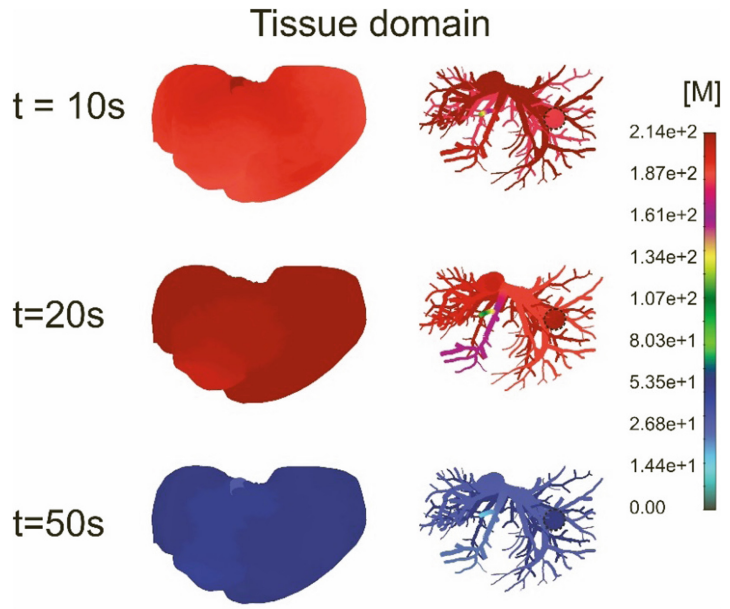

Fig. 5. Concentration field in liver with tumor inside tissue for three different time steps. Left panel- concentration in surrounding tissue domain, right panel- concentration inside large vesicles and tumor (marked with dashed black line).

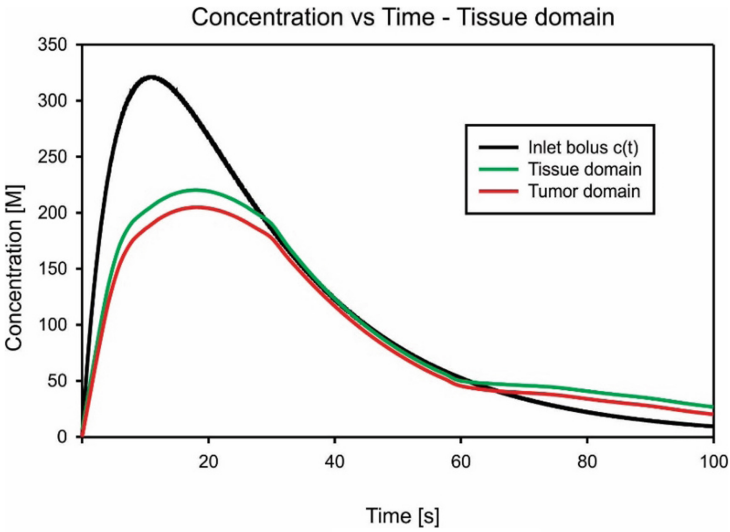

Fig. 6. Mean concentration evolution in liver. The inlet concentration c(t) at large vessels has a bolus character and generates bolus-type profiles of mean concentration in tissue of the liver and within tumor—reduced with respect to c(t). Volumetric fraction of capillaries inside of tumor is $r_V = 0.0687$, and the diffusion coefficient inside of tumor is 10 mm^2/s.

Following these results, we performed another simulation with different parameters inside tumor domain. Volumetric fraction of capillaries was set to be 0.0687, and diffusion coefficient inside tumor was 10 times smaller than in the first case, $D = 10\ mm^2/s$. All other parameters were the same as in the first case. Figure 5 shows concentration field inside tissue domain for three different time steps in case when diffusion coefficient inside of tumor is 10 times smaller.

As it can be seen from Fig. 6, there are differences between concentration curves for tissue and tumor domain, and comparing to the first case – Fig. 4, it is noticeable that concentration in tumor is lower due to smaller diffusion coefficient than in the first case.

4 Conclusions

This study summarized smeared methodology for field problems as a general concept for modeling gradient-driven field problems in complex biological media [20], here applied to diffusion.

Smeared model applicability is demonstrated on one numerical example (a liver with a tumor) as a large biological system.

It may be concluded that the FE models based on the smeared concept for mass transport, offer a computational tool for practical applications in biomedical investigations. Also, this methodology is applicable to larger parametric studies and parameters estimation, as published in [23].

Acknowledgments. The authors acknowledge support from the City of Kragujevac, Serbia.

Funding. This work is supported by the SILICOFCM project that has received funding from the European Union's Horizon 2020 research and innovation programme under grant agreement No 777204. This research was also funded by Ministry of Education and Science of Serbia, grants OI 174028 and III 41007.

References

1. Kojic, M., Filipovic, N., Stojanovic, B., Kojic, N.: Computer Modeling in Bioengineering - Theoretical Background, Examples and Software. Wiley, Chichester (2008)
2. Less, J.R., Skalak, T.C., Sevick, E.M., Jain, R.K.: Microvascular architecture in a mammary carcinoma: branching patterns and vessel dimensions. Cancer Res. **51**, 265–273 (1991)
3. Roberts, W.G., Palade, G.E.: Neovasculature induced by vascular endothelial growth factor is fenestrated. Cancer Res. **57**, 765–772 (1997)
4. Sevick, E.M., Jain, R.K.: Geometric resistance to blood flow in solid tumors perfused ex vivo: effects of tumor size and perfusion pressure. Cancer Res. **49**, 3506–3512 (1989)
5. Sevick, E.M., Jain, R.K.: Viscous resistance to blood flow in solid tumors: effect of hematocrit on intratumor blood viscosity. Cancer Res. **49**, 3513–3519 (1989)
6. Sevick, E.M., Jain, R.K.: Effect of red blood cell rigidity on tumor blood flow: increase in viscous resistance during hyperglycemia. Cancer Res. **51**(51), 2727–2730 (1991)
7. Jain, R.: Determinants of tumor blood flow: a review. Cancer Res. **48**, 2641–2658 (1988)
8. Rangamani, P., Iyengar, R.: Modelling spatio-temporal interactions within the cell. J. Biosci. **32**, 157–167 (2007)

9. Lipowsky, H.H., Zweifach, B.W.: Network analysis of microcirculation of cat mesentery. Microvasc. Res. **7**, 73–83 (1974)
10. Kojic, M., Milosevic, M., Simic, V., Ferrari, M.: A 1D pipe finite element with rigid and deformable walls. J. Serbian. Soc. Comput. Mech. **8**, 38–53 (2014)
11. Ziemys, A., Kojic, M., Milosevic, M., Ferrari, M.: Interfacial effects on nanoconfined diffusive mass transport regimes. Phys. Rev. Lett. **108**, 236102 (2012)
12. Kojic, M., Milosevic, M., Kojic, N., Ferrari, M., Ziemys, A.: On diffusion in nanospace. J. Serbian. Soc. Comput. Mechanics **5**, 84–109 (2011)
13. Kojic, M., Milosevic, M., Kojic, N., Isailovic, V., Petrovic, D., Filipovic, N., Ferrari, M., Ziemys, A.: Transport phenomena: computational models for convective and diffusive transport in capillaries and tissue. In: De, S., Hwang, W., Kuhl, E. (eds.) Multiscale Modeling in Biomechanics and Mechanobiology, pp. 131–156. Springer, London (2015)
14. Kojic, M., Ziemys, A., Milosevic, M., Isailovic, V., Kojic, N., Rosic, M., Filipovic, N., Ferrari, M.: Transport in biological systems. J. Serbian. Soc. Comput. Mech. **5**, 101–128 (2011)
15. Kojic, M., Milosevic, M., Kojic, N., Kim, K., Ferrari, M., Ziemys, A.: A multiscale MD–FE model of diffusion in composite media with internal surface interaction based on numerical homogenization procedure. Comput. Meth. Appl. Mech. Eng. **269**, 123–138 (2014)
16. Kojic, M., Milosevic, M., Simic, V., Koay, E.J., Fleming, J.B., Nizzero, S., Kojic, N., Ziemys, A., Ferrari, M.: A composite smeared finite element for mass transport in capillary systems and biological tissue. Comput. Meth. Appl. Mech. Eng. **324**, 413–437 (2017). https://doi.org/10.1016/j.cma.2017.06.019
17. Kojic, M., Milosevic, M., Simic, V., Koay, E.J., Kojic, N., Ziemys, A., Ferrari, M.: Extension of the composite smeared finite element (CSFE) to include lymphatic system in modeling mass transport in capillary systems and biological tissue. J. Serbian. Soc. Comput. Mech. **11**(2), 108–120 (2017)
18. Milosevic, M., Simic, V., Milicevic, B., Koay, E.J., Ferrari, M., Ziemys, A., Kojic, M.: Correction function for accuracy improvement of the composite smeared finite element for diffusive transport in biological tissue systems. Comput. Meth. Appl. Mech. Eng. **338**, 97–116 (2018). https://doi.org/10.1016/j.cma.2018.04.012. ISSN: 0045-7825
19. Kojic, M., Milosevic, M., Simic, V., Koay, E.J., Kojic, N., Ziemys, A., Ferrari, M.: Multiscale smeared finite element model for mass transport in biological tissue: from blood vessels to cells and cellular organelles. Comput. Biol. Med. **99**, 7–23 (2018). https://doi.org/10.1016/j.compbiomed.2018.05.022
20. Kojic, Milos: Smeared concept as a general methodology in finite element modeling of physical fields and mechanical problems in composite media. J. Serbian. Soc. Comput. Mech. **12**(2), 1–16 (2018)
21. Kojic, M., Milosevic, M., Simic, V., Ziemys, A., Filipovic, N., Ferrari, M.: Smeared multiscale finite element model for electrophysiology and ionic transport in biological tissue. Comput. Biol. Med. **108**, 288–304 (2019)
22. Santagiuliana, R., Milosevic, M., Milicevic, B., Sciumè, G., Simic, V., Ziemys, A., Kojic, M., Schrefler, B.A.: Coupling tumor growth and bio distribution models. Biomed. Microdevices (2019). https://doi.org/10.1007/s10544-019-0368-y
23. Kojic, M., Milosevic, M., Simic, V., Milicevic, B., Geroski, V., Nizzero, S., Ziemys, A., Filipovic, N., Ferrari, M.: Smeared multiscale finite element models for mass transport and electrophysiology coupled to muscle mechanics. Front. Bioeng. Biotechnol. **7**(381), 1–16 (2019). https://doi.org/10.3389/fbioe.2019.00381. ISSN 2296-4185

Tuning Cooperativity of Calcium Activation in Cardiac Muscle

Momcilo Prodanovic[1,2], Boban Stojanovic[1,3], Mladen Maric[1,3], Danica Prodanovic[1,3], and Srboljub M. Mijailovich[4(✉)]

[1] Bioengineering Research and Development Center (BioIRC), Prvoslava Stojanovica 6, 34000 Kragujevac, Serbia
momcilo.prodanovic@gmail.com, bobi@kg.ac.rs, mladen.pmf@outlook.com, dprodanovic95@gmail.com
[2] Faculty of Engineering, University of Kragujevac, Sestre Janjic 6, 34000 Kragujevac, Serbia
[3] Faculty of Science, University of Kragujevac, Radoja Domanovica 12, 34000 Kragujevac, Serbia
[4] Department of Biology, Illinois Institute of Technology, 3101 South Dearborn Street, Chicago, IL 60616, USA
smijailo@gmail.com

Abstract. Early phase diastole and diastolic performance (filling) via resting ventricular wall tension can be affected by abnormalities in relaxation. This is one of the rarely studied effects of mutations in cardiac muscle sarcomere proteins, which are usually assessed using the force-pCa relations of demembranated muscle or transient twitch contractions in intact muscles. The characteristics of calcium sensitivity (pCa_{50}) and cooperativity (Hill coefficient, n_H) may be obtained from force-pCa relations. Using MUSICO simulations, tightly coupled with the experiments, we were able to adjust calcium sensitivity and cooperativity to closely match experimental values by testing the contributions of three mechanisms to contraction and relaxation kinetics: (1) Tm azimuthal movement as a continuous flexible chain (CFC); (2) variations in calcium affinity of cTn; and (3) inclusion of a super-relaxed myosin state (SRX) to reduce the number of myosins that can rebind during relaxation and modulate cooperativity between bound myosin and the CFC.

Simulations provided force-pCa relations where Ca^{2+} affinity to cTnC was increased or decreased to match the observations in the experiments where native cTnC was replaced with either cTnC L48Q or cTnC I61Q, respectively. Simulations demonstrated that the proposed mechanism, where mutated cTnC changes the dissociation rate of calcium, cannot match experimental pCa_{50} values for cTnC mutants nor the observed cooperativity (n_H). Adjusting the affinity of myosin to actin and the confined persistent length (CPL) of the CFC could account for the apparent loss of cooperativity of thin filament activation for both mutants. However, in WT muscle, the predicted cooperativity was significantly lower than observed. Fine-tuning the calcium dependent transition rate from the SRX, though, allowed a close match to the experimental n_H from the force-pCa relations while maintaining CPL values in the physiological range.

Keywords: MUSICO · Thin filament regulation · Cooperativity · Cardiomyopathy · cTnC mutations

N. Filipovic (Ed.): ICCB 2019, LAIS 11, pp. 53–63, 2020.
https://doi.org/10.1007/978-3-030-43658-2_6

1 Introduction

Cardiac myopathies are frequently associated with numerous mutations observed in myosin, thin filament regulatory proteins and ancillary sarcomeric proteins. The calcium regulation of the cyclic interaction of myosin and actin is very important for cardiac transient contractions. Muscle contraction is initiated by thin filament activation, when Ca^{2+} binds to the cardiac troponin C (cTnC) subunit of troponin (cTn). This increases its affinity for the troponin I (cTnI) subunit and, subsequently, reduces cTnI affinity for actin. At low calcium concentrations most of the cTnIs are bound to actin holding the tropomyosin chain in a position that prevents myosin binding to actin and, therefore, prevents force generation and shortening of the cardiac muscle. Increase in calcium concentrations reduces the number of cTnIs bound to actin and increases mobility of thin filament tropomyosin, exposing myosin binding sites on actin allowing for weak and strong myosin-actin cross-bridge formation and contraction. Changes in the Ca^{2+} binding properties of cTn that occur with amino acid variations in cTn subunits, for example in mutations L48Q and I61Q associated with hypertrophic or dilated cardiomyopathy (HCM and DCM) respectively, often affect myofibril and cardiomyocyte Ca^{2+} sensitivity of force and the dynamics of contractile activation and relaxation. These two mutations have increased and decreased (respectively) Ca^{2+} binding affinity of cTn and Ca^{2+}sensitivity of force in demembranated cardiac muscle [1, 2] inducing HCM and DCM phenotypes in rats and transgenic mice.

The predominant method for studying regulation of the Ca^{2+} sensitivity of force has been measurement of the steady-state force as a function of $[Ca^{2+}]$ in the activation solutions (the force-pCa relation) for demembranated cardiac muscle tissue, single cardiomyocytes or myofibrils. Multi-scale computational modeling approaches, such as MUSICO [3, 4], can be used to predict how changes in the force-pCa curve resulting from L48Q and I61Q cTnC mutations affect the dynamics of contraction and relaxation in isolated myofibrils and intact cardiac muscle.

The MUSICO platform contains updated crossbridge cycle with five essential states, and a kinetic scheme of calcium binding to cTnC including the interaction of cTnI to actin. This provided the theoretical framework for simulations of calcium sensitivity of the isometric force, i.e. force-pCa relations, for WT, L48Q and I61Q cTnCs, in demembranated right ventricular trabeculae without or with exchanged mutant cTnCs [2]. However, in isometric twitches at the myofibril level the MUSICO simulations predicted slower relaxation as compared to observations [5, 6]. The reason was that when calcium concentrations are reduced to low levels during relaxation, a significant number of tropomyosin units is still open allowing rapid rebinding of a substantial population of crossbridges in the M.D.Pi state to actin and, therefore, generating force that is manifested as slowed relaxation. This significant population in the M.D.Pi state at low calcium concentrations strongly contributes to isometric force showing a large overestimate of the forces comparing to that observed in force-pCa relation at $pCa < pCa_{50}$.

To resolve these problems, we have developed an alternative approach introducing a super relaxed (SRX) state [7, 8] to our simulations, as a sink for detached myosins in the M.D.Pi state and, therefore, significantly reducing populations of M.D.Pi myosin heads at low calcium concentrations and the flux of rebinding myosins. We have tested the hypothesis that at low calcium concentrations, the SRX state can provide isometric

force at the observed levels in force-pCa relations. Simulations demonstrated that by fine-tuning the calcium dependent transition rate from the SRX, it is possible to get the observed n_H from the force-pCa relations while keeping CPL values in a physiologically realistic range.

2 Methods

The MUSICO platform [3, 4] was adapted to include the calcium binding scheme in the continuous flexible chain model (CFC) for thin filament regulation [9, 10], and the crossbridge cycle was updated to include a SRX state [11]. In this model we make no assumptions of the physical configuration of the parked state. We intend it to be chemically equivalent to the SRX state described in the literature [7, 8] but it may or may not be in the interacting-heads motif (IHM) or J state described structurally.

The spatially explicit 3-D model for a muscle fiber incorporates multiple ordered substructures called myofibrils and each myofibril consists of large number of sarcomeres arranged in series. The sarcomeres are composed of interdigitated thick and thin filaments, where each half of thick filament contains ~150 myosin molecules and is surrounded by six thin filaments emerging from Z-discs on opposite sides of a sarcomere. The thin filament, consisting of 360 to 440 actin monomers, contains the regulatory proteins tropomyosin and troponin essential for calcium regulation of contraction and other auxiliary proteins regulating thin filament length and other functions [3, 4]. The 3-D sarcomere structure is viewed as an array of thin and thick filaments connected by cross-bridges and other elastic elements in a lattice network represented as linear springs [4].

The crossbridge connections in the simulation are formed according to a strain dependent kinetic model of crossbridge cycle in the 3D sarcomere lattice. We expanded the three-state crossbridge model from Mijailovich et al. [3, 4] to include 5 essential states. The crossbridge model is defined by a detached state, M.D.Pi (State 1), a weakly attached or pre-power stroke, A.M.D.Pi (State 2), a post-power stroke state A.M.D (State 3), rigor-like state, A.M (State 4) and a detached state, M.T (State 5). The transition rates between the States 1–4 are defined in Mijailovich et al. [3], and the transitions between States 4–5 and 5–1 are defined by strain independent rates [5, 6]. In order to match the observed force-pCa relations in cardiac muscle we expanded the five-state model to include an SRX or "parked" state, PS (State 6). This state only interacts with M.D.Pi (State 1) and the state transition rates are strain independent. However, the transition rate from PS to M.D.Pi, k_{61}, depends on the calcium concentration [5, 6], where the calcium dependence is defined by four parameters: the baseline rate, k^o_{PS}, the amplitude, k^{max}_{PS}, the Hill coefficient, b, and the calcium concentration at 50% of k^{max}_{PS}, $[Ca_{50}]_{PS}$.

The calcium-dependent kinetics of thin filament regulation in cardiac muscle is defined by allosteric mechanisms in cardiac muscle. It consists of four states (Fig. 1), two TnC closed states, where TnI is attached to actin and TnC has no or one bound calcium, denoted as TnC and CaTnC; and two TnC open states where TnI is dissociated from actin and TnC.TnI is associated with one Ca^{2+} or in rare occasions without bound Ca^{2+} [5]. The equilibrium rate constant of calcium binding to TnC, $K_{Ca} = \tilde{K}_{Ca}[Ca]$, is effectively defined via the forward constant $k_{Ca} = \tilde{k}_{Ca}[Ca]$ where k_{Ca} linearly depends

on the calcium concentration, $[Ca]$, and the calcium independent dissociation constant k_{-Ca}. The dissociation of TnI from the closed A.TnI to the open CaTnC.TnI state is defined by a first-order equilibrium constant, λ when one calcium is bound. With no bound calcium, the transition from A.TnI to TnC.TnI shows a slow dissociation TnI from actin with an attenuated rate $\varepsilon_o\lambda$ and the calcium binding to TnC in TnC.TnI complex is accelerated to k_{Ca}/ε_o keeping the population of A + TnC.TnI state low.

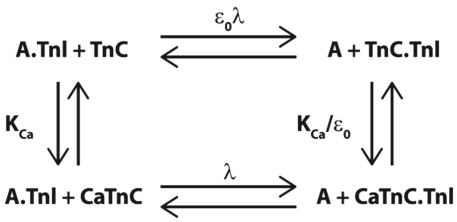

Fig. 1. Kinetics of calcium binding to TnC and interaction of TnI with actin in cardiac muscle. The process is regulated by equilibrium constant K_{Ca} where calcium binds to TnC forming CaTnC. The detachment of TnI from actin to form CaTnC.TnI is defined by λ. Slow dissociation from A.TnI to TnC.TnI is attenuated by ε_0 and the calcium binding to TnC in TnC.TnI complex is accelerated.

Thin filament regulation of myosin interactions with actin is defined by the kinetics of interactions between the Tm-Tn complexes that are, at present, best described by the long range cooperative continuous flexible chain (CFC) model [9, 10]. The CFC model is defined by only three parameters: the tropomyosin pinning angle, ϕ_-, the myosin imposed Tm angular displacement, ϕ_+; and the persistence length of the Tm–Tn confined chain, $1/\xi$.

For modeling all kinetics processes we follow a Monte Carlo approach incorporating spatially explicit myosin binding to regulated actin filaments in a 3D sarcomere lattice [3, 5]. General definitions, calculations of CFC angular positions and its variance, and the coupling between the calcium regulated position of the CFC and myosin cycle states are described in [3, 9, 10].

The instantaneous equilibrium at the level of muscle fiber, that includes interconnected network between actin and myosin filaments by cross-bridges, is defined by a stiffness matrix that includes the elasticity of thick and thin filaments, attached cross-bridges and titin, a vector of all external forces (load) and internal forces generated by the action of cross-bridges. The formulation and solution of the equations defining the mechanical system of sarcomeres in series is obtained by standard finite element procedures for nonlinear systems using an incremental procedure [12–14].

Model Parameters. The input to MUSICO simulations requires a large number of parameters that define sarcomere geometry, myofilaments elasticity, crossbridge stiffness, crossbridge stroke sizes, change in Gibbs energy associated with Pi release, cutoff state transition rates limiting exponentially growing rates of crossbridge cycle and CFC parameters CPL $1/\xi$ and angles ϕ_- and ϕ_+. The values of these parameters are mostly summarized in [3].

The sarcomere length in all simulations is set to 2.25 μm, i.e. at the length used in the Kreutziger et al. experiment [2]. The lattice inter-filament spacing of skinned cardiac muscle, $d_{1,0}$, at sarcomere length of 2.25 μm, has value of ~41.355 nm [15, 16].

The cross-bridge cycling rates used in all simulations are: change in chemical free energy associated with Pi release, $\Delta G_{stroke} = -13\, k_B T$, ADP release rate, $k_{34} = 60\ s^{-1}$, ATP binding and myosin detachment rate, $k_{45} = 10^6\ s^{-1}$; hydrolysis forward rate $k_{51} = 100\ s^{-1}$ and backward rate $k_{15} = 10\ s^{-1}$. The transition rates from and to the "parked" state are obtained through an iterative process of fitting simulations to the experimental data, where the initial values were adopted from Mijailovich et al. [5]: the transition rate to "parked" state $k_{16} = 200\ s^{-1}$, the calcium dependent transition rate from parked state, $k_{61}(Ca)$, is defined by baseline rate $k_{PS}^{o} = 10\ s^{-1}$, the rate at high calcium concentration $k_{PS}^{max} = 400\ s^{-1}$, Hill coefficient of the rate sigmoidal rise is set to be $b = 3$ and calcium concentration, $[Ca_{50}]_{PS} = 1$ μM. In all simulations, the value for $k_B T = 3.978$ pN·nm i.e. at the temperature of the experiment, 15 °C (= 288 °K).

For the kinetics of calcium binding to TnC and the interaction of TnI with actin $\tilde{k}_{Ca} = 5.88{\cdot}10^6\ M^{-1}{\cdot}s^{-1}$, except for cTnC I61Q, TnI attachment rate $k_I = \lambda^- = 375\ s^{-1}$; and the cooperativity coefficient $\varepsilon_o = 0.01$.

The parameter values used in specific simulations are summarized in Table 1, contrasting the differences in parameter values between WT and cTnC mutants.

Because the measurements of the dependence of muscle force as a function of calcium concentration are in units of stress, denoted as tension and the MUSICO predictions

Table 1. Values of parameters used in MUSICO simulations specific for WT and cTnC mutants L48Q and I61Q.

	Description	Parameter	Value		
			WT	**L48Q**	**I61Q**
Calcium Kinetics Parameters	Persistence length of Tm-Tn confined chain	1/ξ (nm)	50	33.33	31.25
	TnI-actin equilibrium rate const. at high Ca^{2+}	λ	10	18.32	1
	Calcium Dissociation Rate from TnC [2]	k_{-Ca} (s^{-1})	75.4	28	237.7
	Calcium binding to TnC	$\tilde{k}_{Ca}$ $(M^{-1}{\cdot}s^{-1})$	$5.88{\cdot}10^6$	$5.88{\cdot}10^6$	$2.65{\cdot}10^7$
Parked State Rates	Backward transition rate	k_{16} (s^{-1})	150	175	175
	Baseline rate	k_{PS}^{0} (s^{-1})	20	20	20
	Amplitude	k_{PS}^{max} (s^{-1})	550	575	275
	Hill function slope	b	10	3	3
	Half activation point of the Hill function	$[Ca_{50}]_{PS}$ (μM)	4	3.25	4

are in terms of force per half myosin filament, we used the methodology described in [3, 4, 17] to recalculate the mean force per half myosin filament to the observed tension. For calculation of the conversion factor we used interfilament spacing at the sarcomere slack length, d_{01}^{slack}, and the fraction of the demembranated rat trabeculae cross-sectional area occupied by myofibrils [18].

3 Results and Discussion

In order to achieve good fits of Kreutziger's experimental force-pCa curves we tested the proposed mechanism of changing calcium dissociation rate from mutated cTnC [1, 2]. Simulations provided force-pCa relations where native cTnC was replaced with either cTnC L48Q or cTnC I61Q with increased or decreased Ca^{2+} affinity, respectively (Fig. 2). We showed that it is possible to achieve experimental pCa_{50} in WT, but failed to match

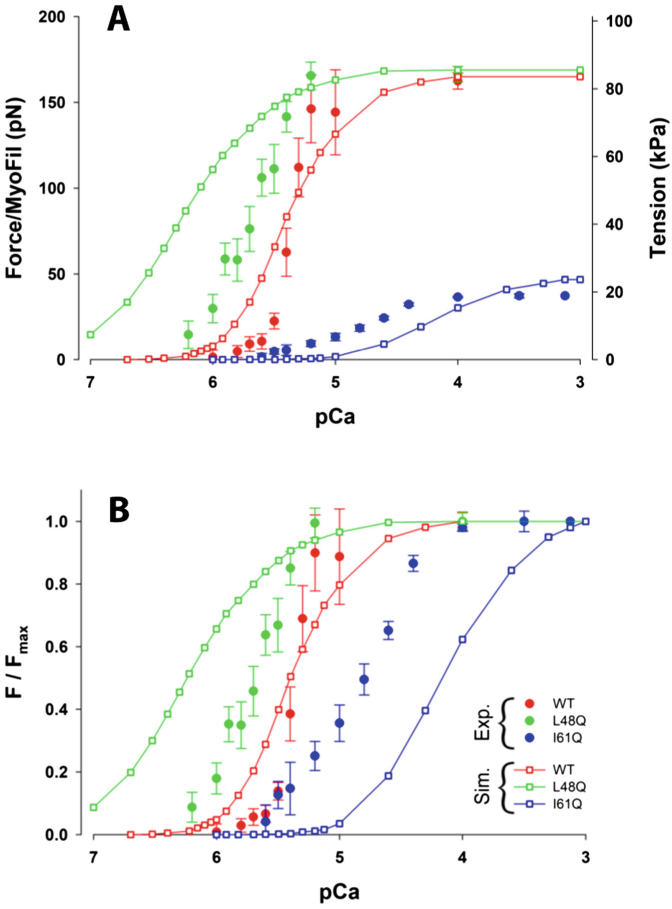

Fig. 2. Comparison between MUSICO simulations using five-state crossbridge model (lines with empty squares) with experiments (field circles with error bars). (A) Absolute values of force and tension; (B) Normalized force for better illustration of calcium sensitivity.

the observed pCa_{50} for cTnC mutants using the k_{-Ca} values from Kreutziger et al. [2]. Simulations also failed to match the reported cooperativity (n_H). Adjusting the myosin affinity to actin and the confined persistent length (CPL) of CFC could account for the apparent loss of cooperativity of thin filament activation for both mutants. However, simulations showed that in WT, the predicted Hill coefficient, n_H, has smaller value than observed with the above adjusted parameters within the range of physiological values. Table 2 shows the sensitivity tests that we ran for three model parameters for WT. Similar behavior was observed in cTnC mutants as well. Taking together, the five-state model shows higher sensitivity to calcium for L48Q and lower sensitivity for I61Q than observed, having a tendency to overestimate forces at low calcium.

Table 2. Sensitivity tests of three key parameters in calcium regulation for WT MUSICO simulations with five-state crossbridge model.

		−50%	**"best fit"**	**+50%**
k_{-Ca}	n_H	1.94	1.86	1.69
	pCa_{50}	5.23	5.36	5.66
1/ξ	n_H	1.13	1.86	2.31
	pCa_{50}	5.60	5.36	5.29
		−20%	**"best fit"**	**+20%**
λ	n_H	1.82	1.86	1.88
	pCa_{50}	5.47	5.36	5.28

This overestimation is reflected in the WT force-pCa relation at $pCa < pCa_{50}$ and therefore resulting in a lower value of n_H than observed. The change of CPL over a reasonable range improved the fit of n_H only modestly, not enough to match the observed values. The main reason for the oversensitivity at low calcium concentrations and attenuated sensitivity at high concentrations is caused by a significant number of crosbridges in the M.D.Pi state resulting in a large flux of myosin binding to actin at low calcium concentrations. This behavior could be also reflected in slow relaxation during twitch contraction where the myosin rebinding flux remains high although the transient concentration falls to very low levels [6].

We proposed updating the five-state model by the addition of a "parked" state (PS) in order to keep the population of the M.D.Pi state at low levels at low calcium concentrations. By fine-tuning the calcium dependent transition rate from the PS, we were able to get close to the observed n_H from force-pCa relations keeping CPL values in a physiological range, as well as close to the observed values of force at very high calcium concentrations. The best fits of Kreutziger's experiments for WT and transgenic mutants

cTnC L48Q and I61Q are shown in Fig. 3, while the comparison of n_H and pCa_{50} are shown in Table 3. Since some of the detached myosins are stored in the PS state, a higher binding rate is needed in order to reach the same force. Thus, it should be noted that k_A had to be increased by about 40% once the "parked" state was included in order to match the maximum force at high Ca concentrations.

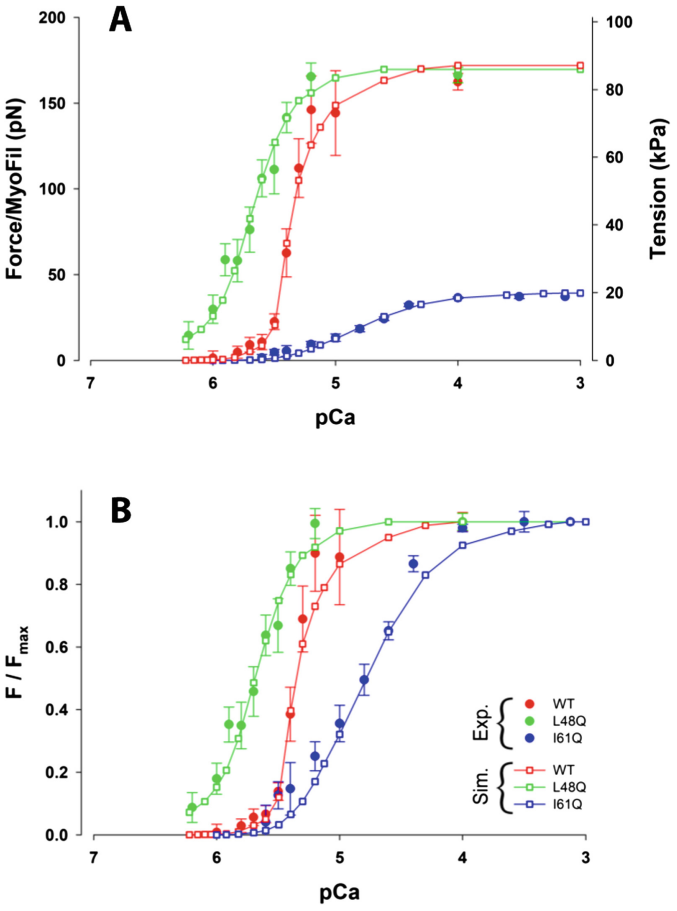

Fig. 3. Comparison between "best fit" MUSICO simulations using six-state crossbridge model with experiments. (A) Absolute values of force and tension; (B) Normalized force.

Sensitivity analysis of parameters in the crossbridge cycle with the "parked" state (PS) on simulating WT behavior showed that increasing parameter b in $k_{61}(Ca)$ by threefold (from 3 to 9) lowered the forces at very low calcium (<1 μM), while slightly increasing the forces at mid-level calcium (from 1 μM to 2 μM) by 15%, effectively increasing n_H by only 0.6%. Furthermore, increasing parameter $[Ca_{50}]_{PS}$ threefold (from 1 μM to 3 μM) significantly decreased the forces at low calcium, up to 7.5 μM, thus increasing n_H by 27%, while slightly decreasing pCa_{50} (<1%). As expected, increasing

the baseline rate, k^o_{PS} twofold (from 10 to 20 s^{-1}) mostly affected forces at lower calcium concentrations up to a twofold increase at 0.6 μM, which had a little effect on increasing n_H (<2%). Changing these three parameters didn't affect the force at high calcium concentrations, which allowed us to freely change them to obtain better n_H fit without affecting the maximum forces. Considering that only parameter $[Ca_{50}]_{PS}$ had a substantial impact on n_H, we also tested the effects of changing the forward rate amplitude, k^{max}_{PS}, and backward transition rate constant, k_{16}. The tests showed that decreasing the backward rate twofold or k^{max}_{PS} by 50% would increase the forces at every calcium concentration but would also increase n_H as well by up to 5%.

Table 3. Comparison of Hill coefficient, n_H, and pCa_{50} between MUSICO predictions and experiments. The six-state model contains "parked" state.

		WT	**L48Q**	**I61Q**
n_H	Sim. five-state	1.86	1.23	1.47
	Sim. six-state	3.85	2.38	1.66
	Exp.	5.74	2.04	1.42
pCa_{50}	Sim. five-state	5.36	6.23	4.15
	Sim. six-state	5.33	5.69	4.78
	Exp.	5.39	5.68	4.81

4 Conclusions

We have tested the hypothesis that force-pCa relations of muscles with the cTnC mutations L48Q and I61Q are defined by increased or decrease Ca^{2+} affinity compared to native cTnC. These mutations are associated with hypertrophic or dilated cardiomyopathy (HCM and DCM), respectively, thus understanding the mechanisms whereby these mutations lead to heart malfunction is essential for developing treatments for these heart diseases.

The MUSICO simulations with the minimal five-state model showed that changing the Ca^{2+} affinity of cTnC of L48Q and I61Q is not sufficient to recapitulate the experimental data. The key disagreement was that the predicted sensitivity of the force-pCa relation for L48Q muscles was much higher and for I61Q much lower than observed. In addition, the predicted slope for the force-pCa relation, n_H, in WT was much lower than observed, and at low calcium concentration, the predicted force overestimates the observed values for both WT and the mutants. The main reason for this behavior is high binding flux at low calcium concentrations caused by large population of myosins in M.D.Pi state. This problem has been resolved by inclusion of a "parked" state in the crossbridge cycle. The key advantage of including the "parked" state in the crossbridge cycle was reduction of the population of crossbridges at low calcium concentrations, followed by a reduction in force and an increase in Hill coefficient, n_H, up to high values

close to that observed in WT muscles. This feature of now the six-state crossbridge model could be the main contributor to accelerating the relaxation phase of twitch necessary to match the observed values [5, 6].

Acknowledgments. This project is supported by the European Union's Horizon 2020 research and innovation programme under grant agreement No 777204. We are also gratefully acknowledging the help of Prof. Thomas C. Irving with editing the final version of the manuscript.

Note: This article reflects only the author's view. The European Commission is not responsible for any use that may be made of the information it contains.

References

1. Davis, J., Davis, L.C., Correll, R.N., Makarewich, C.A., Schwanekamp, J.A., Moussavi-Harami, F., et al.: A tension-based model distinguishes hypertrophic versus dilated cardiomyopathy. Cell **165**, 1147–1159 (2016)
2. Kreutziger, K.L., Piroddi, N., McMichael, J.T., Tesi, C., Poggesi, C., Regnier, M.: Calcium binding kinetics of troponin C strongly modulate cooperative activation and tension kinetics in cardiac muscle. J. Mol. Cell. Cardiol. **50**, 165–174 (2011)
3. Mijailovich, S.M., Stojanovic, B., Nedic, D., Svicevic, M., Geeves, M.A., Irving, T.C., et al.: Nebulin and titin modulate crossbridge cycling and length dependent calcium sensitivity. J. Gen. Physiol. **151**, 680–704 (2019)
4. Mijailovich, S.M., Kayser-Herold, O., Stojanovic, B., Nedic, D., Irving, T.C., Geeves, M.A.: Three-dimensional stochastic model of actin-myosin binding in the sarcomere lattice. J. Gen. Physiol. **148**, 459–488 (2016)
5. Mijailovich, S.M., Prodanovic, M., Vasovic, L., Stojanovic, B., Maric, M., Prodanovic, D., et al.: Modulation of calcium sensitivity and twitch contractions in cardiac muscle with troponin-C mutations: simulations and experiments. Biophys. J. **116**, 116a (2019)
6. Mijailovich, S.M., Nedic, D., Vasovic, L., Stojanovic, B., Powers, J., Davis, J., et al.: Influence of cTn Ca^{2+} binding properties and cooperative mechanisms on cardiac muscle contractile dynamics. Biophys. J. **114**, 500a (2018)
7. McNamara, J.W., Li, A., Dos Remedios, C.G., Cooke, R.: The role of super-relaxed myosin in skeletal and cardiac muscle. Biophys. Rev. **7**, 5–14 (2015)
8. Irving, M.: Regulation of contraction by the thick filaments in skeletal muscle. Biophys. J. **113**, 2579–2594 (2017)
9. Geeves, M., Griffiths, H., Mijailovich, S., Smith, D.: Cooperative [Ca(2) +]-dependent regulation of the rate of myosin binding to actin: solution data and the tropomyosin chain model. Biophys. J. **100**, 2679–2687 (2011)
10. Mijailovich, S.M., Kayser-Herold, O., Li, X., Griffiths, H., Geeves, M.A.: Cooperative regulation of myosin-S1 binding to actin filaments by a continuous flexible Tm-Tn chain. Eur. Biophys. J. **41**, 1015–1032 (2012)
11. Mijailovich, S.M., Stojanovic, B., Nedic, D., Svicevic, M., Gilbert, R.J., Geeves, M.A., et al.: Modulation of crossbridge cycling kinetics and length dependent calcium sensitivity by titin and nebulin. Biophys. J. **104**(2), 310 (2013)
12. Bathe, K.J.: Finite Element Procedures. Prentice-Hall, Englewood Cliffs (1996)
13. Bathe, K.J., Mijailovich, S.M.: Finite element analysis of frictional contact problems. J. de Mechanique et Applique **7**, 31–47 (1988)
14. Mijailovich, S.M., Stamenovic, D., Fredberg, J.J.: Toward a kinetic theory of connective tissue micromechanics. J. Appl. Physiol. **74**, 665–681 (1993)

15. Cazorla, O., Wu, Y., Irving, T.C., Granzier, H.: Titin-based modulation of calcium sensitivity of active tension in mouse skinned cardiac myocytes. Circ. Res. **88**, 1028–1035 (2001)
16. Irving, T.C., Konhilas, J., Perry, D., Fischetti, R., de Tombe, P.P.: Myofilament lattice spacing as a function of sarcomere length in isolated rat myocardium. Am. J. Physiol. Heart Circ. Physiol. **279**, H2568–H2573 (2000)
17. Linari, M., Dobbie, I., Reconditi, M., Koubassova, N., Irving, M., Piazzesi, G., et al.: The stiffness of skeletal muscle in isometric contraction and rigor: the fraction of myosin heads bound to actin. Biophys. J. **74**, 2459–2473 (1998)
18. Cazorla, O., Freiburg, A., Helmes, M., Centner, T., McNabb, M., Wu, Y., et al.: Differential expression of cardiac titin isoforms and modulation of cellular stiffness. Circ. Res. **86**, 59–67 (2000)

Pre-term Birth Prediction at Home: Signal Filtering Influence on the Good Prediction Rate

Alessandro Galassi[1,2(✉)], Charles Muszynski[3], Vincent Zalc[1], Dan Istrate[1], and Catherine Marque[1]

[1] Université de Technologie de Compiègne, Laboratoire BMBI UMR 7338, Compiègne, France
galassi.alessandro.d@gmail.com,
{dan.istrate,catherine.marque}@utc.fr
[2] Faculty of Ingegneria Civile e Industriale, La Sapienza, University of Rome, Rome, Italy
[3] Service de gynécologie et obstétrique, CHU Amiens-Picardie, Salouel, France
cmuszynski@hotmail.fr

Abstract. In this paper, we propose an automatic prediction system allowing to predict high probability of birth within 1–2 weeks from the EHG measurement [1–3]. Despite continuous clinical routine improvements, the preterm rate remains steady. With the aim of avoiding long hospitalization for pregnant women we propose an embedded system which acquires and processes EHG signals. We have already proposed a detection and recognition system for intrauterine contractions using directly the EHG signal obtained from a matrix of 16 electrodes. Since the measurements must be made at home, the decrease of computation power is an important constraint. In this work, we compare the results of the preterm birth prediction algorithm using a filtering step and with only the raw signals. The filtering step is applied directly on the raw signals or only on the automatically detected contractions to reduce computation time. We have applied in this, different filtering methods as denoising step to analyse their influence on the global classification performances. Two types of filtering are evaluated separately or combined: Canonical Correlation Analysis (CCA) and Empirical Mode Decomposition (EMD). The EMD decomposes a signal into a collection of oscillatory modes, called IMFs, which represent fast to slow oscillations in the signal. The CCA is a Blind Source Separation (BSS) method which assumes that the observed multichannel signals reflect a linear combination of several sources which are associated to underlying physiological processes, artefacts, and noise. The global classification results are compared between filtered and not filtered signals.

1 Introduction

According to the World Health Organization, preterm is defined as babies born alive before 37 weeks of gestation. The statistic for preterm death in the world is around 1 million children each year [6]. Most of preterm birth occurs spontaneously: for this reason, an earlier prediction will advance the treatment to prevent preterm birth which is the cause of death or other complications that could have effects on children under 5 years of age.

N. Filipovic (Ed.): ICCB 2019, LAIS 11, pp. 64–79, 2020.
https://doi.org/10.1007/978-3-030-43658-2_7

Infant mortality is measured by the Infant Mortality Rate (IMR) and preterm birth is the biggest contributor to this infant death. Despite continuous clinical routines improvements, the preterm birth rate remains steady.

Cost-effective care and prediction of the risk well in advance are the main factor that must be improved to increase the infant's chance to survive. In addition to this, over 30% of WHO Member States report to have less than 10 medical doctors per 10 000 population. Also, the risk of unnecessary long hospitalization stays high as well as its related [6].

The routine checks utilized for monitoring the contraction use the tocodynamometer measures, which allows the physicians to estimate the number of con-tractions (CTs) and the time between them. The most important limitation of this method is that it does not allow the characterization of the contraction efficiency. One non-invasive method to predict labor could be studying the uterine electrical activity and the features extracted from the ElectroHysteroGram (EHG) signal [1–3]. This non-invasive technique is based on the recording, on the abdomen skin, of the electrical activity related to contractions. By denoising and post-processing the EHG signal, referring to various proposed solutions and methods from many research teams, it is possible to implement a useful system of recognition and classification of the contractions.

We applied the detection, filtering and classification methods to a database of EHG recorded from the University Hospital Centre (CHU) Amiens-Picardie, specialized in preterm delivery threat pregnancies. This work has been developed within the framework of the SafePregnancy@Home project, project funded by the European community Eurostar project.

The goal of the Project SafePregnancy@home is to develop and to validate a home-monitoring device for uterine contraction analysis based on the electrohysterogram (EHG) processing. This will allow doctors to remotely monitor pregnancies and to respond to early warnings of preterm birth as well as to give women a secure feeling in a comfortable home situation. Once a real-time and validated warning is given, medical treatment could be provided to prevent pre-term labor and delay it up to 7 days. With 7 extra days of gestation, risks of mortality and morbidity will drop significantly, hence saving lives. The main expected result is a validated prototype monitoring device for uterine contractions based on EHG for (academic) hospitals and research organizations that can be used for home-care.

2 Methods

As shown in Fig. 1, the adopted system (Fig. 2) includes a 4×4 matrix of electrodes to be applied on the woman's abdomen: a system of 18 Ag/AgCl surface electrodes was used by placing 16 recording electrodes between the woman's pubis and umbilicus and two reference electrodes on each woman's hips. The 4×4 electrode matrix was shifted slightly to the right due to physiological dextrorotation of the uterus. The sixteen 4-mm diameter electrodes were separated from each other by intervals of 17.5 mm (centre to centre). All components of the EHG signal recording system are CE marked.

After the simultaneous acquisition of these 16 signals (sample frequency 1000 Hz), and of the tocodynamometer signal, the electromyographic signals are pre-filtered to remove the high-frequency content that does not represent the EHG (frequency band [0,2–3 Hz]). Once obtained these raw EHG signals, we applied the automatic detection method proposed by [7] to identify and segment the bursts of activity, called from now on Events, in order to distinguish them from the labelled contractions (CTs) that have been manually identified linked to the tocodynamometer measures.

According to [8], we create a new signal composed by the concatenation of the Events/CTs on which we compute different features, following [9], that represent the main characteristics of interest that could be extracted from the EHG for diagnosis purpose. Therefore, whatever the input signal (Events, CTs), the system was implemented to compute the features using a sliding and overlapping window as presented in [8, 13]. A Gaussian Mixture Model (GMM) inspired by [10–12] is then used to make the classification based on the computed features. The signal is transformed in a vector sequence; each vector has the size of the number of features and is computed for each sliding window of the signal.

The GMM classification consists in a two-class-model used to classify records in Imminent Labor (IL: labor will occur within 1 week from the recording time) or normal Pregnancy (P: labor will occur after more than 1 week from the recording time).

In order to improve the results obtained in [8], we tested in this study the effect of adding a denoising step before the computation of the features. The study was focused on two kind of denoising techniques that have been successively used for EHG [4]: the Empirical Mode Decomposition (EMD) and a Blind Source Separation algorithm using Canonical Correlation Analysis (CCA). The aim of this work was to verify and compare how the filtering through these methods could perform better in the prediction of Imminent Labor through two different kind of optimization of the CCA and EMD techniques. The diagram in Fig. 2 indicates the point where the Denoising process takes place.

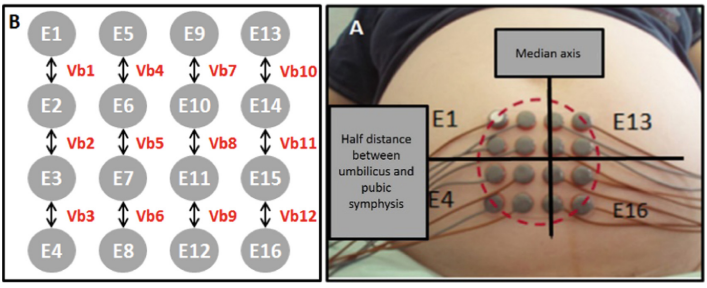

Fig. 1. The 4 × 4 matrix and its position on the woman's abdomen.

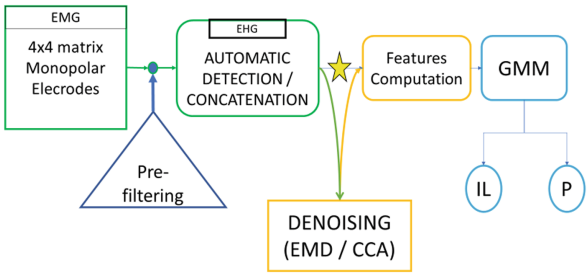

Fig. 2. Block diagram of the proposed system

The **EMD** decomposes a signal into a collection of oscillatory modes, called Intrinsic Mode Functions (IMFs), which represent fast to slow oscillations in the signal: through this decomposition, it is possible to rewrite the signal as a sum of a finite number of functions, the IMFs or oscillatory modes, each one with a different frequency content, based on local properties of the signal. The advantage of using this decomposition is that there is no constraint about time-stability and linearity.

The construction of an IMF depends on two conditions of existence and follows these steps [14]:

(i) The identification of the relative-minimum and the relative-maximum points of the signal,
(ii) The interpolation through two cubic-spline function: one for the upper interpolation u1(t) and one for the lower one l1(t),
(iii) The computation of the mean m1(t) from the two interpolations u1(t) and l1(t),
(iv) The computation of the difference between the original signal and the mean in (iii), to obtain the signal h1(t),
(v) If h1(t) respects the conditions of existence, a new IMF is obtained, if not, make a sifting process following the same criteria from (i) to (iv) applied on the h1(t),
(vi) The next IMF is obtained applying the same process on the residual between the previous IMF and the original signal.

By default, the first approach to the EMD is to get the right number of modes through which it is possible to decompose the signal: different stopping criteria are presented in literature. In this study, we considered that the whole signals of our database were characterized from the same number of IMFs: given this, the number of components to compute is strictly controlled by the number of components that have to be removed. Indeed, the denoising principle based on EMD is to remove the IMFs that contain only noise, followed by the reconstruction of the signal from the remaining IMFs.

The **CCA** is a Blind Source Separation (BSS) method which assumes that the observed multichannel signals reflect a linear combination of several sources which are associated with underlying physiological processes, artifacts, and noise. In this paper the aim of CCA is the denoising of the EHG signal, based on the hypothesis that the bursts of activity related to contractions have higher autocorrelation coefficients than the noise [4].

The BSS problem consists of retrieving unobserved sources from observed mixtures. The idea is to find a matrix which diagonalizes the covariance matrices of the mixed signals [5]. Within this framework the CCA theory allows the separation of the independent sources based on their autocorrelation.

Through CCA, we could find a transformation matrix which maximizes the autocorrelation of each of the recovered signal [15], for this reason we should consider it an Uncorrelated Component Analysis.

The basis for using the CCA to separate the mixed signals into a set of sources, is that it is possible to consider the correlation between the linear combination of the original signal and the linear combination of the same signal shifted by a specific lag. More specifically, the first CCA-component gives us a linear combination of the mixed signals with maximum autocorrelation; the second component gives a new linear combination respecting the constraint that it must be uncorrelated to the first component, etc. It is well explained in [5] that if we have two uncorrelated signals, v(t) with high autocorrelation and w(t) with low autocorrelation, the sum x(t) of these signals will have less autocorrelation than the original signal v(t). We can see it as if the addition of w(t) has corrupted v(t), making it harder to predict. Denoising is done by removing the less correlated sources for the improvement of the SNR.

Therefore, from both the EMD and the CCA methods, we obtained a matrix of components and, at least one of these, is supposed to be linked to the noise. The problem is then to identify which component(s) is related to the only noise. Since the EMD works in the frequency domain, the first IMFs are linked to a useless part of the signal because the algorithm extracts component from the higher frequency to the lower (Fig. 3A). With CCA, we compute the correlation coefficient for each components (Fig. 3B), that permits us to sort them from the higher to the lower.

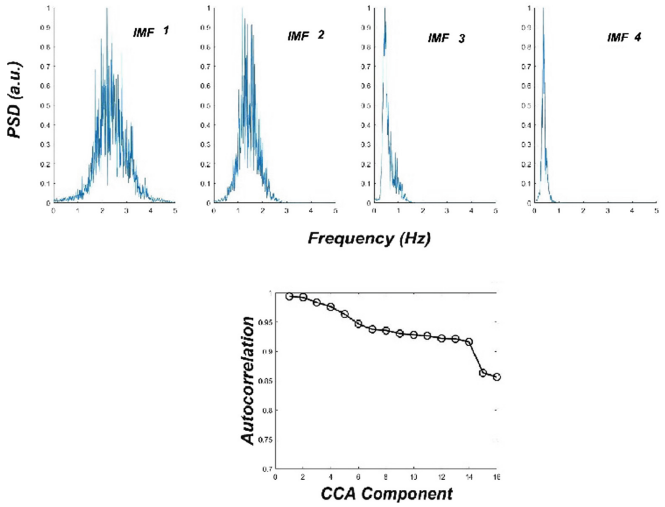

Fig. 3. (A) Normalized PDS of the first 4 IMFs from the EMD; (B) CCA-components evaluated by the autocorrelation.

In this work, we also implemented a default optimization (DO) [8] and an adaptive optimization (AO), in order to select which component(s) has to be removed (Fig. 4).

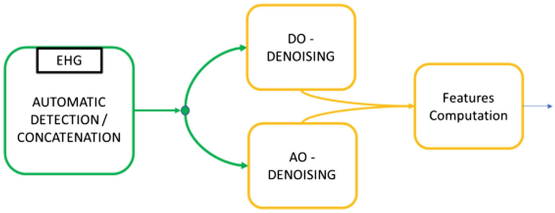

Fig. 4. The scheme for the two optimization approaches.

Default Optimization

With the term DO we indicate that the denoising was made using the same settings for each signal that has been previously optimized in [8].

Adaptive Optimization

The adaptive method for the EMD is based on the research from [1]: we focused on the pregnancy bandwidth. The Power Spectrum Density (PSD) of the EHG is dominated by frequencies below 1 Hz: for this reason, we included the following steps to define the IMFs to reject:

$$A = \int \mathrm{PSD(f)} \cdot \mathrm{df} \quad \text{for } fT < f < fmax$$
$$\alpha = \int \mathrm{PSD(f)} \cdot \mathrm{df} \quad \text{for } 0 < f < fmax$$

with fmax the maximum frequency of each IMF, and $fT = 1{,}5$ Hz.

We removed all the IMFs for which $A \geq 0{,}5 \cdot \alpha$ that corresponds to IMFs presenting high energy related to only high frequency noise and surely not related to any uterine activity.

For the CCA algorithm we defined a threshold value rT on the correlation value r, and removed each component with $r < rT$.

In a previous work, these 2 methods have been combined efficiently, first CCA then EMD, to denoise monopolar EHG [4]. In this work, we decided to test them alone, then combined in 2 different ways CCA-EMD or EMD-CCA, in order to denoise bipolar EHG. We compared thus the classification results obtained when using each of these 4 denoising methods (CCA, EMD, CCA-EMD, EMD-CCA) with the ones obtained with not denoised signals as possible inputs of the system (Fig. 5).

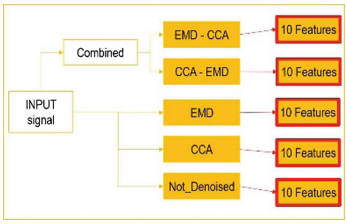

Fig. 5. Different combinations for the denoising process.

For the classification step in IL or P class, we used the GMM algorithm in 3 different ways using as inputs the 10 features computed from each (Fig. 5) denoising method (Fig. 6A), but also by combining the features computed from two different signals output of two denoising methods. We implemented two GMM-Combined methods (Fig. 6B): the Delta (Δ) and the Sigma ($\sum$) methods. For the Delta-GMM, considering the 2 classification results obtained from 10 features each, we applied the criterion in [16] given the priority to the prediction with the highest reliability. For the Sigma-GMM we use 20 features instead of 10, the first 10 obtained from the denoised signal and the last 10 from the Not_Denoised one. We also made the combination using 10 features from EMD with 10 features from CCA.

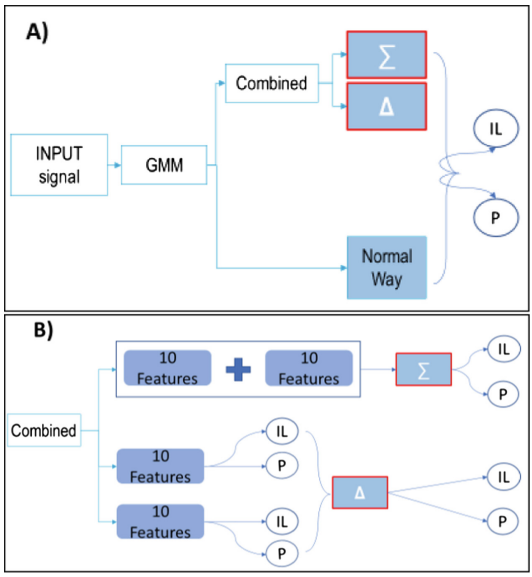

Fig. 6. (A) Three different methods to compute the GMM; (B) the 2 combined methods based on the 2 $\times$ 10 features from two different denoising process.

We have also re-evaluated the number of Gaussian models used for the GMM. Following [8] the optimal number was 18, but as we have changed the data base and added filtering, we defined a new optimal number.

3 Database

Thanks to the collaboration with the University Hospital Centre (CHU) Amiens-Picardie we were able to collect a database of 100 pregnant women with preterm birth risk. For each woman, we record simultaneously the tocodynamometer and the EHG signals as well as the information about weeks of gestation at recording that have been saved as Measurement Week.

The first step was to reject the records with no detected contractions from the tocodynamometer and the ones with very high variability and very low SNR. We also removed the files from women that had an induced childbirth and the ones with bad toco-signal. At the end, the used database included 79 patients.

Another important rejection step was made after the automatic segmentation process: we noticed that after the segmentation algorithm, 6 patients presented no detected *Events*. These records are considered as a part of the database but we were not able to process them in this study the same way as the other ones, that required concatenation of the automatic segmented *Events*.

4 Results

Our proposed system (Fig. 7), makes the comparison of the prediction rates obtained, from a given process applied to the concatenated Events, the whole EHG (TOT) and also to the manually concatenated CTs (Fig. 8). The process includes combination of the 5 different denoising and of the 3 classification methods.

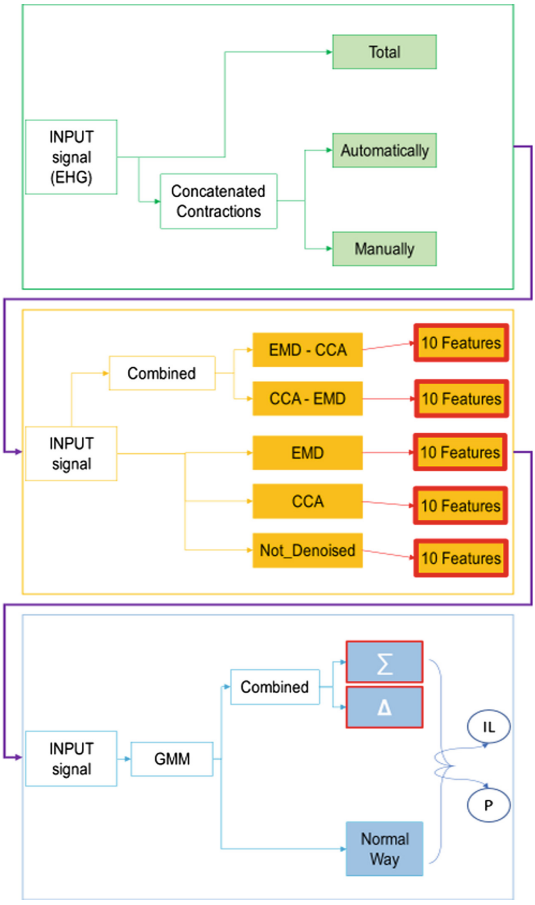

Fig. 7. The block diagram for the whole proposed evaluation system.

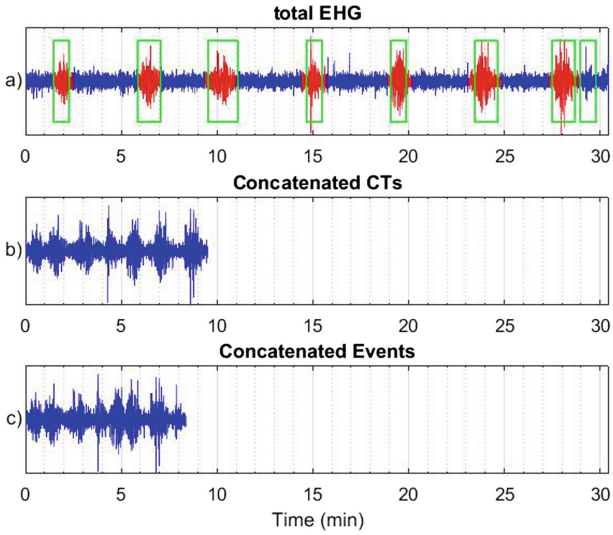

Fig. 8. The three different input signals to be processed: (a) the whole EHG signal (*TOT*) where manually segmented *CTs* are labelled in red and automatic segmented *Events* with green rectangles; (b) concatenation of the *CTs*; (c) concatenation of the *Events*. Notice that, in this case, only one *Event* is not related to any *CT*.

For the different input signals shown in Fig. 8 we have computed the following Features [9] from both the monopolar and the bipolar signals:

1: Detrended Fluctuation Analysis (DFA) [17]
2: Sample Entropy Variance (VarEn) [18]
3: Mean Power Frequency(MPF) [19]
4: Wavelet_h^2 (nonlinear correlation analysis) [20]
5: Modified Approximate Entropy (ModApEn) [13]

Though these Features, we first tested the GMM algorithms with 18 gaussians (as previously used in [8]) and K-Folder test (K = 500) in order to obtain the Confusion Matrix for the classification process between the 2 classes Imminent Labor (***IL***) and Pregnancy (***P***).

Tables 1–3 show the results as well as the mean of the principal diagonal, obtained first for the *Not_Denoised* signals for the 3 kinds of inputs: whole signal (*TOT*, Tables 1), manually segmented contractions (*CTs*, Table 2) and automatic segmentation (*Events*, Table 3).

Table 1. Classification results when processing the whole EHG signals (*TOT*)

	EHG	Target	
		IL	P
Prediction	IL	68.90% ± 25.20%	33.90% ± 11.80%
	P	31.10% ± 25.20%	66.10% ± 11.80%
Mean: 67.50% ± 13.91%			

Table 2. Classification results when processing the manually labelled *CTs*

	CTs	Target	
		IL	P
Prediction	IL	49.00% ± 27.70%	25.30% ± 10.80%
	P	51.00% ± 27.70%	74.70% ± 10.80%
Mean: 61.85% ± 14.87%			

Table 3. Classification results when processing the automatically detected *Events*

	Events	Target	
		IL	P
Prediction	IL	72.50% ± 24.90%	33.50% ± 12.00%
	P	27.50% ± 24.90%	66.50% ± 12.00%
Mean: 69.50% ± 13.82%			

We thus tested the effect of denoising, by applying every combination already described and comparing the *Not_Denoised* results with the *DO* and the *AO*. In particular, for the *AO* we tested different values and set the following thresholds that gave the best results (results not shown):

For the **EMD**

(1) $A = \int PSD(f) \cdot df \quad \text{for } (f_T = 1,5\,Hz) < f < f_{max}$

For the **CCA**

(2) $r < r_T = 0.95$.

We also computed some of the features in order to better see how the denoising affects their distribution (Fig. 9).

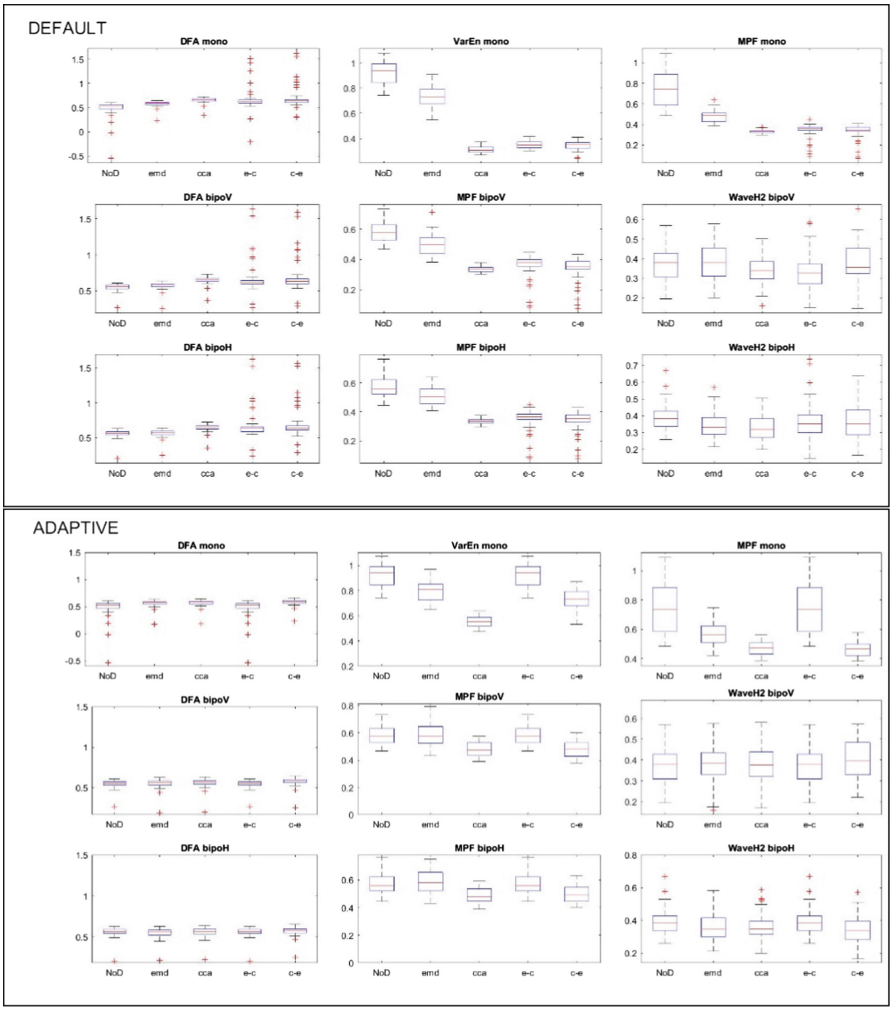

Fig. 9. Features obtained when using DO; **Down**: features obtained when using AO. The features are computed from monopolar (mono) signals or from bipolar (bipo) Horizontal (H) or Vertical (V) signals.

As, for each input signal, we tested 5 denoising method $\times$ 3 classification methods, giving thus 15 tests, the following figures present the results from the best of each test.

Figure 10 presents the results obtained when using the *Normal Way* of classification computed for each kind of input (denoised or not) signal:

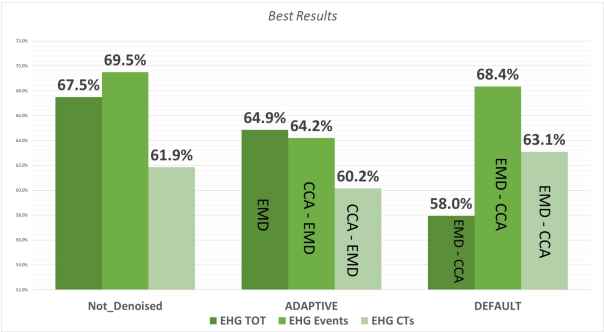

Fig. 10. Best results when using the *Normal – Way* classification. In uppercase the best combined denoising used in each case. The three methods: Not_Denoised, Adaptive Optimization (*AO*) and Default Optimization (*DO*).

Figure 11 presents the results obtained when using the *Combined* classification, both DELTA and SIGMA methods computed for each kind of input (denoised or not) signal:

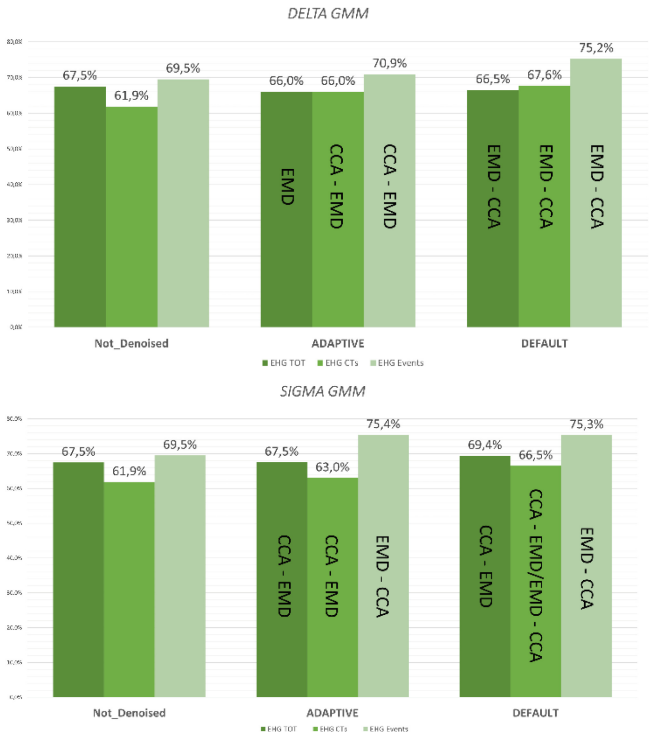

Fig. 11. **Up**: best results from the Delta method; **Down**: best results from the Sigma method. The 2 input signals used are the output signal of the denoising method indicated in the bar, combined with the *Not_Denoised* signal.

We then chose to use the methods that correspond to the best results previously obtained, to optimize again the number of gaussian models in the GMM (Fig. 12).

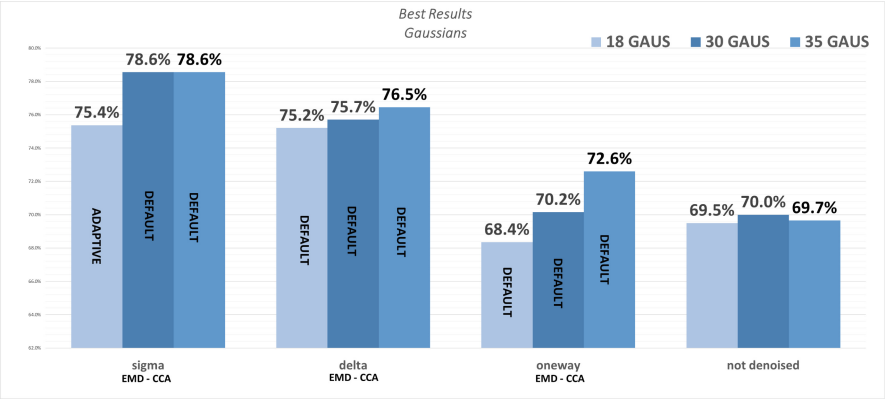

Fig. 12. Comparison of the best results obtained when using 18, 30 and 35 gaussians in the GMMs.

Taking into account computation constraints (that could be of importance for further use of real time and/or home monitoring of pregnancy), we chose to use a number of Gaussians of 30, as a good trade-off between quality of the results and computation time. Table 4 presents the confusion matrix obtained for the *SIGMA* method with a 30 Gaussian model.

Table 4. Classification results using the proposed method.

	Events	Target	
		IL	P
Prediction	IL	78.6% ± 23.8%	21.5% ± 10.0%
	P	21.4% ± 23.8%	78.5% ± 10.0%
Mean: 78.6% ± 12.9%			

5 Discussion

As shown in the Results section, when using the *Normal Way* classification (only one GMM with 10 features as input), the classification is better when using the concatenated *Events* automatically segmented from the *Not_Denoised* signals than with any other input data. But a clear increase (69,5% to 75,3%) in the classification results is obtained by using the *Combined* classification based on 20 features from 2 denoising (or not) processes (Fig. 11). This increase is even more pronounced (up to 78,5%) when optimizing the number of GMM of the model from 18 to 30 (Fig. 12).

First of all, it is possible to make some considerations about the different classification rates obtained with *TOT*, concatenated *Events* and concatenated *CTs*: we made

the hypothesis that the whole EHG record contains information related to the uterine activity (contractions) plus noise. The automatically segmented contractions (*Events*) gave better results than the manually labelled *CTs*, that have been labelled based on the tocodynamometer. This could indicate that the tocodynamometer is not a very efficient way to monitor uterine activity during pregnancy. Indeed, it has been proved that it cannot be used by itself to predict a risk of preterm labor [21]. This study will tend to prove that the information obtained from the automatic detection process succeeds in capturing useful information related to the contractile activity of the uterus, during pregnancy, that are not evidenced by the tocodynamometer.

When the 10 features computed after one denoising process are combined with the 10 features obtained from the not denoised signals, we can see some significant improvement when using the concatenated *Events*. In particular, the combination of the two EMD and CCA seems to give quite always better results than the single denoising.

Figure 13 presents the block diagram for the process that gives the best classification rate, after changing the number of gaussian curves of the GMM. The proposed system is thus: automatic segmentation of the *Events*, concatenation of the *Events*, *Default - EMD_CCA* denoising, classification by using the *SIGMA* combination with a 30 Gaussian model.

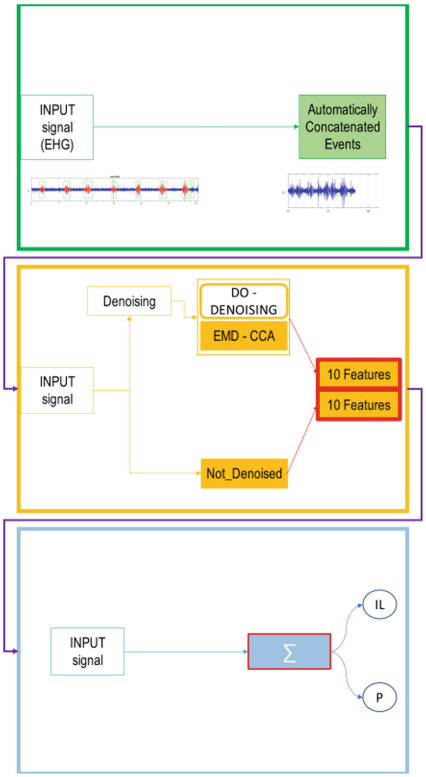

Fig. 13. Best proposed system.

About the Features and the effects of the denoising, the influence of the different combination is not so clear yet. But we can notice differences between the effects of the Adaptive Optimization and Default Optimization on the Sample Entropy and Variance Entropy, that are ones of the most relevant non-linear features evidenced in the bibliography [4]. In general, the EMD works on the frequency domain, it works on the high frequency noise and it has low effects if used alone; the CCA has high efficiency on detecting different uncorrelated noises because it does not work with frequencies. Combining both methods permits thus to reject different kinds of noise, depending not only on their frequency content but also on their autocorrelation.

Looking at the final results, it is interesting to note that the *Sigma*-GMM, combining features computed from the Not-Denoised and from one of the denoising method, gives such good results. Indeed, it shows that there should be some kind of hidden useful information in *the Not_Denoised* signal that are removed through the denoising.

6 Conclusions and Perspectives

Considering the results, it could be interesting to change the threshold for the *Adaptive Optimization* to understand the link between these thresholds and the feature change.

Another field of interest for future exploration should be to understand the relation and difference between concatenated *Events* and *CTs.*

One more interesting thing for further investigation could be to make other tests changing the number of Gaussian models and to verify the logarithmic trend of the good prediction rate while increasing that number.

The proposed system reaches the aim of low-computational costs and increases the good classification rate for the prediction of imminent labor that could be of great interest for clinical purpose. It is now necessary to increase and improve the database to reduce the standard deviation of the results. It should be interested to test this system in a prospective clinical study.

Acknowledgments. This work was founded by the Safepregnancy@home Eurostar project (E!10608) and also by BMBI UMR7338 laboratory. We would like to thank Jean Baptiste Tylcz for his help.

References

1. Devedeux, D., Marque, C., Mansour, S., Germain, G., Duchene, J.: Uterine electromyography: a critical review. Am. J. Obstet. Gynecol. **169**(6), 1636–1653 (1993)
2. Mansour, S., Devedeux, D., Germain, G., Marque, C., Duchene, J.: Uterine EMG spectral analysis and relationship to mechanical activity in pregnant monkeys. Med. Biol. Eng. Compu. **34**(2), 115–121 (1996)
3. Marque, C.K., Terrien, J., Rihana, S., Germain, G.: Preterm labour detection by use of a biophysical marker: the uterine electrical activity. BMC Pregnancy Childbirth **7**(1), S5 (2007)
4. Hassan, M., Boudaoud, S., Terrien, J., Karlsson, B., Marque, C.: Combination of canonical correlation analysis and empirical mode decomposition applied to denoising the labor electrohysterogram. IEEE Trans. Biomed. Eng. **58**(9), 2441–2447 (2011). https://doi.org/10.1109/tbme.2011.2151861

5. Liu, W., Mandic, D.P., Cichocki, A.: Analysis and online realization of the CCA approach for blind source separation. IEEE Trans. Neural Networks **18**, 1505–1510 (2007). https://doi.org/10.1109/tnn.2007.894017
6. WHO. https://www.who.int/news-room/fact-sheets/detail/preterm-birth
7. Happillon, T., Muszynski, C., Zhang, F., Marque, C., Istrate, D.: Detection of movement artefacts and contraction bursts using accelerometer and electrohysterograms for home monitoring of pregnancy. IRBM **39**(6), 379–385 (2018). https://doi.org/10.1016/j.irbm.2018.10.008
8. Tylcz, J.-B., Muszynski, C., Dauchet, J., Istrate, D., Marque, C.: An automatic method for the segmentation and classification of imminent labor contraction from electrohysterograms. IEEE Trans. Biomed. Eng. (2019). https://doi.org/10.1109/TBME.2019.2930618
9. Alamedine, D., Khalil, M., Marque, C.: Comparison of different EHG feature selection methods for the detection of preterm labor. Comput. Math. Methods Med. **2013**, 1–9 (2013)
10. Reynolds, D., Rose, R.: Robust text-independent speaker identification using Gaussian-mixture speaker models. IEEE Trans. Speech Audio Process. **3**(1), 72–83 (1995)
11. Bilmes, J.A.: A Gentle Tutorial of the EM Algorithm and its Application to Parameter Estimation for Gaussian Mixture and Hidden Markov Models, p. 281 (1998)
12. Arthur, D., Vassilvitskii, S.: K-means++: the advantages of careful seeding. In: Proceedings of the Eighteenth Annual ACM-SIAM Symposium on Discrete Algorithms, pp. 1027–1035 (2007)
13. Mischi, M., Chen, C., Ignatenko, T., de Lau, H., Ding, B., Oei, G.S., Rabotti, C.: Dedicated entropy measures for early assessment of pregnancy progression from single-channel electrohysterography. IEEE Trans. Biomed. Eng. **65**(4), 875–884 (2017)
14. Huang, N.E., et al.: The empirical mode decomposition and the Hilbert spectrum for nonlinear and non-stationary time series analysis. Proc. R. S. Lond. Ser. A Math. Phys. Eng. Sci. **454**(1971), 903–995 (1998)
15. Borga, M., Knutsson, H.: A canonical correlation approach to blind source separation. Report LiU-IMT-EX-0062 Department of Biomedical Engineering, Linkping University (2001)
16. Robin, M.: Analyse de l'environnement sonore pour le maintien à domicile et la reconnaissance d'activités de la vie courante, des personnes âgées. Ph.D. thesis, Université de Technologie de Compiègne, April 2018
17. Moslem, B., Diab, M.O., Khalil, M., Marque, C.: Detrended fluctuation analysis of uterine electromyography, pp. 450–453. IEEE, February 2011
18. Hu, M., Liang, H.: Variance entropy: a method for characterizing perceptual awareness of visual stimulus. Appl. Comput. Intell. Soft Comput. **2012**, 1–6 (2012)
19. Terrien, J., Steingrimsdottir, T., Marque, C., Karlsson, B.: Synchronization between EMG at different uterine locations investigated using time-frequency ridge reconstruction: comparison of pregnancy and labor contractions. EURASIP J. Adv. Signal Process. **2010**(1), 1–10 (2010)
20. Diab, A., Hassan, M., Laforet, J., Karlsson, B., Marque, C.: Estimation of coupling and directionality between signals applied to physiological uterine EMG model and real EHG signals. In: XIII Mediterranean Conference on Medical and Biological Engineering and Computing, Sevilla, Spain, pp. 718–721, September 2013
21. Reichmann, J.P.: Home uterine activity monitoring: the role of medical evidence. Obstet. Gynecol. **112**(2), 325–327 (2008)

Antioxidative Properties of Usnic Acid and Its Interaction with Tyrosyl-DNA Phosphodiesterase

Jelena Đorović[1(✉)] and Zoran Marković[1,2]

[1] Bioengineering Research and Development Center - BioIRC, 34000 Kragujevac, Republic of Serbia
jelena.djorovic@kg.ac.rs

[2] Department of Science, Institute for Information Technologies, University of Kragujevac, Jovana Cvijića bb, 34000 Kragujevac, Republic of Serbia

Abstract. In this study are investigated antioxidative properties of usnic acid, as well as its interaction with tyrosyl-DNA phosphodiesterase 1 (TDP1). Antioxidative properties are estimated on the basis of the Density Functional Theory (DFT) calculations. For this propose, full optimization of parent molecule of usnic acid and corresponding radical cation, radicals and anions are done at M05-2X/6-311++G(d,p) level of theory. The CPCM solvation model was applied to approximate the influence of polar and non-polar solvent. Obtained results indicate single electron transfer followed by the proton transfer as thermodynamically the most unfavorable mechanism of antioxidant action. The lowest values are achieved for proton affinity, and that pointed out sequential proton loss electron transfer mechanism as dominant antioxidative mechanism. The second part of this study is the examination of the interaction between usnic acid and TDP1, which is an enzyme responsible for repairing the protein-DNA bond in the cells. In order to perform molecular docking simulation AutoDock 4.0 software is used. Analysis of obtained data specifies interactions with Asn162, Leu168, Gly182, Tyr167 and Ser485 as the most significant. Further, the molecular dynamic simulation is performed using NAMD software. It is noticed that similar interactions are obtained.

1 Introduction

Oxidative stress (OS) and subsequent damage of biomolecules can be reduced using natural and synthetic compounds widely recognized as antioxidants. This is possible due to the ability of antioxidants to form more stable species after scavenging of free radicals. Antioxidants are of high interest in prevention of various diseases, due to hazardous effects of free radical species to human cells and body, generally. However, their behavior in various radical scavenging processes has not been elucidated, doubtlessly. Free radicals and other reactive species are constantly generated in human body. Oxygen is crucial for aerobic organisms, but it produces reactive oxygen species (ROS). When amount of reactive radical species exceeds the capacity of the endogenous antioxidative

N. Filipovic (Ed.): ICCB 2019, LAIS 11, pp. 80–91, 2020.
https://doi.org/10.1007/978-3-030-43658-2_8

protection the system is under oxidative stress. Many diseases such as cancer, inflammation, hypertension, and cardiovascular disorders can be caused as a consequence of the action of free radicals in the human body [1, 2]. The neurodegenerative disorders, in the first place Parkinson's and Alzheimer's diseases, can also have a basis in oxidative stress and changes at the molecular level [2].

Natural compounds with antioxidants properties are present in the food and food industry products. The compounds that are considered as good antioxidants possess some of the properties such as: toxicity, availability, location and concentration, versatility, fast reactions, crossing physiological barriers, and regeneration [3, 4]. Every of these conditions needs to be satisfied in the different manner. When we talk about toxicity of compounds, it is considered that good antioxidant should not be toxic before and after the antioxidant action. Also, an efficient antioxidant should be not only present, but also it should be in adequate concentration in cells. Term versatility considers that a good antioxidant should be able to easily react with different free radicals. One of the possibilities of good antioxidant is fast reactions: react faster with free radicals than the molecules which they protect, and in that way they can efficiently protect biological targets. Further, it is expected that a good antioxidant is able to cross physiologic barriers and be rapidly transported into the cells, where it is needed the most. Antioxidants that have physiological mechanisms to regenerate their original form are expected to be particularly efficient in reducing OS, because it is expected that they could scavenge more than one free radical.

In plant kingdom lichen phenolics represents unique substances, which possess numerous application. One of the most explored compound from this group is usnic acid (UA, Fig. 1). As one of the most characteristic metabolites isolated from lichen, UA is widely distributed in Usnea (Usneaceae), Cladonia (Cladoniaceae), Lecanora (Lecanoraceae), and other lichen genera, with a highest isolated yield of 26% [5]. Usnic acid has been of interest to chemists and pharmacologists since it was first isolated in 1844 [6–8]. Nowdays, UA is commercially offered, and as a pure compound it has been articulated into creams, toothpaste, mouthwash, deodorants, antibiotic ointments and sunscreen products. UA exhibits numerous pharmacological properties such as anti-inflammatory, anti-microbial, anti-viral, anti-oxidant, and anti-cancer [9–11]. It is one of the few commercially available lichen metabolites and has been the most extensively investigated.

In this paper are investigated antioxidative properties of usnic acid, as well as its interaction with tyrosyl-DNA phosphodiesterase 1 (TDP1), by the means of the Molecular Docking and Molecular Dynamic analysis.

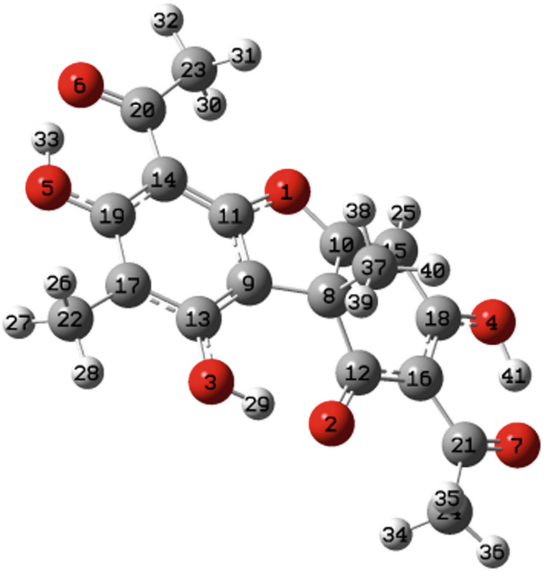

Fig. 1. Optimized geometry of UA.

2 Theoretical Framework

There are various quantum-mechanical methods that can be used to quantify the antioxidant activity [12, 13]. The reactions between the molecule which possess antioxidative properties and free radical can follow two different pathways: H-atom abstraction and radical adduct formation [14, 15]. The first processes include of various different, but similar mechanisms with the same net results. It should be pointed out that the net results of all mentioned antioxidant mechanisms are the same, and that is formation of the more stable radical species, A-O$^{\bullet}$. Here three different mechanism of antioxidant action are examined [16]: hydrogen atom transfer (HAT), single electron transfer followed by the proton transfer (SET-PT) and sequential proton loss electron transfer (SPLET). HAT mechanism is characterized by the hydrogen atom abstraction from antioxidant and transfer to the radical species (Eq. 1). SET-PT is two-step mechanism: the first step is formation of radical cation which is initial species in the second reaction (Eqs. 2 and 3). SPLET mechanism is also consistent from two steps, and the reaction pathways are presented with Eqs. 4 and 5. The reaction enthalpies of these processes can be used as the first parameter in determination of the prefer ability of the process. Generally speaking, HAT is preferred reaction mechanism in non-polar medium, because it does not involve charge separation. Due to processes of charge separation which is present in SET-PT and SPLET mechanisms, it can be supposed that this mechanisms will be favorized in polar medium [17].

$$\text{A-OH} \rightarrow \text{A-O}^{\bullet} + \text{H}^{\bullet} \tag{1}$$

$$\text{A-OH} \longrightarrow \text{A-OH}^{\bullet+} + \text{e}^{-} \tag{2}$$

$$\text{A-OH}^{\bullet+} \longrightarrow \text{A-O}^{\bullet} + \text{H}^{+} \tag{3}$$

$$\text{A-OH} \longrightarrow \text{A-O}^{-} + \text{H}^{+} \tag{4}$$

$$\text{A-O}^{-} \longrightarrow \text{A-O}^{\bullet} + \text{e}^{-} \tag{5}$$

Thermodynamical parameters that describe those mechanisms are: BDE (bond dissociation enthalpy), IP (ionization potential), PDE (proton dissociation enthalpy), PA (proton affinity) and ETE (electron transfer enthalpy). BDE characterize HAT mechanism, while IP and PDE are engaged with SET-PT mechanism. When SPLET mechanism is discussed, values of PA and ETE parameters are analyzed.

BDE, IP, PDE, PA and ETE values are determined from total enthalpies of the individual species, using following equations:

$$\text{BDE} = H\left(\text{A-O}^{\bullet}\right) + H\left(\text{H}^{\bullet}\right) - H(\text{A-OH}) \tag{6}$$

$$\text{IP} = H\left(\text{A-O}^{\bullet+}\right) + H\left(\text{e}^{-}\right) - H(\text{A-OH}) \tag{7}$$

$$\text{PDE} = H\left(\text{A-O}^{\bullet}\right) + H\left(\text{H}^{+}\right) - H\left(\text{A-O}^{\bullet+}\right) \tag{8}$$

$$\text{PA} = H\left(\text{A-O}^{-}\right) + H\left(\text{H}^{+}\right) - H(\text{A-OH}) \tag{9}$$

$$\text{ETE} = H\left(\text{A-O}^{\bullet}\right) + H\left(\text{e}^{-}\right) - H\left(\text{A-O}^{-}\right) \tag{10}$$

The reaction with the free radical species ($\text{RO}^{\bullet}$) also can follow three mentioned mechanisms. First mentioned is HAT mechanism, and reaction with free radical species is occurring by the Eq. (11):

$$\text{A-OH} + \text{RO}^{\bullet} \rightarrow \text{A-O}^{\bullet} + \text{ ROH} \tag{11}$$

The SET-PT mechanism is second described mechanistic pathway of antiradical action. It takes place in two steps as it is illustrated above in Eqs. 2 and 3, but in interaction with free radicals ($\text{RO}^{\bullet}$) is occurring following the next equations:

$$\text{A-OH} + \text{RO}^{\bullet} \longrightarrow \text{A-OH}^{\bullet+} + \text{RO}^{-} \tag{12}$$

$$\text{A-OH}^{\bullet+} + \text{RO}^{-} \longrightarrow \text{A-O}^{\bullet} + \text{ROH} \tag{13}$$

Third investigated mechanism of free radical scavenging is SPLET. The reaction between the antioxidant and the free radical via the SPLET mechanism can be described by the following reactions:

$$\text{A-OH} + \text{ RO}^{-} \longrightarrow \text{A-O}^{-} + \text{ROH} \tag{14}$$

$$\text{A-O}^{-} + \text{ RO}^{\bullet} \longrightarrow \text{A-O}^{\bullet} + \text{RO}^{-} \tag{15}$$

The reaction of examined compound with particular free radicals is thermodynamically favorable if it is exothermic, refer to changes in reaction enthalpy (Eq. 16):

$$\Delta_r H = \left[H(\text{products}) - H(\text{reactants})\right] < 0 \tag{16}$$

Radical inactivation via HAT mechanism (Eq. 17) is characterized by the H-atom transfer from the investigated compounds to the free radical ($RO^{\bullet}$). The values of $\Delta_r H_{BDE}$ can be calculated using the following equation:

$$\Delta_r H_{BDE} = H\left(\text{A-O}^{\bullet}\right) + H(\text{ROH}) - H(\text{A-OH}) - H\left(\text{RO}^{\bullet}\right) \tag{17}$$

The SET-PT mechanism is described using the following thermodynamic parameters:

$$\Delta_r H_{IP} = H\left(\text{A-O}^{\bullet+}\right) + H\left(\text{RO}^{-}\right) - H(\text{A-OH}) - H\left(\text{RO}^{\bullet}\right) \tag{18}$$

$$\Delta_r H_{PDE} = H\left(\text{A-O}^{\bullet}\right) + H(\text{ROH}) - H\left(\text{A-O}^{\bullet+}\right) - H\left(\text{RO}^{-}\right) \tag{19}$$

In case when the antioxidant reacts with the corresponding free radical via the SPLET mechanism, the values of the thermodynamic parameters $\Delta_r H_{PA}$ and $\Delta_r H_{ETE}$ are responsible for that mechanism and can be calculated using the following equations:

$$\Delta_r H_{PA} = H\left(\text{A-O}^{-}\right) + H(\text{ROH}) - H(\text{A-OH}) - H\left(\text{RO}^{-}\right) \tag{20}$$

$$\Delta_r H_{ETE} = H\left(\text{A-O}^{\bullet}\right) + H\left(\text{RO}^{-}\right) - H\left(\text{A-O}^{-}\right) - H\left(\text{RO}^{\bullet}\right) \tag{21}$$

All mentioned free radical scavenging mechanisms have the same product, and that is stable radical of antioxidant. As a consequence of that, they have the same thermodynamic balance, Eq. (22). It could be said that competition between this reactions is present, as well these reactions may be occurring in parallel.

$$\Delta_r H_{BDE} = \Delta_r H_{IP} + \Delta_r H_{PDE} = \Delta_r H_{PA} + \Delta_r H_{ETE} \tag{22}$$

2.1 Computational Methods

The equilibrium geometries of parent molecule of UA and corresponding radical cation, radicals and anions were optimized by DFT method: M05-2X functional and 6-311++G(d,p) basis set. All calculations are performed using Gaussian 09 [18]. The M05-2X functional yields reasonable results for thermochemical calculations of organic, organometallic, and biological compounds [19]. This functional has also been successfully used by independent authors [20–22]. The local and global minima were confirmed to be real minima by frequency analysis (no imaginary frequency were obtained). To evaluate the impact of polar and non-polar solution, water and benzene are used. For this purpose, the CPCM solvation model is applied [23]. The solvent effects are taken into account in all geometry optimizations and calculations. The values for solvation enthalpies of proton and electron are taken from literature [24]. All reaction enthalpies used in equations are calculated at 298 K.

The molecular docking simulations are carried out using the AutoDock 4.0 software [25]. The three-dimensional crystal structures of TDP1 protein were obtained from the Protein Data Bank (PDB IDs: 1JY1) [26]. Preparation of protein for docking is carried out in the Discovery Studio 4.0 (BIOVIA Discovery Studio 2016). The co-crystallized ligand, water molecules and co-factors are removed using this software. In order to add polar hydrogen atoms and to calculate Kollman charges the AutoDockTools (ADT) graphical user interface is used. In molecular docking simulation, the ligand is set as flexible, while the protein remained as rigid structure. The bonds in ligand are set to be rotatable. The Lamarckian Genetic Algorithm (LGA) method is performed for protein - ligand flexible docking. Dimensions of grid box of TDP1 protein are set to 70.201 Å × −3.015 Å × 37.023 Å in order to cover the protein binding site and accommodate ligand to move freely. The molecular docking simulation is done at temperature of 298.15 K. Analysis of docking results and visualizations of linking positions are performed by using BIOVIA Discovery Studio.

Further, molecular dynamic (MD) simulations were done using NAMD software package [27]. For this simulations, as starting structures is used the most stable complex obtained after molecular docking simulations. Equilibration of systems is performed for 1 ns in the term of NVT condition. The production is performed for duration period of 5 ns in the term of NPT condition.

3 Results and Discussion

The reaction enthalpies related to three above mentioned mechanisms of antioxidative action of UA (HAT, SET-PT and SPLET) are calculated. The species necessary to perform these calculations are generated from the most stable conformation of UA, which is taken from literature [28]. The preferred antioxidative mechanism are estimated from the BDE, IP, and PA values. The lowest values indicates which mechanism is thermodynamically the most favorable. One of the requirements for a phenolic compound to show good antioxidative activity is formation of stable phenoxyl radical after free radical scavenging. Obtained results for parameters that describes antioxidant mechanism of action are collected in Table 1. From there presented results for water and benzene, it is clear that in both solvents IP values of OH groups of UA are significantly higher than the corresponding BDE and PA values. This characterize SET-PT mechanism as unfeasible reaction pathway for antioxidant action in polar and non-polar solvents. Since the IP values are higher in comparison to BDEs and PAs, SET-PT mechanism will not be discussed further. The obtained values for BDE and PA are different in investigated solutions. When results obtained for BDE and PA in water are compared, it is notable that significant lower values are achieved for PAs. This fact makes the SPLET mechanism superior over HAT in water.

The obtained results in benzene show a little bit different picture. Namely, if one compare obtained BDEs and PAs it is notable competition between these two mechanisms in position P3 and P5, while in position P4 undoubtedly SPLET is the preferable mechanism of antioxidant action. Further are done examination of the antioxidant reaction pathway in the present of free radical species, since it is known that the scavenging mechanisms of antioxidants are highly influenced by the properties of the scavenged

Table 1. Calculated reaction enthalpies (kJ mol^{-1}) for the antioxidant reactions of UA

Site	Aqueous phase					Benzene				
	HAT	SET-PT		SPLET		HAT	SET-PT		SPLET	
	BDE	IP	PDE	PA	ETE	BDE	IP	PDE	PA	ETE
		509					666			
P3	413		119	217	412	419		189	423	431
P4	451		157	186	480	453		222	388	499
P5	402		108	238	379	412		182	457	390

radical species [29]. Three different free radical species were used: hydroxyl radical ($^{\bullet}OH$), methyl peroxyl radical ($CH_3OO^{\bullet}$), and hydroperoxyl radical ($^{\bullet}OOH$). Hydroxyl and hydroperoxyl radicals are oxygen-derived free radicals included in the complex process of innate immunity and phagocytosis [30]. Their production begins with the activation of NADPH, and their main goal is the destruction of pathogens or other foreign matter. The harmful action of these radicals arises as a result of some autoimmune diseases when immune cells become over-activated and toxic to neighboring healthy cells [31]. Also, the $^{\bullet}OH$ radical is very powerful oxidant and it is product of the Fenton and Haber-Weiss reaction. This radical can initiate reaction with hydrocarbons in the presence of air in which peroxyl radicals are produced. Third mentioned is $CH_3OO^{\bullet}$ radical, and it is used to simulate lipid peroxyl radical, formed in the metabolic reaction of lipid peroxidation.

Table 2. Calculated parameters of the mechanisms free radicals scavenger reactions for UA in kJ mol^{-1}.

UA	Water					Benzene				
	HAT	SET-PT		SPLET		HAT	SET-PT		SPLET	
	ΔH_{BDE}	ΔH_{IP}	ΔH_{PDE}	ΔH_{PA}	ΔH_{ETE}	ΔH_{BDE}	ΔH_{IP}	ΔH_{PDE}	ΔH_{PA}	ΔH_{ETE}
		114					328			
P-3 + $^{\bullet}OH$	−81		−195	−97	17	−81		−409	−174	93
P-4 + $^{\bullet}OH$	−43		−158	−129	85	−48		−375	−209	161
P-5 + $^{\bullet}OH$	−92		−207	−76	−16	−89		−416	−140	52
		207					409			
P-3 + $^{\bullet}OOH$	55		−152	−54	110	63		−345	−111	174
P-4 + $^{\bullet}OOH$	92		−115	−86	178	97		−312	−146	242
P-5 + $^{\bullet}OOH$	43		−164	−33	77	56		−353	−77	133
		215					411			
P-3 + $CH_3OO^{\bullet}$	63		−152	−54	117	71		−340	−106	177
P-4 + $CH_3OO^{\bullet}$	100		−115	−85	186	104		−307	−141	245
P-5 + $CH_3OO^{\bullet}$	51		−163	−33	84	64		−348	−72	136

The enthalpies of reaction are a quantity that can successfully contribute to the understanding of the processes between antioxidant species and free radicals. A direct approach to estimate the change of enthalpy of a reaction is to apply the fundamental thermodynamic relationship, i.e., to subtract the enthalpy of reactants from the enthalpy of products. If the reaction is exothermic, it means that the newly formed radical is more stable than the starting one, implying the reaction path is favorable. Otherwise, if the reaction is endothermic, the reaction path is not favored, because the newly formed radical is less stable than the starting one. The enthalpies of reactants, products, as well as change of enthalpies of reactions of UA with selected free radicals, are calculated to take into account electronic properties of selected free radicals on reaction of analyzed antioxidative mechanisms. The preferred mechanism is assumed from the $\Delta_r H_{BDE}$, $\Delta_r H_{IP}$, and $\Delta_r H_{PA}$ values. The more negative values indicate thermodynamically favorable mechanism. The calculated changes of enthalpies are presented in Table 2. The obtained results indicate that UA inactivates selected free radicals. The analysis of achieved values in both investigated solvents shows that the most reactive $^{\bullet}$OH radical can be inactivated with UA. The results show that in the case of $^{\bullet}$OH much lower values are obtained for $\Delta_r H_{PA}$ than for $\Delta_r H_{BDE}$. It means that there is present competition between HAT and SPLET mechanism, but investigated compound will most likely react with $^{\bullet}$OH radical exclusively via SPLET mechanism. On the other hand, if one discuss results obtained for reaction with $^{\bullet}$OOH and $CH_3OO^{\bullet}$, first it should be point out that lower and negative values are obtained for $\Delta_r H_{PA}$. This fact indicates that for inactivation of these two radicals SPLET is the probable reaction pathway of antioxidative action. Comparison of the obtained values indicates that lower values are realized in reactions with $^{\bullet}$OH radical, which is consequence of its high reactivity. Also, the presented values of reaction enthalpies with above mentioned free radicals one more time confirm that the hydroxyl groups in positions 4 possess better antioxidative capacity than hydroxyl group in position 3 and 5 (Table 2). In addition, the obtained positive values of $\Delta_r H_{IP}$ indicate that SET-PT is not the possible scavenging mechanism in any case under investigation (Table 2), which is in accordance to thermodynamic results presented in Table 1.

To examine interaction of UA with protein, SwissTargetPrediction analysis of ligand (Fig. 1) is performed. This analysis predicts inhibition of TDP1 by UA molecule. TDP1 is an enzyme that is responsible for repairing the protein-DNA bond in the cells by catalyzing hydrolysis of the phosphodiester bond between the tyrosine residue of type I topoisomerase and the 3-prime phosphate of DNA. TDP1 restores DNA molecules in cells by removing blocked complexes of topoisomerase 1 (TOP1)–DNA [32]. Inhibition of TDP1 protein can increase the efficacy of TOP1 inhibitors. It has been suggested that therapeutic selectivity can be achieved by combining the inhibitors and TOP1 and TDP1, and it can be used for the treatment of human cancers [33]. Combined anti-cancer therapy potentially reduces the side effects of chemotherapeutic treatments and allows the use of a lower dose of the drug [34]. The molecular docking study is applied in order to evaluate the inhibitory nature of ligand. The binding energy of protein-ligand complex, as well as identification of the potential ligand binding sites are predicted. Ten different conformations of protein-ligand complex are accomplished from molecular docking simulation. The complex conformation with the lowest binding energy and inhibition constant is selected for further analysis (model 10). The obtained free energy

of binding value (E_b) is -23.93 kJ mol^{-1}, and it includes final intermolecular energy, final total internal energy, torsional free energy, and unbound system's energy. The estimated inhibition constant Ki is 64.12 uM. The smaller value of the Ki indicate the greater binding affinity and the smaller amount of ligand is needed to inhibit the activity of the enzyme.

In the model 10, two types of interactions are present and they form hydrogen bonds and hydrophobic contacts (Fig. 2). Regard hydrogen bonds, it should be pointed out that two types of hydrogen bonds are established: conventional hydrogen bond and carbon hydrogen bond. The lengths of conventional hydrogen bonds are in range 1.94–2.38 Å, and they are formed with Leu168, Arg487 and Gly181 from TDP1. Carbon hydrogen bond is formed between Tyr167 and ligand, and length of this interaction is 3.68 Å.

Hydrophobic alkyl contacts are formed with Ala182, Leu168 and Pro571, while the interactions with Phe166 and Leu168 are characterized as hydrophobic π–alkyl.

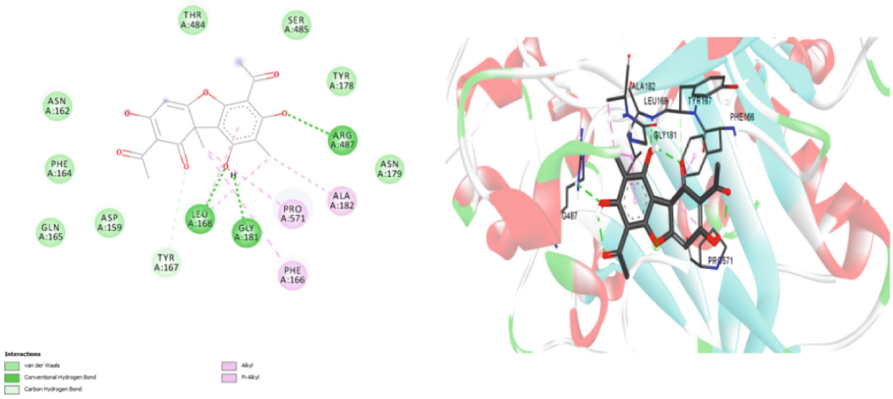

Fig. 2. The best docking positions of protein-ligand complex

Further, the conformational model 10 was used as starting structure for molecular dynamics (MD) simulation. For the process of the equilibration of the system temperature of the system quickly reaches the target value (300 K), and remains stable over the remainder of the equilibration. The analysis of the interactions of the protein-ligand complex obtained after 5 ns production of MD simulation, indicates interactions with some same and also some different amino acids, comparing the complex structure obtained after molecular docking simulation. In this case, the number of hydrogen bonds between TDP1 protein and ligand are numerous, but not significant (Fig. 3). In addition, hydrogen bonds with Leu168 and Gly181 are repeated, like after the docking simulation. Also, after 5 ns of MD simulation are achieved hydrogen bonds with amino acids 147, 150, 162, 177, 178, 179, 180, 568, and those amino acids are Asp, Glu, Asn, Lys, Tyr, Asn, Ser, Ala. Amino acids Ala236 and Ala240 are included in hydrophobic alkyl and π –alkyl contacts, respectively.

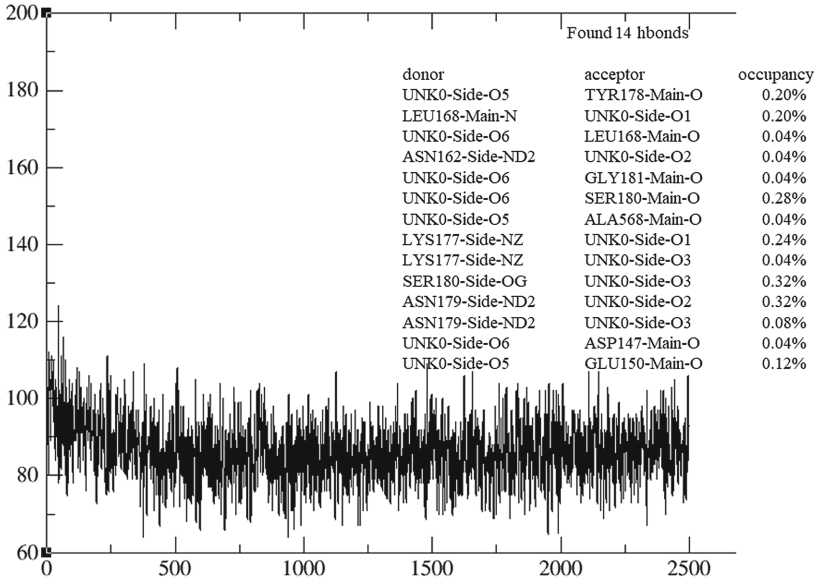

Fig. 3. The stability of system during production period and formed hydrogen bonds.

4 Conclusions

It is known that oxidative stress is main cause of many diseases in modern society. In the last decade, considerable attention is devoted to elucidation of processes of prevention of OS. Additionally, it is considered that antioxidants are responsible for prevention of oxidative damage. The natural antioxidants present in herbals are interesting due to their biological properties. In this study is examined the antioxidant reactivity of usnic acid, natural occurring lichen phenolic compound. The antioxidative properties of UA are inspected theoretically, combining three different approaches. DFT calculations are done in two different solvents (water and benzene), in respect to examine polar and non-polar environment. UA shown good antioxidative properties in both investigated solvents, with the prefer ability of HAT antioxidative mechanism in water, and competition of HAT and SPLET mechanisms in benzene. It should point out, that in both solvent hydroxyl group in position 4 is the most reactive. To confirm these results, calculations are done in present of three harmful free radical species. The obtained results indicates that UA is capable to inactivate selected free radicals. Further, since UA shows good antioxidative properties, examination of its inhibition potency by molecular docking and dynamic simulations are performed. The tyrosyl-DNA phosphodiesterase 1 is chosen for this purpose. The achieved interaction between ligand and TDP1, as well as values of binding energy and inhibition constant, indicates possible binding. The difference between binding modes of the most stable molecular docking structure and structure after MD simulation can be explained by effect of solvent and size of the ligand.

Acknowledgments. The authors acknowledge support of the Ministry of Education, Science and Technological Development of the Republic of Serbia (Grants no. 174028 and 172015).

References

1. Halliwell, B., Gutteridge, J.M.C.: Free Radicals in Biology and Medicine, 3rd edn. Clarendon Press, Oxford (1999)
2. Halliwell, B.: Free radicals and other reactive species in disease. In: Encyclopedia of Life Sciences. Nature Publishing Group (2001)
3. Rose, R.C., Bode, A.M.: Biology of free radical scavengers: an evaluation of ascorbate. FASEB J. **7**(12), 1135–1142 (1993)
4. Galano, A.: Free radicals induced oxidative stress at a molecular level: the current status, challenges and perspectives of computational chemistry based protocols. J. Mex. Chem. Soc. **59**(4), 231–262 (2015)
5. Reyim, M.: Adiljan; Abdulla, A. China Brew. **11**, 122–124 (2010)
6. Ingolfsdottir, K.: Usnic acid. Phytochemistry **61**(7), 729–736 (2002)
7. Araújo, A.A.S., De Melo, M.G.D., Rabelo, T.K., Nunes, P.S., Santos, S.L., Serafini, M.R., Santos, M.R.V., Quintans-Júnior, L.J., Gelain, D.P.: Review of the biological properties and toxicity of usnic acid. Nat. Prod. Res. **29**(23), 2167–2180 (2015)
8. Guo, L., Shi, Q., Fang, J.L., Mei, N., Ali, A.A., Lewis, S.M., Leakey, J.E., Frankos, V.H.: Review of usnic acid and Usnea barbata toxicity. J. Environ. Sci. Health Part C **26**(4), 317–338 (2008)
9. Shrestha, G., St. Clair, L.L.: Lichens: a promising source of antibiotic and anticancer drugs. Phytochem. Rev. **12**(1), 229–244 (2013)
10. Mitrović, T., Stamenković, S., Cvetković, V., Tošić, S., Stanković, M., Radojević, I., Stefanović, O., Čomić, L., Đačić, D., Ćurčić, M., Marković, S.: Antioxidant, antimicrobial and antiproliferative activities of five lichen species. Int. J. Mol. Sci. **12**(8), 5428–5448 (2011)
11. Bačkorová, M., Bačkor, M., Mikeš, J., Jendželovský, R., Fedoročko, P.: Lichen secondary metabolites are responsible for induction of apoptosis in HT-29 and A2780 human cancer cell lines. Toxicol. In Vitro **26**(3), 462–468 (2012)
12. Álvarez-Diduk, R., Galano, A.: Adrenaline and noradrenaline: protectors against oxidative stress or molecular targets? J. Phys. Chem. B **119**(8), 3479–3491 (2015)
13. Petrović, Z.D., Đorović, J., Simijonović, D., Petrović, V.P., Marković, Z.: Experimental and theoretical study of antioxidative properties of some salicylaldehyde and vanillic Schiff bases. RSC Adv. **5**(31), 24094–24100 (2015)
14. Alberto, M.E., Russo, N., Grand, A., Galano, A.: A physicochemical examination of the free radical scavenging activity of Trolox: mechanism, kinetics and influence of the environment. Phys. Chem. Chem. Phys. **15**(13), 4642–4650 (2013)
15. Galano, A., Mazzone, G., Alvarez-Diduk, R., Marino, T., Alvarez-Idaboy, R., Russo, N.: Food antioxidants: chemical insights at the molecular level. Ann. Rev. Food Sci. Technol. **7**, 335–352 (2016)
16. Rimarčík, J., Lukeš, V., Klein, E., Ilčin, M.: Study of the solvent effect on the enthalpies of homolytic and heterolytic N-H bond cleavage in p-phenylenediamine and tetracyano-p-phenylenediamine. J. Mol. Struct. (Thoechem) **952**(1–3), 25–30 (2010)
17. Zhang, H.Y., Ji, H.F.: How vitamin E scavenges DPPH radicals in polar protic media. New J. Chem. **30**(4), 503–504 (2006)
18. Frisch, M.J., Trucks, G.W., Schlegel, H.B., Scuseria, G.E., Robb, M.A., Cheeseman, J.R., Zakrzewski, V.G., Montgomery, J.J., Stratmann, R.E., Burant, J.C., Dapprich, S., Millam, J.M., Daniels, A.D., Kudin, K.N., Strain, M.C., Farkas, O., Tomasi, J., Barone, V., Cossi, M., Cammi, R., Mennucci, B., Pomelli, C., Adamo, C., Clifford, S., Ochterski, J., Petersson, G.A., Ayala, P.Y., Cui, Q., Morokuma, K., Malick, A.D., Rabuck, K.D., Raghavachari, K., Foresman, J.B., Cioslowski, J., Ortiz, J.V., Baboul, A.G., Stefanov, B.B., Liu, G., Liashenko, A., Piskorz, P., Komaromi, I., Gomperts, R., Martin, R.L., Fox, D.J., Keith, T., Al-Laham, M.A., Peng, C.Y., Nanayakkara, A., Challacombe, M., Gill, P.M.W., Johnson, B., Chen, W., Wong, M.W., Andres, J.L., Gonzalez, C., Head-Gordon, M., Replogle, E.S., Pople, J.A.: Gaussian 09, Revision B.01. Gaussian Inc., Wallingford (2009)

19. Zhao, Y., Truhlar, D.G.: The M06 suite of density functionals for main group thermochemistry, thermochemical kinetics, noncovalent interactions, excited states, and transition elements: two new functionals and systematic testing of four M06-class functionals and 12 other functionals. Theoret. Chem. Acc. **120**(1), 215–241 (2008)
20. Marković, Z.S., Marković, J.M.D., Doličanin, Ć.B.: Mechanistic pathways for the reaction of quercetin with hydroperoxy radical. Theoret. Chem. Acc. **127**(1–2), 69–80 (2010)
21. Marković, Z., Milenković, D., Đorović, J., Marković, J.M.D., Stepanić, V., Lučić, B., Amić, D.: Free radical scavenging activity of morin 2′-O− phenoxide anion. Food Chem. **135**(3), 2070–2077 (2012)
22. Zavala-Oseguera, C., Alvarez-Idaboy, J.R., Merino, G., Galano, A.: OH radical gas phase reactions with aliphatic ethers: a variational transition State Theory Study. J. Phys. Chem. A **113**(50), 13913–13920 (2009)
23. Takano, Y., Houk, K.N.: Benchmarking the conductor-like polarizable continuum model (CPCM) for aqueous solvation free energies of neutral and ionic organic molecules. J. Chem. Theory Comput. **1**(1), 70–77 (2005)
24. Tošović, J., Marković, S., Milenković, D., Marković, Z.: Solvation enthalpies and Gibbs energies of the proton and electron – influence of solvation models. J. Serb. Soc. Comput. Mech. **10**(2), 66–76 (2016)
25. Morris, G.M., Huey, R., Lindstrom, W., Sanner, M.F., Belew, R.K., Goodsell, D.S., Olson, A.J.: AutoDock4 and AutoDockTools4: automated docking with selective receptor flexibility. J. Comput. Chem. **30**(16), 2785–2791 (2009)
26. Davies, D.R., Interthal, H., Champoux, J.J., Hol, W.G.: The crystal structure of human tyrosyl-DNA phosphodiesterase, TDP1. Structure **10**(2), 237–248 (2002)
27. Phillips, J.C., Braun, R., Wang, W., Gumbart, J., Tajkhorshid, E., Villa, E., Chipot, C., Skeel, R.D., Kale, L., Schulten, K.: Scalable molecular dynamics with NAMD. J. Comput. Chem. **26**(16), 1781–1802 (2005)
28. Galasso, V.: Probing the molecular and electronic structure of the lichen metabolite usnic acid: a DFT study. Chem. Phys. **374**(1–3), 138–145 (2010)
29. Hussein, M.A.: A convenient mechanism for the free radical scavenging activity of resveratrol. Int. J. Phytomedicine **3**(4), 459–469 (2011)
30. Knight, J.A.: Review: free radicals, antioxidants, and the immune system. Ann. Clin. Lab. Sci. **30**(2), 145–158 (2000)
31. Cooper, G.M.: The development and causes of cancer. In: The Cell: A Molecular Approach, 2nd edn., Boston University, Sunderland, MA. Sinauer Associates (2000)
32. Takagi, M., Ueda, J.Y., Hwang, J.H., Hashimoto, J., Izumikawa, M., Murakami, H., Sekido, Y., Shin-ya, K.: Tyrosyl-DNA phosphodiesterase 1 inhibitor from an anamorphic fungus. J. Nat. Prod. **75**(4), 764–767 (2012)
33. Antony, S., Marchand, C., Stephen, A.G., Thibaut, L., Agama, K.K., Fisher, R.J., Pommier, Y.: Novel high-throughput electrochemiluminescent assay for identification of human tyrosyl-DNA phosphodiesterase (TDP1) inhibitors and characterization of furamidine (NSC 305831) as an inhibitor of TDP1. Nucleic Acids Res. **35**(13), 4474–4484 (2007)
34. Gushchina, V., Nilov, D.K., Zakharenko, A.L., Lavrik, O.I., Švedas, V.K.: Structure modeling of human tyrosyldna phosphodiesterase 1 and screening for its inhibitors. Acta Naturae **9**(2(33)), 59–66 (2017)

Free Radical Scavenger Activity and P-glycoprotein Inhibition Capacity of 1,2,4-Trihydroxyxanthone

Svetlana Jeremić[1(✉)] and Zoran Marković[2]

[1] State University of Novi Pazar, Vuka Karadžića bb, 36300 Novi Pazar, Republic of Serbia
sjeremic@np.ac.rs

[2] Institute of Information Technologies, University of Kragujevac, Jovana Cvijića bb, 34000 Kragujevac, Serbia

Abstract. Some xanthone derivatives isolated from plants possess antifungal, antimicrobial, antioxidative and cytotoxic activities. Therefore, products manufactured from plants that contain xanthones are used as botanical dietary supplements. The operative mechanism of antioxidative action of 1,2,4-trihydroxyxanthone is investigated in this contribution. For this purpose, M06-2X/6-311++G(d,p) method is used. Antioxidative capacity of investigated xanthone is determined in benzene and water as mediums. It is found that, among three possible radicals that this xanthone can generate, the most stable is the one obtained by homolytic cleavage of O-H group in position 4. It was found that HAT (Hydrogen Atom Transfer) is the only operative mechanism for xanthone in benzene. On the other hand, the most favorable mechanism in water is SPLET (Sequential Proton Loss Electron Transfer). It should be emphasized that SET-PT (Single-Electron Transfer followed by Proton Transfer) is not plausible mechanistic pathway in both solvents. Antioxidants express their scavenger capacity in the presence of free radicals. Therefore here is examined scavenger capacity of 1,2,4-trihydroxyxanthone toward $HO^{\bullet}$, $HOO^{\bullet}$ and $CH_3OO^{\bullet}$ radicals. It is found that the investigated xanthone is able to deactivate free radicals *via* competitive HAT and SPLET mechanisms. The observed reactivity of the xanthone toward free radicals decreases following the order: $HO^{\bullet} \gg HOO^{\bullet} > CH_3OO^{\bullet}$. It should be pointed out that reactivity of the xanthone to selected free radicals slightly increases with an increase in solvent polarity.

1 Introduction

As a consequence of metabolic processes occurring in the body, various reactive species are formed. Mostly, these are free radicals, which can be produced by enzymatic reactions involved in phagocytosis, the respiratory chain, and the synthesis of prostaglandins. Free radicals have an unpaired electron, which makes them highly reactive oxidants and therefore damage cells during chain reactions. The immune system functions by suppressing pathogen invasion by producing free radicals and damaging pathogenic cells by produced radical species. Beside internal sources of free radicals, there are numerous external sources of these reactive moieties. Due to a various enzymatic and

N. Filipovic (Ed.): ICCB 2019, LAIS 11, pp. 92–103, 2020.
https://doi.org/10.1007/978-3-030-43658-2_9

non-enzymatic antioxidants, the immune system allows positive and blocks the negative activities of free radicals. When in organism is reached the balance between free radical formation and antioxidant defenses, it results in a phenomenon named homeostasis. On the contrary, disruption of homeostasis caused by excess production of free radicals leads to the phenomenon called oxidative stress. Oxidative stress plays an important role in the aging process as well as in the development of many diseases such as: rheumatoid arthritis, Parkinson's disease, inflammatory diseases, cancers, etc.

Antioxidants are molecules that inhibit the negative effect of free radicals. They enable the maintenance of homeostasis of the organism and prevent the occurrence of oxidative stress. Antioxidants eliminate excess free radicals through several mechanisms and preventing their harmful effects on healthy cells. They easily react with free radicals producing stable radical moiety, which do not participate in further oxidation processes. Increasing the amount of free radicals in the body that leads to the oxidative stress, is caused by various external and internal factors such as pollution, cigarette smoke, drugs, illness, stress, etc. In this case, the needful of an organism for antioxidants increases [1]. There are different endogenous antioxidants involved in immune system of organism. Among them are enzymes, metal binding proteins, bilirubin, thiols, uric acid, etc. Since the body cannot produce some important micronutrients, many plants are used as source of dietary antioxidants. Among plant-derived antioxidants, vitamin C, vitamin E, beta carotene and different polyphenols are widely studied.

Some molecules from the group of xanthones possess antifungal, antimicrobial, antioxidative and cytotoxic activities [2]. Most of plants that consists xanthones and their derivatives are from the families Bonnetiaceae, Clusiaceae and Podostemaceae [3]. Therefore, products manufactured from these plants are used as botanical dietary supplements [2].

Phenolic antioxidants neutralize free radical following several reaction mechanisms. Most of them generate stable radical of the initial antioxidant which has no tendency to further participate in the radical reaction. Radical form of antioxidant can be obtained by cleavage of O-H bond. Here is investigated the operative mechanism of antioxidative action of 1,2,4-trihydroxyxanthone (XA) (Fig. 1).

The immunology system of organism is consisted of numerous enzymatic and non-enzymatic reactions. Among proteins involved in protection of organism from different negative influences, is P-glycoprotein (Pgp). Pgp is located in the cell membrane, and its primary role is to enable the transport of the substances from one to each other site of the membrane. As a part of the immunology systems, it exports numerous toxins out of the cell, ensuring cell protection [4]. A bed feature of Pgp is its low selectivity. It is reflected in the fact that it recognizes many drugs as foreign bodies, and exports them out of the cell. It leads to the lower effectiveness of drugs, and to the phenomenon known as multiple drug resistance (MDR) [4]. The identification of suitable Pgp inhibitors presents a significant task of chemical and pharmacological industry. It could allow more effective medical treatment, and support the process of the healing. Here is examined the possibility of XA to act as inhibitor of Pgp.

2 Theoretical Framework

Many earlier theoretical investigations suggested and defined several possible reaction pathways for generation of stable antioxidant radical [5, 6]. Here are investigated three of them: HAT (hydrogen atom transfer), SET-PT (single-electron transfer followed by proton transfer), and SPLET (sequential proton loss electron transfer). HAT is one-step reaction of homolytic cleavage of O-H bond (Eq. 1). Thermodynamically plausibility of this reaction can be estimated based on Bond Dissociation Enthalpy value (BDE), which can be calculated using Eq. 1.1. In Eq. 1.1 are used abbreviations XA-O$^{\bullet}$, H$^{\bullet}$, and XA-OH to label radicals of XA and hydrogen, and neutral molecule of XA, separated. SET-PT is two-step mechanism (Eq. 2). In the first step electron leaves XA molecule forming radical-cation (XA-OH$^{\bullet+}$). In the second step, proton goes from radical-cation forming radical moiety. The possibility for reaction to follow this reaction pathway can be determine based on the values of Ionization Potential (IP) and Proton Dissociation Enthalpy (PDE), that can be calculated using Eqs. 2.1 and 2.2. SPLET is another two-step mechanism. In its first step proton goes from XA molecule forming anion (XA-O^{-}), while in the second step anion release electron generating XA radical (Eq. 3). Thermodynamically favorableness for this mechanistic pathway can be estimated based on the values of Proton Affinity (PA), Eq. 3.1, and Electron Transfer Enthalpy (ETE), Eq. 3.2. In all of three mentioned mechanisms, as the final product is generated XA radical.

$$\textbf{HAT: } \text{XA-OH} \rightarrow \text{XA-O}^{\bullet}\text{+H}^{\bullet} \tag{1}$$

$$\text{BDE} = H\left(\text{XA-O}^{\bullet}\right) + H\left(\text{H}^{\bullet}\right) - H(\text{XA-OH}) \tag{1.1}$$

$$\textbf{SET}-\textbf{PT: } \text{XA-OH} \xrightarrow{-\text{e}^{-}} \text{XA-OH}^{\bullet+} \xrightarrow{-\text{H}^{+}} \text{XA-O}^{\bullet} \tag{2}$$

$$\text{IP} = H\left(\text{XA-OH}^{\bullet+}\right) + H\left(\text{e}^{-}\right) - H(\text{XA-OH}) \tag{2.1}$$

$$\text{PDE} = H\left(\text{XA-O}^{\bullet}\right) + H\left(\text{H}^{+}\right) - H\left(\text{XA-OH}^{\bullet+}\right) \tag{2.2}$$

$$\textbf{SPLET: } \text{XA-OH} \xrightarrow{-\text{H}^{+}} \text{XA-O}^{-} \xrightarrow{-\text{e}^{-}} \text{XA-O}^{\bullet} \tag{3}$$

$$\text{PA} = H\left(\text{XA-O}^{-}\right) + H\left(\text{H}^{+}\right) - H(\text{XA-OH}) \tag{3.1}$$

$$\text{ETE} = H\left(\text{XA-O}^{\bullet}\right) + H\left(\text{e}^{-}\right) - H\left(\text{XA-O}^{-}\right) \tag{3.2}$$

Antioxidants scavenge free radicals, and thus protect organism against their harmful effect. There are at least three possible mechanisms of free radical scavenging by XA: HAT, SET-PT and SPLET [5, 6]. HAT mechanism is one-step reaction, in which hydrogen atom transfers from XA to free radical (RO$^{\bullet}$), and deactivates it, Eq. 4. The thermodynamic parameter that describes this mechanism is related enthalpy of reaction ($\Delta_{\text{r}}H_{\text{BDE}}$), Eq. 4.1. SET-PT and SPLET are two-step mechanisms. In the first step of SET-PT, electron moves from XA to free radical generating radical-cation of XA

and anion of free radical (RO^-), while in the second step of reaction proton moves from radical-cation, which leads to neutralized free radical, Eqs. 5 and 6. The reaction enthalpies of both reaction steps can be calculated by Eqs. 5.1 and 6.1. ($\Delta_r H_{IP}$ and $\Delta_r H_{PDE}$). In the first step of SPLET, proton transfers from XA to anionic moiety of free radical, Eq. 7. Appropriate enthalpy of reaction ($\Delta_r H_{PA}$) can be calculated using Eq. 7.1. In the second step of SPLET electron moves from anion of XA to free radical, and it can be described by the values of enthalpy of electron transfer ($\Delta_r H_{ETE}$), Eqs. 8 and 8.1.

$$\textbf{HAT:}\quad \text{XA-OH}+\text{RO}^{\bullet} \rightarrow \text{XA-O}^{\bullet}+\text{ROH} \tag{4}$$

$$\Delta_r H_{BDE} = H\left(\text{XA-O}^{\bullet}\right) + H(\text{ROH}) - H(\text{XA-OH}) - H\left(\text{RO}^{\bullet}\right) \tag{4.1}$$

$$\textbf{SET}-\textbf{PT:}\quad \text{XA-OH}+\text{RO}^{\bullet} \rightarrow \text{XA-OH}^{\bullet+}+\text{RO}^{-} \tag{5}$$

$$\Delta_r H_{IP} = H\left(\text{XA-OH}^{\bullet+}\right) + H\left(\text{RO}^{-}\right) - H(\text{XA-OH}) - H\left(\text{RO}^{\bullet}\right) \tag{5.1}$$

$$\text{XA-OH}^{\bullet+}+\text{RO}^{-} \rightarrow \text{XA-O}^{\bullet}+\text{ROH} \tag{6}$$

$$\Delta_r H_{PDE} = H\left(\text{XA-O}^{\bullet}\right) + H(\text{ROH}) - H\left(\text{XA-OH}^{\bullet+}\right) - H\left(\text{RO}^{-}\right) \tag{6.1}$$

$$\textbf{SPLET:}\quad \text{XA-OH}+\text{RO}^{-} \rightarrow \text{XA-O}^{-}+\text{ROH} \tag{7}$$

$$\Delta_r H_{PA} = H\left(\text{XA-O}^{-}\right) + H(\text{ROH}) - H(\text{XA-OH}) - H\left(\text{RO}^{-}\right) \tag{7.1}$$

$$\text{XA-O}^{-}+\text{RO}^{\bullet} \rightarrow \text{XA-O}^{\bullet}+\text{RO}^{-} \tag{8}$$

$$\Delta_r H_{ETE} = H\left(\text{XA-O}^{\bullet}\right) + H\left(\text{RO}^{-}\right) - H\left(\text{XA-O}^{-}\right) - H\left(\text{RO}^{\bullet}\right) \tag{8.1}$$

To investigate the capacity of XA to scavenge free radicals, here are considered reactions of XA with hydroxyl ($HO^{\bullet}$), hydroperoxyl ($HOO^{\bullet}$) and methylperoxyl ($CH_3OO^{\bullet}$) radicals. $HO^{\bullet}$ and $HOO^{\bullet}$ radicals are very reactive oxygen species, involved in complex process of innate immunity and phagocytosis [7]. $CH_3OO^{\bullet}$ is used as a model of alkyl radical formed in different metabolic reactions, as is lipid peroxidation [8].

The physiological pH is 7.4, indicating that in the human body is generally a weak base environment. Under those conditions, deprotonation of hydroxyl groups is possible, producing mono-anionic species. Thus formed anionic species are additionally stabilized by water, as the most abundant solvent in the body, with a solvation effect. Therefore here is performed docking analysis of the mono-anionic species of XA to the Pgp.

3 Computational Details

The geometry optimization and frequency calculation for XA molecule, and its radical and ionic moieties, as for free radical and its derivatives, which participate in observed

reaction steps, are done using Gaussian 09 program package [9]. For that purpose are used M06-2X functional [10] and the split-valence basis set 6-311++G(d,p). The absence of the imaginary frequencies confirmed that the optimized geometry corresponds to the energy minima. All calculations are done at 298.15 K. In order to examine the effect of the polarity of the environment to the optimal reaction mechanism, the calculations are done in benzene and water as models of non-polar and polar solvents. For that purpose is used CPCM solvation model [11]. Used values of enthalpy of solvated proton and electron were calculated by Tošović and coworkers [12].

Docking analysis is performed by using optimized geometries of anions of XA as ligands. The structure of Pgp is taken from Protein Data Bank (PDB ID: 3G5U) [13]. The preparation of Pgp structure for docking analysis, which implies the removing of ligands and water molecules from the protein structure, is carried out using a VMD program [14]. Docking analysis is performed at the whole molecule, using the AutoDock 4.2 program package [15]. The structures of ligands are estimated as flexible, while the structure of Pgp is rigid. All calculations for protein–ligand flexible docking were carried out using the Lamarckian Genetic Algorithm (LGA) method [16]. Grid box with dimensions 40 × 40 × 40, and with a grid spacing of 0.375 Å is used. Analysis of docking results and visualizations of linking positions are performed using BIOVIA Discovery Studio [17].

4 Results and Discussion

4.1 Antioxidative Reaction Mechanisms

XA is molecule with three hydroxyl groups, in positions 1, 2 and 4 (Fig. 1). Stable radical forms of XA can be generated by homolytic cleavage of O-H bonds. In order to it, one of three mechanisms can be followed. Propitiatory of a mechanism can be evaluated by comparing BDE, IP, and PA parameters. The lower the energy of the appropriate parameter indicates the greater probability that the reaction follows the observed reaction path.

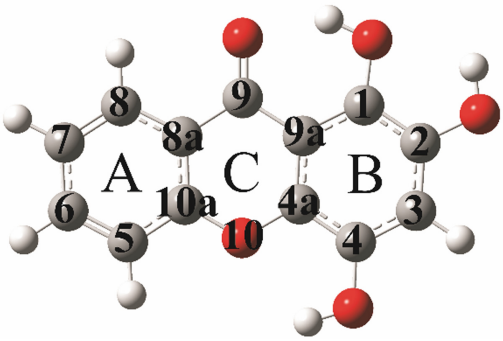

Fig. 1. Optimized geometry of XA with labeled atoms and rings.

Observing enthalpy values of interest from Table 1, one can conclude that in benzene BDEs are the lowest comparing with PA and IP. It means that in non-polar environment HAT is the most favorable reaction pathway. In water as a solvent, the lowest are PAs, implying that in polar solution preferable is SPLET mechanism. In both environments IPs have the highest values. It leads to the conclusion that SET-PT is not operative under any of observed conditions. The least possibility of the reaction to follow SET-PT can be explained by the fact that a in the first step of this mechanism is formed radical cation, which is a highly unstable species.

Table 1. Calculated parameters of the antioxidant mechanisms for XA in kJ mol^{-1}.

	Benzene					Water				
	HAT	SPLET		SET-PT		HAT	SPLET		SET-PT	
	BDE	PA	ETE	IP	PDE	BDE	PA	ETE	IP	PDE
R1	349	440	341	620	161	343	216	322	452	86
R2	351	459	324		163	344	225	314		87
R4	337	442	327		149	337	217	315		80

In the presence of the free radicals, antioxidants exert their antioxidant activity by its ability to deactivate free radicals. This can be accomplished by following multiple reaction mechanisms. Most of them involve the transfer of a hydrogen atom from a hydroxyl group of an antioxidant to a free radical species. Thereby are generated neutralized radical form, and stable radical of antioxidant. Comparing appropriate thermodynamically parameters that describe corresponding reaction steps, it can be established which of observer reaction mechanism is operative. Negative values of appropriate reaction enthalpies indicate exothermic reaction, and favorable mechanistic pathway under the considered conditions. The lower value of reaction enthalpy indicates the more favorableness of the observed reaction mechanism. If the appropriate reaction enthalpy values are positive, but enough low (<40 kJ mol^{-1}), this reaction path may also be referred as thermodynamically possible [18].

Comparing reaction enthalpy values from Table 2, it can be seen that $\Delta_r H_{BDE}$ and $\Delta_r H_{PA}$ values, characteristic for HAT and SPLET mechanisms, are negative for all selected radicals under both environmental conditions. Moreover, $\Delta_r H_{ETE}$ values are for $HO^{\bullet}$ radical negative, and for $HOO^{\bullet}$ and $CH_3OO^{\bullet}$ enough low, especially in water, to refer both HAT and SPLET mechanisms thermodynamically plausible in both solvents. In benzene SPLET is more favorable than HAT. On contrary, in water HAT is more plausible mechanism. Lower $\Delta_r H_{PA}$ than $\Delta_r H_{BDE}$ values in water can be explained by the fact that solvation of XA anion formed in the first step of SPLET does not have great influence to the stability of obtained species. Namely, due to the great velocity of the gendered XA anion, this anion is surrounded with the lower number of solvent molecules than the anion which is precursors of free radicals. Therefore the solvation has more significant influence to the stability of RO^{-}, than to the stability of formed XA-O^{-} moiety. The stability of XA anion is additionally supported by different intramolecular

Table 2. Calculated parameters of the mechanisms of free radicals scavenging reactions for XA in kJ mol^{-1}.

			Δ_rH_{HAT}	Δ_rH_{SPLET}		$\Delta_rH_{SET\text{-}PT}$	
			Δ_rH_{BDE}	Δ_rH_{PA}	Δ_rH_{ETE}	Δ_rH_{IP}	Δ_rH_{PDE}
Benzene	$HO^{\bullet}$	R1	−141	−152	11	291	−432
		R2	−139	−134	−6		−430
		R4	−153	−151	−2		−444
	$HOO^{\bullet}$	R1	−11	−98	87	367	−378
		R2	−9	−80	70		−376
		R4	−23	−97	74		−390
	$CH_3OO^{\bullet}$	R1	−3	−92	89	368	−372
		R2	−1	−73	72		−370
		R4	−15	−90	75		−383
Water	$HO^{\bullet}$	R1	−156	−100	−56	74	−229
		R2	−154	−90	−64		−228
		R4	−161	−98	−63		−235
	$HOO^{\bullet}$	R1	−24	−56	32	162	−184
		R2	−23	−47	24		−183
		R4	−30	−55	25		−190
	$CH_3OO^{\bullet}$	R1	−16	−54	39	168	−186
		R2	−14	−45	30		−185
		R4	−22	−53	31		−192

effects, as are charge distribution and intramolecular hydrogen bonds. Values of Δ_rH_{IP} are high and positive, indicating that SET-PT is inoperative mechanism for here selected radicals scavenging, in polar and non-polar environment.

Observing Δ_rH_{BDE} values related to reactions of scavenging of $HO^{\bullet}$, $HOO^{\bullet}$ and $CH_3OO^{\bullet}$ radicals separately, it can be seen that they are the lowest for hydroxyl radical. It indicates that $HO^{\bullet}$ is the easiest for deactivation by XA. Appropriate reaction enthalpies for peroxyl radicals are significant higher, indicating lower scavenger capacity of XA toward these radicals. Hydroperoxyl radical is somewhat easier to be deactivated by XA than methyl peroxyl radical.

4.2 Stability of XA Radicals

In all considered scavenger process as main reaction product is formed XA radical. This radical is stable enough to be resist to the further radical reaction. Relative stability of the three XA radicals obtained by the homolytic cleavage of O-H groups at positions 1, 2 and 4, can be estimated based on the BDE values from the Table 1. It can be seen that in both solvents the lowest BDEs corresponds to the R4 radical, obtained by the cleavage of O-H group in position 4. On the other hand stability of R1 and R2 radicals

are almost the same. The differences in BDEs for the R1 and R2 radicals are only 1 to 2 kJ mol^{-1}, depending on the solvent conditions.

The highest stability of R4 radical can be explained by the spin density distribution (SDD). It is well known that better SDD leads to the lower values of SDD at the radical center (Fig. 2) [19–21]. It is the consequence of the fact that the unpaired electron is in that case distributed over the larger number of atoms in formed radical. In the same time, the better SDD are in consequence with the higher antioxidant capacity. It can be seen that $SDD_{R1} \approx SDD_{R2} < SDD_{R4}$, which is in accordance with the stability of the radicals of XA.

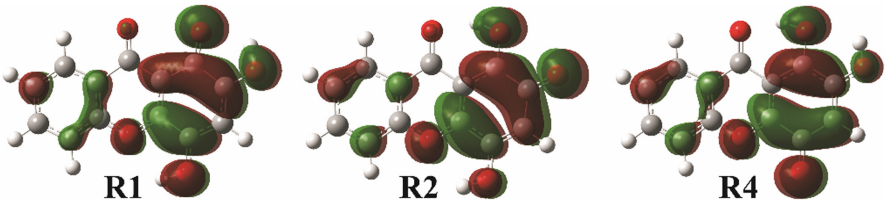

Fig. 2. Three-dimensional map of spin density distribution (SDD) for the free radicals of XA in benzene

Three-dimensional map of SDD for the radicals of here investigated XA indicates that there are very high distribution of unpaired electron at all of three radicals. The spin distribution includes the atoms of all three rings in the molecule, rings A, B, and C (Figs. 1 and 2). The highest distribution is over the ring B. The consequence of the similarly distribution of spin is the relative small differences in the BDE values, compering the most and the least stable radical form (about 15 kJ mol^{-1} in benzene and about 5 kJ mol^{-1} in water).

At the stability of radical a great influence have the presence and the strength of the internal hydrogen bonds. Radicals R1 and R2 are stabilized by the two intramolecular hydrogen bonds. One of them is formed between hydrogen atom of the hydroxyl group and neighbor oxygen atom of the carbonyl group, obtained by the homolytic cleavage of neighbor O-H bond. The lengths of these hydrogen bonds are 2.012 Å and 1.757 Å at the R1 and R2 respectively. The results of NBO analyses confirms that these bonds are formed as the transfer of lone pare electrons from p_y orbital of carbonyl oxygen to the σ^* orbital of O-H bond [22]. The other internal hydrogen bond is formed between hydrogen atom of the hydroxyl group at the position 4, and the etheric oxygen at the position 10 (Fig. 1). The lengths of these bonds are 2.092 Å and 2.151 Å at the R1 and R2 respectively. These bonds are generated as the result of the transfer of lone pare electrons from p_x orbital of the etheric oxygen to the σ^* orbital of O4-H4 bond. Radical R4 is stabilized by the presence of two intramolecular hydrogen bonds among the one is formed between hydrogen of hydroxyl group at position 1, and carbonyl oxygen at position 9, and the other is formed between hydrogen of the hydroxyl group at position 2 and oxygen of the hydroxyl group at position 1. The length of the firs mentioned hydrogen bond is 1.719 Å, and it is built by the transfer of lone pare electrons from O9 carbonyl oxygen to the σ^* orbital of O1-H1 bond. The second hydrogen bond is

2.156 Å, and for its formation is deserve lone pare electron transfer from O1 atom to the σ^* orbital of O2-H2 bond. It can be seen that summarized values of lengths of internal hydrogen bonds that correspond to the observer radicals are the lowest for R4, while the sums of the energies that corresponds to the electron transfers are the highest for R4. It is in the consequence with the highest stability of the R4 radical, and the lowest corresponding BDE values, comparing with the appropriate values that correspond to the R1 and R2 forms.

4.3 Docking Analysis

As a trihydroxy xanthone, XA undergoes to the deprotonation, forming three mono-anionic moieties, A1, A2 and A4, depending if the cleavage of O-H bond occurred at the position 1, 2 or 4, respectively. Relative enthalpy values calculated in water indicates that the most stable is A1. Its standard enthalpy calculated in water is for 9.58 kJ mol^{-1} lower than enthalpy of A2, and for 1.58 kJ mol^{-1} lower than enthalpy of A4. Docking analyses is performed for all of three anions of XA. Bearing on mind that Pgp causes MDR, it was interesting to investigate the possibility of docking of some drug, whose effectiveness can be decreased as a consequence of low selectivity of Pgp. A comparison of the results obtained for docking of selected drug to the Pgp with the once obtained for docking of XA anions, can lead to the conclusion if the presence of XA anion can provide the higher drug activity. Here is docking analysis performed with mitoxantrone (MX), a synthetic anthracene drug, used in the treatment of leukemia and cancer [23, 24]. The results of analyses are presented in Table 3, and on the Fig. 3.

Table 3. Results of docking analysis of A1, A2, A3 and MX, with Pgp. E_b presents free energy of binding in kcal mol^{-1}, and K_i is inhibition constant in μM.

Ligand	E_b (kcal mol^{-1})	K_i (micromolar)
A1	−4.42	575.17
A2	−4.46	536.58
A4	−4.64	394.20
MX	−0.01	$9.85 \cdot 10^5$

The values of energy of binding from Table 3 indicate that all anions of XA link to the Pgb stronger than estimated drug. In the same manner are results of inhibition constant, which are several times lower for anions of XA, than for MX. Among three estimated anions, the highest inhibition potency possesses A4. Moreover, as can be seen from Fig. 3, the positions of docking for MX and for A4 with Pgp are completely the same. All examined XA anions and MX are linked to the Pgp over the amino acids Lys 884, Glu885, Gly 888 and Pro 923. Among intermolecular interactions formed between selected ligand and Pgp, the dominant are conventional and carbon hydrogen bonds, than π – μ and π – alkyl hydrophobic interactions. It indicates that all three anions of XA can protect MX from negative influence of Pgp. One can be assumed that medical therapy

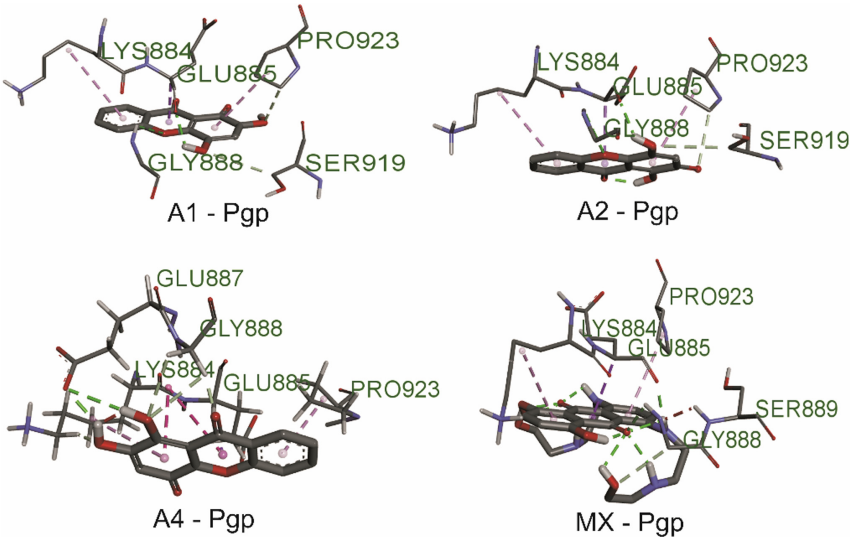

Fig. 3. Positions of docking of A1, A2, A4 and MX with Pgp

requiring the use of MX will be more effective if it is combined with the XA-containing dietary supplement.

The antioxidant and inhibition potency of molecule can be evaluated based on the values of appropriate thermodynamically parameters. On the other hand, it is always usefully if there is possibility to compare the parameters of the antioxidative capacity of investigated molecule, with the parameters of the antioxidativity of some well-known and often studied compound. For that purpose 1,2,4-trihydroxyanthraquinone is chosen, known as purpurin. This is antioxidant with moderate antioxidative capacity, but with numerous beneficial effects and vast applications. While XA can scavenge all of the three here considered radicals in both polar and non-polar conditions, for purpurin has been shown that reaction is thermodynamically plausible for all radicals in water, and in benzene only for hydroxyl radical [25]. In all cases enthalpies of reactions are lower for XA than for purpurin. The purpurin anion can be docked with Pgp, attaching this protein via amino acids Lys 884, Glu885, Gly 888, Ser 919 and Pro 923. The inhibition constant in the case of purpurin is 376.63 μM [25]. All of this indicates that XA exhibit higher antioxidative activity, but somewhat lower inhibition capacity than purpurin.

5 Conclusions

Estimation of the antioxidant potency of 1,2,4-trihydroxyxanthone (XA) was performed using DFT calculations. To imitate lipid and aqueous environment, as the most common reaction mediums in organisms, are used benzene and water as solvents. All conclusions are obtained based on the appropriate thermodynamically parameters of chemical behavior of investigated compound. The antioxidant capacity of polyphenolic antioxidants can be assessed based on its ability to generate stable radical form by the homolytic

cleavage of O-H bond. This process can follow several different mechanisms. It is concluded that the most favorable mechanism for that purpose for XA in benzene is HAT, while in water it is SPLET. SET-PT is not thermodynamically plausible mechanism. As the final product of all of here estimated mechanisms, can be obtained stable radical of investigated antioxidant. XA can generate three radical forms. The most stable is R4 radical, obtained by the cleavage of O4-H4 bond. It is the consequence of the highest spin density distribution in R4, in comparison with the spin density distribution in the R1 and R2 radicals. Moreover, the energy of the intramolecular hydrogen bonds, which contribute to the stability of obtained radical, is the highest for R4. In the presence of reactive oxygen species, polyphenolic antioxidants manifest its antioxidant capacity by the transfer of hydrogen atom from O-H group to the reactive free radical, which leads to the deactivation of free radical moiety. Here is investigated capacity of XA to deactivate hydroxyl ($HO^{\bullet}$), hydroperoxyl ($HOO^{\bullet}$) and methylperoxyl ($CH_3OO^{\bullet}$) radicals. It is found that in both solvents SPLET and HAT are thermodynamically possible reaction pathways, but in benzene SPLET is more favorable than HAT, while in water HAT is more plausible. SET-PT is inoperative mechanism under here estimated conditions. The reactivity of XA toward free radicals decreases following the order: $HO^{\bullet} \gg HOO^{\bullet} > CH_3OO^{\bullet}$. Results of docking analysis indicated that all of three anionic species that XA can generate in physiological conditions can be connected to the Pgp over the exactly same amino acids as the synthetic anthracene drug, mitoxantrone (MX). Therefore, it can be assumed than XA can act as inhibitor of Pgp, and decrease multiple drug resistance caused by Pgp. Comparing scavenger activity and inhibition capacity of XA with appropriate properties of structurally similar anthraquinone purpurin, one can conclude that XA is better antioxidant, but somewhat worse Pgp inhibitor than purpurin.

Acknowledgments. This work was supported by the Ministry of Education, Science and Technological Development of the Republic of Serbia (Projects No. 172015 and 174028).

References

1. Percival, M.: Antioxidants-a review. Clin. Nutr. Insights **31**, 201–205 (1998)
2. Jung, H.A., Su, B.N., Keller, W.J., Mehta, R.G., Kinghorn, A.D.: Antioxidant xanthones from the pericarp of *Garcinia mangostana* (Mangosteen). J. Agric. Food Chem. **54**(6), 2077–2082 (2006)
3. Chase, M., et al.: An update of the Angiosperm Phylogeny Group classification for the orders and families offlowering plants: APG II. Bot. J. Linn. Soc. **141**(4), 399–436 (2003)
4. Donnenberg, V., Donnenberg, A.: Multiple drug resistance in cancer revisited: the cancer stem cell hypothesis. J. Clin. Pharmacol. **45**(8), 872–877 (2005)
5. Marković, Z.: Study of the mechanisms of antioxidative action of different antioxidants. J. Serb. Soc. Comput. Mech. **10**(1), 135–150 (2016)
6. Galano, A., Mazzone, G., Alvarez-Diduk, R., Marino, T., Alvarez-Idaboy, R., Russo, N.: Food antioxidants: chemical insights at the molecular level. Annu. Rev. Food Sci. Technol. **7**, 335–352 (2016)
7. Knight, J.A.: Review: free radicals, antioxidants, and the immune system. Ann. Clin. Lab. Sci. **30**(2), 145–158 (2000)
8. Yoshida, Y., Umeno, A., Shichiri, M.: Lipid peroxidation biomarkers for evaluating oxidative stress and assessing antioxidant capacity in vivo. J. Clin. Biochem. Nutr. **52**(1), 9–16 (2013)

9. Frisch, M.J., Trucks, G.W., Schlegel, H.B., Scuseria, G.E., Robb, M.A., Cheeseman, J.R., Zakrzewski, V.G., Montgomery, J.J., Stratmann, R.E., Burant, J.C., Dapprich, S., Millam, J.M., Daniels, A.D., Kudin, K.N., Strain, M.C., Farkas, O., Tomasi, J., Barone, V., Cossi, M., Cammi, R., Mennucci, B., Pomelli, C., Adamo, C., Clifford, S., Ochterski, J., Petersson, G.A., Ayala, P.Y., Cui, Q., Morokuma, K., Malick, A.D., Rabuck, K.D., Raghavachari, K., Foresman, J.B., Cioslowski, J., Ortiz, J.V., Baboul, A.G., Stefanov, B.B., Liu, G., Liashenko, A., Piskorz, P., Komaromi, I., Gomperts, R., Martin, R.L., Fox, D.J., Keith, T., Al-Laham, M.A., Peng, C.Y., Nanayakkara, A., Challacombe, M., Gill, P.M.W., Johnson, B., Chen, W., Wong, M.W., Andres, J.L., Gonzalez, C., Head-Gordon, M., Replogle, E.S., Pople, J.A.: Gaussian 09, Revision B.01. Gaussian Inc., Wallingford (2009)
10. Zhao, Y., Truhlar, D.G.: The M06 suite of density functionals for main group thermochemistry, thermochemical kinetics, noncovalent interactions, excited states, and transition elements: two new functionals and systematic testing of four M06-class functionals and 12 other functionals. Theoret. Chem. Acc. **120**(1), 215–241 (2008)
11. Takano, Y., Houk, K.N.: Benchmarking the Conductor-like Polarizable Continuum Model (CPCM) for aqueous solvation free energies of neutral and ionic organic molecules. J. Chem. Theory Comput. **1**(1), 70–77 (2005)
12. Tošović, J., Marković, S., Milenković, D., Marković, Z.: Solvation enthalpies and Gibbs energies of the proton and electron – influence of solvation models. J. Serb. Soc. Comput. Mech. **10**(2), 66–76 (2016)
13. Aller, S., Yu, J., Ward, A., Weng, Y., Chittaboina, S., Zhuo, R., Harrell, P., Trinh, Y., Zhang, Q., Urbatsch, I., Chang, G.: Structure of P-glycoprotein reveals a molecular basis for poly-specific drug binding. Science **323**(5922), 1718–1722 (2009)
14. Humphrey, W., Dalke, A., Schulten, K.: VMD: visual molecular dynamics. J. Mol. Graph. **14**(1), 33–38 (1996)
15. Morris, G.M., Huey, R., Lindstrom, W., Sanner, M.F., Belew, R.K., Goodsell, D.S., Olson, A.J.: AutoDock4 and AutoDockTools4: automated docking with selective receptor flexibility. J. Comput. Chem. **30**(16), 2785–2791 (2009)
16. Fuhrmann, J., Rurainski, A., Lenhof, H.P., Neumann, D.: A new Lamarckian genetic algorithm for flexible ligand-receptor docking. J. Comput. Chem. **31**(9), 1911–1918 (2010)
17. BIOVIA Discovery Studio (2016). http://accelrys.com/products/collaborative-science/biovia-discovery-studio/. Accessed 07 May 2016
18. Marković, Z., Marković, S., Dimitrić Marković, J., Milenković, D.: Structure and reactivity of baicalein radical cation. Int. J. Quant. Chem. **112**(8), 2009–2017 (2012)
19. Marković, Z., Jeremić, S., Dimitrić Marković, J., Stanojević Pirković, M., Amić, D.: Influence of structural characteristics of substituents on the antioxidant activity of some anthraquinone derivatives. Comput. Theor. Chem. **1077**, 25–31 (2016)
20. Jeremić, S., Šehović, S., Manojlović, N., Marković, Z.: Antioxidant and free radical scavenging activity of purpurin. Monatshefte für Chemie - Chemical Monthly **143**(3), 427–435 (2012)
21. Jeremić, S., Filipović, N., Peulić, A., Marković, Z.: Thermodynamical aspect of radical scavenging activity of alizarin and alizarin red S. Theoretical comparative study. Comput. Theor. Chem. **1047**, 15–21 (2014)
22. Reed, A.E., Curtiss, L.A., Weinhold, F.: Intermolecular interactions from a natural bond orbital donor-acceptor viewpoint. Chem. Rev. **88**(6), 899–926 (1988)
23. Sharom, F.J.: ABC multidrug transporters: structure, function and role in chemoresistance. Pharmacogenomics **9**(1), 105–127 (2008)
24. Loe, D.W., Deeley, R.G., Cole, S.P.C.: Biology of the multidrug resistance-associated protein, MRP. Eur. J. Cancer **32**(6), 945–957 (1996)
25. Jeremić, S., Amić, A., Stanojević-Pirković, M., Marković, Z.: Selected anthraquinones as potential free radical scavengers and P-glycoprotein inhibitors. Org. Biomol. Chem. **16**(11), 1890–1902 (2018)

Medical Image Processing Using Xilinx System Generator

Tijana Šušteršič[1,2,3(✉)], Vladimir Milovanović[1], Vesna Ranković[1], Nenad Filipović[1,2,3], and Aleksandar Peulić[4]

[1] Faculty of Engineering, University of Kragujevac (FINK), Sestre Janjic 6, 34000 Kragujevac, Serbia
tijanas@kg.ac.rs

[2] Bioengineering Research and Development Center (BioIRC), Prvoslava Stojanovica 6, 34000 Kragujevac, Serbia

[3] Steinbeis Advanced Risk Technologies Institute doo Kragujevac (SARTIK), Kneza Milosa 25, 34000 Kragujevac, Serbia

[4] Faculty of Geography, University of Belgrade, Studentski trg 3, 11000 Belgrade, Serbia

Abstract. Although software implementations of different image processing techniques are suitable for general-purpose use, in order to meet the real time requirements, an image processing technique needs to be realized in hardware. Field Programmable Gate Arrays (FPGAs) have many benefits in applications that include digital signal acquisition, but also processing of large data, especially in real time. Mainly due to the ever-decreasing cost and re-configurability, FPGAs have also found its place in digital signal processing (DSP). Xilinx System Generator is a tool from Xilinx that enables the Mathworks Simulink models to be adapted for FPGA design. For comparative study on several levels in edge detection, CT image of a brain with a tumor is used. Performances of gradient based edge detectors - Robert, Prewitt and Sobel were compared. Even from just visual analysis of results, it can be seen that Prewitt and Sobel methods give better results than Robert method. In contrast, the calculation of Robert operator is simpler in comparison to the other operators and occupies less resources, since only adder-subtractor logic is sufficient to detect the edges. As the implemented algorithms could be part of more complex systems for tumor detection, the design architecture used in this paper can be extended to be used in very complex real time image processing techniques.

1 Introduction

FPGAs have many benefits in applications that include acquisition of digital data, but also processing of large data, especially in real time [1]. Mainly due to the ever-decreasing cost and re-configurability, FPGAs have also found its place in digital signal processing (DSP) [2]. Image processing requires the manipulation of pixels within a digital image to suit the different purposes - filtering [3], medical imaging [4], image compression [5], wireless communication [6], target recognition, video surveillance, robotics application, etc., where high speed parallel data processing is the main request. The parallelism that FPGAs offer, allow processing of images in real time, reducing processing time. The main

N. Filipovic (Ed.): ICCB 2019, LAIS 11, pp. 104–116, 2020.
https://doi.org/10.1007/978-3-030-43658-2_10

drawback of FPGAs is the low level language coding that requires a lot of time to produce a final product, as well as the time needed to redesign the system if there are any requests for that [2].

There are a number of processes that are part of the image processing techniques. Some of them are acquisition, enhancement, restoration, segmentation and analysis that are probably part of every application involving image processing [5]. Mohammed et al. [2] analyzed digital images and processing techniques, specifically point processing algorithms. Hanisha et al. [7] investigated image denoising algorithm with the help of Xilinx System Generator in co-simulation of both software and hardware. Kumar et al. [8] investigated various image processing operations on FPGAs by using Matlab – Simulink coupled with Xilinx system generator tools to convert the image into suitable formats for further processing. A typical image processing flow was used - reading an image from file, image preprocessing, main image processing techniques, post-processing and visual output [8].

Going back to the real time image processing, writing thousands of code lines for image processing using low level language is impractical and time consuming. Therefore for that purpose a tool called Xilinx System Generator (XSG) [1], coupled with graphical interface Simulink in Matlab is used to produce software environment for hardware description [1, 9, 10].

Xilinx System Generator [9] is a tool from Xilinx that enables the coupling between the Mathworks Simulink models to be adapted for FPGA design. Basically, Xilinx specific Blockset are added to the DSP friendly Simulink environment for higher level design [2, 11]. A high-level graphical interface under the Matlab - Simulink makes it very easy to work with in comparison to the other software for hardware description [12]. Downstream FPGA implementation steps such as synthesis and place and route are automatically performed from the Simulink environment to generate *bitstream* FPGA programming file. I/O planning and Clock planning can also be done in order to implement for JTAG hardware co-simulation. After this, a netlist is generated and a draft for the model and programming file in VHDL/Verilog is created.

As already mentioned, designs are made using DSP friendly Simulink modelling environment using a Xilinx specific Blockset [11]. The library of Xilinx System Generator includes over 90 DSP building blocks, allowing faster prototyping and design from a high-level programming stand point [2, 9, 10]. The prerequisite of using System Generator is to have compatible versions of Matlab and System Generator; the System Generator token available along with Xilinx has to be configured in Matlab in order to use the Blocksets [13].

2 Materials and Methods

Although software versions of different image processing technique suitable for general purpose use are available, in order to meet the real time applications, an image processing technique needs to be implemented in hardware [2]. In addition, the processing speed of software versions are sometimes not adequate when real-time applications are demanded, as well as when a large amount of information needs to be processed in a short period

of time (meaning throughput is higher) [14]. FPGA based application-specific hardware design provides higher processing speed in comparison to the equivalent software implementation taking the advantage of architectural parallel nature [14].

This led to the motivation for this paper where we used Matlab/Simulink coupled with Xilinx System Generator tool to preform several image processing algorithms that can be used as intros to the more complicated techniques in medical and biomedical applications. Vivado System Generator 2016.4 was used, and Matlab version was 2016b. The design flow of hardware implementation of image processing using XSG is given in Fig. 1.

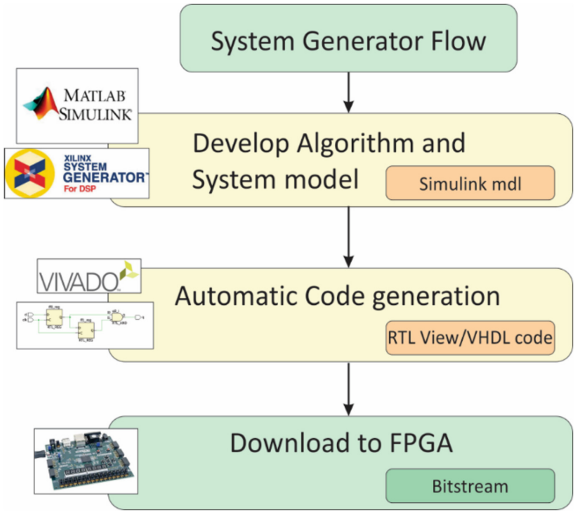

Fig. 1. Design flow of hardware implementation of image processing using XSG

2.1 Software Co-simulation

In Software co-simulation all Xilinx blocks are connected between two blocks - Gateway In and Gateway Out, which behave as input and output respectively for the hardware design [15]. Because Xilinx blocks work with fixed point format, there is a need to convert real world signals, written using floating point, into fixed point and vice versa. Gateway In and Gateway Out blocks act in this sense as translators for converting the signals from one format to another [1, 10, 15].

In order to read the source file and later see the output (image), simple Simulink block sets such as Image Source and Image Viewer can be used [2]. Image pre-processing and image post-processing units are the same independently of the image processing application, and are designed using Simulink blocksets [2, 7]. Image pre-processing subsystem consists of several blocks – Image from file, Transpose, Convert 2-D to 1-D, Frame conversion and Unbuffer (Fig. 2).

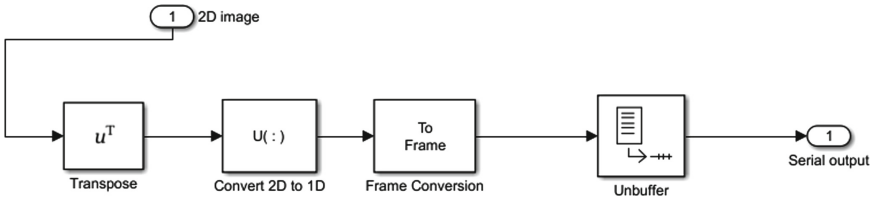

Fig. 2. Image pre-processing module

Since a grayscale image is M-by-N array, where M represents number of rows and N represents number of columns, Image from file block is used to read the representative image matrix [8]. Analogously, a color image would be represented by M-by-N-by-P array, where M and N are rows and columns respectively in each P color plane. Transpose block is used to transpose block from M-by-N matrix to N-by-M matrix. Block Convert 2-D to 1-D serves, as the name itself reads, to convert 2-D image matrix to 1-D (serial) array. Frame conversion has two possibilities – to set the output sampling mode to frame based or sample based and help prepare the data for un-buffering. Unbuffer block unbuffers an M-by-N input into a 1-by-N output, where inputs are unbuffered row wise.

Image post-processing subsystem consists of several blocks again - Data type conversion, Buffer, Convert 1D to 2D, Transpose, Video viewer (Fig. 3).

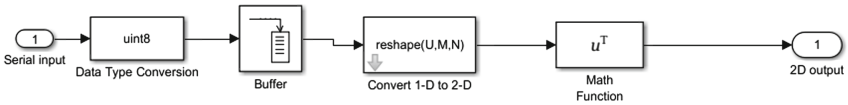

Fig. 3. Image post-processing module

These block help in reconstruction of the image based on 1-D array. First block - Data type conversion is used to convert image signal to different formats, where unsigned integer is used here. Buffer block performs frame-based processing, producing an output with a different frame size by redistributing the data in each column of the input. It should be noted that buffering a signal to a larger frame size would yield an output with a slower frame rate than the input [8]. In order to display the image back on the screen using the Video Viewer, Block Convert 1D to 2D is used to transform 1-D array back to 2-D image matrix.

Further in the text, edge detection algorithms are applied on CT images of brain from real patient. The images were in DICOM format with a tumor in the brain mass. We wanted to show that edge detection is useful in these situations where tissue of interest should be extracted.

2.2 Image Edge Detection

Edge in an image is defined as a point where sharp change in an image exists, where pixel locations have abrupt change in brightness, meaning discontinuity in gray level values. Therefore, edge detection in image processing means identifying and localizing

regions in which these brightness transitions exist [10, 15, 16]. Usually, edge detection techniques are implemented using software, however with the advancement in Very Large Scale Integration (VLSI) technology, hardware implementation of edge detectors has taken over a role in real-time applications [15].

Gradient-based techniques are mostly used for edge detection. They are looking for an edge by finding maximum and minimum in the first derivative of the image. The main edge detection operator is a matrix area gradient operation, which determines the level of variance between different pixels. Then, the edge detection operator is calculated by forming a matrix centered on a pixel that is chosen as the center of the matrix area. If the value of this matrix area is above a given threshold, the middle pixel is classified as an edge [17]. In the sense of mathematical operations, edge detection in image processing means masking operation with suitable filter mask, meaning the input image is convolved with any of the above mentioned filter masks [1].

Application of an edge detection algorithms decreases the amount of details that need to be processed and clears the details that are considered as less important without changing any properties of the image [14]. As a result, many researchers have investigated edge detection algorithms for different purposes. Fuad et al. [15] performed a comparative study of edge detection technique and implemented Canny Edge Detection Algorithm using Xilinx System Generator on a Nexys3 Board. Kabir et al. [14] also implemented another method for edge detection - Sobel edge detection in hardware. Although different edge detection methods are available as software implementations such as Roberts, Prewitt, Sobel method, software versions are suitable for general purpose use. Therefore, according to the motivation for the paper, we further analyze several gradient-based methods for edge detection and implement them in hardware using Xilinx System Generator.

For a given image I, in order to calculate horizontal and vertical gradient of each pixel I(x, y), Eqs. 1–2 are applied according to [18]:

$$G_x(x, y) = horizontal\_mask * I(x, y) \tag{1}$$

$$G_y(x, y) = vertical\_mask * I(x, y) \tag{2}$$

In each pixel (x, y), the horizontal and vertical gradients are combined as in (3), in order to obtain the gradient value:

$$G(x, y) = \sqrt{G_x(x, y)^2 + G_y(x, y)^2} \tag{3}$$

Usually, an approximation of the magnitude is calculated as:

$$G(x, y) = |G_x(x, y)| + \left|G_y(x, y)\right| \tag{4}$$

Where G_x and G_y are the gradients in the x- and y-directions respectively. The orientation of the gradient is calculated as:

$$\theta(x, y) = arctan\left(\frac{G_y(x, y)}{G_x(x, y)}\right) \tag{5}$$

In a lot of real-world applications, Canny method is dominant due to its good localization performance and ability to extract significant edges very well. However, the Canny algorithm consists of extensive pre-processing such as smoothing, as well as post-processing steps such as Non-Maximum Suppression (NMS). It is also more computationally complex than other gradient-based edge detection algorithms such as Roberts, Prewitt and Sobel algorithms [15, 19, 20]. As a result, we will focus on less computationally complex gradient based edge detection methods and compare their performance, resource utilization, performance time, etc.

Robert Method

The main idea behind the Robert method is the use of Robert operator [17]. It is a type of a differential operator that approximates the gradient of an image using discrete differentiation computing the sum of the squares of the differences between diagonally adjacent pixels implemented by two 2 × 2 kernel (mask) written in (6) [1].

$$G_x = \begin{bmatrix} 1 & 0 \\ 0 & -1 \end{bmatrix} \text{ and } G_y = \begin{bmatrix} 0 & 1 \\ -1 & 0 \end{bmatrix} \tag{6}$$

Masks are usually applied separately to the input image, in order to produce separate measurements of the gradient component in x and y direction (G_x and G_y). Local gradients are used by convolving mask coefficients with every pixel. And if we declare p1, p2, p3, p4 as image pixels and G_x and G_y are masks for horizontal and vertical gradient filter respectively, formulas for gradient calculation in both directions are [17, 21] given by:

$$|Gx| = |p1 - p4| \text{ and } |Gy| = |p2 - p3| \tag{7}$$

They are then combined together in order to find the absolute magnitude of the gradient at each point using (4). The design methodology of edge detection using Xilinx System Generator for using Robert algorithm is shown in Fig. 4.

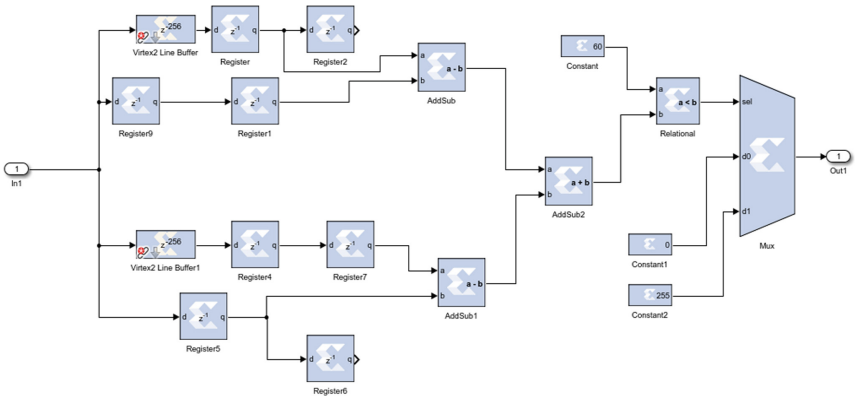

Fig. 4. System Generator DSP sub-model for edge detection using Robert method

Prewitt Method

The main idea behind the Prewitt method is the operator that uses central difference and is considered better than Roberts's operator. Image is convolved with a kernel in horizontal and vertical direction given in (8) [1].

$$G_x = \begin{bmatrix} -1 & 0 & 1 \\ -1 & 0 & 1 \\ -1 & 0 & 1 \end{bmatrix} \quad G_y = \begin{bmatrix} 1 & 1 & 1 \\ 0 & 0 & 0 \\ -1 & -1 & -1 \end{bmatrix} \tag{8}$$

Prewitt edge detection uses moving masks over an image to compute gradient of image. If we define p1, p2, p3,….p9 as image pixels and Gx and Gy are masks for horizontal and vertical gradient filter respectively, then the formulas used for gradient calculation are given as (9) [17, 21]:

$$\begin{aligned} |Gx| &= |(p3 + p6 + p9) - (p1 + p4 + p7)| \\ |Gy| &= |(p7 + p8 + p9) - (p1 + p2 + p3)| \end{aligned} \tag{9}$$

Because of its kernel, Prewitt's method is less vulnerable to noise [1]. The design methodology of edge detection using Xilinx System Generator for using Prewitt algorithm is shown in Fig. 5. Only horizontal mask is presented, but vertical mask is created in the same way analogously.

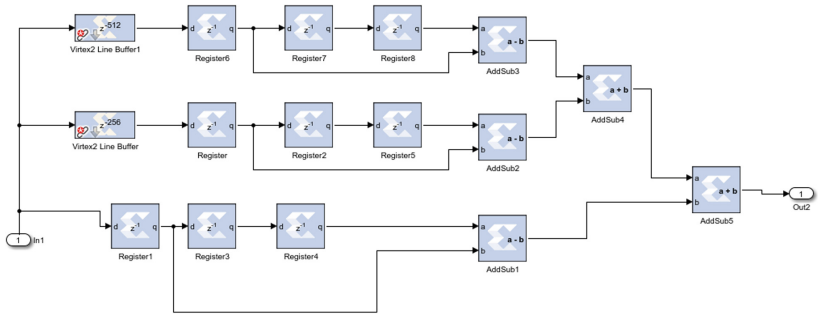

Fig. 5. Simulink – System Generator DSP sub-model for horizontal mask in edge detection using Prewitt method

Sobel Method

The Sobel operator is similar to the Prewitt operator based on central difference, but more weights are put to the central pixels, and mask is therefore given as [1]:

$$G_x = \begin{bmatrix} -1 & 0 & 1 \\ -2 & 0 & 2 \\ -1 & 0 & 1 \end{bmatrix} \quad G_y = \begin{bmatrix} 1 & 2 & 1 \\ 0 & 0 & 0 \\ -1 & -2 & -1 \end{bmatrix} \tag{10}$$

These kernels are created to respond maximally to edges that are vertical and horizontal relatively to the pixel grid, where one kernel is used for each direction x and y. These

kernels can be applied separately on the input image, in order to produce separate calculations of the gradient components in each direction [17]. Same as with other methods, moving masks for Sobel edge detection over an image computes the gradient of image. If we define p1, p2, p3,….p9 as image pixels and Gx and Gy are masks for horizontal and vertical gradient kernels, formulas for gradient calculation are given by [17, 21].

$$|Gx| = |(p3 + 2 \times p6 + p9) - (p1 + 2 \times p4 + p7)|$$
$$|Gy| = |(p7 + 2 \times p8 + p9) - (p1 + 2 \times p2 + p3) \tag{11}$$

Sobel method has the improved noise suppression and is one of the simple operators which gives very good results [18]. The design methodology of edge detection using Xilinx System Generator for using Sobel algorithm is shown in Fig. 6. Only vertical mask is presented, but horizontal mask is created in the same way analogously.

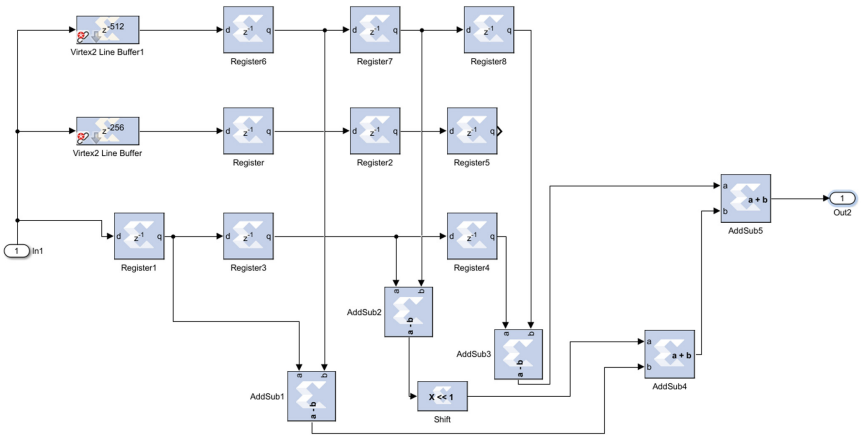

Fig. 6. Simulink – System Generator DSP sub-model for vertical mask in edge detection using Sobel method

2.3 Thresholding Method

After the edge-detection algorithm is applied, it is necessary to determine the strength of the boundaries, as some edges detected may not be the actual edges. One way to achieve this is the use of threshold. Thresholding is done in such a way that each pixel with greater value than the threshold is identified as strong edge and edge pixels weaker than the threshold are deleted, meaning the following formula is applied [8, 15]:

$$F(x, y) = \begin{cases} 255, \text{if } f(x, y) > T \\ 0, \qquad \text{otherwise} \end{cases} \tag{12}$$

where T is the assigned threshold. In the sense of implementation, a Mux is used for comparison and replacement of the pixels with the new values.

2.4 Hardware Co-simulation

The starting point in hardware co-simulation is the generated System Generator model that now needs to be transferred to hardware. After software simulation, System Generator token needs to be configured to allow the model to be compiled into hardware [2]. System Generator token dialog box needs to be configured with adequate settings for compilation, synthesis and clocking. Firstly, compilation Target needs to be chosen by specifying the FPGA platform that will be used. Secondly, synthesis tool is involved in synthesizing the design (settings are hardware language, creating test bench and design that is synthesized and implemented) and clocking tab (settings are period of the system clock (in nanoseconds) and pin location for hardware clock) [1, 2, 7].

Once the block is configured using the aforementioned settings, a bit stream (.bit) file is generated. After the bitstream file is generated, hardware co-simulation target is selected and a block will be generated. For our purposes Artix 7 AC701 Evaluation Platform 1.0 (with the chip xc7a200t-2fbg676) is chosen to test the algorithms. This block can be then added to the design and all the blocks for both software and hardware now co-exist. The complete design with the hardware and software co-simulation subsystems for the edge detection using Sobel method is presented in Fig. 7. All the other designs are created accordingly.

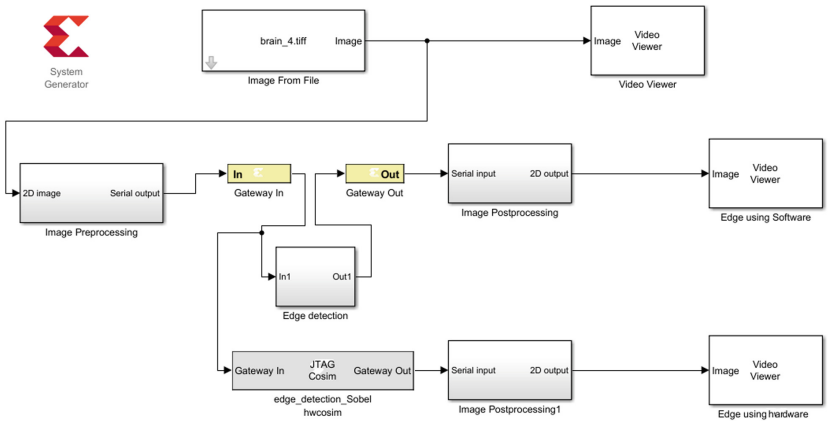

Fig. 7. Software and hardware co-simulation model for the edge detection using Sobel method

3 Results and Discussion

For comparative study on several levels in edge detection, 8 bitmedical images of brain with a tumor are used. Gradient based edge detectors Robert, Prewitt and Sobel performance was compared. Even from just visual analysis of results shown in Fig. 8, it can be seen that Prewitt and Sobel methods give better results than Robert method. In contrast, the calculation of Robert operator is simpler in comparison to the other operators, since only adder-subtractor logic is sufficient to detect the edges.

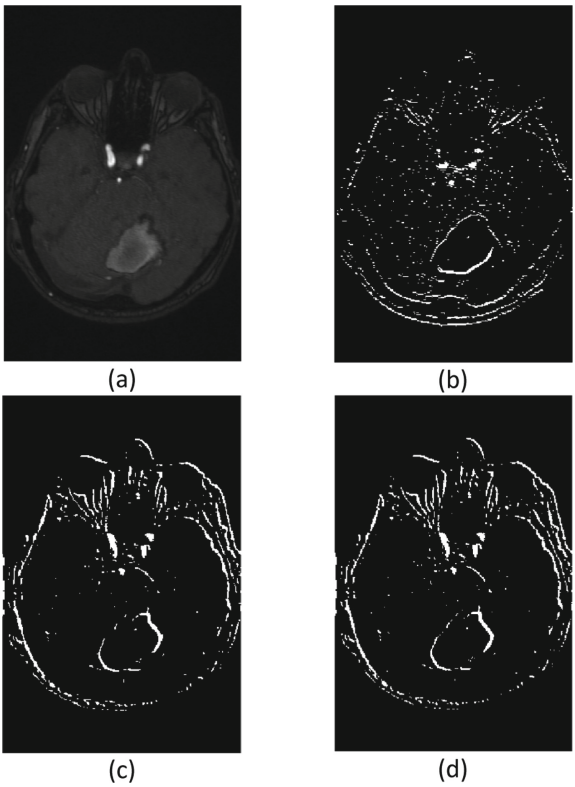

Fig. 8. Original image (a) compared with output images after application of algorithm for edge detection using Robert (b), Prewitt (c) and Sobel (d) methods

Prewitt and Sobel become noise prone depending on the threshold used and some false edges are detected. With the constant threshold, Sobel seems to detect more false edges, and the output is visually better using Prewitt method. After testing with several images with different contrasts it is concluded that Robert method was more efficient in images with lower contrast and presence of noise is reduced. By observation, in the sense of number of edges, it can be also seen that Sobel gives maximum edges whereas Robert provides minimum edges. Sobel operator emphasizes on central pixels and that is why the edges are thicker in comparison to the Robert method.

After this, median filtering was applied and output results both using Prewitt (Fig. 9) and Sobel method before and after filtering show some improvements in terms of noise reduction.

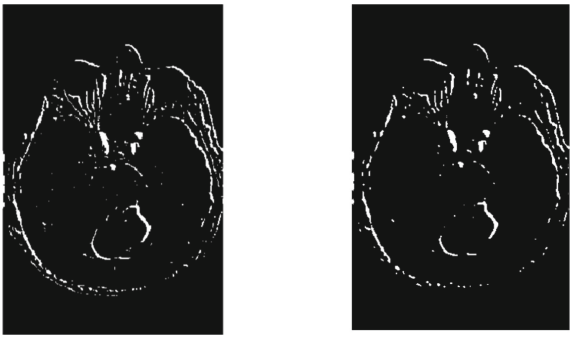

Fig. 9. Output images - algorithm for edge detection using Prewitt methods before (left) and after (right) filtering

All the designs are synthesized and implemented using Xilinx Vivado 2016.4. Table 1 shows a comparative analysis of three analyzed gradient-based edge detection techniques with respect to resource utilization. Since resource utilization explains the complexity of the algorithm it can be seen that Robert is the simplest and Prewitt and Sobel are more complex algorithms. Generally, gradient based classical operators have low latency and high throughput and are used in applications where image processing ne ed to be done in real time [21]. They are the choice when it comes to applications in which accuracy is not a major issue (i.e. monitoring, barcode reader). However, in the field of biomedical or machine vision, additional tools need to be applied in order to increase the accuracy.

Table 1. Post Synthesis resource utilization summary

Edge detection method	BRAMs	LUTs	Registers
Robert method	1	74	112
Prewitt method	1.5	224	266
Sobel method	1.5	224	266
hw_wrapper	2	892	1030

Table 2 provides a comparative analysis regarding the timing paths for the analyzed gradient-based edge detection techniques. Frequency of the clock was 100 MHz. All three algorithms have passed the Timing path analysis without any violations. It can be seen that number of paths reported in Timing analysis when Robert method is used is 8, while with Prewitt and Sobel it is 19.

Therefore, in applications in which medium range contrasted images are of primary concern, Sobel and Prewitt seem to be more adequate.

Table 2. Post Synthesis Timing paths

Edge detection method	Max_Slack (ns)	Min_Slack (ns)	Max_Delay (ns)	Min_Delay (ns)	Number of paths
Robert operator	18.9744	16.9778	2.77057	0.635	8
Prewitt operator	18.9744	16.9778	2.77057	0.635	19
Sobel operator	18.9744	16.9778	2.77057	0.635	19

4 Conclusions

The need for fast prototyping tools such as Xilinx System Generator and Matlab Simulink are very important nowadays due to time-to-market constraints. Xilinx System Generator tool enables the image processing to be created using friendly environment design as processing units are represented by blocks. In addition, not only this tool supports software simulation, but is very efficient in synthesis in FPGAs hardware, allowing the parallelism, robustness and speed to be fully exploited. Some of the feature gains of Simulink/Xilinx System Generator in FPGA design are fast time-to-market for image processing algorithms (development cycle from algorithm to hardware is shortened); user friendly interface (easy to organize system and divide it into subsystems); flexible modelling and simulation (design is easy to debug); easier transfer form software to hardware (the generator creates all necessary files for implementation in Xilinx FPGAs with the possibility to control resource and timing utilization).

In this paper, real-time image processing algorithms for edge detection and thresholding are implemented on FPGA. They are compared in relation to the resulting accuracy, resource utilization, power consumption, maximum frequency etc. The results show that Robert is the most efficient with respect to resource utilization, as only adder-subtractor logic is used, while Prewitt and Sobel have higher accuracy.

The advantage of implementing these algorithms on a FPGA is the full use of large memory, embedded multipliers and creating application-specific hardware design, which provides higher processing speed. As the implemented algorithms could be part of more complex systems, the design architecture used in this paper can be extended to be used in very complex real time image processing systems.

Acknowledgments. This study is supported by the grants from the Serbian Ministry of Education, Science and Technological Development III41007 and OI174028.

References

1. Reddy, G.B., Anusudha, K.: Implementation of image edge detection on FPGA using XSG. In: International Conference on Circuit, Power and Computing Technologies (ICCPCT), Nagercoil, India, March 2016, pp. 1–5. IEEE (2016)

2. Mohammed, A., Rachid, E., Laamari, H.: High level FPGA modeling for image processing algorithms using Xilinx system generator. Int. J. Comput. Sci. Telecommun. **5**(6), 1–8 (2014)
3. Hasan, S., Yakovlev, A., Boussakta, S.: Performance efficient FPGA implementation of parallel 2-D MRI image filtering algorithms using Xilinx system generator. In: 7th International Symposium on Communication Systems, Networks & Digital Signal Processing (CSNDSP 2010), Newcastle upon Tyne, July 2010, pp. 765–769. IEEE (2010)
4. Moses, C.J., Selvathi, D., Rani, S.S.: FPGA implementation of an efficient partial volume interpolation for medical image registration. In: International Conference on Communication Control and Computing Technologies, Ramanathapuram, India, October 2010, pp. 132–137 (2010)
5. Othman, M.F.B., Abdullah, N., Rusli, N.A.B.A.: An overview of MRI brain classification using FPGA implementation. In: IEEE Symposium on Industrial Electronics and Applications (ISIEA), pp. 623–628, Penang, Malaysia, October 2010. IEEE (2010)
6. Tana, H., Sazish, A.N., Ahmad, A., Sharif, M.S., Amira, A.: Efficient FPGA implementation of a wireless communication system using Bluetooth connectivity. In: Proceedings of 2010 IEEE International Symposium on Circuits and Systems, Paris, France, May 2010, pp. 1767–1770. IEEE (2010)
7. Hanisha, V., Kumari, G.V.: Hardware implementation of image denoise filters using system generator. Int. J. VLSI Syst. Des. Commun. Syst. **4**(10), 940–946 (2016)
8. Kumar, K.A., Kumar, M.V.: Implementation of image processing lab using Xilinx System Generator. Adv. Image Video Process. **2**(5), 27–35 (2014)
9. Xilinx: System Generator for DSP User Guide. Xilinx, USA (2009)
10. Gupta, A., Vaishnav, H., Garg, H.: Image processing using Xilinx System Generator (XSG) in FPGA. Int. J. Res. Sci. Innov. **2**(9), 119–125 (2015)
11. Raut, N.P., Gokhale, A.V.: FPGA implementation for image processing algorithms using Xilinx System Generator. IOSR J. VLSI Sig. Process. (IOSR-JVSP) **2**(4), 26–36 (2013)
12. Moreo, A.T., Lorente, P.N., Valles, F.S., Muro, J.S., Andres, C.F.: Experiences on developing computer vision hardware algorithms using Xilinx System Generator. Microprocess. Microsyst. **29**(8–9), 411–419 (2005)
13. Xilinx: Compatibilty Versions of System Generator for DSP with versions of Vivado Design tools," Xilinx (2019). https://www.xilinx.com/support/answers/55830.html. Accessed 25 Jan 2019
14. Kabir, S., Alam, A.A.: Hardware design and simulation of Sobel Edge Detection Algorithm. Int. J. Image Graph. Sig. Process. **6**(5), 10 (2014)
15. Fuad, K.A.A., Rizvi, S.M.: Hardware software co-simulation of Canny edge detection algorithm. Int. J. Comput. Appl. **122**(19), 7–12 (2015)
16. Gonzalez, R.C., Woods, R.E.: Digital Image Processing, vol. 3. Prentice Hall, Upper Saddle River (2008)
17. Yasri, I., bin Hamid, N.H., Yap, V.V.: An FPGA implementation of gradient based edge detection algorithm design. In: International Conference on Computer Technology and Development, Kota Kinabalu, Malaysia, November 2009, vol. 2, pp. 165–169. IEEE (2009)
18. Said, Y., Saidani, T., Smach, F., Atri, M.: Real time hardware co-simulation of edge detection for video processing system. In: 16th IEEE Mediterranean Electrotechnical Conference, Yasmine Hammamet, Tunisia, March 2012, pp. 852–855. IEEE (2012)
19. Xu, Q., Chakrabarti, C., Karam, L.J.: A distributed Canny edge detector and its implementation on FPGA. In: Digital Signal Processing and Signal Processing Education Meeting (DSP/SPE), Sedona, AZ, USA, January 2011, pp. 500–505. IEEE (2011)
20. Xu, Q., Varadarajan, S., Chakrabarti, C., Karam, L.J.: A distributed canny edge detector: algorithm and FPGA implementation. IEEE Trans. Image Process. **23**(7), 2944–2960 (2014)
21. Mahalle, A.G., Shah, A.M.: Hardware co-simulation of classical edge detection algorithms using Xilinx system generator. Int. Res. J. Eng. Technol. (IRJET) **5**(1), 912–916 (2018)

Computer Assisted Analysis of the Hepatic Spheroid Formation

Xhoena Polisi[1], Albana Halili[1,2], Constantin-Edi Tanase[3], Arban Uka[1(✉)], Nihal Engin Vrana[4,5], and Amir Ghaemmaghami[3]

[1] Computer Engineering Department, Epoka University, Tirana, Albania
{xpolisi,ahalili,auka}@epoka.edu.al
[2] Department of Information Technology, Aleksander Moisiu University, Durres, Albania
[3] School of Life Sciences, Faculty of Medicine and Health Sciences, University of Nottingham, Nottingham, UK
{constantin.tanase,amir.ghaemmaghami}@nottingham.ac.uk
[4] INSERM, UMR 1121, 11 Rue Humann Etage 7, 67000 Strasbourg, France
evrana@panbiora.eu
[5] Spartha Medical, Strasbourg, France

Abstract. Computer assisted techniques could enable the use of morphological characteristics of hepatic spheroids as surrogate for their response to various stimuli. The aim of this work is to develop an automatic analysis procedure able to correctly acquire all the important morphological parameters of the hepatic spheroids under static and after stimulation conditions. Within the datasets, several issues can occur related to the non-uniform illumination background and inherent limitation in counting the exact object number when two or more are adjacent. Some of the images include patterns with intensity comparable to the spheroid intensity, such as extended grooves, and they are filtered out based on their eccentricity values. Traditional methods such as Otsu threshold does not segment the spheroid images truthfully due to their energy minimization based approach. To circumvent this limitation initially background removal is applied as a preprocessing step. Filters applied for this depend on the relative size of the spheroids in order not to diminish the image quality. Therefore, we propose a guided automatic threshold value that can discriminate between the background and the spheroids more accurately by finding the critical peak on the pixel intensity histogram. Pixel intensity histograms are composed of three modes and the local minimum after the peak at the lowest values is the threshold value. After applying the new guided thresholding technique, watershed algorithm is used in order to determine the separating nodes between objects that are contiguous to each-other. These two techniques are compared with Gabor filters based methods that are shape based filters. Employing the three methods spheroid parameters including the number, area and the perimeter were determined and their performance and robustness are discussed.

Keywords: Spheroid culture · Segmentation · Guided thresholding

N. Filipovic (Ed.): ICCB 2019, LAIS 11, pp. 117–126, 2020.
https://doi.org/10.1007/978-3-030-43658-2_11

1 Introduction

Hepatic spheroids are the most appropriate model to represent multiple liver functions and toxicity range, providing better results than 2D monolayer with close similar response to the primary human hepatocytes. Many different tools and techniques have been developed to analyze the time dependence of hepatic functions, morphology stability etc. [1]. Imaging is one of the noninvasive techniques that provides important information on the size, shape and number as a function of time and drug exposure. Hepatic spheroids are an attractive model for *in vitro* genotoxicity assessment that closely mimics hepatic functions [2]. Therefore, there is an increase on the usage of hepatic spheroids on cancer research, for evaluation of anticancer drugs [3], modeling tissue biology [4]. Thurber et al. [3] predicted that the antibody-based cancer treatment dosage would be large enough to make a group of antibody overcome cellular internalization. The quantitative measurements were done using flow cytometry method where the counting of the nuclei under microscope in a known volume of tissue determined the cell density. Sirenko et al. used 3D liver spheroids derived from human iPS cells for toxicity assessment employing three dimensional image analysis of several parameters including spheroid size (volume) and shape, cell number and spatial distribution, nuclear characterization, number and distribution of cells. Dissanayaka et al. developed 3D microtissue spheroids of dental pulp cells (DPCs) and find the interaction characterization between DPCs and human umbilical vein endothelial cells (HUVECs) [5] and they report the formation of a favorable microenvironment.

The positive trend in the study of spheroids has been supported continuously by strong experimental evidence and this has led to the development of the all-in-one portable platforms and of the image processing algorithms for the analysis of high content imaging [6]. Optical microscopy and electron microscopy techniques have been widely used and often certain limitations have been overcome by carefully designed algorithms. Scanning electron microscopy (SEM) and transmission electron microscopy (TEM) have also be used for topology analysis, cellular organization, drug penetration etc. Another technique to study the shape/size of the 3D hepatic spheroids is flow cytometry however, the main requirement for this method is that the spheroids have to be in suspension. Currently research is oriented in developing new algorithms and also in developing automatic toolboxes or user-friendly graphical user interfaces (GUI) for researchers with limited knowledge in computer vision. AnaSP [7] and SpheroidSizer [8] are examples of these toolboxes. These two report the calculation of spheroid parameters. AnaSP one uses the largest spheroid in the image as a reference and reports its parameters, whereas SpheroidSizer is limited to calculating the parameters of a single spheroid per image. The latter uses active contours for the segmentation which is a robust to noise and non-uniform illumination but is time expensive.

Successful use of developed software is reported by Veelken et al. [9] who employ a combination between in vitro 3D spheroid invasion culture with irradiation and automated nucleus-based segmentation for single cell analysis. By combining all this information they could illustrate the degrees and types of therapy resistance in cancer cells.

Here, we present three different methods for spheroid image analysis in order to characterize their morphological properties. We propose solutions to challenges not commonly discussed in the literature of spheroid analysis. These challenges are represented by non-uniform background illumination, counting of contiguous spheroids, interfering patterns with spheroid-like texture features and halo creation. The first method analyzed consists of background removal as a pre-processing step followed by Otsu threshold. The second method proposes a new guided threshold technique. The third method is a modified version of the first method by adding also Gabor filters for spheroid detection.

On the second part, the image dataset and its challenges are described. All three methods are described in the Methods section. The results are shown in the fourth section, and a discussion about the image analysis done is reported in the fifth section and conclusions are presented in the last section.

2 Materials

Spheroids Formation and Culture

Terminally differentiated hepatic cells HepaRG™ (ThermoFisher) were maintained according to the supplier's in Williams' medium E with Glutamax I, supplemented with 10% fetal bovine serum, 100 IU/ml penicillin, 100 μg/ml streptomycin, 5 μg/ml bovine insulin, and 50 μM hydrocortisone hemisuccinate. At confluence HepaRG™ were harvested with TrypLE Express and seeded into Aggrewell™400 (StemCell Technologies) plates at a density of 6×10^5 cells per well. Following manufacturer protocol the plate was centrifuged at 100 g for 3 min followed by the incubation at 37 °C with 5% CO_2 for 72 h. HepaRG spheroids were harvested for seeding into the 96 ultra low attachment plate at a concentration of ~100 spheroids per well. At each time point (day 1, 2, 3, 4, 7, 10, 14, 17 and 21) media was replenished and images were acquired using a ZOE Fluorescent Cell Imager. The contrast in all the images is good and the spheroid size is larger than the rest of the objects that appear spuriously. Therefore the objects of interest can be easily detected by computerized techniques (see Fig. 1a). Since the contrast with the background is large, thresholding technique could be used to detect the objects. However, some images pose different challenges for a detailed analysis such as: (i) non-uniform background illumination (43% of the dataset), (ii) existence of two or more contiguous spheroids creating clusters, (iii) presence of patterns with texture and/or pixel intensity similar to the spheroids, and (iv) halo creation at the edges of the spheroids (see Fig. 1b). Halo effects are present when the light of optical microscopes produces a brighter outer boundary around the object thus reducing the measurable size parameters.

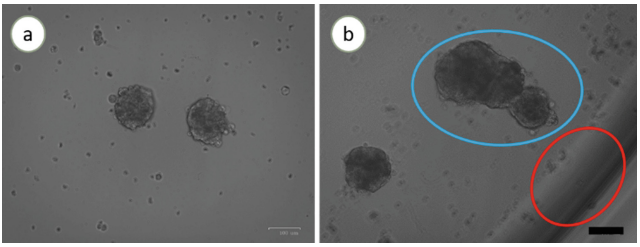

Fig. 1. (a) Hepatic spheroids and (b) the challenges of the dataset, clustering (blue) and edge of the well plate (red).

3 Methods

Threshold based techniques have been used widely as they are satisfactory in many different conditions. They can be applied both locally and globally depending on the illumination gradient. Otsu threshold automatically performs clustering-based image segmentation by determining the optimum threshold value that separates two distinct classes so that their intra-class variance is minimal. On their paper, Xu et al. [10] have shown that the value of Otsu threshold is equal to the average of the mean levels of two classes partitioned by this threshold. This approach is used in this work as two classes are identified: (i) the background as black and (ii) the spheroids as white. Counting the spheroids provides essential information and in order to differentiate the contiguous ones watershed segmentation is used. This technique finds "watershed ridge lines" by treating it as a surface where light pixels represent high elevations and dark pixels represent low elevations. Spheroid shape tends to be circular, so the eccentricity value tends to be towards the value 0. The pattern, in the contrary, has a more elliptical shape, so the eccentricity value tends to be towards the value 1. By using this property of the shapes of the objects, the pattern can be filtered by removing every object that has an elliptical shape.

Here in this work, we use three different methods for low density spheroids image analysis. The first method involves background removal as the preprocessing step followed by Otsu thresholding technique. The second method consists of guided thresholding technique which employs careful analysis of the histogram. The third method uses Gabor filters to detect spheroids after background removal is used as a pre-processing step. All these three methods use watershed segmentation to divide the adjacent spheroids from each other and in the end the morphological properties of the spheroids such as area, perimeter and eccentricity are extracted.

Method 1: Background Removal and Otsu Thresholding

It is known that applying smooth filters such as Gaussian filter etc. to original images blurs the image and the edges become less distinct. It is also known that subtracting the blurred image from the original one or vice versa depending on the case, it can enhance and stronger the edges of the objects. The above steps can be used with a small size kernel, i.e. from 3×3 to 7×7. The same filter class if used with a kernel size 3–6 times larger than the object of interest, can remove the background. This is the first method

proposed with the application of smooth filtering for background approximation and then subtracting the original image from it. This method uses the fact that the subtraction of the background will make the spheroids more visible and the illumination of the background will be attenuated. It uses the fact that too much smoothing can give us an approximation of the background, and then we subtract the original image from it (see Fig. 2). This new method looks like it solved the problem of the background illumination. Otsu threshold in this case looks like it makes a good differentiation of the background versus spheroids.

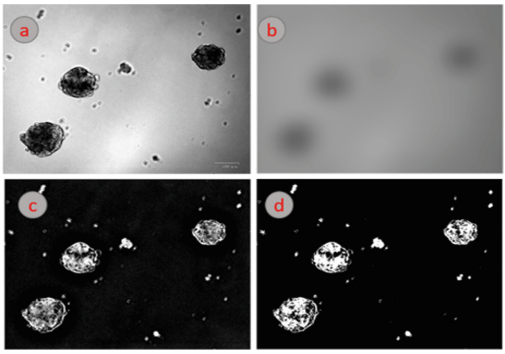

Fig. 2. Spheroid detection using background removal as the pre-processing step

Method 2: Using Guided Threshold Technique

Using Otsu method to separate the spheroids from the background without a pre-processing step does not provide the optimal threshold value. The histograms of the images were carefully analyzed and the best threshold values determined manually were compared with the values found by Otsu method. The new threshold values (shown in red in Fig. 3a) were smaller than the automatic ones (in blue). It was observed that the difference between these two values was not significant. The histograms exhibit tri-modal pattern and the correct threshold value is the first local minima considering that the spheroids are darker than the background. This new technique is denoted as guided threshold in this work.

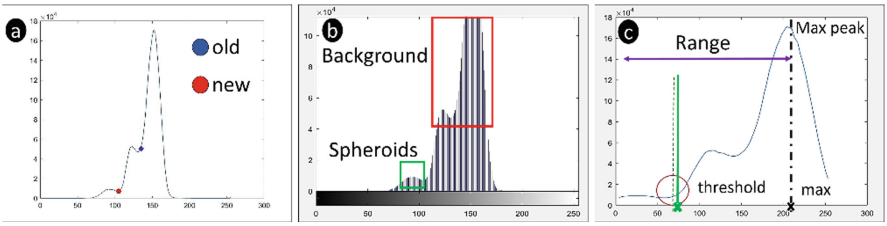

Fig. 3. Histogram analysis of an image and the different threshold values

Method 3: Using Gabor Filters to Detect the Spheroids

The third method follows the same preprocessing step of the first method to adjust the non-uniform background illumination. Then Gabor filters, a filter bank with different magnitudes and wavelength are employed to detect spheroids. Principal component analysis identifies the strongest features and enhances them more by multiplying its coefficients with the result image when constructing the final gabor magnitude (see Fig. 4).

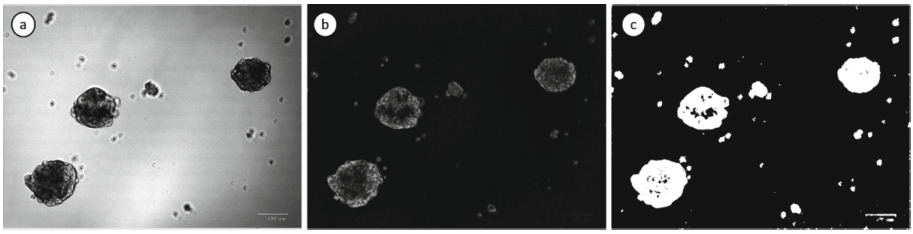

Fig. 4. Spheroid detection using Gabor filters

4 Results and Discussion

The algorithms are run on all images of the dataset and the results are given. As mentioned before, the newly developed threshold analysis technique is based on histogram analysis that proves to be very successful in a better segmentation. In Fig. 5, the segmentation results of both of these two techniques are shown. The guided threshold facilitates a better calculation of the area and perimeter of the spheroids.

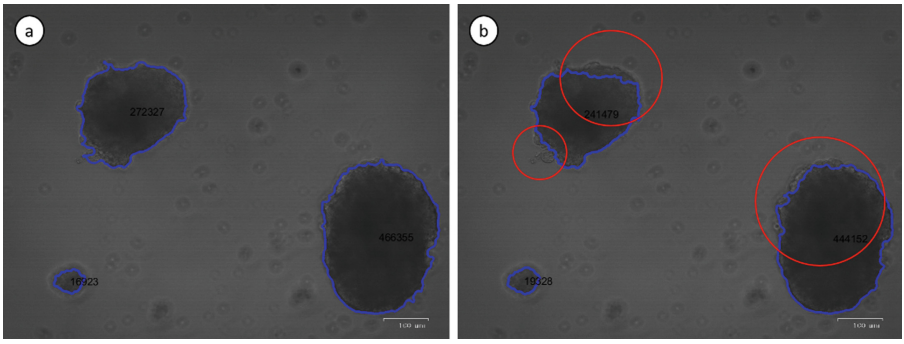

Fig. 5. (a) Spheroids detected by new guided threshold and (b) by the Background removal and Otsu thresholding

The third method employing Gabor filters proves to be more effective than the first two methods because of its inherent object shape-based detection ability. It also shows

better performance in minimizing the negative effects of the halo existence and is also more robust to the large variance of the quality of the images (see Fig. 6). Among the three methods, Gabor filters detects more noise objects, and needs to have a further object size filtering because the undesired objects have a similar (round) shape to the spheroids themselves.

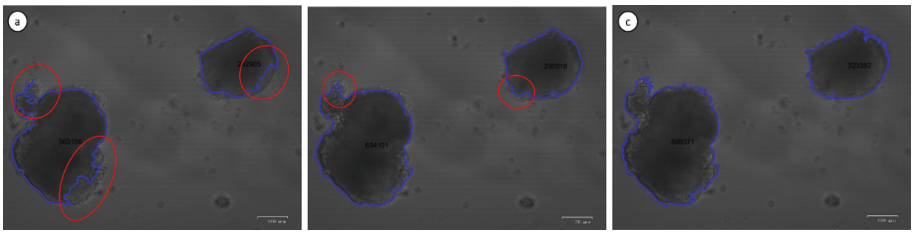

Fig. 6. (a) Background removal and Otsu thresholding, (b) new guided threshold and (c) using Gabor filters

All three methods are used on the images and then the morphological characteristics of the spheroids such as area, perimeter, radius and eccentricity are obtained as this provides a quantitative comparison among the three. Based on qualitative analysis of the figures above, a higher similarity between the results of the guided threshold and Gabor filters is expected and both of them would exhibit a more distinct superiority over the first method.

Results of important spheroid parameters as a function of time are shown in Figs. 7 and 8. Average of spheroid number and total area covered by the spheroids for all the images taken on the same day are reported in Fig. 7. The total area covered by the spheroids is found to be lower for the first method and the other two methods draw a more similar pattern. The average spheroid number does not change for the three different

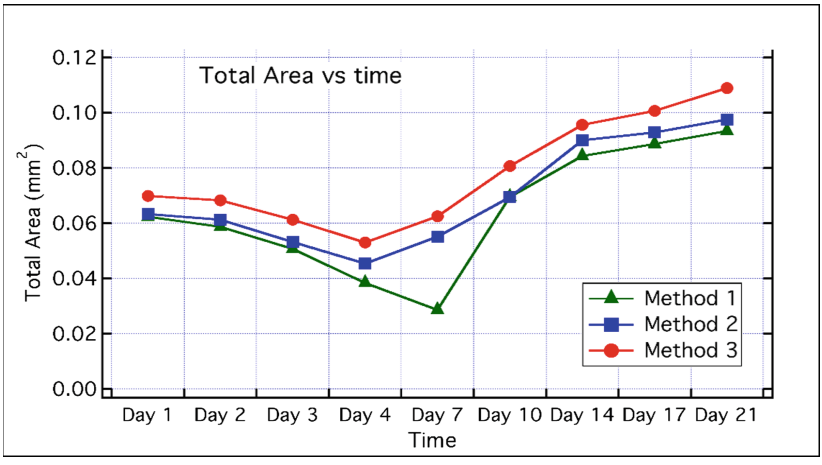

Fig. 7. Total area covered by spheroids as a function of time

methods. The difference in the total area found using the three methods depends mainly on the ability to determine the correct shape of the objects and the ability to minimize the halo effect.

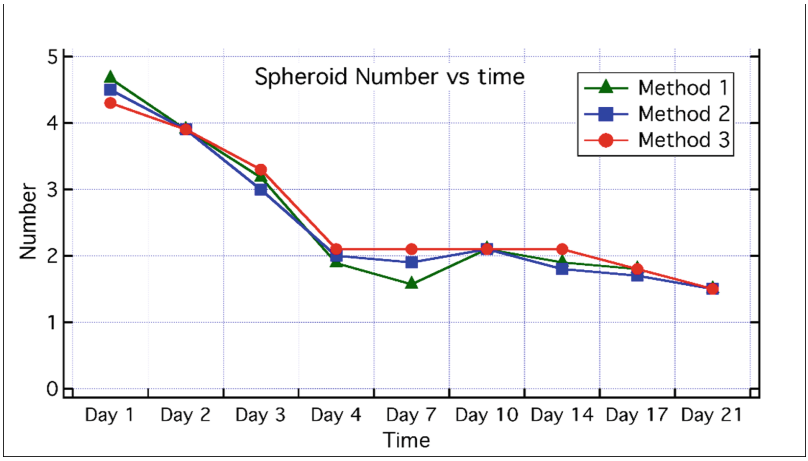

Fig. 8. Graph of the number of spheroids detected through time

When comparing the number of spheroids detected per each day, we see that all the algorithms show almost the same number. Since the number of spheroids comes from the fact how good watershed was able to differentiate adjacent spheroids, the trend is almost the same. There is a decrease of the number of spheroids from day 1 to day 21 (see Fig. 8).

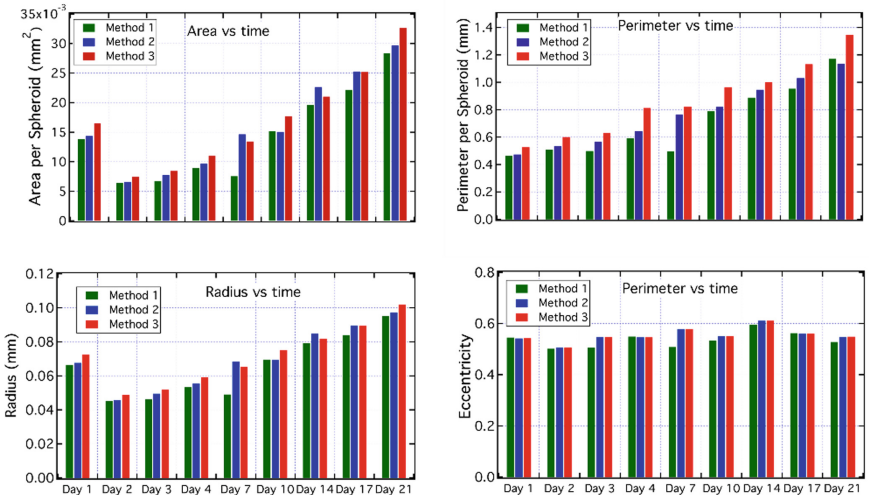

Fig. 9. Spheroids characteristics as a function of time

When comparing the individual characteristics of the spheroids through time, we may check the graphs below in Fig. 9. We notice the same rising trend after a drop in day 2 for the new guided threshold and the Gabor filters method for average spheroid area, perimeter and radius and the same values for eccentricity. Whereas using the first method, we notice a drop of the values in day 7. The values of eccentricity however, are very comparable to the other methods.

5 Conclusions and Future Work

In this work a thorough analysis of images from hepatic spheroids dataset was conducted. Different approaches are commonly used by researchers based on different challenges that depend on specific datasets. Here, a new threshold based technique is reported and this is compared with Otsu method and with the Gabor filter segmentation. The guided threshold technique is very robust to non-uniform background illumination that is a common challenge in the analysis of bright field images. Gabor filter segmentation was more robust than the other two to large variance of spheroid image features and can be conducted in an unsupervised manner. All methods were compared based on the quantitative outcomes of the morphological analysis of the spheroids. Both background removal method and the new guided threshold method are semi-automated on the part of the pattern filtering. This consists of manually changing some parameters for some images with uncommon features present such as the edges of the well. This problem is overcome by the third method (Gabor filters), which requires in only 3% of the images to change the noise object filtering parameter. In conclusion, the analysis of these algorithms enables an automatic investigation of high throughput data. Therefore, this platform can be a valuable asset used for assessment of 3D spheroid to evaluate the risk assessment of various compounds (drugs, biomaterials, etc.).

Acknowledgments. This project has received funding from the European Union's Horizon 2020 research and innovation program under grant agreement No 760921 (PANBioRA).

References

1. Mandon, M., Huet, S., Dubreil, E., Fessard, V., Le Hégarat, L.: Three-dimensional HepaRG spheroids as a liver model to study human genotoxicity in vitro with the single cell gel electrophoresis assay. Sci. Rep. **9**(1), 1–9 (2019)
2. Bovard, D., Sandoz, A., Luettich, K., Frentzel, S., Iskandar, A., Marescotti, D., Trivedi, K., Guedj, E., Dutertre, Q., Peitsch, M.C., Hoeng, J.: A lung/liver-on-a-chip platform for acute and chronic toxicity studies. Lab Chip **18**, 3814–3829 (2018)
3. Thurber, G.M., Wittrup, K.D.: Quantitative spatiotemporal analysis of antibody fragment diffusion and endocytic consumption in tumor spheroids. Cancer Res. **68**(9), 3334–3341 (2008)
4. Sirenko, O., Hancock, M.K., Hesley, J., Hong, D., Cohen, A., Gentry, J., Carlson, C.B., Mann, D.A.: Phenotypic characterization of toxic compound effects on liver spheroids derived from iPSC using confocal imaging and three-dimensional image analysis. Assay Drug Dev. Technol. **14**(7), 381–394 (2016)

5. Dissanayaka, W.L., Zhu, L., Hargreaves, K.M., Jin, L., Zhang, C.: In vitro analysis of scaffold-free prevascularized microtissue spheroids containing human dental pulp cells and endothelial cells. J. Endod. **41**(5), 663–670 (2015)
6. Costa, E.C., Moreira, A.F., de Melo-Diogo, D., Gaspar, V.M., Carvalho, M.P., Correia, I.J.: 3D tumor spheroids: an overview on the tools and techniques used for their analysis. Biotechnol. Adv. **34**(8), 1427–1441 (2016)
7. Piccinini, F.: AnaSP: a software suite for automatic image analysis of multicellular spheroids. Comput. Methods Programs Biomed. **119**(1), 43–52 (2015)
8. Chen, W., Wong, C., Vosburgh, E., Levine, A.J., Foran, D.J., Xu, E.Y.: High-throughput image analysis of tumor spheroids: a user-friendly software application to measure the size of spheroids automatically and accurately. JoVE (J. Visualized Exp.) **89**, e51639 (2014)
9. Veelken, C., Bakker, G.-J., Drell, D., Friedl, P.: Single cell-based automated quantification of therapy responses of invasive cancer spheroids in organotypic 3D culture. Methods **128**, 139–149 (2017)
10. Xu, X., Xu, S., Jin, L., Song, E.: Characteristic analysis of Otsu threshold and its applications. Pattern Recogn. Lett. **32**(7), 956–961 (2011)

Investigation of Coumarin Derivative 3-(1-*o*-toluidinoethylidene)-chromane-2,4-dione: IR Spectroscopic Characterization, NBO, and AIM Analysis and Molecular Docking Studies

Edina Avdović[1](✉), Dušan Dimić[2], and Dejan Milenković[1]

[1] Institute of Information Technologies, Department of Science, University of Kragujevac, 34000 Kragujevac, Serbia
edina.avdovic@pmf.kg.ac.rs

[2] Faculty of Physical Chemistry, University of Belgrade, Studentski trg 12-16, 11000 Belgrade, Serbia

Abstract. Various derivatives of coumarin have previously shown a wide range of biological activities. In this contribution, 3-(1-*o*-toluidinoethylidene)-chromane-2,4-dione (**1**) was analyzed by various theoretical techniques in order to understand the potential binding to anti-tumor target agents. The experimental IR spectrum was assigned and compared to theoretical in order to verify the applicability of applied DFT level of theory (B3LYP-D3BJH/6-311+G(d,p)). The Hirshfeld surface analysis (HSA) performed on the crystal structure of title compound allowed the analysis of inter-atomic interactions that lead to the crystal formation. The Natural Bond Orbital (NBO) and Quantum Theory of Atoms in Molecules (QTAIM) gave in-depth insight of the interactions governing the structure of molecule. Molecular docking towards UQCRB protein was used to investigate the possible interactions with proteins. The stability of molecules and various reactive positions make it a potential anti-tumor agent and further experimental studies are needed.

1 Introduction

Coumarin derivatives are compounds that basically contain a simple 2*H*-1-benzopyran-2-one structure. It was first isolated by Vogel in 1820 from Tonka wood in South America [1]. It should be noted that coumarin-based compound daphnin was isolated in 1812, from the plant *Daphne alpina* (*Thimelaeaceae*). However, the structure of that compound, namely (8-hydroxy-7-O-β-D-glucosylcoumarin), was solved in 1830. So today it can be safely said that daphnin was the first isolated coumarin [2–4]. Coumarin derivatives usually occur as secondary metabolites present in different parts of the plants: root, bark, tree, fruit and leaves [5–7]. More than 300 derivatives of coumarin have been identified from different natural sources such as plant families: *Rutaceae*, *Apiaceae*, *Asteraceae*, *Moraceae*, *Leguminosae*, etc. [8–10]. In addition to the plant world, some of the derivatives are isolated from microorganisms and animals [2–4].

N. Filipovic (Ed.): ICCB 2019, LAIS 11, pp. 127–142, 2020.
https://doi.org/10.1007/978-3-030-43658-2_12

Simple coumarin does not have pronounced biological activity, but its derivatives with numerous substituents at various positions such as hydroxyl, alkyl, benzoyl, furanyl, and pyranosyl groups, have a wide range of the biological and pharmacological activities: antibacterial, antifungal, antioxidant, anticoagulant, and cytotoxic [11–14]. In recent years coumarin derivatives have played a significant role in research in biochemistry, medicinal chemistry and bioorganic chemistry, because of their multi-biological activities. For example, it has been found that dicumarol from sweet clover, is a major cause of hemorrhagic disease, deadly to livestock. This compound in the plants is formed by the condensation of two molecules of 4-hydroxycoumarin via formaldehyde. Thanks to intensive research, it has been found that dicumarol has good anticoagulant properties [15]. In addition, numerous hydroxycoumarin derivatives are potential drugs today, they can be used in medicine as anticoagulants, cytostatics, antibiotics, etc. [13, 16–19].

The molecular docking studies have proved as very important tools for the analysis of interactions between coumarin derivatives and biologically important proteins [20, 21]. Ubiquinol-Cytochrome C Reductase Binding Protein (UQCRB) was chosen in this contribution because of its biological importance. This protein is involved in the transfer of electrons across the mitochondrial inner membrane and plays an important role in complex III stability [22]. In recent research, it was presented that down-regulation of this protein inhibits angiogenesis and suggested that UQCRB could be a novel therapeutic target for angiogenesis regulation [23]. The process of angiogenesis is responsible for embryonic development and tissue or organ regeneration. This process is important for the progression of tumors and hepatic fibrosis in pathological conditions, [24]. Application of small bioactive molecules that bind to the UQCRB suppresses hypoxia-induced tumor angiogenesis. This data demonstrates that UQCRB could be applied as a target agent in new approaches for human cancer and mitochondria-related disease investigation [25].

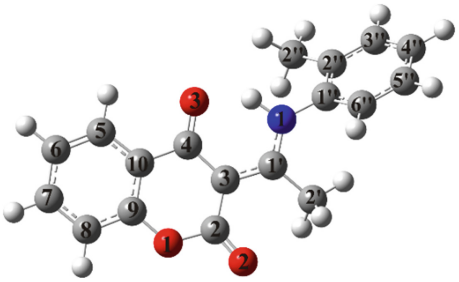

Fig. 1. Structure of 3-(1-*o*-toluidinoethylidene)-chromane-2,4-dione (**1**).

In our previous publications, syntheses of the new derivatives of 4-hydroxycoumarin and their cytotoxic and antimicrobial activity is described [26–31]. Some of these compounds showed excellent cytotoxicity on some cell lines as well as antimicrobial activity on some strains of microorganisms [26–29]. In this paper, due to the significant biological results of similar compounds, the reactivity of 3-(1-(*o*-toluidino)ethylidene)-chroman-2,4-dione (**1**) (Fig. 1) [28] will be tested against the UQCRB protein and analyzed by the Natural Bond Orbital (NBO), Quantum Theory of Atoms in Molecules (QTAIM), and Molecular Docking. Also, a detailed vibration analysis will be described from the

results obtained by comparing the experimental and simulated IR spectra to verify the applicability of the selected level of theory.

2 Materials and Methods

Starting compound 3-(1-o-toluidinoethylidene)-chromane-2,4-dione was obtained as previously explained. The IR spectrum was recorded on the Perkin-Elmer Spectrum One FT-IR spectrometer (KBr pellet technique, 4000–400 cm^{-1}).

Hirshfeld surface analysis was performed using CrystalExplorer17 [32] based on the experimental crystallographic structure of the compound **1** [28]. The geometry units were extracted from crystallographic information files (CIF) obtained from the Cambridge Crystallographic DatabaseCentre (CCDC No. 1817645). The Gaussian 09 program package [33] was used for the optimization of the structure of compound **1** and to create the wavefunction files containing the data needed for the Quantum Theory of Atoms in Molecules (QTAIM) analysis, based on the work of Bader [34, 35]. The Multiwfn program [16] was employed to process the wavefunction files for topology analysis of **1**. In addition, the Natural Bond Orbital analysis (NBO) was done using NBO 5.0 [36]. All density functional theory calculations were performed using the B3LYP-D3BJ functional in combination with a 6-311+G(d,p) basis set.

The AutoDock 4.0 software was used for the molecular docking simulation [37] according to the procedures described elsewhere [38–40]. The three-dimensional crystal structure of UQCRB was obtained from the Protein Data Bank (PDB IDs: 1BCC) [23, 27]. The preparation of protein for docking by removing the co-crystallized ligand, water molecules and co-factors was performed in the Discovery Studio 4.0 [41]. The AutoDockTools (ADT) graphical user interface was used to calculate Kollman charges and to add polar hydrogen. The investigated molecule (**1**) was prepared for docking by minimizing its energy at B3LYP-D3BJ/6-311+G(d,p) level of theory. The molecule was analyzed as a flexible ligand, while the protein remained as a rigid structure in the ADT. All bonds of **1** were set to be rotatable. The Geistenger method for calculation of partial charges was employed. The Lamarckian Genetic Algorithm (LGA) method was employed for protein-ligand flexible docking. For molecular docking simulation, the grid boxes with dimensions 20 Å × 20 Å × 20 Å of UQCRB protein were used in order to cover the protein binding site and accommodate ligand to move freely.

3 Results and Discussion

Vibrational Analysis

The geometry of the examined compound was optimized in the gas phase, using the B3LYP-D3BJ/6–311+G(d,p) theoretical model. It has been previously shown that this level of theory predicts well the vibrational spectra of similar compounds [27, 29]. The IR frequencies were calculated using the same level of theory. The experimental and simulated wavenumbers, together with the assignment, are shown in Table 1. The values of all calculated wavenumbers were higher than the experimental. The reason lies in experimental conditions (KBr pellet) and the fact that theoretical spectra were

simulated for molecules in the gas phase, therefore no intermolecular interactions were considered. The correlation between experimental and theoretical wavenumbers was performed to determine the correction factor. The calculated wavenumbers are scaled using factor 0.9670. The quality of this comparison is evaluated by obtained values of correlation coefficient (R = 0.999) mean absolute error (AAE = 4.26) and mean relative error (ARE = 0.60) which confirm that the theoretical model used describes well the vibrational motion and structure of the molecules (Table 1, Fig. 2).

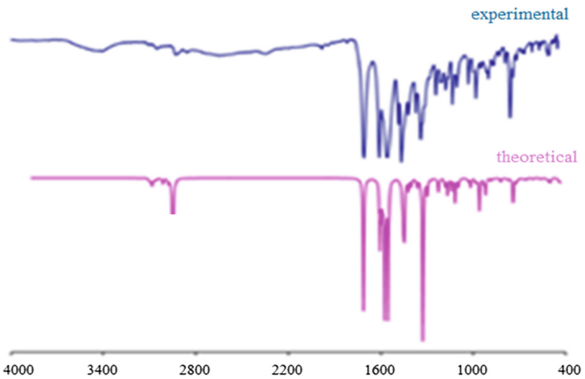

Fig. 2. The experimental and theoretical spectra of the investigated compound (calculated at B3LYP-D3BJ/6-311G+(d,p).

The comparison of theoretical and experimental IR spectra of **1** is shown in Fig. 2. There are three distinct regions in the presented spectra: between 4000 and 2000 cm^{-1}, between 2000 and 1000 cm^{-1}, and below 1000 cm^{-1}. The most pronounced bands in the IR spectrum in the high-frequency region (4000–2000 cm^{-1}) are assigned to different vibrational modes of the C–H and N–H groups. Considering the structure of the examined compound, the band positioned at 3405 cm^{-1} (Table 1) can be assigned to the absorption of hydrogen-bonded N–H group. The moiety O3–C4–C3–C1′–N1–H is observed in structurally similar molecules [26, 27, 29], and it is always described as important for stabilization. This is a so-called hydrogen bond formed by resonance [42]. In the theoretical spectrum the band belonging to N–H vibration is observed at lower wavenumbers due to the fact that molecule was analyzed in the gas phase, therefore no intermolecular interactions were possible. Low-intensity bands that are characteristic of C–H stretching vibrations (aromatic rings I and II, and methyl group) (3107, 3048, 2854, 2350 cm^{-1}) also occur in the high-frequency region (Table 1). The vibration contributions for normal stretching modes (PED values in Table 1), in the range 3405–2350 cm^{-1}, were awarded almost exclusively to N–H and C–H stretching modes (85–99%).

The most intense bands in the IR spectrum can be found in the range 2000–1000 cm^{-1}. These bands are positioned at 1710 cm^{-1} (C=O stretching), 1558 cm^{-1} (C=N stretching), and 1610 cm^{-1} (C–C stretching). Medium and strong bands belong to the bending modes H–C–C (1421 cm^{-1}) and H–C–H (1373 cm^{-1}). Weak bands at

1215, 1179, and 1136 cm^{-1} are assigned to the mixed modes that include C–C stretching, C–N–H and H–C–C bending vibrations. The values of experimental wavenumbers are well-reproduced in the theoretical spectrum with a difference of several cm^{-1}.

Bands that appear below 1000 cm^{-1} can be described as medium and weak. Medium bands are positioned at 904,795, 762, 721 and 669 cm^{-1} and they are due to the mixed vibrational modes including stretching (C–C (acyclic moieties)) and bending (C–C–C, H–C–C, H–C–H, C–N–C, and O–C–O) modes of the first and second benzene ring, aliphatic chain and pyrone ring, as well as combinations of different in-plane and out-of-plane (H–C–C–C, H–C–C–H, O–C–C–C) torsion vibrations. Weak bands are more numerous (Table 1, Fig. 2) and they include some of the previously mentioned vibrational modes.

Table 1. Comparison of the experimental and calculated vibrational wavenumbers and proposed assignments of **1** (scaling factor is 0.9670).

Mode	Experimental wavenumbers	Theoretical wavenumbers (cm^{-1}) B3LYP-D3BJ/6-311+G(d,p)		Vibrational assignments with PED (%)
	IR (cm^{-1})	Unscaled	Scaled	
	3405 w			$\nu_{NH\ (a)}(99)$
105	3107 vw	3207	3101	$\nu_{CH\ (b\text{-}I,\ b\text{-}II)}(99)$
97	3048 w	3158	3054	$\nu_{CH\ (-CH3\ (a))}(90)$
95	2854 w	3115	3013	$\nu_{CH\ (b\text{-}I,\ b\text{-}II)}(90)$
93	2350 w	3064	2963	$\nu_{CH\ (-CH3\ (a))}(85)$
92	1982 w	3050	2949	$\nu_{CH\ (a)}(95)$
90	1710 vs	1771	1713	$\nu_{C=O\ (p)}(90)$
89	1610 vs	1662	1607	$\delta_{CN\ (a)}(50)$
84	1558 vs	1606	1553	$\nu_{CC\ (b\text{-}I)}(50)$
76	1421 m	1470	1421	$\delta_{HCH\ (-CH3\ (a))}(59)$
72	1341 s	1373	1328	$\delta_{HCC\ (b\text{-}I)}(29)$
65	1215 w	1262	1220	$\delta_{CNH\ (a)}(30)$
64	1179 w	1225	1184	$\nu_{CC\ (p)}(48)$
61	1136 w	1181	1142	$\delta_{HCC\ (b\text{-}I)}(32)$
48	951 w	982	949	$\tau_{HCCH\ (b\text{-}I)}(30)$
45	904 m	917	887	$\delta_{CCC\ (p)}(20)$
44	875 w	894	864	$\delta_{CNH\ (a)}(40)$
43	866 w	882	853	$\tau_{HCCC\ (b\text{-}I,\ b\text{-}II)}(25)$
41	832 w	851	823	$\nu_{CC\ (\text{-}CH3\ (a))}(20)$
40	795 m	810	784	$\delta_{HCC\ (b\text{-}II)}(10)$ (b)
39	762 m	801	774	$\tau_{HCCH\ (b\text{-}I)}(40)$
36	721 m	748	723	$\tau_{HCCH\ (b\text{-}II)}(30)$

(*continued*)

Table 1. (*continued*)

Mode	Experimental wavenumbers	Theoretical wavenumbers (cm^{-1}) B3LYP-D3BJ/6-311+G(d,p)		Vibrational assignments with PED (%)
	IR (cm^{-1})	Unscaled	Scaled	
34	689 w	710	687	$\tau_{CCCO\ (p)}(40)$
33	680 w	700	677	$\tau_{HCCH\ (b\text{-}I)}(40)$
32	669 m	694	671	$\delta_{OCO\ (p)}(25)$
30	620 w	637	616	$\delta_{CCC\ (b\text{-}I,\ b\text{-}II)}(20)$
29	574 w	584	565	$\delta_{HCH\ (-CH3\ (a))}(30)$
21	456 w	452	437	$\delta_{HCC\ (b\text{-}II)}(30)$
R				0.999
AAE				4.26
ARE				0.60

a, b-I, b-II, p denote for alkyl side chain, benzene ring (I-first ring attached to pyrone ring and II-second ring attached to N atom) and pyrone moiety, $-CH_3$ stand for methyl moiety, ν – stretching modes; δ – bending modes; τ – torsional modes; vw – very weak; w – weak; m – medium; s – strong; vs – very strong)

Hirshfeld Surface Analysis

Hirshfeld surface analysis (HSA) was first proposed by Spackman and Byrom [43] and comprehensively reviewed in [44]. This method focuses on analyzing the so-called Hirshfeld surface (HS) to reveal weak interactions between monomers in molecular crystal. HSA, in fact, is a kind of inter-fragment (or inter-monomer) surface, which is defined based on the concept of Hirshfeld weight. Probably HS is the most reasonable way to define an inter-fragment surface. Hirshfeld weighting function of an atom can be expressed as:

$$w_A^{\mathrm{Hirsh}}(\mathrm{r}) = \frac{\rho_A^0(\mathrm{r})}{\sum\limits_B \rho_B^0(\mathrm{r})} \tag{1}$$

where ρ_A^0 denotes the density of atom A in free-state. Summing up the weight of all atoms in a fragment yields Hirshfeld weight of this fragment:

$$w_P^{\mathrm{Hirsh}}(\mathrm{r}) = \sum_{A \in P} w_A^{\mathrm{Hirsh}}(\mathrm{r}) \tag{2}$$

HS of fragment P is just the isosurface of $w_P^{\mathrm{Hirsh}} = 0.5$. HSs are built in a crystal structure based on the electron distribution calculated as the sum of spherical electron densities of an atom. Each point on the HSA represents two distances: (1) the distance from the nearest nuclei to the external surface (d_e) and (2) the distance from the nearest nuclei to the internal surface (d_i). The HSA is mapped with the normalized contact distance (d_{norm}) and regions of important intermolecular interactions are presented by

Graphical plots. The value of d_{norm} is represented by red, white, or blue when the intermolecular contacts are shorter, equal, or longer to the vdW separation of nuclei, respectively.

HSA was performed in order to get insight into the role of the intermolecular interaction in the stabilization of **1** via crystal packing. HSA (3D) and fingerprint plots (2D) were drawn by CrystalExplorer17 using an experimental structure input file (CIF) (Fig. 3) [28]. The most significant intermolecular interactions in the crystal lattice of the studied molecule, **1**, are listed in Table 2 and shown in Fig. 3. The intermolecular interactions, such as H···H, O···H and C···H contacts, play a crucial role in the crystal packing of molecule **1.** The H···H intermolecular interactions have the largest contribution in the crystal lattice (50.4%) and they play a major role in crystal lattice stability [45]. The minimum H···H contacts are 2.176 Å for molecule **1** (Table 2 and Fig. 3), respectively. It is important to mention that these contact distances are longer than twice the van der Waals radius of a hydrogen atom. These interactions are represented by a blue color in Fig. 3.

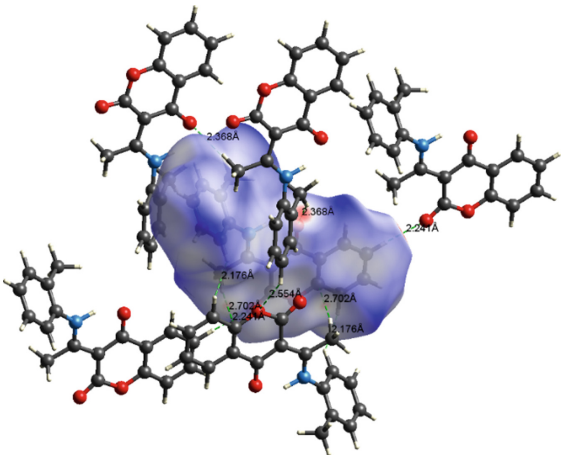

Fig. 3. Graphical plot of the most important intermolecular contacts in **1.**

Table 2. Summary of the most important intermolecular contacts and their percentage contributions in the crystal structure of the studied molecule **1**. The minimum contact distances are in angstroms.

Contacts	%	Contact distances (Å)
C···H/H···C	16.7	2.702
H···H/H···H	50.4	2.176
H···O/O···H	19.4	2.368–2.554

The O···H intermolecular contacts are the second type of close contact that makes a large contribution (19.4%) to the crystal lattice of **1**. The contact distances for these interactions are 2.241, 2.368 and 2.554 Å, respectively. These interactions have shorter contact distances than sums of the van der Waals radius of individual atoms (H and O) and they are represented by red color (Fig. 3).

The H···C intermolecular contacts also showed a high contribution of 16.7% to the overall fingerprint plot. It is found that the minimum contact distance in **1** to be 2.702 Å. This contact is less than the van der Waals radii sum of the C and H atoms with representation by red color (Fig. 3).

Reactivity Parameters, NBO and QTAIM Analysis

In order to evaluate the donor-acceptor interactions in the molecule **1**, the NBO analysis was performed for the investigation of electronic structure [46, 47]. The second-order perturbation theory analysis of the Fock matrix was used. The intramolecular interactions cause the loss of occupancy from the localized NBO of the Lewis structure into an empty non-Lewis orbital. For each donor (i) and acceptor (j), the stabilization energy ($E(2)$) associated with the delocalization between i and j is determined as:

$$E(2) = \Delta E_{ij} = q_i \frac{(F_{ij})^2}{(E_j - E_i)} \tag{1}$$

where q_i is the donor orbital occupancy, E_i, E_j is diagonal elements (orbital energies) and $F_{i,j}$ is the off-diagonal NBO Fock matrix element. It should be pointed out that the higher value of $E(2)$ symbolizes the stronger interaction between electron donors and electron acceptors. The strong intramolecular hyperconjugative interactions obtained by the second-order perturbation theory analysis of the Fock matrix are given in Table 3.

The strongest stabilization interactions are formed within pyrone ring and ethylidene bridge that lead to the stabilization of this part of molecule and cause it planarity. These interactions include π(N–C1″) → π*(C3–C1), π(C3–C1) → π*(O3–C4), π(C3–C1) → π*(O2–C2) and π(C6″–C5″) → π*(N–C1″) with energies between 110.8 and 205 kJ mol^{-1}. The highest value of the interaction energy was calculated for the intramolecular charge transfer from π(C3″–C4″) to C2″ with value of 216 kJ mol^{-1}. The interactions within aromatic rings are also very important for stabilization, as for example π(C7–C8) → π*(C9–C10) with energy 118.2 kJ mol^{-1}.

Additionally, there are strong intermolecular hyperconjugative interactions from (LP2) O1 to π*(C2–O2) and π*(C9–C10), and from (LP2) O2 to σ*(C2–O1) with energies 155.2, 118.3 and 139.3 kJ mol^{-1}, respectively. A strong hydrogen bond (1.63 Å) is formed between N1−H···O3. This result is expected since it is well known that the NH groups are good hydrogen bond donors. On the other hand, the electron pairs on the oxygen of the C=O groups are much better hydrogen bond acceptors than the oxygen of the OH groups. The NBO analysis revealed that the electron density is donated from the p orbitals of the oxygen atom O3 into the proximate σ* antibonding N1–H bond (Table 3). This hydrogen bond additionally stabilizes the structure with 73.8 kJ mol^{-1}. Again, similar was observed for the analogous coumarin derivatives [27, 29] with the interaction energy that is the same, proving that the strength of hydrogen bond is not dependent on substituents. Intermolecular interactions of methyl group also stabilize the

overall structure through LP2(C2″) → π*(N1–C1″) and LP2(C2″) → π*(C3″–C4″) with energies 246.2 and 292.3 kJ mol^{-1}.

Table 3. Some selected second-order interaction energies for **1.**

Donor (i)	Acceptor (j)	E(2)/kJ mol^{-1}	E(j)-E(i)/a.u.	F(i, j)/a.u.
πN1–C1″	π*C3–C1′	205.1	0.32	0.113
πC3–C1′	π*O3–C4	159.2	0.26	0.09
πC3–C1′	π*O2–C2	139.3	0.28	0.087
πC9–C10	π*O3–C4	110.8	0.27	0.076
πC6″–C5″	π*N1–C1″	138.4	0.19	0.085
πC3″–C4″	LP1 C2″	216.0	0.15	0.094
πC7–C8	π*C9–C10	118.2	0.26	0.078
LP2 O3	σ*N1–H	73.8	0.68	0.099
LP2 O1	π*O2–C2	155.2	0.35	0.104
LP2 O1	π*C9–C10	118.3	0.35	0.093
LP2 O2	σ*O1–C2	139.3	0.58	0.126
LP1 C2″	π*N1–C1″	246.2	0.04	0.133
LP1 C2″	π*C3″–C4″	292.3	0.13	0.107

One of the tools for describing various intramolecular interactions is Bader's Quantum Theory of Atoms in Molecules (QTAIM) based on the electron density distribution (ρ) and Laplacian of electron density ($\nabla^2\rho$) at the (3, +1) ring critical points (RCPs) and (3, −1) bond critical points (BCPs) [36]. The important parameters of the stabilization of the investigated molecule are BCPs and RCPs. In this study, the QTAIM analysis was employed for the investigation of the ring and bond critical points between atoms of interest. Two types of interactions exist, the shared interactions (covalent bonds) and closed-shell interactions (ionic bonds, van der Waals bonds and hydrogen bonds). Only the second type of interaction was examined as they additionally stabilize the structure. The value of the electron density of hydrogen bonds is from 0.001 to 0.06 eA with small, but positive Laplacian [21]. On the other hand, the covalent interactions have an electron density of the order of 0.1 eA and negative Laplacian. The RCP is always found within a ring of chemically bonded atoms, and it represents a point within a structure with minimum electron density [22]. BCPs and RCPs can be used as the measure of the strength of the intramolecular hydrogen bond [23, 24] (Table 3).

The rigidity of the coumarin part is proven when properties of RCPs (electron density, Laplacian of electron density, kinetic (G) and potential (V) electron densities) were compared. There are five RCPs, as determined in the Multiwfn program (Fig. 4). Two of RCPs are in aromatic rings, and Table 4 shows that electron density and Laplacian have almost the same values. The parameters of RCP 2 are similar to those for

3-(1-((2-hydroxyphenyl)amino)ethylidene)chroman-2,4-dione also showing that these parameters are not influenced significantly by the substituents on aromatic rings [29]. The third RCP is found in pyrone ring and due to the lack of aromaticity and presence of electronegative atoms, the electron density and Laplacian are lower.

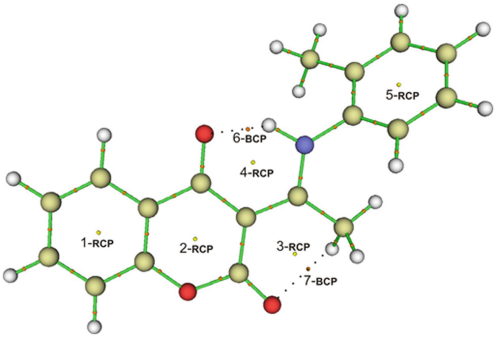

Fig. 4. The BCPs (orange points) and RCPs (yellow points) of the investigated compound.

Two other ring structures are found within the structure of investigated compound. The first one is already mentioned and includes the quasi-six membered ring with hydrogen bond. The value of electron density and Laplacian are 0.0192 eA and 0.128 eA. These values are comparable to those of pyrone ring and again prove the importance of this ring structure for stability of molecule. The values of electron density and Laplacian in BCP between O3 and H are higher than those typically expected for hydrogen bonds, but still lower than those for covalent bonds. The second ring structure is also enclosed by a weak hydrogen bond and it comprises of the following atoms O2–C2–C3–C1′–C2′–H. The value for electron density and Laplacian are 0.0175 eA and 0.070 eA which falls into non-covalent interactions. The methyl group is rotatable therefore it is expected that average values for the parameters are calculated.

Table 4. QTAIM descriptors of molecule **1.**

RCP/BCP No.	ρ	$\nabla^2\rho$	V	G
1	0.0216	0.159	−0.025	0.032
2	0.0192	0.131	−0.021	0.027
3	0.0138	0.075	−0.012	0.015
4	0.0192	0.128	−0.021	0.026
5	0.0215	0.158	−0.024	0.032
6	0.0588	0.165	−0.061	0.051
7	0.0175	0.070	−0.013	0.015

Molecular Docking Analysis

The online server, PASS (Prediction of Activity Spectra for Substances), was designed as a tool for evaluating the general biological potential of an organic drug-like molecule. This server provides simultaneous predictions of many types of biological activity based on the structure of the organic compounds [48, 49]. Some of the possible protein targets of **1** include Membrane integrity agonist, CYP2C12 substrate, Cholestanetriol 26-monooxygenase inhibitor, Ubiquinol-cytochrome-c reductase inhibitor, etc. (Table 5).

The inhibition of **1** towards Ubiquinol-Cytochrome C Reductase Binding Protein (UQCRB) was selected because of the biological importance of this protein and possible role in anti-cancer activity. The value of Pa (probability to be active) for this system is 0.777 (Table 5), as predicted by the PASS analysis. Protein-ligand binding energy and identification of the potential ligand-binding sites were determined from this study as well. These results are given in Table 6 and Fig. 5. The ligand conformation which showed the lowest binding energy (best position) was determined based on the ligand docking results. The position and orientation of ligand inside the protein receptor and the interactions with amino acids that bond to the ligand was analyzed and visualized with Discovery Studio 4.0 and AutoDockTools.

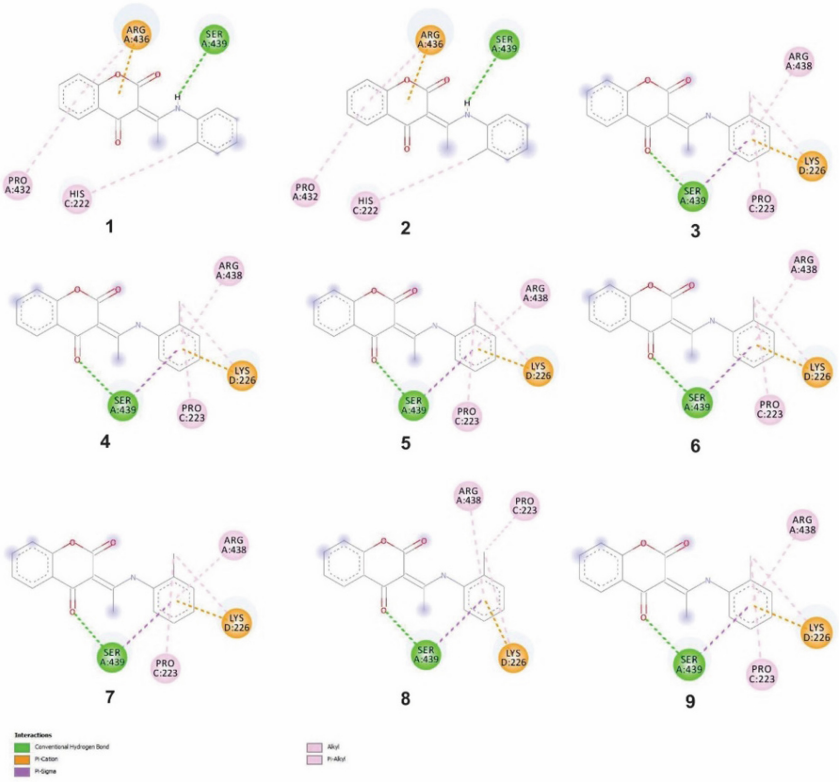

Fig. 5. Docking positions of **1** and UQCRB protein with the lowest energy.

Table 5. PASS prediction for the activity spectrum of **1**.

Pa > 0,7	Pi	Predicted activity
0,827	0,030	Membrane integrity agonist
0,826	0,030	CYP2C12 substrate
0,791	0,004	Cholestanetriol 26-monooxygenase inhibitor
0,799	0,017	CYP2H substrate
0,775	0,004	4-Nitrophenol 2-monooxygenase inhibitor
0,772	0,005	CYP2B5 substrate
0,752	0,010	Oxidoreductase inhibitor
0,777	**0,041**	**Ubiquinol-cytochrome-c reductase inhibitor**
0,710	0,006	General pump inhibitor

Table 6. The estimated values of free energy of binding (ΔG_{bind}, kJ mol^{-1}), binding constants (K_{i}) for various conformations of ligand **1** towards UQCRB protein, distance (Å) and pairwise interaction energies (E_{i}, kJ/mol^{-1}) of H-bonds.

Conformer	ΔG_{bind}, (kJ/mol^{-1})	K_{i} (μM)	H-Bond	Å	E_{i} (kJ/mol)
1	−25.44	35.1	A:SER439:CO---HN:LIG A:SER439:HO---HN:LIG	2.571 2.603	−0.40 −0.36
2	−25.31	37.1	A:SER439:CO---HN:LIG A:SER439:HO---HN:LIG	2.472 2.713	−0.55 −0.25
3	−23.85	66.2	A:SER439:OH---OC:LIG	1.948	−2.45
4	−23.85	66.2	A:SER439:OH---OC:LIG	1.951	−2.44
5	−23.85	66.6	A:SER439:OH---OC:LIG	1.967	−2.39
6	−23.81	66.7	A:SER439:OH---OC:LIG	1.926	−2.50
7	−23.81	68.0	A:SER439:OH---OC:LIG	1.890	−2.52
8	−23.77	68.6	A:SER439:OH---OC:LIG	1.915	−2.52
9	−23.77	68.7	A:SER439:OH---OC:LIG	1.951	−2.44

The results from Table 6 show that very similar values of free energy of binding, between −23.77 and −25.44 kJ mol^{-1}, were obtained for nine conformers. When specific interactions shown in Fig. 5 are observed the relative differences in thermodynamic parameters can be explained. All of the conformers bind to protein with the same interactions, but their energy depends on specific binding site.

The most stable conformer in active position forms two hydrogen bonds with C=O and OH groups of SER439. These bonds have lengths of 2.571 and 2.603 Å and pairwise interaction energies −0.40 and −0.36 kJ mol^{-1}, respectively. ARG436 forms two weak

π-cation and π-alkyl interaction with chroman and benzene rings. On the other hand, HYS222 and PRO432 form weak alkyl-π interaction with the benzene ring of the ligand (Fig. 5).

Other conformers also have hydrogen bonds formed with SER43 which proves the importance of this amino acid for the binding of molecules to the active site of protein. The distance between amino acid and active molecule varies from 1.951 and 2.713 Å. The weaker interactions are formed with ARG436, HIS222, LYS226, and PRO223 through alkyl-π interaction and π-cation interaction. It is assumed that it is actually the number of these weak interactions, not their type that determines the stability of binding. Therefore the most reactive positions, as determined by NBO and QTAIM analyses, are the positions that form interactions with proteins of interest.

4 Conclusions

The experimental and theoretical analysis of coumarin derivative, 3-(1-o-toluidinoethylidene)-chromane-2,4-dione (**1**), was performed. The experimental and theoretical vibrational spectra were compared and it was shown that the correlation between them is 0.999 with the average absolute error of 4.26 cm^{-1}. This was taken as a proof that the selected level of theory, B3LYP-D3BJ/6-311+G(d,p), describes well the experimental structure. The significant intermolecular contacts obtained from Hirshfeld analyses of the solid-state crystal structures of molecule **1** were investigated. The obtained results showed that the H···H intermolecular interactions have the largest contribution in the crystal lattice (50.4%) and they play a major role in crystal lattice stability.

In order to understand the type, nature, and strength of intramolecular interactions in molecule **1,** the AIM and NBO analyses were performed. A particular focus was placed on the characterization of hydrogen-bonding interactions. The NBO analysis exposed that the electron density is donated from the *p* orbitals of the O4 into the σ* antibonding N1–H bond. In this case, the hydrogen bond additionally stabilizes the structure of **1** with 73.8 kJ mol^{-1} and it forms the quasi-six membered ring. The electron density and Laplacian with values of 0.0192 eA and 0.128 eA also show that this bond is stronger than most non-covalent interactions.

The molecular docking study in the active position of UQCRB protein proved that the title molecule forms various interactions with amino acids. All conformers had hydrogen bonds with C=O and OH groups of SER439. What differed various conformers were weak interactions, alkyl-π and π-cation interaction, especially their number with neighboring amino acids. Therefore it was concluded that the stability of molecule and various active positions make it a promising agent for future studies towards anti-tumor agents.

Acknowledgments. This study is supported by the grants from the Ministry of Education, Science and Technological Development of the Republic of Serbia through grants OI172016, OI172015, OI172040, and OI174028.

References

1. Abernethy, J.L.: The historical and current interest in coumarin. J. Chem. Educ. **46**(9), 561 (1969)
2. Murray, R.D.H.: Naturally occurring plant coumarins, pp. 1–119 (1997)
3. Murray, R.D.H.: Naturally occurring plant coumarins, pp. 199–429. Springer, Vienna (1997)
4. Atta-ur-Rahman, Shabbir, M., Ziauddin Sultani, S., Jabbar, A., Iqbal Choudhary, M.: Cinnamates and coumarins from the leaves of *Murraya paniculata*. Phytochemistry **44**(4), 683–685 (1997)
5. Erdelmeier, C., Sticher, O.: Coumarin derivatives from *Eryngium campestre*. Planta Med. **51**(05), 407–409 (1985)
6. Dandriyal, J., Singla, R., Kumar, M., Jaitak, V.: Recent developments of C-4 substituted coumarin derivatives as anticancer agents. Eur. J. Med. Chem. **119**, 141–168 (2016)
7. Magadula, J.J., et al.: Mammea-type coumarins from *Mammea usambarensis* Verdc. Biochem. Syst. Ecol. **56**, 65–67 (2014)
8. Ojala, T., et al.: Antimicrobial activity of some coumarin containing herbal plants growing in Finland. J. Ethnopharmacol. **73**(1–2), 299–305 (2000)
9. Cottigli, F., et al.: Antimicrobial evaluation of coumarins and flavonoids from the stems of *Daphne gnidium* L. Phytomedicine **8**(4), 302–305 (2001)
10. Rosselli, S., et al.: The cytotoxic properties of natural coumarins isolated from roots of *Ferulago campestris* (Apiaceae) and of synthetic ester derivatives of aegelinol. Nat. Prod. Commun. **4**(12), 1701–1706 (2009)
11. Hodák, K., Jakesová, V., Dadák, V.: On the antibiotic effects of natural coumarins. VI. The relation of structure to the antibacterial effects of some natural coumarins and the neutralization of such effects. Cesk. Farm. **16**(2), 86–91 (1967)
12. Cravotto, G., Nano, G.M., Palmisano, G., Tagliapietra, S.: An asymmetric approach to coumarin anticoagulants via hetero-Diels–Alder cycloaddition. Tetrahedron Asymmetry **12**(5), 707–709 (2001)
13. Velasco-Velázquez, M.A., et al.: 4-hydroxycoumarin disorganizes the actin cytoskeleton in B16–F10 melanoma cells but not in B82 fibroblasts, decreasing their adhesion to extracellular matrix proteins and motility. Cancer Lett. **198**(2), 179–186 (2003)
14. Al-Ayed, A., Hamdi, N.: A new and efficient method for the synthesis of novel 3-Acetyl coumarins oxadiazoles derivatives with expected biological activity. Molecules **19**(1), 911–924 (2014)
15. Morrison, S.A., Esnouf, M.P.: The nature of the heterogeneity of prothrombin during dicoumarol therapy. Nat. New Biol. **242**(116), 92–94 (1973)
16. Salinas-Jazmín, N., de la Fuente, M., Jaimez, R., Pérez-Tapia, M., Pérez-Torres, A., Velasco-Velázquez, M.A.: Antimetastatic, antineoplastic, and toxic effects of 4-hydroxycoumarin in a preclinical mouse melanoma model. Cancer Chemother. Pharmacol. **65**(5), 931–940 (2010)
17. Egan, D., James, P., Cooke, D., O'Kennedy, R.: Studies on the cytostatic and cytotoxic effects and mode of action of 8-nitro-7-hydroxycoumarin. Cancer Lett. **118**(2), 201–211 (1997)
18. Finn, G., Creaven, B., Egan, D.: Modulation of mitogen-activated protein kinases by 6-nitro-7-hydroxycoumarin mediates apoptosis in renal carcinoma cells. Eur. J. Pharmacol. **481**(2–3), 159–167 (2003)
19. Joao Matos, M., Vina, D., Vazquez-Rodriguez, S., Uriarte, E., Santana, L.: Focusing on new monoamine oxidase inhibitors: differently substituted coumarins as an interesting scaffold. Curr. Top. Med. Chem. **12**(20), 2210–2239 (2012)
20. Pingaew, R., et al.: Synthesis, biological evaluation and molecular docking of novel chalcone–coumarin hybrids as anticancer and antimalarial agents. Eur. J. Med. Chem. **85**, 65–76 (2014)

21. Liu, X.-H., et al.: Synthesis and molecular docking study of novel coumarin derivatives containing 4,5-dihydropyrazole moiety as potential antitumor agents. Bioorg. Med. Chem. Lett. **20**, 5705–5708 (2010)
22. Cho, Y.S., Jung, H.J., Seok, S.H., Payumo, A.Y., Chen, J.K., Kwon, H.J.: Functional inhibition of UQCRB suppresses angiogenesis in zebrafish. Biochem. Biophys. Res. Commun. **433**(4), 396–400 (2013)
23. Sun, Y., et al.: Identification of UQCRB as an oxymatrine recognizing protein using a T7 phage display screen. J. Ethnopharmacol. **193**, 133–139 (2016)
24. Jung, H.J., Kwon, H.J.: Exploring the role of mitochondrial UQCRB in angiogenesis using small molecules. Mol. BioSyst. **9**(5), 930 (2013)
25. Jung, H.J., Kim, Y., Chang, J., Kang, S.W., Kim, J.H., Kwon, H.J.: Mitochondrial UQCRB regulates VEGFR2 signaling in endothelial cells. J. Mol. Med. **91**(9), 1117–1128 (2013)
26. Dimić, D.S., et al.: Synthesis and characterization of 3-(1-((3,4-dihydroxyphenethyl)amino)ethylidene)-chroman-2,4-dione as potential anti-tumor agent. Oxid. Med. Cell. Longev. **2019** (2019). Article ID 2069250
27. Avdović, E.H., et al.: Synthesis, spectroscopic characterization (FT-IR, FT-Raman, and NMR), quantum chemical studies and molecular docking of 3-(1-(phenylamino)ethylidene)-chroman-2,4-dione. Spectrochim. Acta Part A Mol. Biomol. Spectrosc. **195**, 31–40 (2018)
28. Avdović, E.H., et al.: Preparation and antimicrobial activity of a new palladium(II) complexes with a coumarin-derived ligands. Crystal structures of the 3-(1-(o-toluidino)ethylidene)-chroman-2,4-dione and 3-(1-(m-toluidino) ethylidene)-chroman-2,4-dione. Inorganica Chim. Acta **484**, 52–59 (2019)
29. Avdović, E.H., et al.: Spectroscopic and theoretical investigation of the potential anti-tumor and anti-microbial agent, 3-(1-((2-hydroxyphenyl)amino)ethylidene)chroman-2,4-dione. Spectrochim. Acta Part A Mol. Biomol. Spectrosc. **206**, 421–429 (2019)
30. Avdović, E.H., Milenković, D., Dimitrić-Marković, J.M., Vuković, N., Trifunović, S.R., Marković, Z.: Structural, spectral and NBO analysis of 3-(1-(3-hydroxypropylamino)ethylidene)chroman-2,4-dione. J. Mol. Struct. **1147**, 69–75 (2017)
31. Avdović, E.H., et al.: Synthesis, characterization and cytotoxicity of a new palladium(II) complex with a coumarin-derived ligand 3-(1-(3-hydroxypropylamino)ethylidene)chroman-2,4-dione. Crystal structure of the 3-(1-(3-hydroxypropylamino)ethylidene)-chroman-2,4-dione. Inorganica Chim. Acta **466**, 188–196 (2017)
32. Turner, M.J., McKinnon, J.J., Wolff, S. K., Grimwood, D.J., Spackman, P.R., Jayatilaka, D., Spackman, M.A.: CrystalExplorer17. University of Western Australia (2017)
33. Frisch, M.J., Trucks, G.W., Schlegel, H.B., Scuseria, G.E., Robb, M.A., Cheeseman, J.R., Zakrzewski, V.G., Montgomery, J.J., Stratmann, R.E., Burant, J.C., Dapprich, S., Millam, J.M., Daniels, A.D., Kudin, K.N., Strain, M.C., Farkas, O., Tomasi, J., Barone, V., Cossi, M., Cammi, R., Mennucci, B., Pomelli, C., Adamo, C., Clifford, S., Ochterski, J., Petersson, G.A., Ayala, P.Y., Cui, Q., Morokuma, K., Malick, A.D., Rabuck, K.D., Raghavachari, K., Foresman, J.B., Cioslowski, J., Ortiz, J.V., Baboul, A.G., Stefanov, B.B., Liu, G., Liashenko, A., Piskorz, P., Komaromi, I., Gomperts, R., Martin, R.L., Fox, D.J., Keith, T., AlLaham, M.A., Peng, C.Y., Nanayakkara, A., Challacombe, M., Gill, P.M.W., Johnson, B., Chen, W., Wong, M.W., Andres, J.L., Gonzalez, C., HeadGordon, M., Replogle, E.S., Pople, J.A.: Gaussian 09, Revision B.01. Gaussian Inc., Wallingford (2009)
34. Bader, R.F.W.: A bond path: a universal indicator of bonded interactions. J. Phys. Chem. A **102**, 7314–7323 (1998)
35. Bader, R.F.W.: Atoms in molecules. Acc. Chem. Res. **18**(1), 9–15 (1985)
36. Glendening, E.D., Badenhoop, J.K., Reed, A.E., Carpenter, J.E., Bohmann, J.A., Morales, C.M., Weinhold, F.: NBO 5.0. Theoretical Chemistry Institute, University of Wisconsin, Madison (2001)

37. Morris, G.M., et al.: AutoDock4 and AutoDockTools4: automated docking with selective receptor flexibility. J. Comput. Chem. **30**(16), 2785–2791 (2009)
38. Milenković, D., et al.: Reactivity of the coumarine derivative towards cartilage proteins: combined NBO, QTAIM, and molecular docking study. Monatshefte fur Chemie **149**, 159–166 (2017)
39. Dimić, D., et al.: Experimental and theoretical elucidation of structural and antioxidant properties of vanillylmandelic acid and its carboxylate anion. Spectrochim. Acta Part A Mol. Biomol. Spectrosc. **198**, 61–70 (2018)
40. Dimić, D., Milenković, D., Marković, Z., Marković, J.D.: Structural and spectral analysis of 3-metoxytyramine, an important metabolite of dopamine. J. Mol. Struct. **1134**, 226–236 (2017)
41. BIOVIA Discovery Studio 2016. Accelrys Studio Inc., San Diego (2016)
42. Gilli, G., Bellucci, F., Ferretti, V., Bertolasi, V.: Evidence for resonance-assisted hydrogen bonding from crystal-structure correlations on the enol form of the β-diketone fragment. J. Am. Chem. Soc. **111**, 1023–1028 (1989)
43. Spackman, M.A., Byrom, P.G.: A novel definition of a molecule in a crystal. Chem. Phys. Lett. **267**(3–4), 215–220 (1997)
44. Spackman, M.A., Jayatilaka, D.: Hirshfeld surface analysis. CrystEngComm **11**(1), 19–32 (2009)
45. Grabowsky, S., Dean, P.M., Skelton, B.W., Sobolev, A.N., Spackman, M.A., White, A.H.: Crystal packing in the 2-R,4-oxo-[1,3-a/b]-naphthodioxanes – hirshfeld surface analysis and melting point correlation. CrystEngComm **14**(3), 1083–1093 (2012)
46. Dimić, D., Petković, M.: Control of a photoswitching chelator by metal ions: DFT, NBO, and QTAIM analysis. Int. J. Quantum Chem. **116**, 27–34 (2015)
47. Dimić, D.: The importance of specific solvent–solute interactions for studying UV–vis spectra of light-responsive molecular switches. Comptes Rendus Chim. **21**(11), 1001–1010 (2018)
48. Khurana, N., Ishar, M.P.S., Gajbhiye, A., Goel, R.K.: PASS assisted prediction and pharmacological evaluation of novel nicotinic analogs for nootropic activity in mice. Eur. J. Pharmacol. **662**(1–3), 22–30 (2011)
49. Goel, R.K., Singh, D., Lagunin, A., Poroikov, V.: PASS-assisted exploration of new therapeutic potential of natural products. Med. Chem. Res. **20**(9), 1509–1514 (2011)

Advanced Modelling Approach of Carotid Artery Atherosclerosis

Smiljana Djorovic[1,2(✉)], Igor Saveljic[1,2], and Nenad Filipovic[1,2]

[1] Faculty of Engineering, University of Kragujevac (FINK), Sestre Janjic 6, 34000 Kragujevac, Serbia
smiljana@kg.ac.rs

[2] Bioengineering Research and Development Center (BioIRC), Prvoslava Stojanovica 6, 34000 Kragujevac, Serbia

Abstract. With a fast progression of computational methods and medical imaging techniques, the advanced simulations of carotid arteries can be approached aiming to address different medical conditions and support the clinical practice. Within this context, the main purpose of this study was to computationally model the biological and mechanical processes related to the plaque progression, as well as to predict plaque regions and mechanisms which are prone to atherosclerosis development within the carotid artery. We have focused on two patient-specific models and application of Finite Element Analysis (FEA) which together enable investigation of the parameter such as shear stress distribution, as well as mechanical response of stenotic zones. After performed the three-dimensional (3D) simulation of plaque progression, the results have shown stenoses in Internal Carotid Artery (ICA), in case of both patients. The degree of ICA stenosis is the most important predictor of cerebral infarction among patients with atherosclerosis. Therefore, its estimation is significant for further steps in medical treatment. The increased shear stress was present at the stenoses due to high blood velocities, while low shear stress was present at the carotid bifurcation, which may indicate the possibility for further plaque progression. This approach will be further improved and used for risk stratification models, by detecting the parameters of unstable and stable carotid plaques related to the risk of stroke, which is objective of our future studies.

1 Introduction

Carotid artery disease constitutes the primary cause of ischemic cerebrovascular events and accounts for an estimated 750,000 victims per year from stroke in the USA [1], and an even higher burden in morbidity and healthcare costs, due to long-term disability. Approximately 10% [2] to 20% [3] of ischemic strokes in the world is caused by carotid atherosclerosis solely. Atherosclerosis is an inflammatory disease induced by cholesterol deposits and cellular proliferation, which presents lumen occlusion due to building up of plaque within the arterial wall. Untreated carotid atherosclerosis disease alters blood flow, promotes thrombus and embolus formation that lead to ischemic stroke.

Carotid atherosclerosis disease is a time progressive and it does not happen suddenly [4], but in many times the symptoms reveals in final stages of the disease.

N. Filipovic (Ed.): ICCB 2019, LAIS 11, pp. 143–150, 2020.
https://doi.org/10.1007/978-3-030-43658-2_13

The atherosclerosis can be classified into (i) symptomatic and (ii) asymptomatic subgroups. In case of asymptomatic atherosclerosis, usually in progressed stage of disease, i.e. after formation of mild and sever stenosis (50% and above) symptoms can be observed. Therefore, it is important to understand mechanisms of atherosclerosis before it turns to symptomatic and cause clinical events such as Transitional Ischemic Attack (TIA) and stroke. The mechanisms have been examined by experts in different fields (medical scientists, biochemists and bioengineers) knowing the vital importance of carotid artery's role in cerebrovascular system. With that aim, the main purpose of this study was to analyze the biomechanical behavior of two patient-specific carotid arteries, by simulating the atherosclerosis progression. The CT scan images were used for creation of the three-dimensional (3D) patient-specific models. The shear stress distribution was determined using Finite Element Method (FEM) approach and employing equations for plague progression.

The rest of the paper is organized as follows. Section 2 describes previously studies related to methods used for 3D reconstruction of arteries and computational simulations of carotid atherosclerosis disease. The types of imaging data which can be used for the 3D geometrical reconstruction are summarized. Procedure for creation of the 3D patient-specific models which required use of several software packages is presented in Sect. 3.1. The Sect. 3.2 describes general concept of the Finite Element Analysis (FEA) for simulation of atherosclerotic plaque progression (blood flow and mass transport). The main aspects of computational simulation and boundary conditions are described. Also, it should be noted that PAK *in-house* solver was employed for performing the computational simulation. The Sect. 4 covers discussion of results given for two patient-specific carotid arteries, confirming the presence of stenoses at Internal Carotid Arteries (ICAs), which corresponds to the most common atherosclerotic zone in real-life situations. Finally, Sect. 5 presents the main conclusions of this study and plans for further improvements.

2 Related Work

2.1 3D Reconstruction of Arteries

In the recent years, the 3D reconstruction of blood vessels has been widely used as a way to determine the correct diagnosis of disease. Namely, accurate characterization of carotid artery's geometry is vital for our understanding of the atherosclerosis pathogenesis [5]. 3D reconstruction concerns the detailed 3D surface generation and visualization of specific anatomical structures, such as arteries, vessels, organs, body parts and abnormal morphologies (tumors, lesions, injuries, etc.). Meshing and rendering techniques are used for completing the seamless boundary surface, generating the volumetric mesh, followed by smoothing and refinement. Furthermore, 3D reconstruction constitutes the necessary step towards biomedical modeling of organs, dynamic functionality, diffusion processes, hemodynamic flow and fluid dynamics in arteries, as well as mechanical loads and properties of body parts, tumors, lesions and vessels, such as wall/shear stress and strain and tissue displacement [6].

The process of blood vessels' 3D reconstruction can be divided into three steps: (i) segmentation of 2D image, (ii) Smoothing of the blood vessel curve and (iii) 3D

reconstruction of blood vessels (Fig. 1). Algorithms used for vessel segmentation can be considered as the key element for developing automated diagnostic systems [7]. There is no one segmentation method that can be used to extract vasculature from every medical image. Some of the methods used for segmentation are focused on pattern recognition techniques, such as thresholding combined with component analysis, while other popular approach is to apply explicit vessel models to extract the vessel contours. Some segmentation methods require pre-processing before segmentation. This is often situation if the image quality is not good or if there is noise. Also, sometimes post-processing is required in order to reduce the segmentation problems, such as over-segmentation. The future in segmentation methods is oriented toward development of more accurate and faster automated techniques. Therefore, the more accurate and less time-consuming methods for creation of patient-specific models are necessary in order to take into consideration the individual anatomy of the patient.

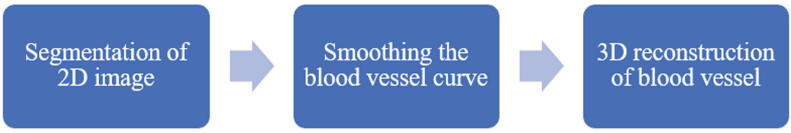

Fig. 1. The process of the 3D reconstruction of the blood vessel.

During the reconstruction of carotid artery's geometry, imaging data acquired from different diagnostic procedures can be used (Ultrasound (US), Magnetic Resonance Imaging (MRI) and Computed Tomography (CT) are most often). The US imaging can be used for automated lumen and adventitial border delineation of carotid artery wall [8], as well as for measurement of wall thickness, blood velocities, and identification of patients with a histologically unstable carotid plaque [9]. Comparing with the US, the CT and MRI are widely used for reconstruction of patient-specific geometries [10].

2.2 Computational Simulations of Plague Progression

Numerical biomechanics has been proved to be an efficient tool for understanding vascular diseases including atherosclerosis. In order to reconstruct geometry and create model for these types of computational studies, the data from diagnostic tools such as CT scan, US, MRI, as well as angiography, Laser Doppler Anemometer (LDA), Power Doppler Imaging (PDI), Doppler Sonography (DS) etc., have being implementing.

A complex geometry of carotid artery and blood flow regime convenient for Low-Density Lipoprotein (LDL) accumulation make it disposed to atherosclerosis. Scientists have proven that atherosclerotic plaque formation and progression are associated with low wall shear stress (WSS) regions and that LDL concentration leads to penetration of excessive levels of LDL particles to subendothelial layer [11]. It is indicated that LDL surface concentration increases in regions associated with high infiltration rate (high blood pressure) and low WSS.

Also, realistic different inlet velocity profile, obtained from color Doppler US, and carotid bifurcation geometry, extracted from CT imaging, have used to study flow regime

in a stenosed carotid artery [12]. The mechanisms of atherosclerosis have been used to provide insights for understanding the processes which lead to the plaque initiation and development, as well as to predict plaque regions and mechanisms which are prone to disease progression [13, 14].

Furthermore, examination of carotid atherosclerosis is challenging due to interaction of blood constituents with arterial wall and mechanical reactions which cause initiation and progression of atherosclerotic plaque. Many researchers have performed Fluid-Solid Interaction (FSI) analysis in order to investigate a complex interaction between artery wall and blood in carotid atherosclerosis disease [15, 16]. In addition, Tomaso et al. [4] combined experimental and numerical methods of biomechanical and biochemical atherosclerosis progression modeling and introduced a promising outline for determination of patient-specific plaque growth simulation. Although researchers have been simulated different aspects of carotid atherosclerosis disease, it is obvious that models which consider biochemical and biomechanical aspects of atherosclerosis progression are more accurate.

3 Materials and Methods

This section presents the 3D reconstruction of two patient-specific carotid arteries and simulation procedure of atherosclerosis development which covers blood flow and mass transport. In general, modelling of atherosclerotic plaque development is schematically presented in Fig. 2 and includes 3D reconstruction, blood flow modelling, as a first step to simulation of atherosclerosis disease, and finally, the plaque growth modeling.

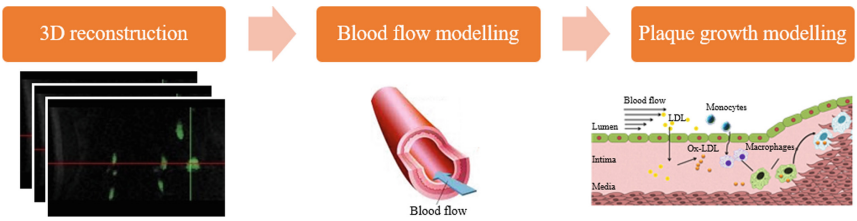

Fig. 2. Modelling of atherosclerotic plaque development; the general concept.

3.1 Patient-Specific 3D Models

In order to perform the computational analysis of atherosclerosis development, the 3D patient-specific models were created. CT scan images were used to create the carotid geometries containing the following branches: Common Carotid Artery (CCA), External Carotid Artery (ECA) and Internal Carotid Artery (ICA). Implementation of several different software packages contributed to the optimization of surface elements, 3D elements, and preparation of the model for the blood flow simulation coupled with the mass transfer and diffusion within the blood vessel wall.

The region of interest selected in the segmentation process was converted to the 3D surface model using an adapted algorithm which resulted in stereolithography (STL) representation of boundary surface. After obtaining the initial 3D models, optimization of the surface meshes was performed, in order to create meshes suitable for the computational simulation. After reconstruction of the carotid arteries, the *in-house* software was used for creation of eight-node brick elements. The datasets for these two patients were separately imported into PAK *in-house* solver for further simulation of blood flow and mass transport through the carotid arteries [17].

3.2 Numerical Analysis

In the presented study, the average blood properties such as dynamic viscosity of 0.00365 Pa·s and density of 1050 kg/m^3 were prescribed with aim to perform analysis which reflects the realistic human blood flow. In addition, the following boundary conditions were employed: prescribed blood velocity at the inlet of the arterial segment; physiological resistance pressure at the arterial outlets.

The LDL mass transfer through the blood lumen and arterial wall was governed by different sets of equations in order to computationally simulate atherosclerosis progression for the specific patients. The transport of LDL in the lumen of the carotid artery and through its arterial tissue were coupled by Kedem-Katchalsky equations. The blood flow in the lumen was simulated by the 3D Navier–Stokes equations, together with the continuity equation. The mass transfer in the lumen was modeled using convective diffusion equations, while convective diffusion reactive equations were used for modeling mass transfer in the arterial wall. The fluid filtration (mass transfer across the wall of the blood vessel) was modelled with the Darcy's law. Also, the biomolecular parameters and adhesion molecules were used for computer simulation. These methods are explained in detail by Filipovic et al. [14]. In addition, the 3D mesh-moving Arbitrary Lagrangian-Eulerian (ALE) formulation was applied to follow the wall displacements and change of the carotid wall geometry during the plaque growth [18].

4 Results and Discussion

In atherosclerosis diagnostic process arterial wall properties, plaque composition and hemodynamical parameters can precisely comprehend the progression of disease. With that aim, computational modelling of atherosclerosis has been performed in recent years. Based on previous experiences, this work was focused on modeling of two patient-specific carotid arteries using the CT scan images. The 3D blood flow and the LDL transport through the lumen and artery wall, coupled with plaque progression in the carotid artery wall were simulated based on FEM. The biomolecular parameters and adhesion molecules were prescribed for the computer simulation. The appropriate boundary conditions were also prescribed. Mass transfer within the blood lumen and through the arterial wall was coupled with the blood flow and modelled by the convection–diffusion equation. Kedem–Katchalsky equations described the LDL transport in lumen of the carotid artery and through the vessel tissue. The 3D blood flow was governed by the

Navier–Stokes equations, together with the continuity equation. PAK *in-house* solver was employed for the computational simulation.

The results of simulated carotid plaque progression were examined for two patient-specific models (Patient#1 and Patient#2) presenting the shear stress distributions (Fig. 3). Alterations of shear stress distribution during the simulated plaque progression can be noticed by comparing Patient#1 and Patient#2, which may depend on patient-specific geometries. Further development of atherosclerosis leads to increasement of plaque volume and decreasement of lumen diameter, which causes progression of stenotic zone. Decreased diameters of the ICAs and presence of the stenotic zones (marked with yellow circles) can be seen in case of both patients. The degree of ICA stenosis is the most important predictor of cerebral infarction among patients with atherosclerosis, and its estimation is significant for further steps in medical treatment.

The shear stress is increased at the stenoses and its maximum values for the atherosclerotic patients are 7.00 Pa (Patient#1) and 10.1 Pa (Patient#2), respectively. The increased shear stress is caused by high blood velocities through the stenoses, which may vary depending on the obtained geometry. In addition, low shear stress is present at the carotid bifurcation zone in case of both patients, which may indicate the possibility for further plaque progression.

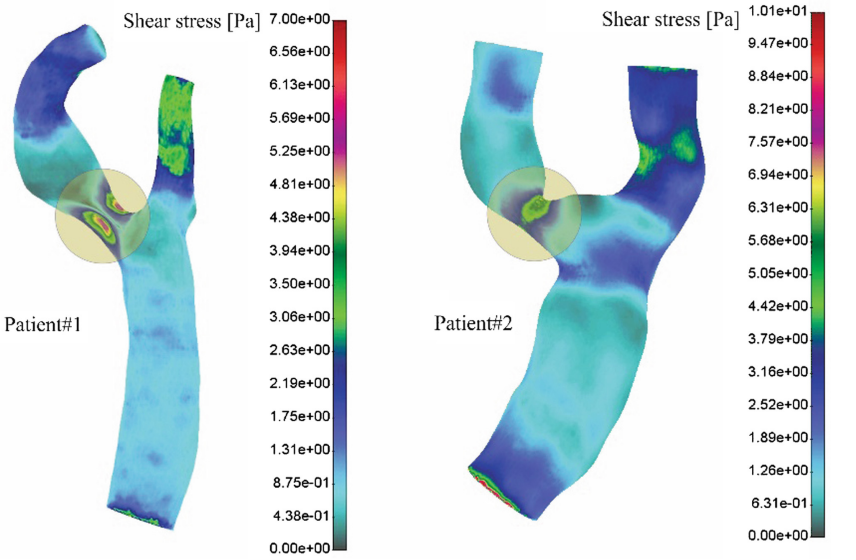

Fig. 3. Shear stress distribution: atherosclerotic carotid artery of Patient#1 and Patient#2, respectively.

The performed study was built on previous experiences in simulations of atherosclerotic plaque progression within the carotid artery and the obtained results are comparable to the previous works [14, 19, 20]. The presence of stenotic zones in the ICAs corresponds to the usual appearance, and their further development can be determined by using presented numerical method. Beside this type of study, the objective of our future studies

will be the automatic plaque detection and plaque type characterization in imaging data, knowing that plaque type is an important risk factor in asymptomatic atherosclerotic patients.

In summary, these computational models and simulation of atherosclerosis includes some limitations. Firstly, the carotid arteries in the human body might react differently, as they do not have the same embryological origin. Second, the adopted physiological properties and inlet blood velocities had average values which do not correspond to patient-specific characteristics. Third, plaque components should be included in the models. Also, quantification of the real patient-specific plaque progression has to be investigated in order to validate the computational models.

5 Conclusions

Carotid atherosclerosis disease is one of most prevalence cerebrovascular diseases and takes many lives yearly. Many researches have made the efforts to understand formation, progression and regression of carotid artery stenosis. Moreover, determination of plaque location for a specific patient, coupled with computer simulation of plaque progression in time, has a potential benefit for prediction of atherosclerosis development.

Based on previous experiences, this study included the 3D simulation of atherosclerosis in order to investigate the relation between the patient-specific geometry, shear stress distribution and disease progression. Two patient-specific carotid arteries were taken into account, using the CT scan images for creation of 3D models. The results of the analysis have shown that stenotic zones appear in the ICAs, together with increased shear stress due to hemodynamics conditions. On the other hand, low shear stress was present at the carotid bifurcation in case of both patients, which indicates the possibility for further plaque progression.

Although still affected by several simplifications, the present study can be considered as further step towards the prediction of disease progression. Therefore, more realistic patient-specific models will be investigated in the next studies, with aim to constantly improve the computational determination of plaque location and its progression in time, as well as contribute to the daily medical practice.

Acknowledgments. This paper is supported by TAXINOMISIS project that has received funding from the European Union's Horizon 2020 research and innovation programme under grant agreement No 755320. This article reflects only the author's view. The Commission is not responsible for any use that may be made of the information it contains. The research is also supported by the Ministry of Education, Science and Technological Development of the Republic of Serbia (project numbers III41007 and OI174028).

References

1. Sobieszczyk, P., Beckman, J.: Carotid artery disease. Circulation **114**, e244–e247 (2006)
2. Chaturvedi, S., Sacco, R.: How recent data have impacted the treatment of internal carotid artery stenosis. J. Am. Coll. Cardiol. **65**(11), 134–143 (2015)

3. Petty, G.W., Brown, R.D., Whisnant, J.P., Sicks, J.D., Michael O'Fallon, W., et al.: Ischemic stroke subtypes a population-based study of incidence and risk factors. Stroke **30**, 2513–2516 (1999)
4. Tomaso, G.D., Pichardo-Almarza, C., Agu, O., Díaz-Zuccarini, V.: A Multiscale and patient-specific computational framework of atherosclerosis formation and progression: a case study in the aorta and peripheral arteries. Procedia Comput. Sci. **51**, 1118–1127 (2015)
5. Kamenskiy, A.V., MacTaggart, J.N., Pipinos, I.I., Bikhchandani, J., Dzenis, Y.A.: Three-dimensional geometry of the human carotid artery. J. Biomech. Eng. **134**(6), 0645021–0645027 (2012)
6. Babu, S.J.: A survey of volumetric visualization techniques for medical images. Int. J. Res. Stud. Comput. Sci. Eng. **2**(4), 34–39 (2015)
7. Kirbas, C., Quek, F.: A review of vessel extraction techniques and algorithms. ACM Comput. Surv. (CSUR) **36**(2), 81–121 (2004)
8. Kumar, P.K., Araki, T., Rajan, J., Laird, J.R., Nicolaides, A., Suri, J.S.: State-of-the-art review on automated lumen and adventitial border delineation and its measurements in carotid ultrasound. Comput. Methods Programs Biomed. **163**, 155–168 (2018)
9. Salem, M., et al.: Identification of patients with a histologically unstable carotid plaque using ultrasonic plaque image analysis. Eur. J. Vasc. Endovasc. Surg. **48**(2), 118–125 (2014)
10. Milašinović, D., Ivanović, M., Tengg-Kobligk, H., Böckler, D., Filipović, N.: Software tools for generating CFD simulation models of blood flow from ct images, and for postprocessing. J. Serb. Soc. Comput. Mech. **2**(2), 51–58 (2008)
11. Nematollahi, A., Shirani, E., Mirzaee, I., Sadeghi, M.R.: Numerical simulation of LDL particles mass transport in human carotid artery under steady state conditions. Scientia Iranica **19**, 519–524 (2012)
12. Lee, S.E., Lee, S.W., Fischer, P.F., Bassiouny, H.S., Loth, F.: Direct numerical simulation of transitional flow in a stenosed carotid bifurcation. J. Biomech. **41**, 2551–2561 (2008)
13. Djorovic, S., Saveljic, I., Filipovic, N.: Computational simulation of carotid artery: from patient-specific images to finite element analysis. J. Serb. Soc. Comput. Mech. **13**(1), 120–129 (2019)
14. Filipovic, N., Teng, Z., Radovic, M., Saveljic, I., Fotiadis, D., Parodi, O.: Computer simulation of three dimensional plaque formation and progression in the carotid artery. Med. Biol. Eng. Comput. **51**(6), 607–616 (2013)
15. Cilla, M., Borras, I., Pena, E., Martinez, M., Malve, M.: A parametric model for analysing atherosclerotic arteries: On the FSI coupling. Int. Commun. Heat Mass Transf. **67**, 29–38 (2015)
16. Xiaojuan, T., Peiyi, G., Lina, J., Yan, L., Binbin, S.: Subject-specific fully-coupled and one-way fluid-structure interaction models for modeling of carotid atherosclerotic plaques in humans. Med. Sci. Monit. **21**, 279–3290 (2015)
17. Kojic, M., Filipovic, N., Stojanovic, B., Kojic, N.: Computer Modeling in Bioengineering - Theoretical Background, Examples and Software. Wiley, Chichester (2008)
18. Filipovic, N., Mijailovic, S., Tsuda, A., Kojic, M.: An implicit algorithm within the arbitrary Lagrangian-Eulerian formulation for solving incompressible fluid flow with large boundary motions. Comput. Methods Appl. Mech. Eng. **195**, 6347–6361 (2006)
19. Filipovic, N., Saveljic, I., Nikolic, D., Milosevic, Z., Kovacevic, P., Velicki, L.: Numerical simulation of blood flow and plaque progression in carotid–carotid bypass patient specific case. Comput. Aided Surg. **20**(1), 1–6 (2015)
20. Djorovic, S., Saveljic, I., Filipovic, N.: Numerical analysis of plaque progression in 3D patient specific model of carotid artery. In: CMBEBIH 2019, IFMBE Proceedings, vol. 73, pp. 337–340. Springer, Banja Luka (2020)

Effect of Hip Implant Surface Modification on Shear Stress Distribution

Aleksandra Vulović[1,2,3(✉)] and Nenad Filipović[1,2,3]

[1] Faculty of Engineering, University of Kragujevac, Sestre Janjić 6, 34000 Kragujevac, Serbia
{aleksandra.vulovic,fica}@kg.ac.rs
[2] Bioengineering Research and Development Center (BioIRC), Prvoslava Stojanovića 6, 34000 Kragujevac, Serbia
[3] Steinbeis Advanced Risk Technologies Institute doo Kragujevac, Kneza Milosa 25, Kragujevac, Serbia

Abstract. Hip replacement surgery is one of the most common procedures in the world. Annually, more than 1 million hip replacement surgeries are performed worldwide, while it is anticipated that this number will double in the next decade. After the damaged or worn out hip joint is replaced with the artificial hip joint, bone healing process starts. In order to ensure the long and proper function of the artificial joint, the connection between the bone and the inserted implant should be as strong as possible. However, if the established connection is not strong enough, the implant starts to loosen. Experimental studies have indicated that implants with a rough surface form a stronger connection with a bone. The goal of this paper was to numerically analyze different spherical shapes on the implant surface. The results obtained numerically are considered to be a very helpful addition to the experimental studies. Numerical analysis of the implant surfaces has been performed using the Finite Element Method. The obtained results include distribution of the shear stress on the implant surface. This type of stress is important for this study because in order to promote bone ingrowth, the shear stress should be minimized. Our study considered the interaction between cortical bone and implant with rough surface. Material properties and boundary conditions were adapted from literature.

Keywords: Hip implant · Implant surface · Finite element analysis

1 Introduction

Hip replacement surgery is one of the most commonly performed procedures in the world. More than 1 million hip replacement procedures are performed annually and it is expected that this number will double during the next decade [1]. The procedure is performed when the hip joint is damaged or worn out. Although this is one of the safest procedures, complications can happen. Most common complication is the need for revision surgery as a result of aseptic loosening. One way to avoid aseptic loosening is to ensure that the connection between the femoral bone and the hip implant will be strong, which means reducing the micro movements between bone and the implant.

N. Filipovic (Ed.): ICCB 2019, LAIS 11, pp. 151–159, 2020.
https://doi.org/10.1007/978-3-030-43658-2_14

In vivo experiments have indicated that this connection can be improved by increasing the surface roughness of cylindrical implants [2].

Surface modification techniques, such as surface texturing and surface coating, have been used to increase the life of artificial hip implants. Surface modifications are usually done on the femoral head in order to improve tribological performance [3–5]. The effect of surface modifications has mostly been analyzed using experimental studies. However, with a significant technological improvement during the past decades, we are able to analyze this problem using numerical methods, such as Finite Element Method (FEM). Application of FEM indicated that mechanical properties of porous fibre-reinforced composites implant could be changed in order to improve shear stress distribution at the bone-implant interface [6]. Noyama et al. [7] have used FEM to optimize the groove angle on the proximal medial region of the femoral stem and the stem material based on the obtained stress values.

Experimental studies have indicated that the shear stress on the hip implant - bone interface needs to be minimized in order to improve the implant - bone connection after the hip implant has been inserted. In our previous work [8], we have used FEM to obtain shear stress distribution on the implant topographies using boundary conditions that correspond to a person standing. This paper is a continuation of our work of analyzing implant topographies in order to find the topography with lowest shear stress values. In this paper, we will present shear stress distribution of additional three surface topographies.

2 Materials and Methods

2.1 Geometries

The first step in our research was the development of the models that will be analyzed using the Finite Element Method. Our goal was to analyze the interaction between the cementless femoral implant and the femoral bone. Since we have considered interaction in the femoral shaft, only two layers (cortical femoral bone and hip implant) had to be created (Fig. 1).

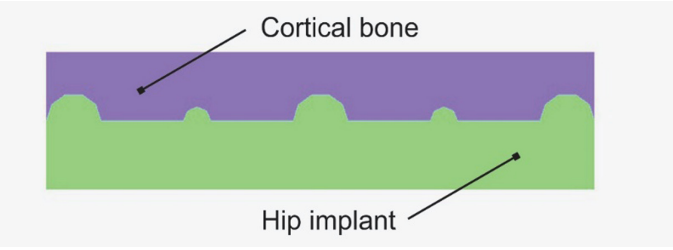

Fig. 1. Layers of the model

The models were created using software for Computer Aided Design (CAD). The model dimensions were in millimeters, while the topography dimensions were in micrometers. As a result, the models were scaled 1000 times in order to make it easier for the model creation and preparation for the FE analysis. Considering the significant dimension difference, we have decided to focus only on the small area of interaction. The created models are presented in Fig. 2.

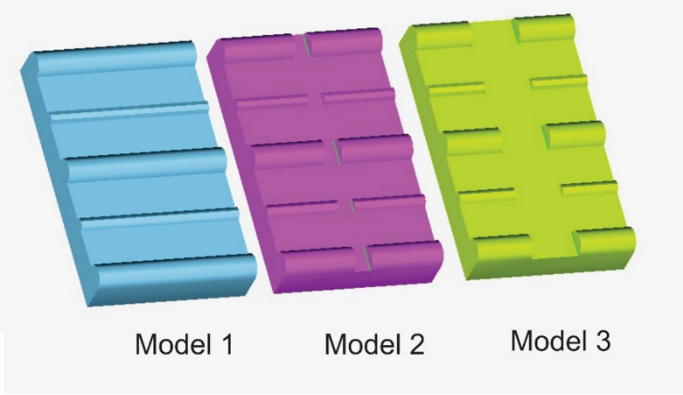

Fig. 2. Overview of the implant models

As it can be seen in previous figures, for the geometry of topographies we have chosen to use half cylinders with two different radius values. Model 1 had one half cylinder per model's width, while models 2 and 3 had two half cylinders per model's width. The difference between models 2 and 3 was in the length between these half cylinders. As it can be noticed from the Figs. 2 and 3, the length was smaller in model 2.

After the models had been created, they were exported as .stl files which were used to create a mesh for each model. The mesh for each model was created manually. The number of nodes and elements per model is given in Table 1.

Table 1. Number of nodes and elements per model (cortical bone and implant)

Model	Number of nodes	Number of elements
Model 1	74466	65280
Model 2	74813	65298
Model 3	74840	65376

2.2 Material Properties

Material properties of cortical bone and hip implant were used for the finite element analysis. Material properties of cortical bone and hip implant were considered to be isotropic, homogeneous and linear elastic. For the analyzed hip implant titanium alloy Ti6Al4V was chosen. Applied material properties of cortical bone and hip implant were taken from the literature and the values are shown in Table 2.

Table 2. Applied material properties

Material	Young's Modulus [GPa]	Poisson ratio	Reference
Cortical bone	16.7	0.3	[9]
Implant	109	0.34	[10]

2.3 Boundary Conditions

For the simulations, we have used the following model constraints:

- The upper surface of the cortical bone was fixed
- The bottom surface of the implant was locked in the z direction
- The sideways of the cortical bone and implant were locked in the x direction

Everything else was allowed to move in all three directions.

The applied load was obtained from the simulation of interaction between femoral bone and hip implant without modifications under walking static condition [8]. The constraints used for this simulation were adapted from [11]. The overview of constraints and load can be seen in Fig. 3.

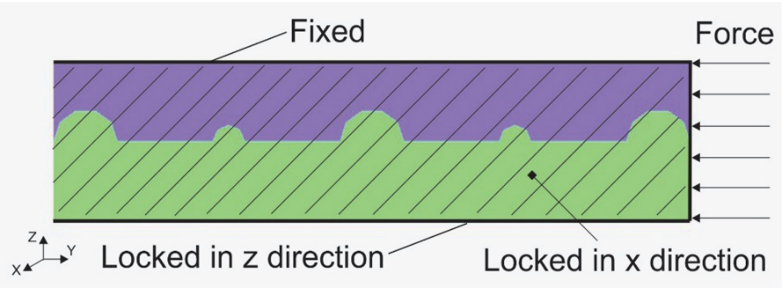

Fig. 3. Overview of load and constraints

In order to simulate micro motions, contact with friction between cortical bone and implant elements was defined. The friction coefficient was 0.39 [10].

3 Results and Discussion

The shear stress distribution of the first implant model can be seen in Fig. 4. The calculated shear stress values were in the range from 0.00749 to 3.209 MPa.

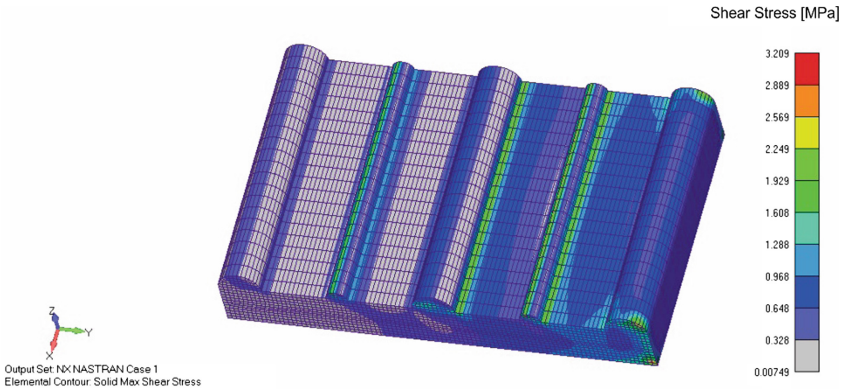

Fig. 4. Shear stress distribution for implant model 1

As it can be noticed from Fig. 4, higher shear stress values were calculated closer to the right side of the model, where the force was applied. On the left side of the model, the calculated values were between 0 and 1.5 MPa.

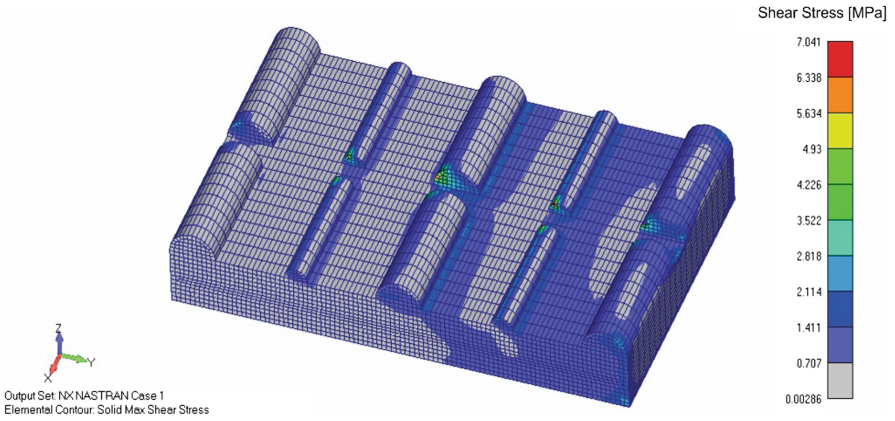

Fig. 5. Shear stress distribution for implant model 2

The shear stress distribution of the second implant can be seen in Fig. 5. The calculated shear stress values of the second model were in the range from 0.0286 to 7.041 MPa.

The shear stress distribution for the third implant can be seen in Fig. 6. This model had the highest calculated shear stress values (in the range from 0.0994 to 8.897 MPa).

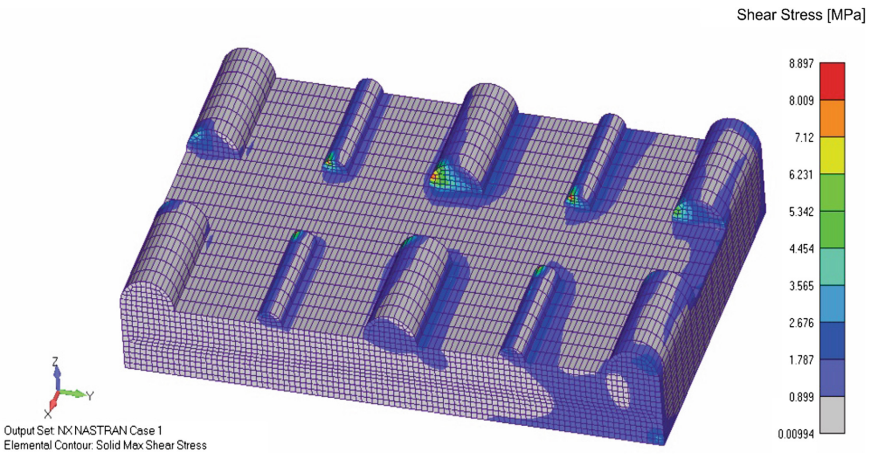

Fig. 6. Shear stress distribution for implant model 3

As in previously published paper [8], not having one half cylinder per model's width leads to increased shear stress values. It can be noticed that increased distance between two half cylinders led to increased shear stress values (Figs. 4 and 5). For models 2 and 3, the highest values were calculated on the second, third and fourth half cylinder (from the right side).

Comparison of the shear stress distributions for all three models can be seen in Fig. 7.

In order to promote bone ingrowth, shear stress at the implant-bone interface should be minimized [6], which means that topography used for the first implant would be the best choice. This is in accordance with our previous study [8]. Comparing those results with results presented in this paper (Table 3), we could say that model 1 presented here would be a better choice for hip implant topography based on the shear stress value comparison.

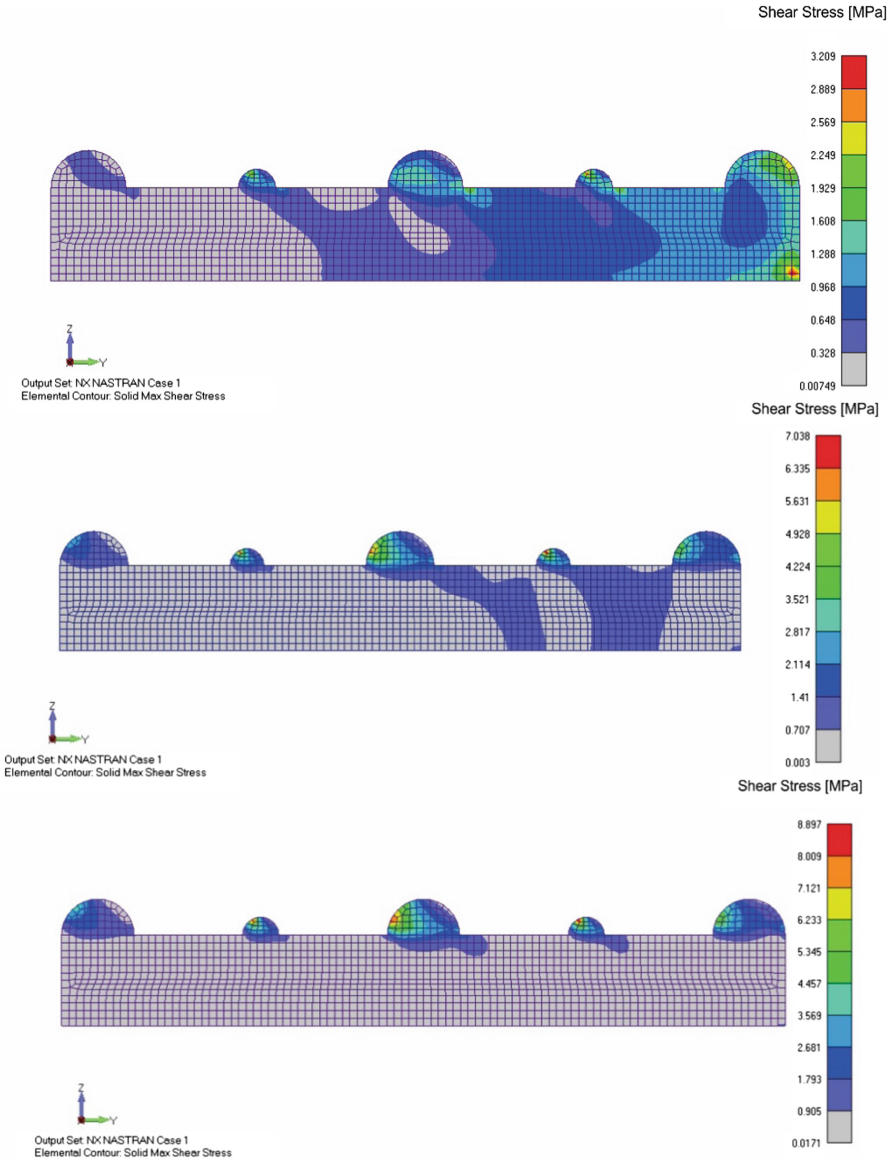

Fig. 7. Comparison of shear stress distribution – YZ plane cross section

Table 3. Comparison with previously published results

Model 1	Model 1 [8]
3.209 MPa	4.145 MPa

4 Conclusion

The application of the finite element method in this type of is important as it provides us with results that would be hard to obtain otherwise. However, as with all numerical studies there are some limitations. In this case, the main limitation is the applied force. That force depends on a person's weight, which means that these results only correspond to the person of an average weight.

The results obtained in this study, indicate that model 1 would be the best choice out of three models presented in this paper. The shear stress values for model 1 indicate that it would be a better choice for implant topography than the model presented in our previous study. Although, the numerical results can help us choose an implant topography, it is important to state that each body will have different reaction to the inserted implant, which is something we cannot know based on the simulations. The presented results are a promising step forward in our research of the modified hip implant surfaces. Every new analysis brings us closer to a better understanding of what type of topography would be the optimal choice for hip implant.

Acknowledgments. This project has received funding from the European Union's Horizon 2020 research and innovation program under grant agreement No. 760921 - PANBioRA. This article reflects only the author's view. The Commission is not responsible for any use that may be made of the information it contains. The research has also been carried out with the support of the Ministry of Education, Science and Technological Development, Republic of Serbia with projects III41007 and OI174028.

References

1. Shan, L., Shan, B., Graham, D., Saxena, A.: Total hip replacement: a systematic review and meta-analysis on mid-term quality of life. Osteoarthritis Cartilage **22**(3), 389–406 (2014)
2. Loberg, J.M.I., Hansson, S., Ahlberg, E.: Characterisation of titanium dental implants I: critical assessment of surface roughness parameters. Open Biomater. J. **2**, 1–8 (2010)
3. Ito, H., Kaneda, K., Yuhta, T., Nishimura, I., Yasuda, K., Matsuno, T.: Reduction of polyethylene wear by concave dimples on the frictional surface in artificial hip joints. J. Arthroplasty **15**, 332–338 (2000)
4. Choudhury, D., Urban, F., Vrbka, M., Hartl, M., Krupka, I.: A novel tribological study on DLC-coated micro-dimpled orthopedics implant interface. J. Mech. Behav. Biomed. Mater. **45**, 121–131 (2015)
5. Roy, T., Choudhury, D., Ghosh, S., Mamat, A.B., Pingguan-Murphy, B.: Improved friction and wear performance of micro dimpled ceramic-on-ceramic interface for hip joint arthroplasty. Ceram. Int. **41**(1), 681–690 (2015)
6. Mattila, R.H., Laurila, P., Rekola, J., Gunn, J., Lassila, L.V., Mäntylä, T., Aho, A.J., Vallittu, P.K.: Bone attachment to glass-fibre-reinforced composite implant with porous surface. Acta Biomaterialia **5**, 1639–1646 (2009)
7. Noyama, Y., Nakano, T., Ishimoto, T., Sakai, T., Yoshikawa, H.: Design and optimization of the oriented groove on the hip implant surface to promote bone microstructure integrity. Bone **52**(2), 659–667 (2013)
8. Vulović, A., Filipović, N.: Computational analysis of hip implant surfaces. J. Serb. Soc. Comput. Mech. **13**(1), 109–119 (2019)

9. Aradhya, K.S.S., Doddamani, M.R.: Characterization of mechanical properties of SiC/Ti-6Al-4V metal matrix composite (MMC) using finite element method. Am. J. Mater. Sci. **5**(3C), 7–11 (2015)
10. Das, S., Sarangi, S.K.: Finite element analysis of femur fracture fixation plates. Int. J. Basic Appl. Biol. **1**(1), 1–5 (2014)
11. Chalernpon, K., Aroonjarattham, P., Aroonjarattham, K.: Static and dynamic load on hip contact of hip prosthesis and Thai femoral bones. Int. J. Med. Health Biomed. Bioeng. Pharm. Eng. **9**, 251–255 (2015)

Deep Learning Based Approach for Assessment of Primary Sjögren's Syndrome from Salivary Gland Ultrasonography Images

Milos Radovic[1,2(✉)], Arso Vukicevic[2,3], Alen Zabotti[4], Vera Milic[5], Salvatore De Vita[4], and Nenad Filipovic[3]

[1] Everseen - R&D Centre - Belgrade, Milutina Milankovica 1z, Belgrade, Serbia
mradovic@kg.ac.rs
[2] Bioengineering Research and Development Center BioIRC Kragujevac, Prvoslava Stojanovica 6, 34000 Kragujevac, Serbia
[3] Faculty of Engineering, University of Kragujevac, Sestre Janic 6, 34000 Kragujevac, Serbia
[4] Azienda Ospedaliero Universitaria, Santa Maria Della Misericordia di Udine, Udine, Italy
[5] School of Medicine, Institute of Rheumatology, University of Belgrade, Belgrade, Serbia

Abstract. Salivary gland ultrasonography (SGUS) has shown a good potential for diagnosing Primary Sjögren's syndrome (pSS). However, existing scoring procedures (based on the manual analysis and grading of images) need further improvements before being established as standardized diagnostic tools. In this study we developed a deep learning based approach for fast and accurate segmentation of salivary glands extended with the scoring of pSS. Total 471 SGUS images were annotated in terms of semantic segmentation and de Vita scoring system. The dataset has been augmented using standard technique (rotation, flip, random crop) and used for training of a deep learning method for segmentation and classification. Our model achieved 0.935 intersection over union (IoU) for segmentation of salivary glands and 0.854 accuracy for classification of pSS stage on validation images. Here, we give an overview of these achievements and show the results.

Keywords: Deep learning · Instance segmentation · Primary Sjögren's syndrome

1 Introduction

Primary Sjögren's syndrome is a chronic autoimmune disease, with the reported rate of occurrence within a range from 200 to 3000 per 100.000 individuals [1]. As recommended in a series of standardized international guides, diagnosis of pSS is performed by accounting of examined clinical symptoms, results of autoantibody tests and salivary gland biopsy. In order to reduce screening costs and avoid invasive procedures there has been a series of initiatives that aim to establish the salivary gland ultrasonography (SGUS) as pSS diagnostic tools [2–7]. However, diagnostic procedure from SGUS images are affected by individual human factors and decisions may vary from physician to physician. For this reason, international experts have recently concluded that there is still no gold standard for SGUS-based pSS diagnosis [8].

N. Filipovic (Ed.): ICCB 2019, LAIS 11, pp. 160–167, 2020.
https://doi.org/10.1007/978-3-030-43658-2_15

Computer-aided diagnosis (CAD) from medical images has been relying on manual feature engineering for a long time. One such example is [9], where the authors extracted 907 histogram-based and descriptive statistics features from segmented salivary glands and fed them into the multilayer perceptron neural network to predict the pSS score. The main drawbacks of this approach is the fact that it doesn't provide a solution for segmentation of salivary glands but relies on other methods to resolve it as a preprocessing step.

Recent developments of deep learning approaches change the perspective in the area of computer vision including medical image analysis [10] as well. In order to enable computer-aided diagnosis of pSS from SGUS, there are two successive steps that need to be resolved: (1) segmentation of salivary glands from SGUS images and (2) scoring of the segmented SGs with respect to a corresponding pSS scoring criteria. In [11], authors utilized deep learning approaches to perform semantic segmentation of salivary glands, however, scoring of the segmented SGs remained unresolved. In this study we present a real-time deep learning based approach that resolves both steps, i.e. it performs fast and accurate segmentation of salivary glands and provides the scoring of the pSS. Flowchart of the proposed approach is depicted in Fig. 1.

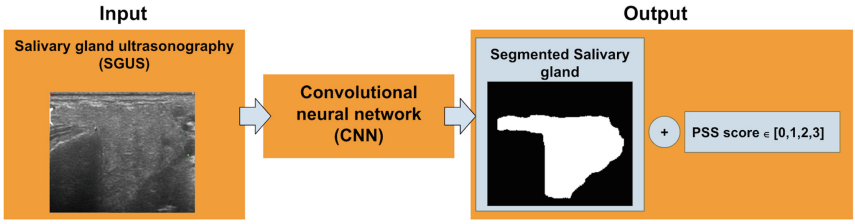

Fig. 1. Flowchart of the proposed approach.

The rest of the article is organized as follows. In Sect. 2 we describe instance segmentation including the Mask R-CNN as one of the most powerful deep learning architectures for the task. In Sect. 3 we describe the dataset and summarize results, while in the last section we present conclusions regarding the advantages of the proposed approach as well as it's potential to be established as an effective tool in medical practice with the final goal to supplement or replace current invasive tests.

2 Instance Segmentation

Instance segmentation is a computer vision task of detecting and delineating each distinct object of interest appearing in an image. In practice, it is often confused with semantic segmentation but major difference between the two exists. Namely, semantic segmentation does not separate instances of the same class. It only predicts the category of each pixel. On the other hand, instance segmentation is another approach for segmentation which does distinguish between separate objects of the same class. Instance segmentation can be seen as a combination of detection and semantic segmentation (see Fig. 2).

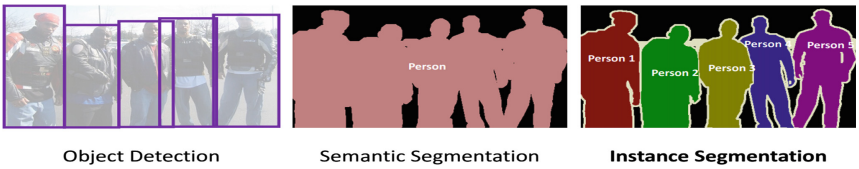

Fig. 2. Example for different visual tasks. (Image taken from [12]).

Instance segmentation has a wide application domain (e.g. autonomous vehicles, satellite image processing, etc.) and for this reason a lot of research has been conducted in the area. One of the most popular approaches for instance segmentation is Mask R-CNN [13]. However, recently, other approaches have been proposed as well [14–17].

The biggest drawback of instance segmentation is that it requires all training examples to be labeled with segmentation masks which is time-consuming. However, recently in [18] authors proposed an approach that enables training instance segmentation models on a large set of categories all of which have bounding box annotations, but only a small fraction of which have mask annotations.

Mask R-CNN

Mask R-CNN [13] is a CNN architecture for instance segmentation that is built on top of the Faster R-CNN [19] architecture by adding a branch to build a mask. The main components of the Mask R-CNN model are: (1) Feature Extraction Network that outputs feature maps to be used as inputs to the following component, (2) Region Proposal Network (RPN) that detects region of interests (ROIs) from the previously extracted feature maps, (3) ROI Align that warps the variable size ROIs into a predefined size shape, (4) Detection branch consisting from fully connected layers to make classification and bounding box prediction, and (5) Segmentation branch responsible for segmentation (i.e. outputting a mask). Simplified architecture of the Mask R-CNN with all described components is given in Fig. 3.

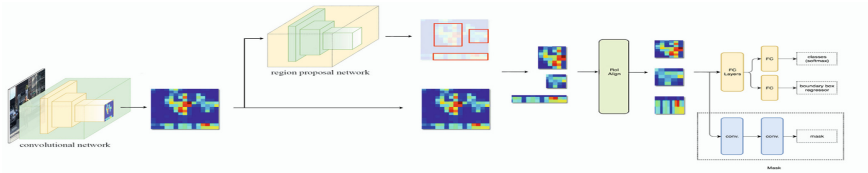

Fig. 3. Mask R-CNN architecture. (Image taken from [20]).

In this research we utilized the Mask R-CNN architecture as it stands for one of the most powerful deep learning architecture for instance segmentation tasks. The neural network is optimized using stochastic gradient descent method with momentum. Values of the learning rate, momentum constant and number of training epochs were set to 0.0002, 0.9 and 100000, respectively.

3 Results

3.1 Dataset Description

The proposed study represents the result of HarmonicSS (https://www.harmonicss.eu) project, which is the EU commission funded initiative of leading Sjögren's syndrome experts with the goal to envelop international cohorts and develop procedures that will ease clinicians' training, diagnosis and treatment of the pSS disease. In this study, we used 471 SGUS images that had been annotated in terms of semantic segmentation (masks) and de Vita scoring system (PSS_score $\in$[0,3]) by medical experts. All images have 720 $\times$ 1280 resolution. In order to prepare the dataset for training of the Mask R-CNN, annotations are converted to a format suitable for instance segmentation methods in a way that every pixel contains label and every image contains accompanying XML file with bounding box coordinates. Examples of annotated images are depicted in Fig. 4.

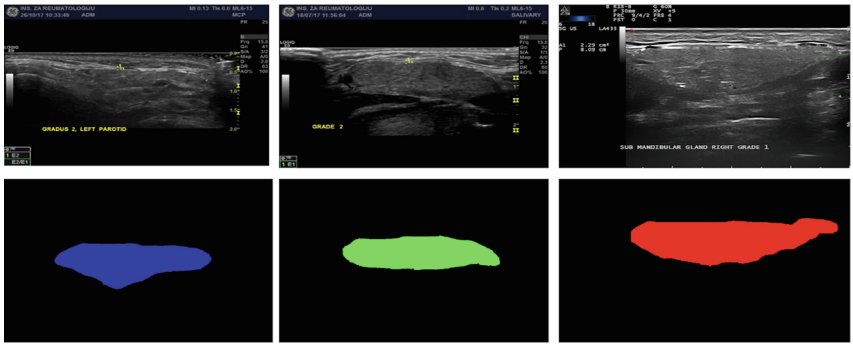

Fig. 4. Sample images from the dataset (top) with corresponding annotations (bottom). Different colors represent different classes (pSS scores): red - stage 0, green - stage 1 and blue - stage 2 (stage 3 example is omitted due to space limitation).

In order to train the neural network, we split the dataset into training dataset (~80%) and validation dataset (~20%). In order to overcome the fact that dataset is modest and prevent model from overfitting we applied online data augmentation using standard techniques: (1) rotation (with 50% probability), (2) horizontal flip (with 50% probability) and (3) random crop (with minimum 50% of salivary gland covered).

3.2 Results on the Salivary Gland Segmentation and pSS Score Prediction Tasks

In this section we present evaluation procedure and results of the Mask R-CNN for the salivary gland segmentation and pSS score prediction tasks. One of the metrics that can be used for the problem presented in this work is Mean Average Precision (MAP). Average precision (AP) is a popular metric in measuring the accuracy of object detectors (like Faster R-CNN [19], SSD [21], etc.) and it computes the average precision value for recall value over 0 to 1. MAP is usually Average Precision (AP) averaged over a set of Intersection over Union (IoU) thresholds (the minimum IoU to consider a positive match). For instance, AP@[.5:.95] corresponds to the average AP for IoU from 0.5 to

0.95 with a step size of 0.05. The metric described above is initially established for object detection tasks, but can be successfully applied to instance segmentation tasks as well by calculating IoU on masks instead of bounding boxes.

The problem that we are solving in this work is specific in terms that every image contains exactly one object (salivary gland) and for this reason, within evaluation procedure, we take the prediction (output of the Mask R-CNN) with the highest probability and filter out all the others. In addition, instead of using MAP we used the following metrics:

- IoU calculated on the accumulated confusion matrix (all images from the validation dataset):

$$IoU(c) = \frac{\sum_i \quad (o_i == c \wedge y_i == c)}{\sum_i \quad (o_i == c \vee y_i == c)}$$

where $\wedge$ is a logical *and* operation, $\vee$ is a logical *or* operation, c stands for the 'gland' class, o_i stands for predictions and y_i stands for targets. We compute IoU by summing over all the pixels i of the dataset. This metric ranges between 0 (worst) and 1 (best) and it is utilized for evaluating the salivary gland segmentation task.

- Precision, Recall, Accuracy and F1 score that are utilized to evaluate pSS score (pSS $\in$[0,1,2,3]) prediction task (all metrics ranges between 0 - worst and 1 - best).

Mask R-CNN obtained 0.935 IoU value on the validation dataset (96 images) for the salivary gland segmentation task. In addition, Table 1 summarizes the results on the pSS score prediction task both micro and macro averaged.

Table 1. Results on the pSS classification task.

Class	No. of samples	Precision	Recall	F1 Score	Accuracy
Stage 0	28	0.96	0.93	0.95	0.854
Stage 1	15	0.56	0.67	0.61	
Stage 2	47	0.89	0.87	0.88	
Stage 3	6	1.00	0.83	0.91	
Micro avg	96	0.85	0.85	0.85	
Macro avg	96	0.85	0.83	0.84	

Results given in Table 1 confirm high potential of deep learning approaches for the pSS score prediction task. Obtained F1 score ranges from 0.61 for stage 1 class up to 0.95 for stage 0 class, with macro averaged value of 0.84. In addition, Mask R-CNN showed great potential for segmenting the salivary gland as well (with obtained 0.935 IoU value). Comparison of ground truth (targets) with predictions of three random images from the validation dataset is given in Fig. 5.

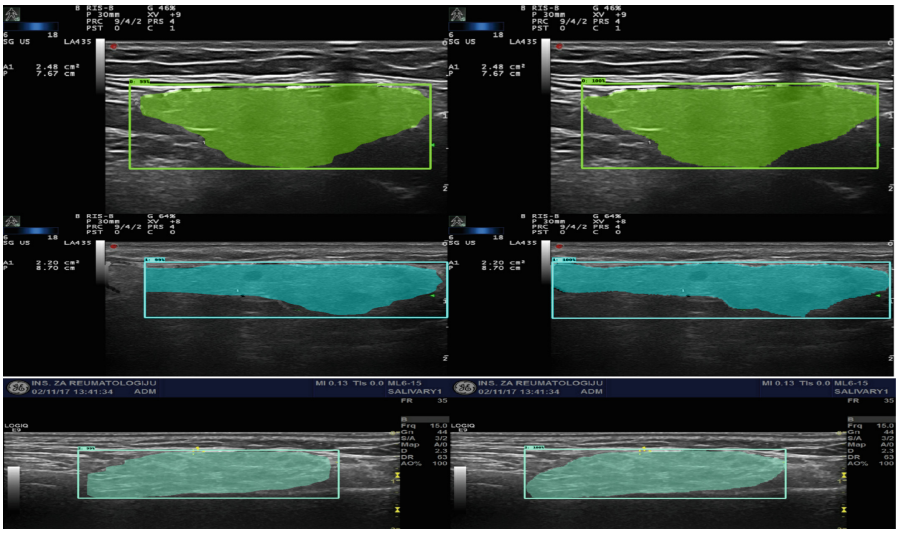

Fig. 5. Comparison of ground truth (right part on each image) with predictions (left part on each image) of three random images from the validation dataset. Different colours correspond to different pSS scores: (1) stage 0 (top image), (2) stage 1 (middle image), and (3) stage 2 (bottom image).

The Mask R-CNN approach was trained on Nvidia 1070Ti graphical processing unit (GPU) and the system can be run at 12 frames per second (FPS).

4 Conclusions

In this work we showed a high potential of deep learning approaches for real-time assessment of the pSS from SGUS images. The presented approach does not require any image preprocessing or feature engineering and it presents end-to-end solution for salivary gland segmentation and pSS score prediction. With further increase of the HarmonicSS cohort, that is required for further validation, the presented method could be established as an effective tool for noninvasive assessment of pSS with the final goal to supplement or replace current invasive tests.

Acknowledgments. This study was funded by the Serbian government (grant agreements III41007 and ON174028) and EU Horizon 2020 RIA programme (HarmonicSS, grant 731944).

References

1. Mavragani, C.P., Moutsopoulos, H.M.: Sjögren syndrome. CMAJ **186**(15), E579–E586 (2014)
2. Hocevar, A., Ambrozic, A., Rozman, B., Kveder, T., Tomsic, M.: Ultrasonographic changes of major salivary glands in primary Sjogren's syndrome. Diagnostic value of a novel scoring system. Rheumatology **44**(6), 768–772 (2005)

3. Salaffi, F., Carotti, M., Iagnocco, A., Luccioli, F., Ramonda, R., Sabatini, E., De Nicola, M., Maggi, M., Priori, R., Valesini, G., Gerli, R., Punzi, L., Giuseppetti, G.M., Salvolini, U., Grassi, W.: Ultrasonography of salivary glands in primary Sjögren's syndrome: a comparison with contrast sialography and scintigraphy. Rheumatology **47**(8), 1244–1249 (2008)
4. Milic, V.D., Petrovic, R.R., Boricic, I.V., Marinkovic-Eric, J., Radunovic, G.L., Jeremic, P.D., Pejnovic, N.N., Damjanov, N.S.: Diagnostic value of salivary gland ultrasonographic scoring system in primary Sjogren's syndrome: a comparison with scintigraphy and biopsy. J. Rheumatol. **36**(7), 1495–1500 (2009)
5. Milic, V.D., Petrovic, R.R., Boricic, I.V., Radunovic, G.L., Pejnovic, N.N., Soldatovic, I., Damjanov, N.S.: Major salivary gland sonography in Sjögren's syndrome: diagnostic value of a novel ultrasonography score (0–12) for parenchymal inhomogeneity. Scand. J. Rheumatol. **39**(2), 160–166 (2009)
6. De Vita, S., Lorenzon, G., Rossi, G., Sabella, M., Fossaluzza, V.: Salivary gland echography in primary and secondary Sjögren's syndrome. Clin. Exp. Rheumatol. **10**(4), 351–356 (1992)
7. Luciano, N., Baldini, C., Tarantini, G., Ferro, F., Sernissi, F., Varanini, V., Donati, V., Martini, D., Mosca, M., Caramella, D., Bombardieri, S.: Ultrasonography of major salivary glands: a highly specific tool for distinguishing primary Sjögren's syndrome from undifferentiated connective tissue diseases. Rheumatology **54**(12), 2198–2204 (2015)
8. Jousse-Joulin, S., Nowak, E., et al.: Salivary gland ultrasound abnormalities in primary Sjögren's syndrome: consensual US-SG core items definition and reliability. RMD Open **3**(1), e000364 (2017)
9. Vukicevic, A., Filipovic, N., Milic, V., Zabotti, A., Hocevar, A., Di Lucia, O., Filippou, G., De Vita, S., Frangi, A.F., Tzioufas, A.: Radiomics-based assessment of Primary Sjogren's Syndrome from salivary gland ultrasonography images. IEEE J. Biomed. Health Inform. (2019). https://doi.org/10.1109/jbhi.2019.2923773
10. Litjens, G., Kooi, T., Bejnordi, B.E., Setio, A.A.A., Ciompi, F., Ghafoorian, M., Van Der Laak, J.A., Van Ginneken, B., Sánchez, C.I.: A survey on deep learning in medical image analysis. Med. Image Anal. **42**, 60–88 (2017)
11. Radovic, M., Vukicevic, A., Zabotti, A., Milic, V., De Vita, S., Filipovic, N.: Deep learning based approach for assessment of primary Sjögren's syndrome from salivary gland ultrasonography images. In: 8th International Conference on Computational Bioengineering (ICCB2019) (2019)
12. Liu, Y.: The Confusing Metrics of AP and mAP for Object Detection/Instance Segmentation (2018). https://medium.com/@yanfengliux/the-confusing-metrics-of-ap-and-map-for-object-detection-3113ba0386ef
13. He, K., Gkioxari, G., Dollár, P., Girshick, R.: Mask R-CNN. In: 2017 IEEE International Conference on Computer Vision (ICCV), Venice, Italy (2017)
14. Huang, Z., Huang, L., Gong, Y., Huang, C., Wang, X.: Mask scoring R-CNN. In: Conference on Computer Vision and Pattern Recognition (CVPR) (2019)
15. Chen, K., Pang, J., Wang, J., Xiong, Y., Li, X., Sun, S., Feng, W., Liu, Z., Shi, J., Ouyang, W., Change Loy, C., Lin, D.: Hybrid task cascade for instance segmentation. In: Conference on Computer Vision and Pattern Recognition (CVPR) (2019)
16. Chen, X., Girshick, R., He, K., Dollár, P.: TensorMask: a foundation for dense object segmentation. In: International Conference on Computer Vision (ICCV) (2019)
17. Bolya, D., Zhou, C., Xiao, F., Jae Lee, Y.: YOLACT: real-time instance segmentation. In: International Conference on Computer Vision (ICCV) (2019)
18. Hu, R., Dollár, P., He, K., Darrell, T., Girshick, R.: Learning to segment every thing. In: Conference on Computer Vision and Pattern Recognition (CVPR) (2018)
19. Ren, S., He, K., Girshick, R., Sun, J.: Faster R-CNN: towards real-time object detection with region proposal networks. In: Conference on Computer Vision and Pattern Recognition (CVPR) (2016)

20. Hui, J.: Image segmentation with Mask R-CNC (2018). https://medium.com/@jonathan_hui/image-segmentation-with-mask-r-cnn-ebe6d793272
21. Liu, W., Anguelov, D., Erhan, D., Szegedy, C., Reed, S., Fu, C.Y., Berg, A.C.: SSD: single shot multibox detector. In: European Conference on Computer Vision (ECCV) (2016)

Author Index

N. Filipovic (Ed.): ICCB 2019, LAIS 11, p. 169, 2020.
https://doi.org/10.1007/978-3-030-43658-2